



Universiteit
Leiden
The Netherlands

A radio view of dust-obscured star formation

Vlugt, D. van der

Citation

Vlugt, D. van der. (2023, December 6). *A radio view of dust-obscured star formation*. Retrieved from <https://hdl.handle.net/1887/3665936>

Version: Publisher's Version

License: [Licence agreement concerning inclusion of doctoral thesis in the Institutional Repository of the University of Leiden](#)

Downloaded from: <https://hdl.handle.net/1887/3665936>

Note: To cite this publication please use the final published version (if applicable).

A radio view of dust-obscured star formation

Proefschrift

ter verkrijging van
de graad van doctor aan de Universiteit Leiden,
op gezag van rector magnificus prof.dr.ir. H. Bijl,
volgens besluit van het college voor promoties
te verdedigen op woensdag 6 december 2023
klokke 12:30 uur

door

Dieuwertje van der Vlugt
geboren te Hillegom, Nederland
in 1994

Promotor: Prof.dr. H.J.A Röttgering

Co-promotor: Dr. J.A. Hodge

Promotiecommissie: Prof.dr. I.A.G. Snellen

Prof.dr. M.T. Kriek

Prof.dr. P.P. van der Werf

Prof.dr. M. Franx

Dr. E. da Cunha

(University of Western Australia)

Dr. J.A. Zavala

(National Astronomical

Observatory of Japan)

Copyright © 2023 D. van der Vlugt

ISBN: 978-94-6419-965-9

Cover: Wassily Kandinsky, 'Stars', 1938, JSP Estate Collection, nr. 158, via Wikimedia Commons.

Printed by: Gildeprint

Heelal
Hoe verder men keek,
hoe groter het leek.
- Jules Deelder (1981)

Contents

1	Introduction	1
1.1	The Λ CDM Universe	1
1.2	Formation of galaxies	3
1.3	Tracing galaxy evolution	4
1.3.1	Star formation	4
1.3.2	Tracers of star formation	5
1.4	Determining star formation with radio observations	8
1.4.1	The radio spectrum	12
1.4.2	Dust-unbiased star formation	15
1.5	The cosmic star formation rate density	19
1.5.1	Dust-obscured star formation	19
1.6	This thesis	23
1.7	The future	23
2	An ultra-deep multi-band VLA survey of the faint radio sky:	
	Source catalog and number counts	27
2.1	Introduction	28
2.2	Observations and data reduction	32
2.2.1	Observations	32
2.2.2	Calibration	33
2.2.3	Bandwidth and time smearing	33
2.2.4	Imaging	35
2.2.5	Confusion	36
2.3	Final image and Cataloging	37
2.3.1	Source detection and characterization	40
2.3.2	Resolved sources	40
2.3.3	Flux boosting	44
2.3.4	Flux density uncertainties at 3 GHz	44
2.3.5	Astrometry	45
2.3.6	Completeness	46
2.3.7	Reliability	48
2.3.8	Source catalog	50

2.4	Results	50
2.4.1	Radio source counts	50
2.4.2	The sub- μ Jy source counts at 3 GHz compared to observations	55
2.4.3	The sub- μ Jy source counts at 3 GHz compared to simulations	60
2.4.4	The sub- μ Jy source counts at 10 GHz	62
2.5	Summary & Conclusions	66
2.A	Postage stamp images	69
3	New constraints on the cosmic star formation history	71
3.1	Introduction	72
3.2	Data and sample selection	74
3.2.1	Radio data	74
3.2.2	Counterparts	75
3.2.3	Sample selection	76
3.2.4	VLA-COSMOS 3 GHz Large Project	78
3.3	Analyses	79
3.3.1	Estimating the LF	79
3.3.2	Constraining the LF	80
3.3.3	COSMOS-XS: Pure luminosity evolution	81
3.3.4	COSMOS-XS + VLA-COSMOS 3 GHz samples: Luminosity and density evolution	84
3.4	A comparison with luminosity functions from the literature	88
3.4.1	Radio	88
3.4.2	Far-infrared	88
3.4.3	UV	92
3.4.4	Radio vs. FIR vs. UV	95
3.4.5	Evolution parameters	96
3.5	Potential biases and additional caveats	97
3.5.1	AGN contamination	97
3.5.2	Radio spectral indices	101
3.6	Cosmic star formation rate history	101
3.6.1	Calculating the SFRD	101
3.6.2	Luminosity evolution vs. density and luminosity evolution	102
3.6.3	FIR-radio conversion	104
3.6.4	Comparison with the literature	105
3.7	Summary & Conclusions	110
3.A	Cosmic variance	113

3.B	Luminosity functions of star-forming galaxies	115
3.C	Posterior distributions	118
4	New constraints on the optically dark population	121
4.1	Introduction	122
4.2	Data and sample selection	123
4.2.1	COSMOS-XS	123
4.2.2	Counterparts and sample selection	123
4.2.3	‘Optically dark’ sources	124
4.3	Contribution of the ‘optically dark’ population to the SFRD	128
4.3.1	Constraining the LF	128
4.3.2	SFRD	131
4.3.3	Discussion	132
4.4	Summary & Conclusions	135
5	ALMA confirms optically dark population at $z > 3$	137
5.1	Introduction	138
5.2	Data and sample selection	139
5.2.1	Selection of dark sources	139
5.2.2	ALMA follow-up observations and data reduction	140
5.2.3	Multi-wavelength photometry	142
5.3	Properties of the galaxies	144
5.3.1	Line identification	144
5.3.2	Redshifts	146
5.3.3	SED fitting	146
5.3.4	Far-infrared luminosity	148
5.3.5	Star formation rates	151
5.3.6	Radio-FIR correlation	153
5.4	Contribution to the cosmic star formation rate density history	155
5.5	Summary & Conclusions	159
5.A	ALMA spectra	161
5.B	SED fitting results	161
5.C	Line fitting results	161
	Bibliography	173
	Summary	183

Nederlandse samenvatting	187
Publications	193
Curriculum Vitae	195
Acknowledgments	197

1 | Introduction

How the present-day Universe formed is a challenging question, and the study of galaxies (including their gas, stars and dust) can be used to help uncover the history of the Universe. In this thesis, we use radio observations to understand how galaxies and star formation evolved from a period when the Universe was only ~ 1 billion years old to the present day. Remarkably, the foundations for the formation of galaxies were established shortly after the Big Bang, more than 13 billion years ago. We thus begin with a short introduction to the very early Universe before discussing the specifics of tracing galaxy evolution with deep radio observations. We then give an overview of the scientific chapters of this thesis. We end this chapter with a brief look toward the future.

1.1 The Λ CDM Universe

In 1936, Hubble discovered that the radial velocities of galaxies are related to their distance by

$$v = H_0 d, \quad (1.1)$$

where d is the proper distance, an invariant distance measure which is the same for all observers, and H_0 is the Hubble constant, which is measured to be approximately $70 \text{ km s}^{-1} \text{ Mpc}^{-1}$ (e.g., Bennett et al. 2013; Brout et al. 2022). The finding of Hubble is best explained by an expanding Universe.¹ Extrapolating back in time would mean that the current observed Universe must have originated from an extremely dense and hot state. This theory is known as the hot Big Bang which can be described with the Λ CDM model. As the currently accepted cosmological model, Λ CDM is the most simple parametrization of the hot Big Bang model and describes the evolution of the Universe with only six parameters. The discovery of the cosmic microwave background (CMB) lends strong support for the hot Big Bang (Penzias & Wilson 1965). The CMB is the afterglow of the early Universe and formed about 380,000 years ago when, after cooling, the protons and electrons in the primordial plasma recombined. Consequently, the photons, previously bound to the matter, could move freely and the Universe became transparent to photons. These photons are observed

¹ Other theories like the steady state model were long considered but have fallen in disfavor in light of the discovery of the CMB; see also Section 1.4.

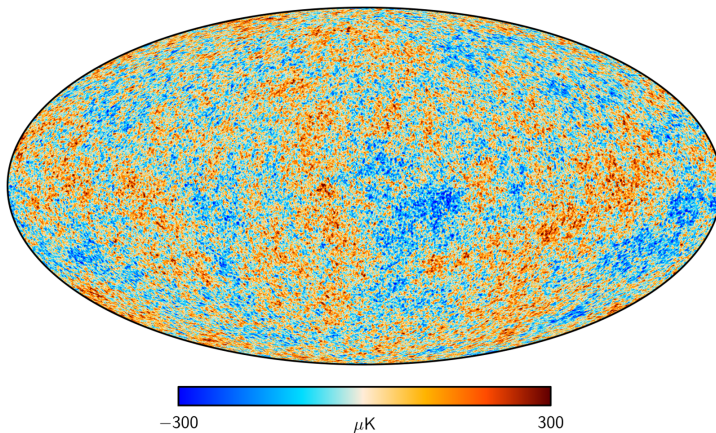


Figure 1.1: The temperature fluctuations in the cosmic microwave background from the four-year Planck satellite observations from the Planck Collaboration et al. (2020). The CMB is the afterglow of the early Universe and constitutes the earliest observable light from the Universe. The CMB is highly uniform and has an average temperature of 2.73 K. The color scale in this figure represents the small deviations in temperature of the order of μK . Slightly over-dense regions in the CMB give rise to future sites of galaxy formation.

as the CMB, redshifted to microwave wavelengths. High-precision measurements of the CMB, shown in Fig. 1.1, show tiny temperature fluctuations at the 10^{-5} level (Baumann 2009) which are associated with the primordial density fluctuations of the Universe.

The primordial fluctuations are thought to have been seeded in the epoch known as ‘Inflation’ which was introduced in order to explain the flatness, homogeneity and isotropy of the Universe today. The rapid expansion allowed for the ‘quantum flutterings’ to become classical fluctuations detectable as temperature fluctuations in the CMB (see Fig. 1.1; Clesse 2015). The form of the CMB, an almost perfect black-body spectrum with tiny fluctuations, is in accordance with the Cosmological Principle; the Universe looks statistically the same from all the possible points of view, in all the possible directions in which it is observed. This requires a causal connection in its beginning which is explained by the period of inflation. The entire observable Universe emerged out of the same causal region before the onset of inflation (Clesse 2015).

The ΛCDM model does not explain the nature and origin of dark energy and dark matter. Dark matter was introduced to explain the observed velocity dispersions within galaxy clusters (e.g., Springel et al. 2005) and rotational velocity curves of galaxies (e.g., Rubin & Ford 1970). Both indicated the existence of a large matter component that was not observed. Observations of merging clusters indicate that dark

matter particles are collisionless and only interact through gravity. The most famous example of this is the Bullet cluster, which showed that the dark matter component of the cluster could bypass the gas (Markevitch et al. 2004). The dark matter thus did not show evidence of interactions other than gravitational interactions. However, no experiment to date has successfully detected dark matter particles. The final element of the Λ CDM model is dark energy, which is called ‘dark’ since its nature remains unclear. The evidence for dark energy, a force acting against the pull of gravity, comes from distance measurements of supernovae showing that the Universe expands and that this expansion is accelerated (for a review see Peebles & Ratra 2003).

1.2 Formation of galaxies

Current theories of structure formation trace structure growth from the gravitational collapse of small perturbations, seen in the CMB, in a Universe dominated by cold dark matter (CDM). In the framework of CDM models, the collapse of structures proceeds bottom-up on larger and larger scales, giving rise to a hierarchy of smaller structures that are incorporated into larger ones at later times (White & Rees 1978).

The evolution of the Universe can be distinguished into different epochs. Dark matter perturbations start to grow fast after the radiation dominated era, when the Universe was dominated by the effects of radiation.² Baryonic matter perturbations start to grow after recombination, they then follow the dark matter perturbations and grow in density and size until they turn non-linear. According to the Λ CDM scenario, galaxies form within the dark matter haloes out of the baryons. Unlike dark matter, which is collisionless, gas can dissipate thermal energy through radiative cooling. The hot gas in haloes, heated in virialization and mergers, cools radiatively and condenses as it sinks towards the potential well minimum. When a region in such a dense cloud becomes dense enough, it collapses and forms stars. Many of these dense clouds together will form groups of stars and eventually galaxies.

In the first phase of structure formation, the Universe remained in a neutral state. When the first stars, galaxies and quasars formed, they produced energetic photons and began to re-ionize the hydrogen in the Universe. This started around $z \approx 15 - 50$ and is called the epoch of re-ionization (Loeb & Barkana 2001; Barkana & Loeb 2001). Around 1 billion years after the Big Bang (Wise 2019), re-ionization was complete, and structures in the Universe continued forming and growing. After this epoch, the Universe was full of low density ionized plasma, making galaxies observable. The

² The rapid expansion of the Universe during the radiation dominated epoch nearly suppresses structure growth during this period.

electrons were sufficiently far apart that the amount of scattering interactions of photons and electrons were much less frequent. At $z \approx 2$ the peak of star formation (e.g., Madau & Dickinson 2014) and quasar activity (e.g., Croton et al. 2006) took place, where most of the black hole and galaxy growth is believed to occur. Matter and dark energy are the dominant components in the present-day Universe ($z = 0$) (e.g., Frieman et al. 2008).

The formation of stars and galaxies is an inefficient process; only $\sim 10\%$ of the baryonic mass is locked up in stars and cold gas (e.g., Shull et al. 2012). This means that there is a mechanism suppressing star formation by injecting energy in the interstellar medium (ISM) to prevent the gas in galaxies from cooling. Supernova explosions are such a phenomena as they inject energy in their surrounding medium and can drive galaxy-wide outflows, In addition, it is believed that supermassive black holes (SMBHs) residing in the center of galaxies (active galactic nuclei; AGN) drive outflows. Semi-analytical models have shown that these high-velocity outflows are important for regulating the growth of massive galaxies (e.g., Croton et al. 2006; Sijacki et al. 2007), as their feedback can heat the halo gas surrounding the galaxy which quenches the star formation and growth of the galaxy.

1.3 Tracing galaxy evolution

The evolution of a galaxy is shaped by many factors and complex processes. Observing and characterizing the properties of galaxies across galaxy populations and cosmic time give us one way to gain insight into these processes. Stars are the most visible constituents of galaxies, and thus understanding the evolution of star formation helps us understand how galaxies evolve.

1.3.1 Star formation

Stars form when molecular clouds collapse under their own gravity. To describe the radiation from newly formed stars, we can use a model know as a Simple Stellar Population (SSP). Such a model assumes the stars that it describes to be born at roughly the same time, and also from the same gas, meaning they have the same initial chemical composition (Bruzual 2010). A galaxy can then simply be described as a combination of SSPs. To then model the evolution of stars in the SSP, we can use stellar evolution models, which provide complete sets of stellar evolutionary tracks for stars of different mass and metallicity. The path which a star follows across the Hertzsprung-Russel diagram, a diagram showing the relation between the

luminosity of a star and their stellar classification, is called an evolutionary track. The metallicity of the stars stems from the initial composition as assumed in the SSP and the mass of stars is determined by the assumed initial mass function (IMF), which describes the initial distribution of masses for the population of stars born in molecular clouds. Commonly used forms of the IMF are the Salpeter (1955) power law, the Kroupa (2001) broken power law and the Chabrier (2003) log-normal. To convert the theoretical predictions from the SSPs into observables, theoretical and empirical spectral libraries are needed.

To characterize a galaxy across the electromagnetic spectrum, we make use of spectral energy distributions (SEDs) which describe the total energy emitted as a function of wavelength. An SED is a combination of stellar emission, possible AGN activity, and dust attenuation and emission. An SED can thus be constructed from multiple SSPs taking into account the star formation history (SFH) of the galaxy. The SFH describes the evolution of the amount of star formation over time. Since stars form metals during their evolution, the SFH also includes metallicity evolution. Because the shape of the SFH is complex, it is usually parameterized with a simple analytical function. To now construct the SED, the amount of dust in a galaxy should be taken into account. Dust can attenuate the UV light emitted by stars and this light gets reprocessed by the dust emitting in the infrared. The effect of dust can be seen in Fig. 1.2. The figure shows the unattenuated light in blue and the dust reprocessed emission in red. The comparison of the two lines, especially at optical wavelengths ($\lambda \lesssim 1.0 \mu\text{m}$), shows how the shape of the stellar emission and infrared emission is altered by dust attenuation.

The emission of galaxies observed at different wavelengths can be modelled using an SED fitting code which uses the SSPs, SFHs and dust attenuation models to describe the observations. The fitted SED can be used to estimate fundamental properties such as the stellar mass, dust mass and the star formation rate (SFR; e.g., da Cunha et al. 2015). The SFR is an essential quantity describing the evolution of a galaxy – it describes how quickly a galaxy is converting the available gas into stars over time.

1.3.2 Tracers of star formation

SED models of galaxies have shown us how observables at different wavelengths can be linked to the physical properties of a galaxy, and specifically the star formation. In the following sections, we will discuss how different tracers can be used to study the star formation of a galaxy.

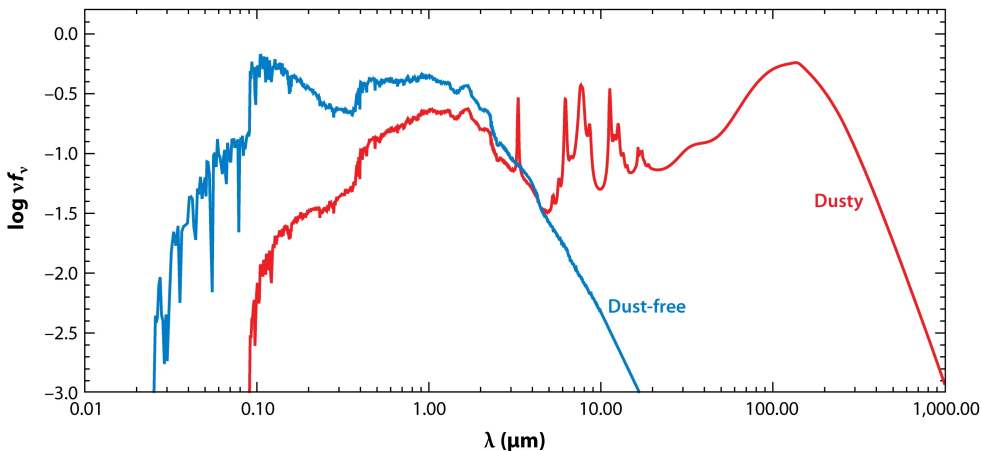


Figure 1.2: Example of a spectral energy distribution (SED) from Conroy (2013). The SED shows the amount of light emitted by a galaxy with the unattenuated light in blue and the attenuated emission in red. Comparing the unattenuated and attenuated emission shows the effect of dust attenuation on a galaxy’s SED.

Ultraviolet

In principle, ultraviolet (UV) light is the most direct tracer of SFR in dust-free environments across timescales of $\sim 10\text{--}200$ Myr (Kennicutt & Evans 2012). In the absence of an (unobscured) AGN, the unattenuated light with wavelengths ranging from $\lambda \sim 0.125\ \mu\text{m}$ to $\lambda \sim 0.25\ \mu\text{m}$ originates mainly from massive stars with lifetimes of $10\text{--}200$ Myr and directly traces young stellar populations and hence the UV luminosity and SFR are linearly correlated (Kennicutt 1998). UV observations can thus be used to constrain the unobscured star formation out to very high redshifts ($z \simeq 9$; e.g., McLure et al. 2013; Bouwens et al. 2015; Bowler et al. 2015; Finkelstein et al. 2015; McLeod et al. 2015; Bouwens et al. 2016; Parsa et al. 2016; Mehta et al. 2017; Ono et al. 2018; Oesch et al. 2018; Bouwens et al. 2021). Measuring the SFR becomes uncertain for star-forming galaxies (SFGs) containing dust because dust can attenuate the UV emission. For SFGs that lie on the main sequence (MS, the nearly linear relation between SFR and stellar mass followed by most SFGs) this can result in an attenuation of $0.5\text{--}3$ magnitudes (e.g., Salim & Narayanan 2020). For strongly dust-obscured galaxies the dust attenuation can be much higher.

UV observations thus need significant and uncertain corrections for dust obscuration. Also UV observations are unable to detect the most extreme SFGs in which star formation is completely enshrouded in dust (e.g., Smail et al. 1997; Lutz et al. 2011; Riechers et al. 2013; Casey et al. 2014a; Dudzevičiūtė et al. 2020). Therefore,

knowledge on how the dust attenuation evolves with redshift is mandatory to study the redshift evolution of SFGs.

Infrared

Dust in the ISM, heated by young massive stars, re-emits absorbed UV light at longer wavelengths and can thus be studied in the far-infrared (FIR) or sub-millimeter (sub-mm) to trace the SFR. The dust itself is partly produced in supernova explosions which occur during the last evolutionary stages of massive stars ($M > 8M_{\odot}$; e.g., Rho et al. 2008). In addition, it has been argued that dust grains grow in the ISM by the accretion of metals on to grains (Inoue 2003). Some dust also originates from the evolutionary stage of low/intermediate mass asymptotic giant branch (AGB) stars (e.g., Gehrz 1989). Because newly formed stars are bright, SFGs have most of their dust heated by young stellar populations and the emitted FIR will thus directly trace the obscured SFR. The SFR and FIR luminosity are linearly correlated (Kennicutt 1998), where the total FIR luminosity is measured between (rest-frame) 8-1000 μm . Current FIR observations are able to constrain the dust content and SFR of galaxies up to a redshift $z \sim 6$ (e.g., Rodighiero et al. 2010; Gruppioni et al. 2013; Rowan-Robinson et al. 2016; Koprowski et al. 2017; Dudzevičiūtė et al. 2020; Lim et al. 2020). However, the measurements beyond $z \simeq 2$ are uncertain, as source confusion and blending limit the ability to detect faint objects at low resolution. For example, the resolution of the infrared space telescope *Herschel* ranges from 5'' to 36'' whereas a high-redshift galaxy has a typical size of 1''. Neighboring galaxies can thus blend together in observations of infrared telescopes making it difficult to observe and infer the SFRs of these galaxies.

Ground-based sub-mm/mm continuum observations of dusty galaxies can help to overcome some of the problems in FIR observations (e.g., Chapman et al. 2005; Hodge et al. 2013; Swinbank et al. 2014; Dunlop et al. 2017; Dudzevičiūtė et al. 2020; Zavala et al. 2021). In particular, ground-based interferometer arrays (e.g., the Atacama Large Millimeter/sub-millimeter Array (ALMA) which will be discussed in more detail in Section 1.4.1) offer high-resolution observations and hence do not suffer from source blending, though their fields of view are typically small. In addition, singly ionized carbon ([CII]) has been found to correlate with SFR and could therefore be used as a dust-unbiased SFR indicator at low and possibly at high- z (e.g., De Looze et al. 2014; Matthee et al. 2019). [CII] was recently used in several studies conducted with ALMA to study the SFR and its evolution with redshift (Gruppioni et al. 2020; Khusanova et al. 2021; Loiacono et al. 2021).

Radio

Long-wavelength ($\lesssim 100$ GHz) radio emission is another tracer of recent star formation (Condon 1992). Radio emission in galaxies below rest-frame frequencies $\lesssim 30$ GHz is dominated by synchrotron radiation arising from cosmic ray electrons gyrating in the galaxy's magnetic fields (e.g., Sadler et al. 1989; Condon 1992; Clemens et al. 2008; Tabatabaei et al. 2017). These charged cosmic-ray particles are accelerated in shocks launched by supernovae of stars with $M > 8 M_{\odot}$ in SFGs. These massive stars have lifetimes of $\lesssim 3 \times 10^8$ years, so their supernova rates are proportional to the recent SFR. However, SMBHs in AGN can also accelerate the electrons that produce synchrotron emission. The radio emission originating from star formation is a tracer of the SFR which is, unlike UV, not attenuated by dust. In contrast to FIR observations, radio observations often have a high spatial resolution and can cover larger areas of the sky than interferometric sub-mm observations with high angular resolution. Therefore, radio observations offer an alternative way of studying the star formation in galaxies.

1.4 Determining star formation with radio observations

Radio observations are used in this thesis to trace the star formation in galaxies. Radio waves of astronomical origin were first discovered in 1931 by Karl Jansky using a self-constructed radio telescope. Since then, the capabilities of radio telescopes have been immensely improved. Not only have the antennas themselves been upgraded, but also new techniques such as interferometry, developed in the 1950s, have been introduced.

Aperture synthesis

Before 1950 it was impossible to connect observed radio emission with known objects observed at optical wavelengths. The angular resolution of the single-dish radio telescopes that existed back then was too bad. Fortunately, interferometry offered a solution, and Martin Ryle developed the aperture synthesis technique needed to conduct radio observations using multiple antennas. The angular resolution of a telescope is given as $\theta \sim \lambda/D$ where λ is the wavelength and D is the diameter of the telescope. This means that to reach a resolution of $\sim 1''$ at $\lambda \sim 1$ mm, a 2km diameter dish would be needed. Instead, an array of smaller dishes can be used to achieve

high angular resolutions at radio frequencies. When observing a galaxy with an array, the signal from the observed object arrives at each antenna at a different time (due to different travel lengths) depending on the location of the antenna in the array. In aperture synthesis, the signals are then combined in a correlator, where the time delay is measured and compensated for. The time delay gives positional information about the emitting object. The distance between the antennas is called the baseline length and in an interferometer the angular resolution is now, instead of one number, a range of angular sizes: $\lambda/B_{\max} < \theta < \lambda/B_{\min}$ with B_{\max} the maximum baseline in the array and B_{\min} the minimum baseline in the array. The full potential of aperture synthesis is only realized when large numbers of antennas are used simultaneously.

One pair of antennas will only sample one baseline in one direction whereas three antennas will give three baselines, which means sampling the source six times. Thus, for N antennas the source will get sampled $N(N-1)$ times. In addition, more antennas will sample more of the source over time using the Earth's rotation. The rotation will constantly change the position of the antennas with regard to the observed source, causing the direction of the baselines to change with respect to the observed section of the sky and thus sampling different parts of the source. With the development of aperture synthesis, high-resolution radio observations became possible, enabling easier cross-correlation with optical sources. The new technique helped pinpoint strong radio emission observed in, for example, the optically faint galaxy Cygnus A (e.g., Jennison & Das Gupta 1953) and the young supernova remnant Crab Nebula (e.g., Bolton et al. 1949). Observations using aperture synthesis also showed compact strongly emitting radio sources named quasi-stellar objects without an obvious optical counterpart (e.g., Matthews & Sandage 1963). We now know these quasi-stellar objects as quasars which are extremely luminous AGN.

Since the 1950s, not only have radio telescopes been upgraded and developed but also sophisticated calibration techniques have been introduced to produce robust radio maps. To produce a radio image using the observations of an interferometer, many steps such as phase and flux calibration, removing corrupted data, and imaging and performing a deconvolution of the image are needed. This process is called data reduction, and it is designed to mitigate known issues in radio observations. The steps to produce radio continuum observations are covered in **Chapter Two** of this thesis.

The VLA

The radio observations presented in this thesis were carried out with The Very Large Array (VLA). This array was constructed in the 1970s and uses the aperture synthesis

technique. The VLA is an interferometer situated on the Plains of San Agustin in USA at an altitude of approximately 2000m. The array consists of 27 antennas, of 25m diameter, distributed on-site in a Y-shaped configuration. The resulting total collecting area of all antennas is equivalent to a 130m dish. The distances between the antennas can be changed, giving the array the ability to increase or decrease the angular resolution. The four different configurations that can be set are named, from highest to lowest angular resolution, A, B, C and D. The original VLA underwent a major upgrade in 2012 that was emphasized by renaming it the ‘Karl G. Jansky Very Large Array’. The radio observations presented in this thesis profited from this upgrade as the significantly increased bandwidths of the upgraded array now allow for observations of the radio sky down to several hundred nJy beam⁻¹ sensitivities. The upgraded VLA provides continuous frequency coverage from 1 to 50 GHz, with two additional narrower bands centered around 90cm and 4m.

Number counts and luminosity functions

The depth achievable in modern radio surveys now allows for observations of faint (μ Jy) radio-emitting objects, thus enabling constraints on the nature of these populations (e.g., Rujopakarn et al. 2016; Murphy et al. 2017; Smolčić et al. 2017a; Owen 2018; Bondi et al. 2018; Mauch et al. 2020). The simplest statistical analysis that can be performed with a flux-limited radio survey is counting the number of galaxies. Despite the simplicity, this can provide very useful information, as the shape of the number of sources as a function of flux is tightly related to the evolutionary properties of the sources and the geometry of the Universe. If the Universe were Euclidean, the number of sources expected to be found above some flux density S would be $N \propto S^{-3/2}$, or described as the differential number counts: $n = dN/dS \propto S^{-5/2}$. The 2C radio survey (Shakeshaft et al. 1955) showed that the number counts differed from the counts expected from an Euclidean Universe, which was evidence for an evolving Universe (Ryle & Scheuer 1955). Due to some controversy, known as the ‘Sidney-Cambridge controversy’ (Sullivan 1984), about the understanding of source confusion in the 2C radio survey, it took the discovery of the CMB (Penzias & Wilson 1965) to confirm the prediction of the expanding Universe and the hot Big Bang model, but this also showed the power of early radio surveys.

Source counts from radio surveys are currently recognized as essential data in describing the different radio source populations. At high flux densities, the source counts are well-constrained and found to be dominated by AGNs that follow a smooth power-law distribution down to $S_{1.4\text{GHz}} \sim 1$ mJy (e.g., Condon & Mitchell 1984; Windhorst et al. 1990). Below 1 mJy, the Euclidean-normalized source counts flatten

(e.g., Richards 2000; Huynh et al. 2005; Biggs & Ivison 2006; Owen & Morrison 2008; Bondi et al. 2008; Padovani et al. 2015). It is now widely accepted that this observed flattening is due to the emergence of SFGs and radio-quiet AGN, which begin to contribute significantly only at these faint flux densities (e.g., Rowan-Robinson et al. 1993; Seymour et al. 2004; Padovani et al. 2009). Deeper radio observations and $P(D)$ analyses on confusion-limited surveys show evidence of a further steepening of the number counts below $S_{1.4\text{GHz}} \sim 50 \mu\text{Jy}$ (e.g., Condon et al. 2012; Vernstrom et al. 2014, 2016; Smolčić et al. 2017a; Prandoni et al. 2018; Mauch et al. 2020). The composition of this ultra-faint radio population was previously uncertain, but it was expected from simulations and observations that the fraction of SFGs will become significant ($> 60\%$) below $S_{1.4\text{GHz}} \sim 100 \mu\text{Jy}$ (Smolčić et al. 2017b). Constraints on the ultra-faint radio populations at high resolution are useful for predictions for future radio surveys with new and upcoming facilities such the ASKAP, MeerKAT, ngVLA, and SKA, where source confusion noise may be an issue. The number counts presented in **Chapter Two** are constrained with observations achieving sub- μJy r.m.s noise levels, and are thus probing the ultra-faint radio population.

A more advanced analysis of radio surveys involves measuring the cosmic density of sources in bins of luminosity, thus constraining the luminosity function (LF). To construct the LF, the redshift need to be established for the observed sources. Determining the LF for different galaxy populations (e.g., SFG or AGN) can help constrain the evolutionary paths of these populations. The local LF is well-established (e.g., Condon et al. 2002; Best et al. 2005; Mauch & Sadler 2007; Condon et al. 2019) and often used to constrain the LF out to higher redshifts. To do this, the local LF is evolved to fit the high-redshift data. We can distinguish two extreme cases for this evolution: 1) pure luminosity evolution (PLE), meaning the density of sources is constant but luminosities vary with cosmic epoch, and 2) pure density evolution (PDE), which implies the co-moving density of sources of any luminosity varies. Radio studies to-date have observed radio LFs but struggled to reach the knee of the LF (L_*), or the point at which there is a break from the power law describing the LF, at $z > 1$. Because these studies are most sensitive to the SFG population above the knee, the density and luminosity evolution parameters may become degenerate, preventing a precise estimate of the knee location. The VLA-COSMOS 1.4 GHz Large Project and the VLA-COSMOS 3 GHz Large Project from, respectively, Smolčić et al. (2009b) and Novak et al. (2017) thus assumed pure luminosity evolution rather than luminosity and density evolution (Condon & Mitchell 1984) in order to fit the radio LF out to $z \sim 5$. Recently, Malefahlo et al. (2022) used a Bayesian approach to reach below the 5σ detection limit of Novak et al. (2017) but still only constrained pure

luminosity evolution. Enia et al. (2022) used a 1.4 GHz-selected sample to constrain the evolution of the radio LF up to $z \sim 3.5$ by fitting a modified Schechter function (equivalent to fitting both luminosity and density evolution). By constraining the LF and its evolution as is described in **Chapter Three**, it is possible to estimate the cosmic star formation rate density as a function of cosmic time.

1.4.1 The radio spectrum

Radio emission in SFGs has two components related to star formation: free-free emission and synchrotron radiation. Free-free emission is produced during an interaction between charged particles (electrons and protons). Young massive stars ($M \geq 10 - 15M_{\odot}$) create short-lived ionized regions know as HII-region from which the free-free emission originates (Kennicutt & Evans 2012). Free-free emission provides thus a first-hand view on star formation. In addition, unlike UV emission, dust obscuration plays only a minor role, and therefore free-free emission is potentially the most accurate tracer of star formation (e.g., Mezger & Henderson 1967; Turner & Ho 1983, 1985; Klein & Graeve 1986; Kobulnicky & Johnson 1999; Murphy et al. 2012, 2015; Nikolic & Bolton 2012).

Free-free emission is described by a flat power-law $S \propto \nu^{-0.1}$ (e.g., Condon 1992); see Fig. 1.3. At rest-frame frequencies of $\nu \geq 30$ GHz the total radio emission is dominated by free-free radiation (e.g., Condon 1992; Murphy et al. 2011; Klein et al. 2018). This constitutes the faintest part of the radio SED, as can be seen in Fig. 1.3. At $\nu \geq 200$ GHz, free-free emission is no longer the dominant emission term, as thermal emission from dust grains becomes more prevalent. Free-free emission provides information on the star formation process independent of FIR and synchrotron emission. However, isolating the free-free component and measuring its flux density is difficult. Recently, studies have now done this successfully in samples of galaxies beyond the local universe (Algera et al. 2021, 2022). The work in these companion studies was made possible by the ultra-deep 10 GHz radio observations presented in **Chapter Two**.

In comparison to free-free emission, synchrotron emission can be more easily observed. It arises from fairly old ($\geq 10^7$ yr) electrons that traveled some distance (≥ 1 kpc) from the supernova remnants associated with massive stars ($M \geq 8M_{\odot}$) in which they were accelerated (Condon 1992). The emission is described by a power-law $S \propto \nu^{-0.7}$ (e.g., Condon 1992) as can be seen in Fig. 1.3. Such massive stars are short lived, and as such their supernova rate is related to a galaxy's recent star formation rate, albeit with a short delay (≤ 30 Myr; Bressan et al. 2002). Problematically for

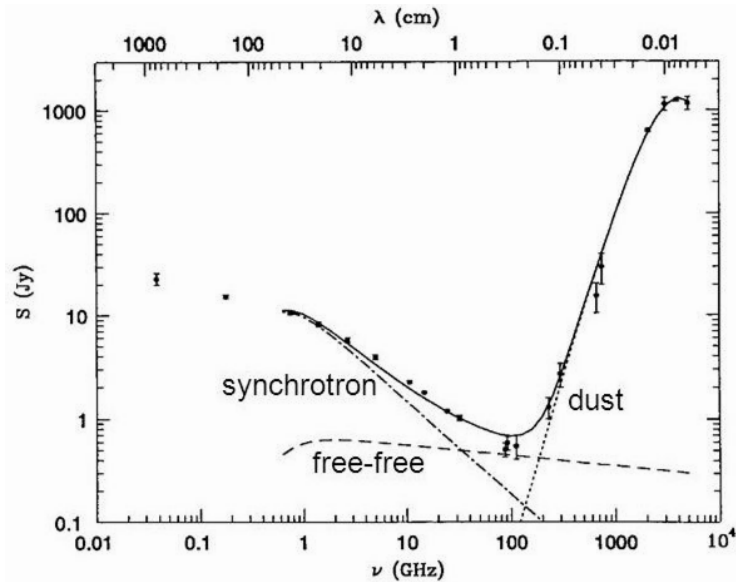


Figure 1.3: Example of a spectral energy distribution (SED) of the starburst galaxy M82 adapted from Klein et al. (1988). The SED shows the flux density as a function of frequency, in this case, from the radio to the far infrared. The solid line shows the total emission from the galaxy. The dot-dashed line shows the synchrotron emission and the dashed line shows the free-free thermal emission. The dotted line $\nu \geq 100$ GHz shows the dust thermal emission. At low frequencies, the synchrotron component is dominant, while at $\nu \geq 30$ GHz, free-free emission overtakes the synchrotron contribution. At higher frequencies, $\nu \geq 200$ GHz, dust overtakes free-free emission.

studying star formation with radio observations, not only supernovae but also AGN can produce powerful radio emission.

AGN

When studying the star formation in galaxies using radio observations, it is important to verify that the observed radio emission is indeed produced by stars. AGN and SFGs are difficult to disentangle in the radio regime because an accreting SMBH in an AGN can also accelerate the electrons that produce synchrotron emission. Synchrotron emission can thus not only be used to study star formation but also to study the black hole accretion activity in the Universe (e.g., Jarvis & Rawlings 2000; Smolčić et al. 2009a; Rigby et al. 2011; McAlpine et al. 2013; Best et al. 2014; Delvecchio et al. 2014, 2017; Sabater et al. 2019). When radio luminosity is used as a proxy for tracing star formation, AGN are considered as contamination of the star-forming sample.

AGN are traditionally classified in two main categories: steep ($\alpha < -0.5$) and flat-

spectrum ($\alpha > -0.5$), where the radio spectrum is described by a power-law $S \propto \nu^\alpha$. Not only SFGs but also AGN can thus have a steep radio spectrum ($\alpha \sim -0.7$). Flatter spectra are typical of compact core emission and are thus only associated with AGN. Constraining the radio spectrum can thus be one method to separate AGN from SFGs. However, using only this method would still leave many AGN in the sample. In addition, the diagnostic might not be available for the vast majority of the sample since multiple radio continuum frequency observations are needed. Therefore, several other methods have been developed for identifying different types of AGN and separating them from SFGs (e.g. Hickox et al. 2009; Mendez et al. 2013; Smolčić et al. 2017b; Delvecchio et al. 2017) using mid-IR data, far-IR data, X-ray information and multi-band optical/IR photometry. A companion study to this thesis by Algera et al. (2020a) used the ultra-deep radio survey presented in **Chapter Two** and the multi-wavelength data available over the field to investigate the composition of the radio population. The sources identified as SFGs are used in **Chapter Three** to determine the evolution of SFR with redshift.

Radio source redshifts

To perform more advanced analysis with a sample of radio sources, such as measuring the LF, redshifts are needed. Fitting a SED model to the stellar and dust emission is a commonly used tool to derive the redshift. However, since the radio spectrum is a featureless power law (Fig 1.3), it can not, alone, be used to constrain the redshift. Multi-wavelength data, either from photometric or spectroscopic surveys, are thus needed to find redshifts for radio sources. Photometric surveys give the average brightness of a galaxy over a fixed wavelength band, with a single measurement point per band, whereas spectroscopic surveys deliver a high-resolution spectrum of a galaxy. Probing photometric redshifts with photometric surveys is cheaper and can be done over larger survey areas, but it delivers more uncertain redshifts. Obtaining a full spectrum with a spectroscopic survey is time consuming but gives more information with details on atomic and molecular lines used to infer the spectroscopic redshifts. These redshifts are measured to high precisions and are therefore more reliable than photometric redshifts. However, it is not cheap to obtain spectroscopic redshifts for large numbers of galaxies, particularly when they are dusty. Targeting CO transitions at millimeter wavelengths with, e.g., ALMA, is a relatively efficient method of obtaining accurate redshifts for radio sources with photometric redshifts.

Redshifts via CO line scans with ALMA

ALMA is an interferometer that started operating in 2011. It is currently the largest millimeter telescope in the world (Wootten & Thompson 2009), and is located on the Chajnantor plateau, in the Atacama Desert, Chile, at an altitude of over 5000m. The array is comprised of 66 antennae: the main array of 50 12m antennae, an array of twelve 7m antennae (Atacama Compact Array; ACA), and a further four 12m antennae (Total Power Array; TPA). The main array offers angular resolutions from a few arcseconds to milli-arcseconds and is a factor of 10-20 \times more sensitive than its precursors for spectral line detections. Additionally, ALMA is 10-100 \times more sensitive for continuum detections. ALMA has enabled many advances in our understanding of star formation at $z > 1$ (Hodge & da Cunha 2020). Of particular interest for this thesis is ALMA’s frequency coverage (35-950 GHz) and sensitivity which enables it to target CO transitions and thus obtain spectroscopic redshifts for gas/dust-rich sources at high ($z > 1$) redshift. This technique is further discussed and used in **Chapter Five**.

1.4.2 Dust-unbiased star formation

Radio observations probe recent star formation ($\lesssim 30$ Myr; Bressan et al. 2002) and are especially valuable for three reasons: 1) Radio emission is not overwhelmed by stellar populations older than 10^8 yr; 2) radio maps can be made with sub-arcsecond resolution; and most importantly 3) radio emission is not attenuated by dust, so that even the most extreme SFGs enshrouded in dust can be observed (e.g., Condon 1992). The discovery of sub-millimeter galaxies (SMGs) (e.g., Downes et al. 1999; Smail et al. 1999; Frayer et al. 2004) showed the importance of a more complete census of star formation history over cosmic time. In particular, since these galaxies are heavily attenuated in the rest-frame UV (e.g., Simpson et al. 2014; Franco et al. 2018; Dudzevičiūtė et al. 2020), they are often missed in UV observations. Via high angular resolution ALMA observations, we can uncover faint SMGs missed by UV-surveys: also classified as ‘optically dark’ sources (e.g., Gruppioni et al. 2020; Gómez-Guijarro et al. 2022; Shu et al. 2022; Xiao et al. 2023). Radio observations can also be used to identify ‘optically dark’ galaxies as has been recently shown (Talia et al. 2021; Enia et al. 2022). To determine the SFR of these galaxies observed in radio surveys, the radio luminosity needs to be linked to the SFR. However, the steps to translate observed synchrotron emission to a SFR, such as supernova explosion, acceleration of electrons by the supernova, propagation of cosmic rays and energy loss, are non-trivial and poorly understood. Fortunately, observations show a tight and ubiquitous

correlation between FIR and radio luminosity, offering a way to derive SFRs from radio observations.

The far-infrared-radio correlation

Given the different timescales of the various processes involved, it is quite remarkable that radio emission triggered by star formation is empirically found to correlate well with the FIR emission of SFGs: the FIR-radio correlation (e.g., Helou et al. 1985). The correlation is parameterized using the dimensionless parameter q_{TIR} as introduced by Helou et al. (1985):

$$q_{\text{TIR}} = \log_{10} \left(\frac{L_{\text{FIR}}}{3.75 \times 10^{12} \text{ W}} \right) - \log_{10} \left(\frac{L_{1.4 \text{ GHz}}}{\text{W Hz}^{-1}} \right). \quad (1.2)$$

where FIR-luminosity L_{FIR} is measured between 8 and 1000 μm , and $L_{1.4 \text{ GHz}}$ is the radio luminosity at 1.4 GHz. The radio SFR can now be derived using the correlation as $\text{SFR} \propto 10^{q_{\text{TIR}}} L_{1.4 \text{ GHz}}$ (e.g., Delhaize et al. 2017). Besides being used to calibrate radio luminosity as a tracer of SFR, the FIR-radio correlation is also often used for the classification of galaxies. For example, a sample of galaxies observed in a radio survey used for constraining the star formation at a given redshift should only consist of sources with radio emission originating from star formation. Therefore one would ideally quantify the emission coming from star formation and AGN in all sources. It is, however, easier to simply remove sources that show an excess in radio emission compared to what is expected from the FIR-radio correlation (radio-excess AGN, e.g., Del Moro et al. 2013; Delvecchio et al. 2017; Algera et al. 2020a). Radio-loud AGN are easily removed by this method, as these sources show a large offset from the FIR-radio correlation. A major uncertainty is the ability to distinguish composite sources, which emit low-level AGN emission, from SFGs (e.g., Padovani et al. 2009; Bonzini et al. 2013).

Radio-SFR calibrations and source classification rely thus on this empirical FIR-radio correlation, which appears to hold across more than five magnitudes in luminosity and persists out to high redshifts (e.g., Helou et al. 1985; Yun et al. 2001; Bell 2003), albeit with ill-constrained redshift evolution (e.g., Sargent et al. 2010; Magagnoli et al. 2015; Calistro Rivera et al. 2017a; Delhaize et al. 2017). Though, there is some discussion about whether the redshift evolution can be ascribed to selection biases (Sargent et al. 2010; Algera et al. 2020b; Smith et al. 2021; Molnár et al. 2021) or whether the FIR-radio correlation should have an additional dependency on mass (Delvecchio et al. 2021; McCheyne et al. 2022). From a theoretical point of view,

the observed evolution is difficult to explain. The evolution contradicted the evolution predicted by theoretical studies: high redshift galaxies were expected to become radio-dim due to inverse Compton losses on the CMB but observations showed that these galaxies appeared increasingly bright. The exact physical processes driving the relation remain unclear, and predictions for the redshift evolution of the FIR-radio correlation are also often conflicting (e.g., Murphy 2009; Lacki & Thompson 2010). Dealing with selection biases is non-trivial and not accounting for such biases would lead to artificial observed evolution in the FIR-radio correlation (e.g., Sargent et al. 2010).

The selection biases are most easily explained by introducing K-corrections which convert the flux of a source from observed-frame to rest-frame. The strength of the K-correction depends on the shape of the SED. For example, FIR/sub-mm observations profit from a negative K-correction for high-redshift sources as these observations probe the Rayleigh-Jeans tail of the dust SED. Hence, a dusty galaxy with a fixed far-infrared luminosity and temperature will have an almost constant apparent flux density in the sub-millimeter waveband as a function of redshift. Radio observations lack this negative k-correction, and sources at higher redshift thus become increasingly faint. As a result, radio sources at higher redshifts ($z \geq 2.5$) that would be detectable with FIR/sub-mm observations become too faint for most radio surveys to be detectable. Differences in the sensitivity of radio- and FIR-surveys to galaxies at high redshift if not properly taken into account, will thus result in a biased result.

Measurements of the FIR-radio correlation also suffer from contamination of AGN. The FIR-radio correlation only applies for SFGs, since the correlation arises because the same population of massive stars that heats up dust-producing FIR emission also produces supernovae that generate synchrotron radiation. An AGN in galaxies can also be a source of radio emission. These AGN-hosting galaxies will therefore be offset from the FIR-radio correlation. Such sources should thus be removed from the sample to measure the FIR-radio correlation without introducing an artificial evolution (Molnár et al. 2018). Since the FIR-radio correlation is an integral part of the estimation of SFRs from radio observations, studying the correlation and understanding its origin remains of great importance. The impact of the assumed FIR-radio correlation on the measurements of the evolution of the SFR with redshift will be further discussed in **Chapter Three**.

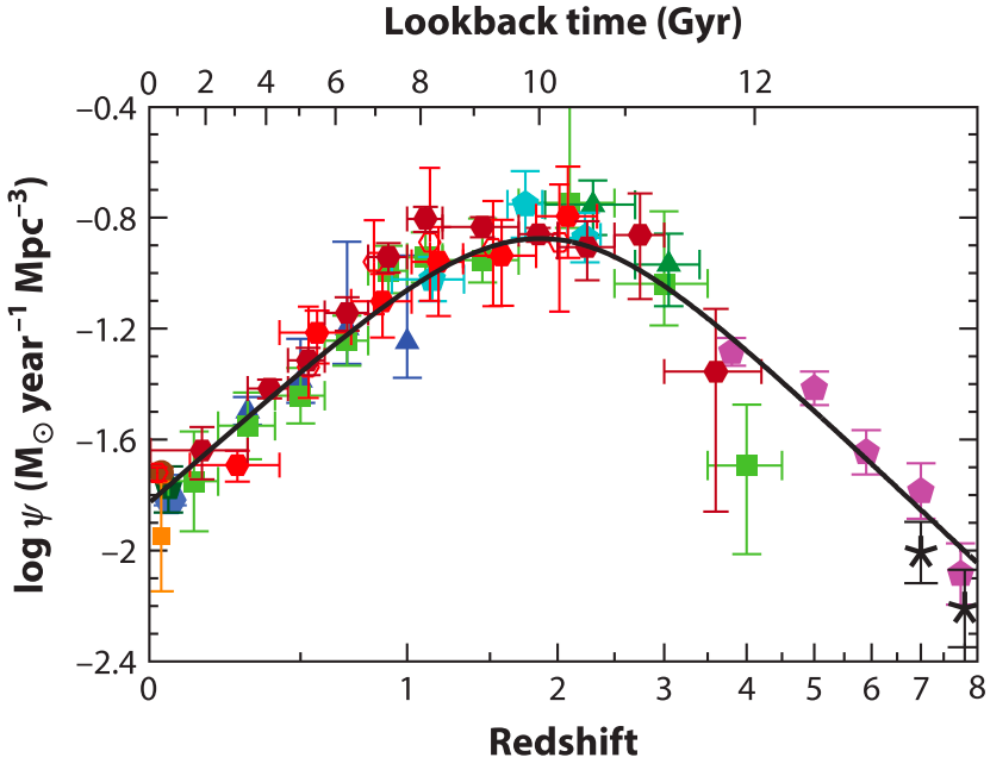


Figure 1.4: A compilation of measurements of the cosmic star formation rate density (SFRD) history by Madau & Dickinson (2014). The function shows the amount (mass) of stars created from gas per year and cubic mega-parsec as a function of cosmic time. From the compilation, we can see that the SFRD rapidly rises up to $z \sim 2$ and declines afterwards. Red and orange points represent measurements from IR observations, while green, blue and purple points are from UV observations. Most measurements at high redshift ($z > 2$) depend on UV observations.

1.5 The cosmic star formation rate density

The evolution of the star formation rate per unit volume, or the star formation rate density (SFRD; Madau & Dickinson 2014), as a function of redshift is one of the most fundamental tools to understand how star formation proceeds globally across cosmic time. It gives the SFR across all galaxies, at a given moment in cosmic history. Several tracers can be used to trace the SFR – and thus the SFRD – as discussed in Section 1.3.2. A compilation showing various UV (e.g., McLure et al. 2013; Bouwens et al. 2015; Bowler et al. 2015; Finkelstein et al. 2015; McLeod et al. 2015; Bouwens et al. 2016; Parsa et al. 2016; Mehta et al. 2017; Ono et al. 2018; Oesch et al. 2018; Bouwens et al. 2021) and IR-based (e.g., Rodighiero et al. 2010; Gruppioni et al. 2013; Rowan-Robinson et al. 2016; Koprowski et al. 2017; Dudzevičiūtė et al. 2020; Lim et al. 2020) measurements of the SFRD from Madau & Dickinson (2014) is shown in Fig. 1.4. As can be seen from this compilation, the SFRD increases from the formation of the first galaxies at $z > 10$ up until $z \sim 2$, after which the SFRD declines. The peak at $z \sim 1 - 3$ is known as the ‘epoch of galaxy assembly’. During this period half the stellar mass observed in the present-day universe was formed. Studying galaxies at this epoch is thus crucial to understand how galaxies evolved from this period to the present day. In addition, it is well established that the majority of the star formation happens on galaxies that lie on the MS.

Owing to the sensitivity of telescopes such as the Hubble Space Telescope (*HST*), most of the studies measuring the SFRD at high-redshift ($z > 2$) use UV observations (Fig. 1.4), a wavelength range prone to dust attenuation. Therefore, understanding how much of the star formation is obscured by dust is mandatory to study the redshift evolution of the SFRD, particularly as dust obscuration might play a non-negligible role even out to $z > 4$ (Casey et al. 2018; Bouwens et al. 2020). This motivates the work using radio observations as a dust-unbiased tracer of the SFRD presented in **Chapter Three**.

1.5.1 Dust-obscured star formation

The importance of dust emission, and thus dust-obscured star formation, was first seen from the comparison of the FIR background emission with the UV and optical background. The FIR background emission was first measured with the Cosmic Background Explorer (COBE) satellite. This instrument set out to assess the energy spectrum of the Universe at far-infrared wavelengths and additionally measured an emission that could not be explained by galactic sources: the cosmic infrared

background (e.g., Puget et al. 1996). The infrared background is approximately comparable to that of the UV, which suggests that total luminosity UV surveys only probe about half of all the star formation that has ever occurred. The other half of the star formation is thus obscured by dust.

Since then, many observational studies have been conducted and reached varying conclusions about the relative contribution of the dust-obscured population to the cosmic SFRD. To study star formation at high redshifts, FIR observations are key, since they trace the dust in galaxies, as explained in Section 1.3.2. However, the constraints on the SFRD beyond $z \simeq 2$ are uncertain because the measurements of the FIR LF used to derive the SFRD become more challenging. Source confusion and blending limit the ability to detect faint objects in low resolution *Herschel*/SPIRE observations at $z \simeq 3 - 4$. Such observations are thus biased towards a less representative population of bright sources. In addition, these observations can be significantly contaminated by AGN, as these sources are more numerous at high redshift (Gruppioni et al. 2013; Symeonidis & Page 2021).

ALMA observations have helped to overcome some of these problems by offering high-resolution observations and being less susceptible to AGN contamination, as they are predominantly sensitive to the cool dust in the star-forming population at high redshift (Hodge & da Cunha 2020). But even with these advantages, sub-mm observations are still impractical to carry out over the large areas that are needed to overcome cosmic variance, which can have a strong impact on any counting statistic (e.g., Moster et al. 2011; Simpson et al. 2019; Gruppioni et al. 2020; Loiacono et al. 2021), because of the small field of view. Cosmic variance in the sub-mm can be overcome by combining a wide-field single dish observation with interferometric follow-up observations (Simpson et al. 2020). However, such observations are expensive. Therefore, we still have poor constraints on the high-redshift dusty SFG population, which was illustrated by Casey et al. (2018) using two extreme models as shown in Fig. 1.5. The dust-poor line in the figure assumes the dusty SFG population peaks at $z \sim 2$, and that UV-luminous sources dominate the SFRD at $z \sim 4$; sources such as the ‘optically dark’ sources mentioned in Section 1.4.2 are rare in this model. The dust-rich line assumes dusty SFGs are as numerous at $z \sim 2$ as at $z \sim 4$. Neither of the two extreme models could be ruled out by the data sets available.

Recently, Zavala et al. (2021) presented a FIR-based estimate of the dust-obscured star formation out to $z = 6 - 7$ using the Mapping Obscuration to Reionization with ALMA (MORA) survey. Using only 13 sources detected sources at 2mm, number counts at 1.2 and 3mm, and the semi-empirical modelling from Casey et al. (2018), they estimated the dust-obscured star formation to be $\sim 35\%$ of the total SFRD at

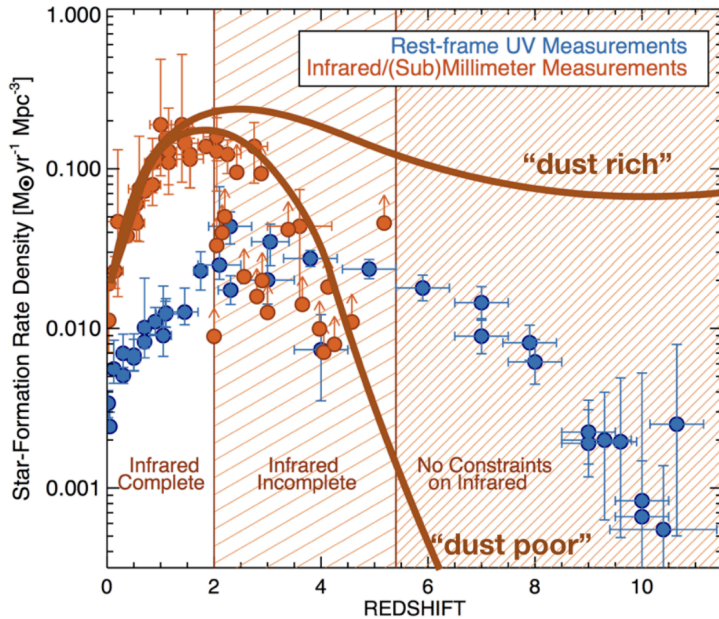


Figure 1.5: A compilation of cosmic star formation rate density measurements at UV wavelengths (blue points) and millimeter wavelengths (orange points) by Casey et al. (2018). The UV measurements have not been corrected for dust attenuation. Using deep HST imaging, the UV measurements reach beyond $z > 10$. Observations of obscured emission in galaxies is incomplete at $z > 2$ and completely unconstrained at $z > 5$. Casey et al. (2018) tests two dramatically different possibilities for the obscured fraction of the SFRD, shown by the dark orange lines.

$z \sim 5$, albeit with significant uncertainties due to low number statistics. This study suggests that dusty star formation already plays an important role at high redshift.

In addition to FIR observations, radio observations can be a powerful way to constrain the importance of dust-obscured star formation out to high redshift (e.g., Novak et al. 2017; Ocran et al. 2020; Cochrane et al. 2023). Radio observations also have the advantage of observing a larger field of view, thus having lower costs to obtain a statistical sample with which to constrain the SFRD. Previously, Novak et al. (2017) used the VLA-COSMOS 3 GHz Large Project to derive the SFRD. By observing the 2 deg² COSMOS field down to an r.m.s. of 2.5 μ Jy, they were able to observe main sequence galaxies out to $z \sim 1.5$. To trace main sequence galaxies out to higher redshifts, however, radio observations with sub- μ Jy r.m.s. noise levels are necessary. **Chapter Three** describes how we use a new ultra-deep radio survey to do just this.

Thanks to their sensitivity to dust-obscured star formation, radio observations

can also be used to uncover the ‘optically dark’ galaxy population introduced in Section 1.4.2: extremely dust-obscured sources that are invisible even in deep optical/UV imaging. Different observational works have studied these sources and show that the contribution of ‘optically dark’ sources appears to increase up to $z \sim 3.5$ and decrease thereafter. However, the constraints still span a wide range of over an order of magnitude at $3 \lesssim z \lesssim 6$. For example, Franco et al. (2018) found that 20% of the 1.1mm sources are not detected with HST down to a depth of $H \sim 28$ mag, while Wang et al. (2019) and Gruppioni et al. (2020) determined that the contribution of their dark sample ranged from, respectively, $\sim 10\%$ of the SFRD from LBGs at similar redshifts to equal to the total extinction-corrected contribution from all the known UV-selected galaxies at $z \sim 5$. Recently, observations of ‘optically dark’ sources have also been conducted with James Webb Space Telescope (*JWST*; Barrufet et al. 2023; Pérez-González et al. 2023). They determined that these sources are mostly dusty SFGs and found a similar contribution as determined by Wang et al. (2019). Radio observations have been shown to identify ‘optically dark’ galaxies that contribute most significantly to the cosmic SFRD (Talia et al. 2021; Enia et al. 2022). **Chapters Four & Five** discuss the discovery and verification of ‘optically dark’ sources in new deep radio observations, as well as their contribution to the SFRD.

The COSMOS-XS survey

In order to carry out the analyses described above, this thesis presents the VLA COSMOS-XS survey, which provides new deep radio observations at two frequencies: 10 and 3 GHz (i.e., the VLA’s X- and S-bands). The survey was conducted in the COSMOS field (Scoville 2007), a 2 deg^2 field which has been observed with all leading ground-based and satellite facilities, yielding a rich multi-wavelength data set (e.g., Laigle et al. 2016; Weaver et al. 2022). The COSMOS field was previously observed with the VLA at 1.4 GHz ($\sigma \sim 10 - 15 \mu\text{Jy beam}^{-1}$, Schinnerer et al. 2010), and more recently at 3 GHz ($\sigma \sim 2.3 \mu\text{Jy beam}^{-1}$), yielding about four times more radio sources compared to the 1.4 GHz data (Smolčić et al. 2017a). Although these observations provide valuable data over the entire 2 deg^2 COSMOS field, they still lack the depth to detect main sequence galaxies above $z \sim 1.5$. The COSMOS-XS survey presented in this thesis is one of the deepest radio surveys to-date, reaching sub- μJy sensitivities, and giving it the ability to trace main sequence galaxies over the full ‘epoch of galaxy assembly’ ($z \sim 1 - 3$). Importantly, it is ~ 5 times deeper than the previous 3 GHz observations conducted in the COSMOS field (Smolčić et al. 2017a). When combined with the rich multi-wavelength data, this survey yields a unique data set with which to study the faintest radio source populations that can currently be probed.

1.6 This thesis

In this thesis, we present the radio observations from the brand-new VLA COSMOS-XS survey and use them to trace dust-unbiased star formation over cosmic time. The thesis is organized as follows:

In **Chapter Two**, we discuss the details of the COSMOS-XS survey and present the radio catalogs. The deep 10 and 3 GHz observations enable us to investigate the Euclidean-normalized source counts down to the μJy level. We show that our observations are consistent within the uncertainties with other results at 3 and 1.4 GHz, but extend to fainter flux densities than previous direct detections.

In **Chapter Three**, we use the 3 GHz-selected sample of SFGs identified in the COSMOS-XS survey to study the evolution of the radio LF. We present evidence for significant density evolution over the observed redshift range, and we use the radio LFs to derive the dust-unbiased SFRD out to $z \sim 4.6$. Using this dust-unbiased survey, we present evidence for a significant underestimation of the SFRD based on the UV LFs at high redshift.

In **Chapter Four**, we use the COSMOS-XS survey to identify a robust sample of ‘optically dark’ galaxies. Using a new ‘Super-deblended’ FIR catalog based on the COSMOS-XS priors, we derive FIR-based photometric redshifts for the sources between $2 < z < 5$. We then quantify their contribution to the total SFRD, suggesting that they play a non-negligible role at high ($z > 3$) redshift.

In **Chapter Five**, we present new ALMA spectral scan observations with the aim of determining spectroscopic redshifts for a sub-sample of 10 radio-selected ‘optically dark’ galaxies. We find CO-based redshift solutions that confirm that the ‘optically dark’ sources targeted lie at $z \gtrsim 3$, with a median redshift of $z = 3.95 \pm 0.62$. By integrating the luminosity functions found in Chapter Four to the flux limit of the targeted sub-sample, we determine that the SFRD is in agreement with the SFRD found for the 10 ALMA detected ‘optically dark’ sources. This confirms the cosmic importance of these sources at high ($z > 3$) redshift.

1.7 The future

At the time of writing, the first results from the James Webb Space Telescope (*JWST*) have been published and started providing ground-breaking views of galaxy formation (e.g., Bouwens et al. 2023). *JWST* is equipped with four instruments – the Near Infrared Camera (NIRCam) and Near Infrared Spectrograph (NIRSpec), an imager and spectrograph respectively operating at $\lambda = 0.6 - 5\mu\text{m}$, the Mid-Infrared Instru-

ment (MIRI), a camera and spectrograph operating at $\lambda = 5 - 27\mu\text{m}$ and the Near Infrared Imager and Slitless Spectrograph (NIRISS), a spectrograph operating at the same wavelength as NIRSpec but with lower resolution and a wider field of view. *JWST* enables sub-arcsecond resolution near-infrared sensitive observations of dust-obscured galaxies at rest-frame optical-NIR wavelengths from which the structure of dust emission can be measured out to high redshifts. Early studies already showed the power of *JWST* to study ‘optically dark’ galaxies, sources discussed in this thesis, and to provide a complete census of these galaxies at $z = 2 - 8$ based on rest-frame optical imaging (e.g., Barrufet et al. 2023; Pérez-González et al. 2023). The NIRcam and MIRI also allow to identify possible AGN contamination, and will thus improve the selection of SFGs needed to constrain the evolution of star formation out to high redshift ($z > 3$).

The 6-m single-dish telescope Cerro Chajnantor Atacama Telescope-prime telescope (CCAT-p) is set for first light in 2024. It operates at mm/sub-mm wavelengths (1.4mm-350 μm). It will have a very wide field-of-view (a diameter of 2° at 350 μm) but a limited angular resolution. One of the primary goals of CCAT-p is to trace the evolution of the dust obscured star formation in galaxies. The planned 350 μm surveys covering $\sim 100 \text{ deg}^2$ will detect $\geq 600,000$ galaxies of which ≥ 1000 are expected to be in the redshift range between $z \sim 5$ and $z \sim 8$ (Chapman et al. 2022). With these IR emission measurements, this CCAT-p survey will provide extensive measurements of the dust-obscured star formation activity at an epoch in which the amount of dust-obscuration in SFGs is still debated as discussed in this thesis.

Radio interferometry will be revolutionized thanks to the Square-Kilometre Array (SKA). This interferometer will observe between 50 MHz and 24 GHz and will extend to flux density limits more than three orders of magnitude deeper than currently possible (De Zotti et al. 2019). The construction of the SKA started in December 2022 and the deployment will be phased. The first phase (SKA-mid) will consist of 197 dishes operating at 350 MHz-15.3 GHz (with the aim of being expanded to 20 GHz) in South Africa with maximum baselines of 156km. These baselines provide sub-arcsecond resolutions with fields of view with diameters of $\sim 10-100$ arcmin. The lower frequency companion (SKA-low) will operate in Australia at 50–350 MHz and will consist of $\sim 131,000$ antennae with maximum baselines of 65km. The basic increase in depths obtainable with this array will be an opening up of direct detections of MS galaxies at higher redshift than currently possible with the JVLA as discussed in this thesis (e.g., De Zotti et al. 2019). A survey like the COSMOS-XS survey could be undertaken with the SKA within a fraction of the observing time used for the COSMOS-XS survey.

The Low Frequency Array (LOFAR; van Haarlem et al. 2013) is a SKA pathfinder interferometer working at low (< 1 GHz) and ultra-low (< 100 MHz) radio frequencies. It is centered in the Netherlands, with antennas around Europe, and took its first observations of the radio sky in 2010. LOFAR consists of two sets of antennas in each station, the Low Band Antennas (LBA, 10-90 MHz) and the High Band Antennas (HBA, 110-240 MHz). It is able to map 10 deg^2 regions of the sky in a single pointing with high resolutions. Prospects for future studies of radio-selected SFGs with LOFAR are bright. For example, the LOFAR Deep Fields survey, reaching sensitivities of $\sim 13 \mu\text{Jy beam}^{-1}$, will build up a large sample sample of SFGs enabling the study of dust-obscured star formation as described in this thesis. In addition, LOFAR is currently updated to LOFAR 2.0. This is a staged expansion of the technical capabilities of LOFAR and will ensure that LOFAR remains scientifically relevant throughout the decade. The upgrade includes improved electronics, better designed LBA dipoles, ~ 6 new stations in the Netherlands and new international stations. LOFAR 2.0 will also allow for simultaneous observations with high-band and low-band antennas enabling to combine information from both antennas (Edler et al. 2021).

2 | An ultra-deep multi-band VLA survey of the faint radio sky: Source catalog and number counts

Abstract

We present ultra-deep, matched-resolution Karl G. Jansky Very Large Array (VLA) observations at 10 and 3 GHz in the COSMOS field: the COSMOS-XS survey. The final 10 and 3 GHz images cover $\sim 16 \text{ arcmin}^2$ and $\sim 180 \text{ arcmin}^2$ and reach median *r.m.s.* values at the phase center of $0.41 \mu\text{Jy beam}^{-1}$ and $0.53 \mu\text{Jy beam}^{-1}$, respectively. Both images have an angular resolution of $\sim 2''$. To account for the spectral shape and resolution variations across the broad bands, we image all data with a multi-scale, multi-frequency synthesis algorithm. We present source catalogs for the 10 and 3 GHz image with 91 and 1498 sources, respectively, above a peak brightness threshold of 5σ . We present source counts with completeness corrections included that are computed via Monte Carlo simulations. Our corrected counts at 3 GHz are consistent within the uncertainties with other results at 3 and 1.4 GHz, but extend to fainter flux densities than previous direct detections. The 3 GHz number counts exceed the counts predicted by the semi-empirical simulations developed in the framework of the SKA Simulated Skies project, consistent with previous P(D) analyses. Our source counts suggest a steeper luminosity function evolution for faint star-forming sources. The semi-empirical Tiered Radio Extragalactic Continuum Simulation (T-RECS) predicts this steeper evolution and is in better agreement with our results at 10 and 3 GHz within the expected variations from cosmic variance. In summary, the multi-band, matched-resolution COSMOS-XS survey in the COSMOS field provides a high-resolution view of the ultra-faint radio sky that can help guide next-generation radio facilities.

van der Vlugt, Algera, Hodge, Novak, Radcliffe, Riechers, Röttgering, Smolčić, Walter

Published in The Astrophysical Journal, 907, 5 (2021)

2.1 Introduction

Over the last decade, a number of multi-wavelength (UV to radio) studies have revealed that the star formation history of the universe (SFHU, i.e., the total star formation rate (SFR) per unit of co-moving volume) went through several phases. The SFR apparently rose after the first galaxies formed (e.g., Bouwens et al. 2014a, 2015) and reached its peak during the ‘epoch of galaxy assembly’ at $1 \lesssim z \lesssim 3$. Subsequently, the SFR density declined rapidly to the present (e.g., Madau & Dickinson 2014 and references therein). It is well established that the majority of the star formation activity happens in galaxies that lie on the main sequence (MS), exhibiting an intrinsic scatter of ~ 0.3 dex, between SFR and stellar mass (e.g., Brinchmann et al. 2004; Noeske et al. 2007; Elbaz et al. 2007). Not only does the relation exist in the local universe (e.g., Brinchmann et al. 2004; Salim et al. 2007) but is found to hold to $z \sim 4$ or even higher, albeit with a strong redshift evolution (e.g., Daddi et al. 2007; Pannella et al. 2009; Karim et al. 2011; Speagle et al. 2014; Schreiber et al. 2015; Salmon et al. 2015; Tomczak et al. 2016; Kurczynski et al. 2016). An accurate measurement of the SFR and its relation to stellar mass at all epochs is key for a better understanding of galaxy evolution.

Several tracers across the electromagnetic spectrum can be used to measure this SFR, each with their own unique strengths and weaknesses. For example, ultraviolet (UV) light originates mainly from massive stars and thus directly traces young stellar populations. UV based observations need, however, uncertain and significant model-dependent dust corrections to account for dust obscuration (e.g., Carilli et al. 2008; Siana et al. 2008, 2009; Magdis et al. 2010; Chary & Pope 2010; Bouwens et al. 2012). Infrared (IR) observations trace the absorbed UV emission that is thermally reprocessed by dust surrounding newly formed stars. However, the resolution of IR observations is often insufficient to provide reliable multi-wavelength identifications. In addition, the presence of poly-cyclic aromatic hydrocarbon (PAH) emission features redshifted ($z > 0.8$) into the $24\mu\text{m}$ band, commonly used as an estimator for the total-IR emission, makes the required K-correction uncertain.

Long-wavelength radio emission is another potential tracer of recent star formation (Condon 1992). Radio emission in galaxies below rest frame frequencies $\lesssim 30$ GHz is dominated by synchrotron radiation arising from cosmic ray electrons gyrating in the galaxy magnetic fields (e.g., Sadler et al. 1989; Condon 1992; Clemens et al. 2008; Tabatabaei et al. 2017). These charged cosmic-ray particles are accelerated in shocks launched by supernovae of stars with $M > 8 M_{\odot}$ in SFGs. These massive stars have lifetimes of $\lesssim 3 \times 10^8$ years, so their supernova rates are proportional to

the recent SFR. This is supported by the tight correlation observed in SFGs between IR emission, originating from dust that has been heated by young and massive stars, and radio emission (the IR-radio correlation; e.g., de Jong et al. 1985; Helou et al. 1985; Yun et al. 2001; Bell 2003; Dumas et al. 2011). Deep radio observations in the synchrotron regime can thus be used to constrain SFRs. Radio observations can also provide high spatial resolution to allow for reliable counterparts matching. Distant galaxies in the GHz radio regime often have spectral energy distributions (SEDs) that can be parameterized by a featureless power-law, leading to a simple and robust K-correction. Radio observations in the synchrotron regime thus offers a unique opportunity to study the SFH of the Universe (e.g., Condon et al. 2002; Seymour et al. 2008; Smolčić et al. 2009b; Jarvis et al. 2015; Calistro Rivera et al. 2017b; Novak et al. 2017) at a wavelength that is free from selection biases due to dust obscuration.

However, there are two challenges in using radio emission in the synchrotron regime as a tracer of star formation. The first is the ‘contamination’ by active galactic nuclei (AGN). It is hard to disentangle AGN and SFGs in the radio regime as an accreting supermassive black hole (SMBH) in an AGN can also accelerate the electrons that produce synchrotron emission. To attempt to correct for this, several methods have been developed for identifying different types of AGN and separating them from SFGs (e.g., Hickox et al. 2009; Mendez et al. 2013; Smolčić et al. 2017b; Delvecchio et al. 2017; Algera et al. 2020a) using mid-IR data, far-IR data (FIR), X-ray information and multi-band optical/IR photometry. Synchrotron emission can thus not only be used to study star formation but also to study the black hole accretion activity in the Universe (e.g., Jarvis & Rawlings 2000; Smolčić et al. 2009a; Rigby et al. 2011; McAlpine et al. 2013; Best et al. 2014; Delvecchio et al. 2014, 2017; Sabater et al. 2019).

The second challenge is the depth achievable in radio surveys. With the improving capabilities of modern interferometers along with sophisticated calibration techniques, surveys of the faint μJy radio emitting objects are able to constrain the faint populations (e.g., Rujopakarn et al. 2016; Murphy et al. 2017; Smolčić et al. 2017a; Owen 2018; Bondi et al. 2018; Mauch et al. 2020). At high flux densities, the source counts are well-constrained and found to be dominated by AGNs that follow a smooth power-law distribution down to $S_{1.4\text{GHz}} \sim 1 \text{ mJy}$ (e.g., Condon & Mitchell 1984; Windhorst et al. 1990). Below 1 mJy, the Euclidean-normalized source counts flatten (e.g., Richards 2000; Huynh et al. 2005; Biggs & Ivison 2006; Owen & Morrison 2008; Bondi et al. 2008; Padovani et al. 2015). It is now widely accepted that this flattening observed is due to the emergence of SFGs and radio-quiet AGN

which begin to contribute significantly (e.g., Rowan-Robinson et al. 1993; Seymour et al. 2004; Padovani et al. 2009). New deep radio observations and $P(D)$ analyses on confusion limited surveys show evidence of a further steepening of the number counts below $S_{1.4\text{GHz}} \sim 50 \mu\text{Jy}$ (e.g., Condon et al. 2012; Vernstrom et al. 2014, 2016; Smolčić et al. 2017a; Prandoni et al. 2018; Mauch et al. 2020). The composition of this ultra faint radio population is still uncertain but it is expected from simulations and observations that the fraction of SFGs will become significant ($> 60\%$) below $S_{1.4\text{GHz}} \sim 100 \mu\text{Jy}$ (Smolčić et al. 2017b). Constraints on the ultra-faint radio populations at high resolution are useful for predictions for future radio surveys with new and upcoming facilities such the ASKAP, MeerKAT, ngVLA, and SKA, where source confusion noise may be an issue.

Survey depth is also a challenge for radio surveys at observing frequencies $\geq 10\text{ GHz}$. Such surveys measure flux densities closer to the rest-frame frequencies $\nu \geq 30\text{ GHz}$ where the total radio emission is dominated by free-free radiation (e.g., Condon 1992; Murphy et al. 2011; Klein et al. 2018) which constitutes the faintest part of the radio SED. Although more difficult to detect, free-free emission provides independent information on the star formation process. Free-free emission directly originates from the HII-regions where massive stars form and thus provides a first-hand view on star formation. In addition, unlike UV emission, dust obscuration plays only a minor role, and therefore free-free emission is potentially the most accurate tracer of star formation (e.g., Mezger & Henderson 1967; Turner & Ho 1983, 1985; Klein & Graeve 1986; Kobulnicky & Johnson 1999; Murphy et al. 2012, 2015; Nikolic & Bolton 2012).

A limitation to high frequency observations is the smaller primary beam area, as this area decreases with frequency ($\Omega_{\text{pb}} \propto \nu^{-2}$). This limits the area that is covered at a certain depth. Low frequencies have therefore been favored and radio continuum surveys probing free-free emission are still sparse in the literature.

The majority of extra-galactic radio surveys are conducted at 1.4 and 3 GHz, where the radio emission of galaxies is intrinsically brighter than at higher frequencies, and large areas can be imaged with a single pointing. In the last decade, several studies have been conducted to trace the synchrotron emission from galaxies (e.g., Schinnerer et al. 2007, 2010; Morrison et al. 2010; Smolčić et al. 2017a; Prandoni et al. 2018). The COSMOS field has been observed with the Very Large Array (VLA) at 1.4 GHz ($\sigma \sim 10 - 15 \mu\text{Jy beam}^{-1}$, Schinnerer et al. 2010), and more recently at 3 GHz with substantially better sensitivity ($\sigma \sim 2.3 \mu\text{Jy beam}^{-1}$), yielding about four times more radio sources compared to the 1.4 GHz data (Smolčić et al. 2017a); see Fig. 2.1. Although these observations provide valuable data over the entire 2 deg^2 COSMOS

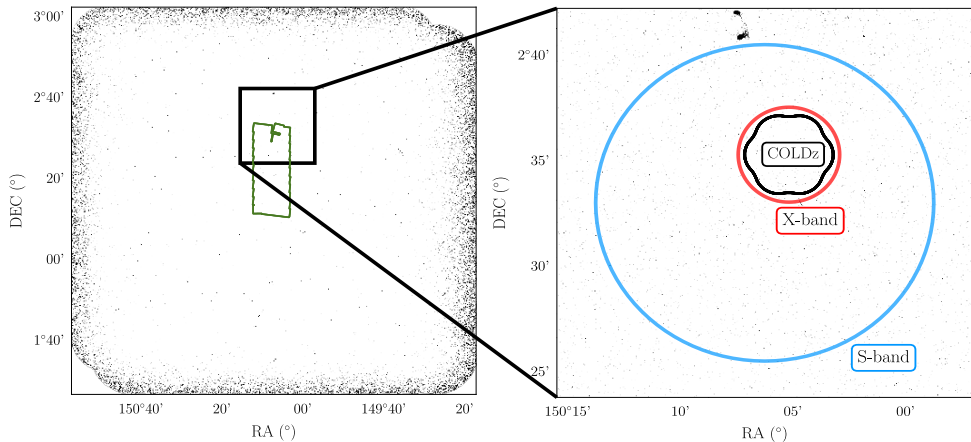


Figure 2.1: The full 3 GHz mosaic as imaged by Smolčić et al. (2017a) of the 2 deg² COSMOS field. The green polygon indicates the footprint of the CANDELS WFC3 imaging (Nayyeri et al. 2017). The inset of 340 arcmin² shows the position of the X- and S-band primary beam. Additionally, the seven-pointing mosaic at 34 GHz, part of the COLDz project (Pavesi et al. 2018), is shown with the black contour.

field, enabling some of the most comprehensive studies to-date of the SFG population and radio AGN population, they are equivalent to ~ 2 hours per pointing. The resulting sensitivity only allows for the detection of typical SFGs out to $z \sim 1.5$ (Novak et al. 2017), the epoch where the various SF tracers begin to diverge (e.g., Ilbert et al. 2013). In order to observe MS galaxies over the full epoch of galaxy assembly ($z \sim 1 - 3$) a sub- μ Jy survey is essential.

The significantly increased bandwidths of the upgraded NSF’s Karl G. Jansky Very Large Array (VLA) now allows for observations of the radio sky down to several hundred nJy beam⁻¹ sensitivities. We have taken advantage of these recent upgrades to the VLA to do an ultra-deep-matched-resolution survey in both X- and S-band (10 GHz and 3 GHz). This COSMOS-XS survey is one of the deepest radio surveys to-date, reaching sub- μ Jy sensitivities and is ~ 5 times deeper than the previous 3 GHz observations conducted in the COSMOS field (Smolčić et al. 2017a). When combined with the rich COSMOS multi-wavelength data, this survey thus yields a unique data set to test the composition of the faintest radio source populations that can currently be probed.

The combined S- and X-band observations will enable us to study the properties and importance of AGNs and SFGs in a dust-unbiased way and to make predictions for the populations to be detected by future surveys. This paper (hereafter Paper I), describes the 10 and 3 GHz observations and examines their implications for the

ultra-faint source counts. In a companion paper (Algera et al. 2020a, hereafter Paper II), we match the obtained catalogs with the multi-wavelength data available in the COSMOS field to distinguish between AGNs and SFGs. The obtained populations are then used to constrain the composition of the ultra-faint source counts.

This paper is organized as follows: in Section 2.2 we describe the VLA 10 and 3 GHz observations, calibration, imaging and catalog extraction. In Section 2.3, we present the final images and describe the source-detection method and the compilation of the source catalog. This section also includes an analysis of the quality of the catalog. In Section 2.4 we discuss the derivation of the completeness-corrected radio source counts. Finally, Section 2.5 summarizes and concludes this work. Throughout this paper, the spectral index, α , is defined as $S_\nu \propto \nu^\alpha$, where S is the source flux density, and ν is the observing frequency. We assume a spectral index of -0.7 unless otherwise stated.

2.2 Observations and data reduction

2.2.1 Observations

The COSMOS-XS survey (see Table 2.1) consists of the combination of a single deep S-band pointing centered on R.A.=10:00:25, Decl.=+02°33′00″ (see Fig. 2.1) in the B-configuration and an additional single X-band pointing observed in the C-array centered on the COSMOS/AzTEC-3 protocluster at $z \sim 5.3$, coordinates R.A.=10:00:20.7, Decl.=02°35′17″ (see Fig. 2.1). The chosen configurations provide a resolution of $\sim 2''$ in X- and S-band which is large enough to avoid resolving out faint sources. The X-band surveys overlaps with the COLDz survey (Pavesi et al. 2018; Riechers et al. 2019), one of the deepest 34 GHz continuum surveys, covering $\sim 10 \text{ arcmin}^2$, to-date. The S-band pointing is chosen to be slightly offset from the X-band pointing to overlap more with the CANDELS-COSMOS field (Nayyeri et al. 2017). The X- and S-bands were observed for 90h and 100h, respectively. These data were taken between 2014 December 4 and 2016 February 27 with the individual observations constituting either two- or five-hour observing blocks. For the X-band observations, J1024-0052 was used as the phase calibrator, while for the S-band observations, J0925+0019 was used as the phase calibrator. For both bands, 3C286 served as both the flux and bandpass calibrator. The X-band covers a bandwidth of 4096 MHz centered at 10 GHz, and is separated into 32 spectral windows 128 MHz wide. All four polarization products were recorded and a 2s signal-averaging time was used. The S-band covers a bandwidth of 2048 MHz centered at 3 GHz, and is sepa-

rated into 16 spectral windows 128 MHz wide. Again all four polarization products were recorded and a 5s signal-averaging time was used.

2.2.2 Calibration

The calibration of the X- and S-band visibilities was performed using CASA¹ version 5.0.0. Extensive use was made of the NRAO VLA reduction pipeline.² Radio frequency interference (RFI) constitutes the major uncertainty in our data calibration. We experimented with different methods and tools (`rflag`, `A0flagger` (Offringa 2010)) to remove the RFI. However, the unmodified pipeline resulted in the best image.

Before running the pipeline, Hanning smoothing was applied to lessen Gibbs ringing from strong spectral features such as strong, narrow RFI. The pipeline runs several flagging rounds to flag bad or unnecessary data such as the initial few integration points of a scan where not all antennas may be on source. To flag RFI the pipeline performed several rounds of flagging using the `rflag` algorithm. The pipeline uses the `gencal` and `gaincal` tasks to derive the necessary calibration solutions. `setjy` was used to set the flux scale of the observations (Perley & Butler 2013) and the flux density calibrator was 3C286. During the calibration, no time or bandwidth averaging was performed so as to minimize time and bandwidth smearing effects (see Section 2.2.3).

In the X-band two spectral windows (SPWs), SPW 32 and SPW 33, were heavily flagged (> 85%) because of RFI. For the S-band only SPW 4 was found to be heavily corrupted by RFI and was flagged almost entirely by the pipeline. After the pipeline was run on the 10 and 3 GHz data, the target field was split off using the task `split` and, respectively, 24.9% and 25.8% of the split off data was flagged.

2.2.3 Bandwidth and time smearing

An antenna receiver has a finite bandwidth which causes bandwidth smearing. This effect radially smears peak brightness while the integrated flux densities are conserved. Bandwidth smearing is a function of distance from the pointing center. The theoretical prediction from Condon et al. (1998) for the reduction of peak response is given by $I/I_0 = 1/\sqrt{1+0.46\beta^2}$, where $\beta = (\Delta\nu/\nu_0) \times (\theta_0/\theta_{HPBW})$. If we calculate the reduction at 20% of the peak primary beam sensitivity using the VLA channel width $\Delta\nu = 2$ MHz, central frequency $\nu_0 = 3$ GHz and a beam size of $\theta_{HPBW} = 2''$, we find an offset of $\sim 1\%$. When we compare the peak brightness over the total

¹ <http://casa.nrao.edu/>

² <https://science.nrao.edu/facilities/vla/data-processing/pipeline>

Table 2.1. 10 and 3GHz pointing centers and total observing time.

Band	Central frequency [GHz]	Configuration	Center (J2000) R.A.	Decl.	Total integration time [hours]	Primary beam FWHP [arcmin]	central r.m.s. [μ Jy]
S	3	B	$10^{\text{h}}00^{\text{m}}25^{\text{s}}$	$+02^{\circ}33'00''$	100	15	0.53
X	10	C	$10^{\text{h}}00^{\text{m}}20^{\text{s}}.7$	$+02^{\circ}35'17''$	90	4.5	0.41

Table 2.2. Overview of the wide-field imaging parameters for the 10 and 3 GHz image.

Band	Robust	Pixel size [arcsec]	w -Planes	Restoring Beam [arcsec]
S	0.5	0.4	400	2.14×1.81
X	0.5	0.42	128	2.33×2.01

flux density for point-like sources ($0.9 \leq S_{\text{peak}}/S_{\text{int}}$) with $S/N > 6$ as a function of distance from the pointing center, we find that an offset of $\sim 4\%$ is present. This is, however, not distance dependent, and thus unlikely to be related to bandwidth smearing.

For the 10 GHz observations, we calculate a reduction of $\sim 0.01\%$ at 20% of the peak primary beam sensitivity using the VLA channel width $\Delta\nu = 2$ MHz, central frequency $\nu_0 = 10$ GHz and a beam size of $\theta_{\text{HPBW}} = 2''$. The $S_{\text{peak}}/S_{\text{int}}$ distribution of point-like sources ($0.9 \leq S_{\text{peak}}/S_{\text{int}}$) with $S/N > 6$ with distance also shows no distance dependent offset. Therefore, we do not apply any corrections at 10 and 3 GHz for the bandwidth smearing effect.

The individual observations were concatenated after the calibration steps using the CASA task `concat`. These data were subsequently averaged in time using `split` with an averaging time of 21s for the X-band and 6s for the S-band. Averaging visibility data in the time domain causes a similar distortion to bandwidth smearing, but in the opposite direction (i.e., tangentially). The averaging time used should lead to an amplitude loss of at most one percent for a point source located at the first null of the primary beam due to loss of coherence.³

2.2.4 Imaging

Imaging of the concatenated data-sets was performed both with CASA task `clean` and standalone imaging algorithm `WSclean` (Offringa et al. 2014). For our purposes, the main difference between the two algorithms is the method of taking into account the interferometric w -term during deconvolution. We opted for `WSclean` to create the final images, based on its faster processing compared to CASA’s `clean`. However, differences between the CASA `clean` and `WSclean` images are minimal (see also Offringa et al. 2014); hence, the choice of algorithm has no effect on the end product.

`WSclean` produces images by jointly gridding and deconvolving the measurement set, which is called joined-channel deconvolution (Offringa & Smirnov 2017). Spectral behavior of sources can be captured during deconvolution by setting the param-

³ <https://science.nrao.edu/facilities/vla/docs/manuals/oss2013B/performance/fov/t-av-loss>

ters `-channels-out` and `-join-channels`. The data is then imaged in separate channels across the band. During deconvolution, `WSClean` finds peaks in the full-band image and deconvolves these in each channel independently.

For the 10 GHz image, we weight our image via Briggs weighting with a robust parameter of 0.5 (Briggs 1995) and apply w -stacking using the minimum recommended number of 128 layers (`-nwlayers`). We use the joined-channel deconvolution technique, specified by setting `-channels-out` to 32 (i.e., one per SPW) and specifying parameter `-join-channels`. A power law is fit to account for in-band spectral variations (similar to the multi-term multi-frequency synthesis algorithm used in CASA's `tclean` with `nterms=2`; Rau & Cornwell 2011). In addition, we utilize auto-masking of sources after first cleaning down to 3σ , whereupon masked sources are further cleaned down to 0.5σ (parameters `-auto-mask` and `-auto-threshold`, respectively). The combination of these settings for `-auto-mask` and `-auto-threshold` is a good general setting for `WSClean`, which leaves almost no residuals behind. The resulting image reaches an r.m.s.-sensitivity of $\sigma = 0.41 \mu\text{Jy beam}^{-1}$ (Table 2.2).

For the 3 GHz image, we take a similar approach as described above, but with a few changes in the imaging parameters. The number of layers for w -stacking is increased to 400. We find that w -term artifacts persist for imaging with 128 layers and increasing the number to 400 solves these issues. We also do not fit the spectral variations with a power-law because of the large noise fluctuations at the beam edge caused by a bright source (see Fig. 2.4). The `-channels-out` parameter is set to 16 (i.e., one per SPW). The resulting image reaches an r.m.s.-sensitivity of $\sigma = 0.53 \mu\text{Jy beam}^{-1}$ (Table 2.2).

Because primary beam correction via projection-based gridding is not yet operational, we take the primary beam model from the CASA `widebandpbcor` task⁴ which takes the frequency dependence of the beam into account.

2.2.5 Confusion

Finally, we note that the source confusion is negligible in the deep 3 GHz VLA observation (only the S-band image is considered as it has the highest source density). The beam size is $2''.14 \times 1''.81$, which results in 3.16×10^6 beams deg^{-2} . At the faintest flux density bin of our number count measurements for the S-band (see Section 2.4.2), we find $\sim 1 \times 10^4$ sources deg^{-2} . This translates to one source per ~ 316 beams, and implies that confusion is not an issue. Following Condon et al. (2012), source confusion becomes important at one source per 25 beams. This confusion limit depends on

⁴ This task was run by means of CASA version 5.3, which has an updated beam shape model.

the slope of the scale-free power law approximation for the number counts

$$n(S) = kS^{-\gamma}, \quad (2.1)$$

where K is the count normalization and $1 < \gamma < 3$ is the differential count slope (Condon et al. 2012). For the calculation of the confusion limit we assumed a slope of $\gamma = 2.0$. We expect source confusion to contribute approximately $0.01 \mu\text{Jy beam}^{-1}$ to the noise following Equation (27) from Condon et al. (2012).

2.3 Final image and Cataloging

The final 10 and 3 GHz images are shown in Fig. 2.3 and Fig. 2.5, respectively. The central r.m.s. noise level is relatively smooth for both images (see also Fig. 2.2 and 2.4). The 3 GHz image shows a small number of artifacts (see, e.g., the Northern part of the image shown in Fig. 2.5). The artifacts are localized around bright sources and have little impact on the majority of the map, as can be seen from Fig. 2.4.

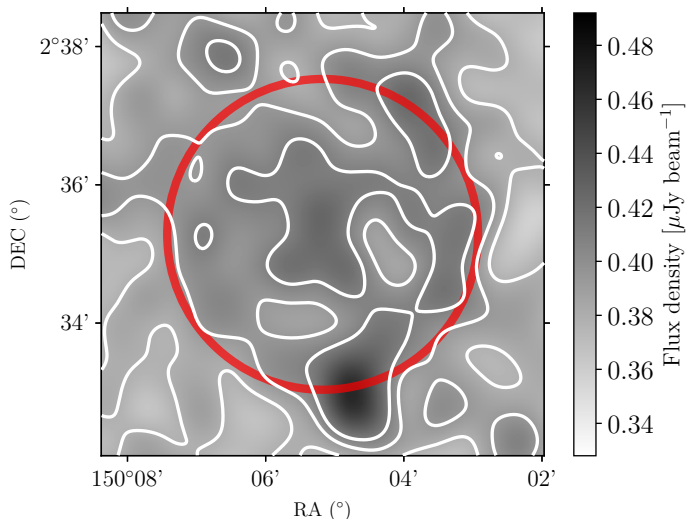


Figure 2.2: The r.m.s. map of the 10 GHz observation before primary beam correction. The image size is 41 arcmin^2 . The r.m.s. map is created with PyBDSF. The red circle indicates the HPBW of the primary beam at 10 GHz, which corresponds to $4'.5$. The gray-scale shows the r.m.s. noise from 0.8σ to 1.2σ , where $\sigma = 0.41 \mu\text{Jy beam}^{-1}$. The contours are plotted at $[0.38, 0.39, 0.41] \mu\text{Jy beam}^{-1}$.

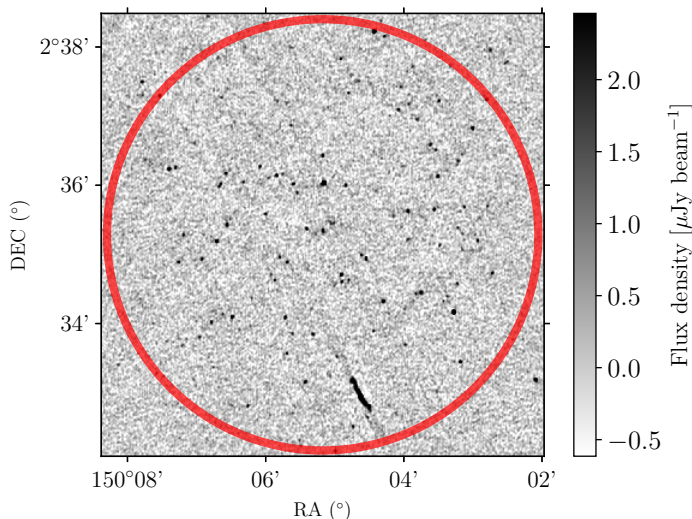


Figure 2.3: Final calibrated 10 GHz image before primary beam correction. The size is the same as in Fig. 2.2. The red circle indicates the point where the primary beam sensitivity is 20% of its peak. The gray-scale shows the flux density from -1.5σ to 6σ , where $\sigma = 0.41 \mu\text{Jy beam}^{-1}$ is the median r.m.s. within the primary beam FWHP. The corresponding brightness temperature r.m.s. value is $\sigma = 1.25 \text{ mK}$. The image is matched in resolution and depth for a spectral index of -0.7 with the 3 GHz image.

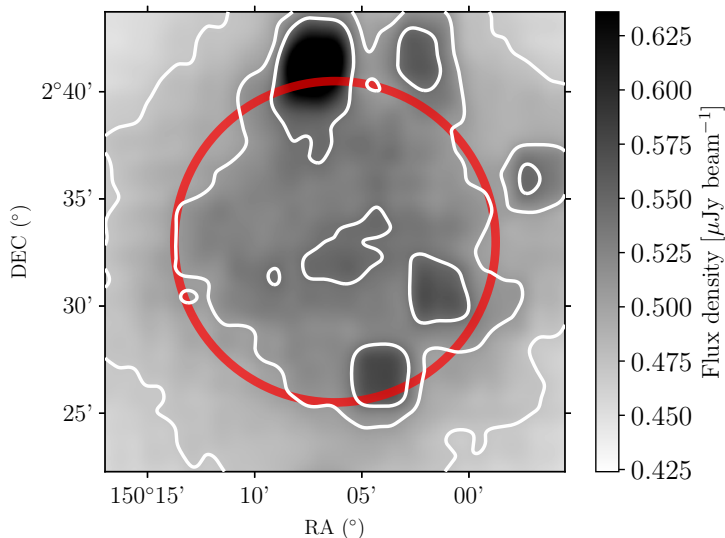


Figure 2.4: The r.m.s. map of the 3 GHz observation before primary beam correction. The image size is 460 arcmin^2 . The r.m.s. map is created with PyBDSF. The red circle indicates the HPBW of the primary beam at 3 GHz, which corresponds to $15'$. The gray-scale shows the r.m.s. noise from 0.8σ to 1.2σ , where $\sigma = 0.53 \mu\text{Jy beam}^{-1}$. The contours are plotted at $[0.47, 0.51, 0.54] \mu\text{Jy beam}^{-1}$.

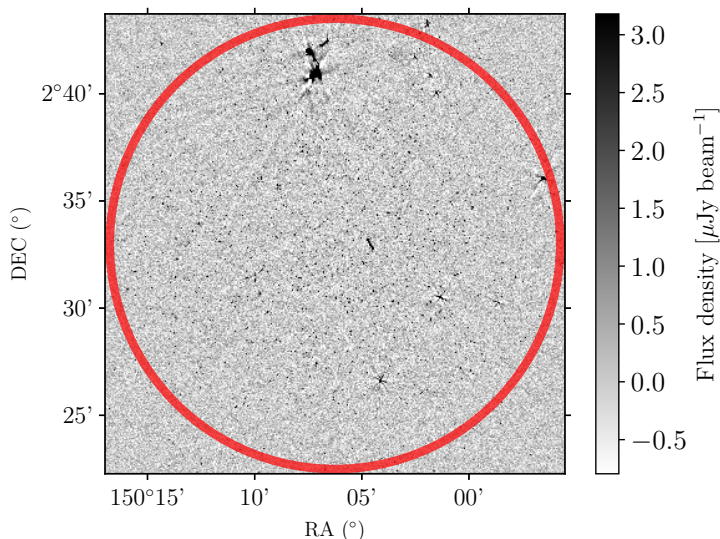


Figure 2.5: Final calibrated 3 GHz image before primary beam correction. The size is the same as in Fig. 2.4. The red circle indicates the point where the primary beam sensitivity is 20% of its peak. The gray-scale shows the flux density from -1.5σ to 6σ , where $\sigma = 0.53 \mu\text{Jy beam}^{-1}$ is the median r.m.s. within the primary beam FWHP. The corresponding brightness temperature r.m.s. value is $\sigma = 18.0 \text{ mK}$.

2.3.1 Source detection and characterization

We compiled a source catalog using PyBDSF⁵ (Mohan & Rafferty 2015) to detect and characterize sources. We ran PyBDSF on the final image, using the pre-primary-beam-corrected image as the detection image.

PyBDSF identifies peaks of emission above a given threshold (`thresh_pix`) that are surrounded by contiguous pixels with emission greater than a minimum (`thresh_isl`). PyBDSF fits the identified island with one or more Gaussians, which are subsequently grouped into sources. This happens if all the pixels on the line joining their centers have a value greater than `thresh_isl` and if the length of this line is less than half the sum of their FWHMs. The total flux density of the sources is estimated by adding those from the individual Gaussians, while the central position and source size are determined via moment analysis.

The spatial variation of the image noise was estimated by sliding a box across the image in overlapping steps, calculating the r.m.s. of the pixels within the box and interpolating the values measured from each step. The resulting r.m.s. map provides PyBDSF with an estimate of the spatial variation of the image noise for detection thresholding purposes. The r.m.s. maps for the 10 (see Fig. 2.2) and 3 GHz image (see Fig. 2.4) are determined with a sliding box of `rms_box` = (120, 60) pixels and `rms_box` = (400, 100) pixels (i.e., a box size of 400 pixels every 100 pixels), respectively.

For source extraction, we used `thresh_pix` = 5.0σ and `thresh_isl` = 3.0σ (i.e., the limit at which flux density is included in the source for fitting). Fig. 2.2 and 2.4 illustrate the variation in r.m.s. noise determined across the image and shows the increase in local r.m.s. as a result of calibration artifacts near bright sources. We used the `group_tol` parameter with a value of 1.0 as a larger value (allowing for larger sources to be fitted) was not necessary. Sources are classified as ‘S’ for single sources and ‘M’ for multiple Gaussian sources. The parameters of the Gaussian fitted to the source are reported by PyBDSF.

For the 10 GHz (3 GHz) images, the total number of sources detected by PyBDSF within 20% of the peak primary beam sensitivity is 93 (1498), of which 90 (1392) are single-component sources; sources fitted by a single Gaussian.

2.3.2 Resolved sources

In order to determine whether our identified source components are resolved, we make use of the ratio between integrated flux density (S_{int}) and peak brightness (S_{peak}) which is a direct measure of the extension of a radio source. For an unresolved source, the peak brightness equals the total flux density. Noise influences the measurements of S_{int} and S_{peak} ; therefore, the $S_{\text{int}}/S_{\text{peak}}$ distribution gets broadened towards the low signal-to-noise end. The effect of noise on the $S_{\text{int}}/S_{\text{peak}}$ ratio can be determined by performing Monte Carlo simulations in which simulated sources are added to the pre-primary-beam-corrected image and then retrieved the same way as the observed data. We simulate 100 mock sources and inserted these in the real image. This is

⁵ <http://www.astron.nl/citt/pybdsf/>

repeated 200 times, simulating 20,000 sources in total. The method described below is used to derive the upper envelope of the $S_{\text{int}}/S_{\text{peak}}$ distribution for both the 10 and 3 GHz image.

Sources are injected as Gaussians with their FWHM equal to the beam size and they are thus unresolved by construction. We only insert point sources to quantify how the noise ‘resolves’ unresolved sources. The peak brightness of the sources are drawn from the real source distribution to generate a realistic mock catalog. We fitted a power law of the form $n = a \times S^{-\gamma} + b$ (see Equation 2.1) to the binned measured peak brightness distribution, and draw fluxes between 3σ and 60σ randomly from this distribution. The mock sources are assigned a position that is at least 20 pixels ($\sim 8''$) away from both real sources and other mock sources. The position of the mock source also has to lie within the 20% power point of the primary beam. The position was randomly chosen until both restrictions are satisfied.

After all mock sources are inserted, we run PyBDSF with the exact parameters as performed for the real sources. Since the extraction is carried out on a map containing both real and mock emission, the real sources are always recovered and had to be filtered out in order to keep only simulated sources in the extracted catalog.

The recovered $S_{\text{int}}/S_{\text{peak}}$ distribution as a function of S/N is shown in Fig. 2.6. To determine the 95% envelope in Fig. 2.6, a curve (red line) is fitted to the 95th percentile of logarithmic bins across the S/N, where $N = \sigma_{\text{local}}$ as measured by PyBDSF. The shape of the envelope was chosen following Bondi et al. (2008). The fit for the 10 GHz image simulations is given by $S_{\text{int}}/S_{\text{peak}} = 1.14 + 11.6 \times (S/N)^{-1.64}$. The fit for the 3 GHz image simulations is given by $S_{\text{int}}/S_{\text{peak}} = 1.07 + 14.0 \times (S/N)^{-1.69}$.

We consider sources from our catalog that lie above this envelope to be resolved. For the 10 GHz image there are 12 (13%) resolved sources and for the 3 GHz image there are 475 (32%) resolved sources. For sources that lie under the envelope, the integrated flux density was set equal to the peak brightness. The resolved sources are flagged as resolved in the final catalog presented in Section 2.3.8. Note that not all the PyBDSF sources with multiple Gaussian components are resolved by this criterion as each component is considered separately. Conversely, not all single-component sources are unresolved.

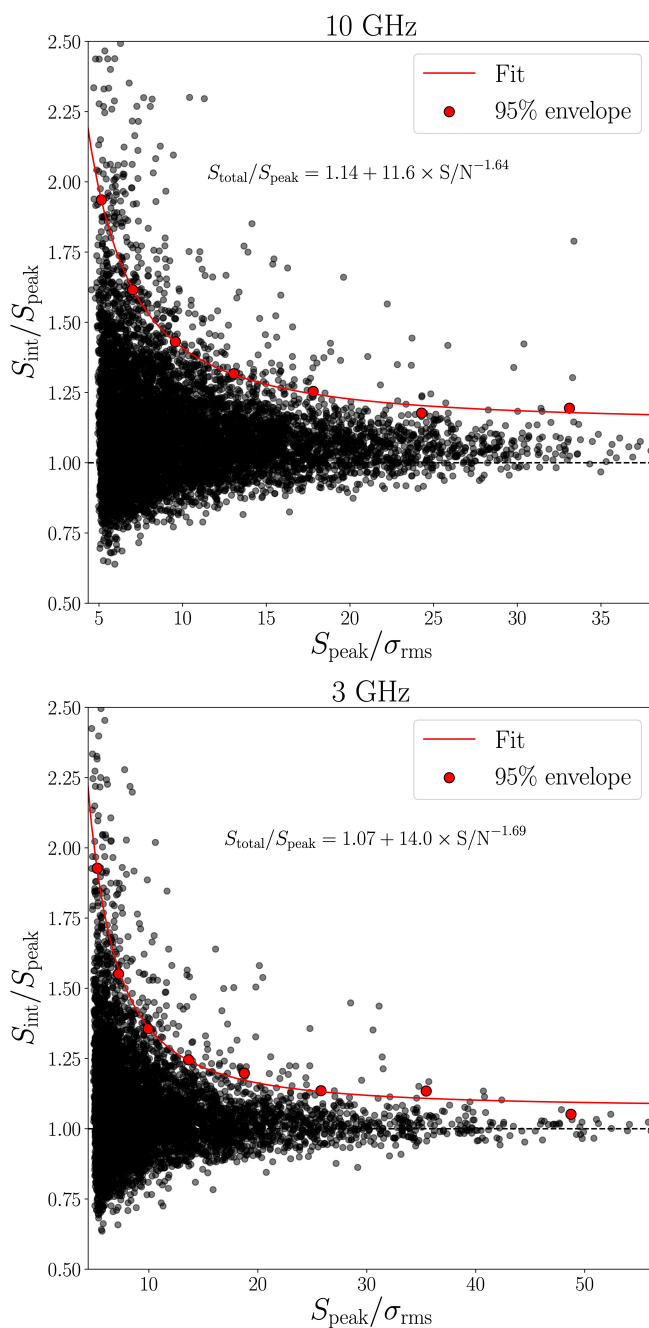


Figure 2.6: The simulated ratio of integrated flux density to peak brightness as a function of signal-to-noise ratio for unresolved sources from the 200 Monte Carlo simulations for the 10 GHz image (upper panel) and the 3 GHz image (lower panel). For logarithmic bins in signal-to-noise ratio, the red points show the threshold below which 95% of the sources lie in that bin. The red line shows the fit to this upper envelope. Applying these thresholds to the real data, we find that, respectively, 13% and 32% of the sources are resolved.

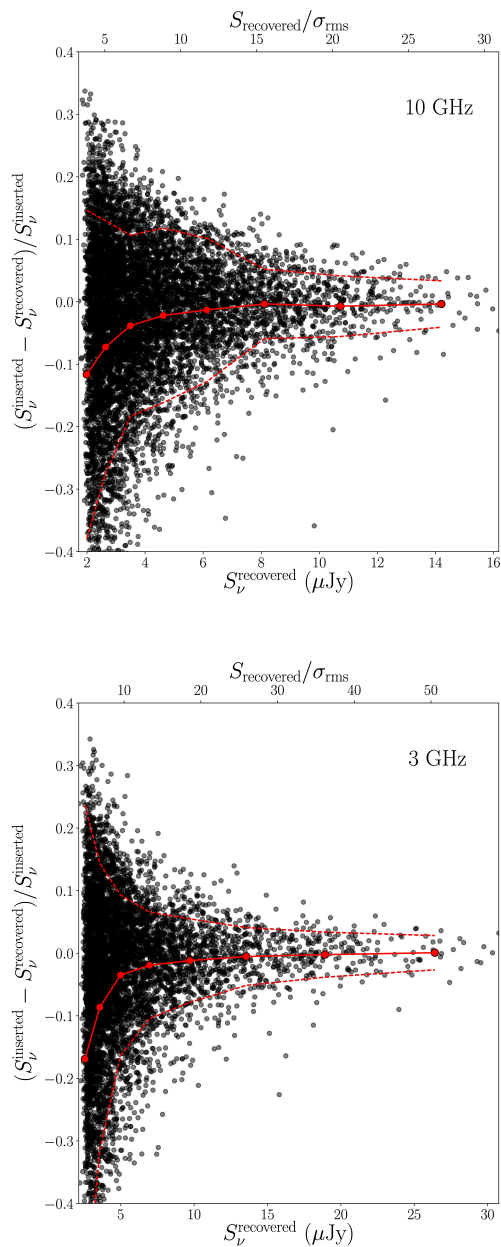


Figure 2.7: The simulated ratio of (inserted flux density - recovered flux density) to inserted flux density as a function of the recovered flux density. The upper panel shows the distribution for the 10 GHz image and the lower panel shows the distribution for the 3 GHz image. The solid red line denotes the median of 8 logarithmic bins (indicated by the red points) across the flux density range and the dashed lines mark the 1σ upper and lower bounds in those bins. The effect of flux boosting at the faint end is illustrated by the rapid downturn below about $3 \mu\text{Jy}$ for 10 GHz and 3 GHz.

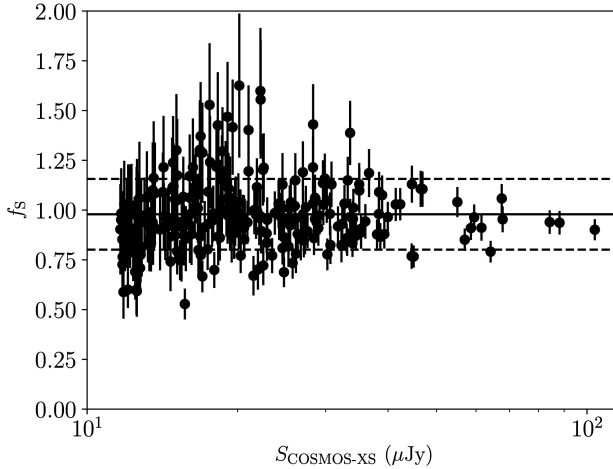


Figure 2.8: Flux comparison between our sample and the VLA-COSMOS 3 GHz Large Project (Smolčić et al. 2017a). The median ratio of 0.98 with a standard deviation of 0.18 shows that the flux densities are on the same flux scale.

2.3.3 Flux boosting

The noise fluctuations in the image may influence the flux measurements of the extracted sources. Since the counts of faint sources increase with decreasing flux density, there should be a sea of faint sources below the noise level that may influence the source extraction. There is therefore a probability that intrinsically faint sources are detected at higher flux because of noise fluctuations. This effect, called flux boosting, is extremely important at low S/N where flux measurement can be overestimated.

The degree of flux boosting (the probability that faint sources are detected at higher flux density because of noise fluctuations) can be estimated by examining the output-to-input flux density of the simulations described in the above section. Fig. 2.7 shows the distribution of the recovered flux density minus the inserted flux density normalized by the inserted flux density as a function of recovered flux density, where we calculated the mean and standard deviation in logarithmic bins.

The effect for flux boosting is, as expected, greatest at the flux limit of our survey. For the 10 GHz (3 GHz) image, sources with $S/N \simeq 5$ are boosted by 11% (15%) on average. The boosting effect quickly decreases with S/N; we find that sources with $S/N \simeq 10$ are boosted by less than 5% on average. Therefore, we do not correct for flux boosting.

2.3.4 Flux density uncertainties at 3 GHz

In order to determine any systematic offsets, we have compared our flux densities to those of the VLA-COSMOS 3 GHz Large Project. For the comparison, we selected

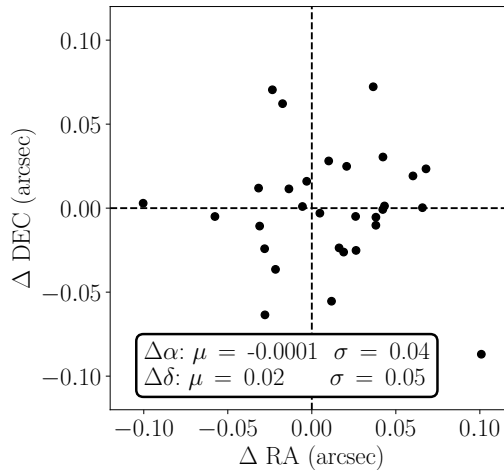


Figure 2.9: Astrometry comparison between 3 GHz and 1.4 GHz VLBA data for 30 VLBA sources (Herrera Ruiz et al. 2017). Median and standard deviation for Δ R.A. and Δ Decl. are reported in the panel. The positions of sources detected at 3 GHz are in excellent agreement with the positions as reported in the VLBA-COSMOS 1.4 GHz survey (Herrera Ruiz et al. 2017).

only sources that could be detected at high signal to noise in the VLA-COSMOS 3 GHz Large Project catalog which has a flux density limit of $S/\sigma > 5 = 11.5\mu\text{Jy}$. We also consider only unresolved sources in the VLA-COSMOS 3 GHz Large Project catalog to rule out resolution effects. This yielded a sample of 250 objects. For this sub-sample of sources, we determined the ratio of peak brightness between the COSMOS-XS survey and the VLA-COSMOS 3 GHz Large Project $f_S = S_{\text{COSMOS-XS}}/S_{\text{Smolcic+2017}}$. The result of this comparison is shown in Fig. 2.8. We measured a median ratio of 0.98 with a standard deviation of 0.18. The plot shows that the flux scale is in good agreement with the VLA-COSMOS 3 GHz Large Project one over the entire flux range probed. We see also no systematic offsets in this subset with distance from the phase center.

2.3.5 Astrometry

To assess our astrometric accuracy, we have compared the positions of 30 sources at 3 GHz with $S/N > 20$ with the positions detected in the Very Long Baseline Array (VLBA)-COSMOS 1.4 GHz survey (Herrera Ruiz et al. 2017). The matching radius used to find the 3 GHz sources in the Herrera Ruiz et al. (2017) catalog was $0''.4$. The results, shown in Fig. 2.9, yield an excellent agreement with a mean offset of $-0''.0001$ in Δ R.A. and $0''.02$ in Δ Decl. We find a standard deviation of $0''.04$ for Δ R.A. and $0''.05$ for Δ Decl. We note that we did not correct the catalog entries for the offsets found.

2.3.6 Completeness

To quantify the completeness of the catalog, we performed another set of Monte Carlo simulations where we added simulated sources to the pre-primary-beam-corrected image. Injecting sources into the image allows us to account for the varying noise across the field. We use the same approach as in Section 2.3.2 but when the position of the source was determined, the input flux density of the source was reduced, dependent on position within the primary beam. By doing this we account for the decreasing sensitivity with increasing distance from the pointing center due to the primary beam attenuation. Because the beam sensitivity is not uniform and decreasing, the effective area over which we are sensitive to a given flux density S decreases rapidly with the flux density itself. By inserting primary beam-corrected flux densities, the derived completeness correction automatically includes the effect of variation of sensitivity as a function of distance from the map center.

To allow for a better estimate of the completeness in terms of integrated flux densities, the mock sources also include a percentage of extended sources: Gaussians with FWHM larger than the beam size. The mock sources get, therefore, besides a S_{peak} also a major axis, minor axis and a S_{int} assigned. To generate an angular size distribution for the mock sources, we drawn randomly from two skewed Gaussians, one for the major axis and one for the minor axis. These Gaussians are determined by fitting to the normalized distribution of the fitted Gaussian parameters as measured for the real sources by PyBDSF.

The total flux density was chosen to be either their integrated flux density if resolved, or their peak brightness if unresolved. To determine whether a simulated source was resolved or unresolved, we use the same $S_{\text{int}}/S_{\text{peak}}$ envelope as described in Section 2.3.2.

Recovered mock sources are found by matching the retrieved catalog to the mock catalog. A retrieved source was considered to be matched with the inserted mock source if it was found within $0''.5$ of the inserted mock source position. Sources with a counterpart were flagged as recovered sources.

The completeness of a catalog represents the probability that all sources above a given flux density are detected. We have estimated this by giving the fraction of mock sources that are recovered using the same detection parameters. In Fig. 2.10 we plot the fraction of detected sources in our simulation as a function of integrated flux density, accounting for the primary beam. This detection fraction is largely driven by the variations in r.m.s. across the image and the primary beam. The error on the correction is the standard deviation of the calculated correction over all 200 realizations of the mock catalog. We thus estimate that the catalog is 85% complete above a flux density of $10 \mu\text{Jy}$ for the 10 GHz image and above a flux density of $15 \mu\text{Jy}$ for the 3 GHz image.

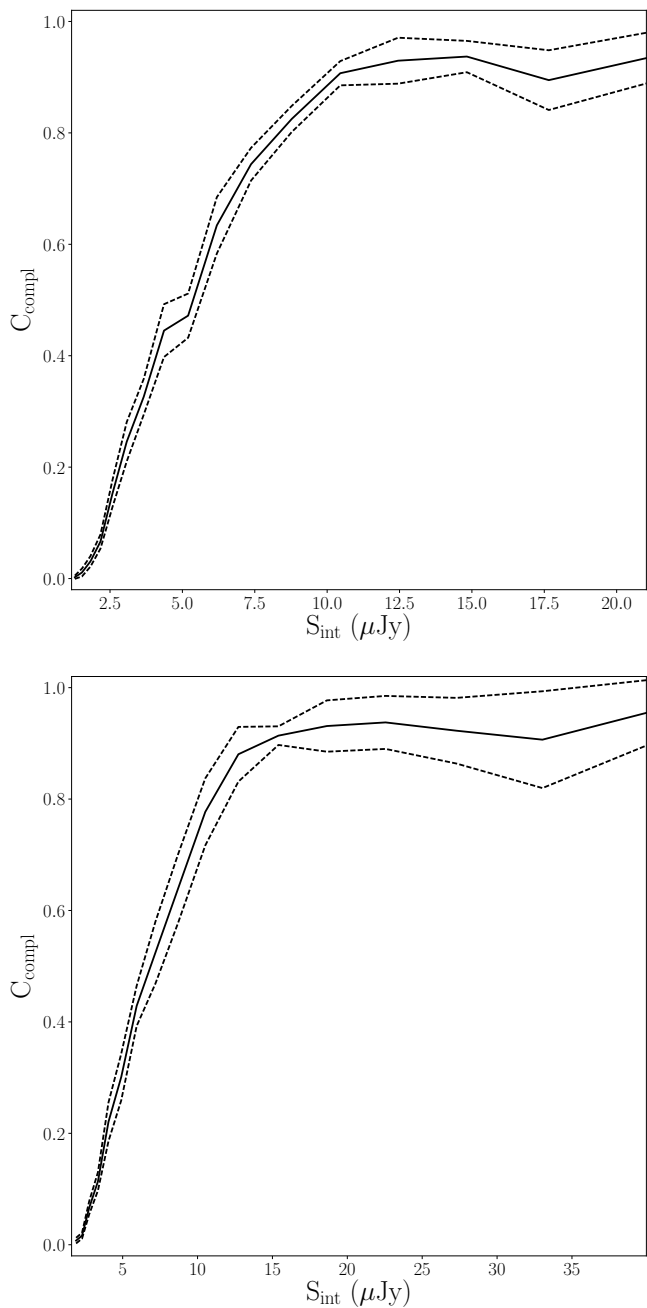


Figure 2.10: Completeness of the 10 GHz (upper panel) and the 3 GHz (lower panel) source catalog as a function of flux density. The solid black line shows the mean completeness of all Monte Carlo runs and the dotted black lines show the standard deviation. The completeness is above $\sim 85\%$ for $10 \mu\text{Jy}$ and for $15 \mu\text{Jy}$ for the 10 GHz and the 3 GHz source catalog, respectively. Note that the completeness does not reach 100% because effects of the primary beam are also included.

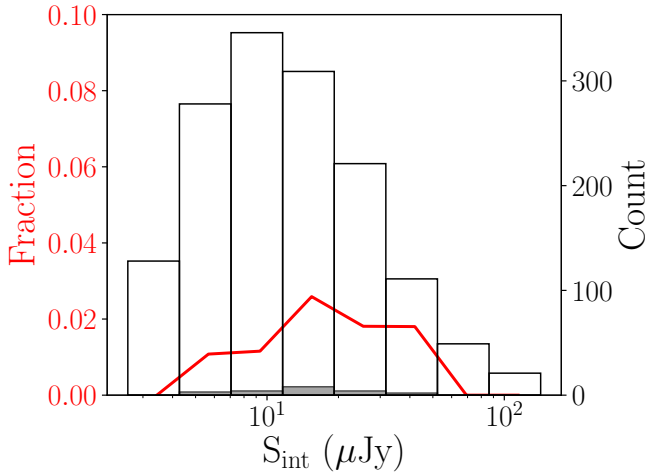


Figure 2.11: Fraction of false detections (red line) as a function of flux density. The open (filled) histogram shows the number of components cataloged in the observed 3 GHz map (detected in the inverted map). These data are also listed in Table 2.4. The false-detection rate is always smaller than 3%, and is 1% overall.

2.3.7 Reliability

The reliability of a source catalog indicates the probability that all sources above a given flux density are real sources and not accidental detections of background features or noise. To assess the false-detection rate of our source extraction, we ran PyBDSF on the inverted (i.e., multiplied by -1) continuum map, within 20% of the peak primary beam sensitivity, with the same settings used for the main catalog. Since there is no negative emission on the sky, every source detected in the inverted map is by definition a noise peak (i.e., a false detection). The false-detection rate is determined from the number ratio of negative sources over positive sources per flux density bin. Errors are calculated based on Poissonian errors on the number of sources per flux density bin.

For the inverted 10 GHz image, no sources were detected above our catalog threshold of 5σ ; thus the false-detection rate was determined to be zero. The false-detection rate found for the 3 GHz image is shown in Fig. 2.11 with the red line. The number counts for both the real and falsely detected sources are also shown. In total there are 22 negative detections for the 3 GHz image, which results in a total false-detection rate of $\sim 1\%$. These sources are located around bright sources and are thus likely caused by the artifacts surrounding these sources.

Table 2.3. Sample of the 3GHz COSMOS-XS catalog.

Source ID (1)	R.A. [deg] (2)	$\sigma_{R.A.}$ [arcsec] (3)	Decl. [deg] (4)	$\sigma_{Decl.}$ [arcsec] (5)	S_{int} [μJy] (6-7)	S_{peak} [$\mu Jy \text{ beam}^{-1}$] (8-9)	σ_{local} [$\mu Jy \text{ beam}^{-1}$] (10)	Gaussians (11)	Resolved (12)
COSMOS-XS J100027.60+023634.21	150.11501	0.14907	2.6095	0.19592	4.04 \pm 1.11	3.52 \pm 0.67	0.65	S	U
COSMOS-XS J100014.35+023147.58	150.0598	0.03873	2.52988	0.04186	15.58 \pm 1.03	13.74 \pm 0.62	0.6	S	U
COSMOS-XS J100055.00+022849.80	150.22917	0.02603	2.4805	0.03019	52.54 \pm 2.4	46.48 \pm 1.44	1.41	S	R
COSMOS-XS J100031.26+023642.93	150.13026	0.03604	2.61192	0.04184	17.77 \pm 1.16	16.04 \pm 0.69	0.68	S	U
COSMOS-XS J100004.85+023559.51	150.02019	0.12507	2.59986	0.12439	7.01 \pm 1.43	6.21 \pm 0.85	0.84	S	U
COSMOS-XS J100056.66+022635.42	150.23607	0.02513	2.44317	0.03391	101.17 \pm 3.56	76.85 \pm 2.22	2.14	S	R
COSMOS-XS J100029.99+022903.64	150.12494	0.06062	2.48434	0.1729	5.85 \pm 1.63	3.19 \pm 0.66	0.66	M	U
COSMOS-XS J100046.61+023443.89	150.1942	0.2192	2.57886	0.10006	7.25 \pm 1.37	5.54 \pm 0.84	0.83	S	U
COSMOS-XS J100013.14+022550.66	150.05477	0.06633	2.43074	0.09338	22.27 \pm 2.2	17.69 \pm 1.34	1.32	S	R
COSMOS-XS J100004.59+023301.50	150.01914	0.05262	2.55042	0.06861	11.75 \pm 1.31	11.05 \pm 0.77	0.76	S	U

Notes. The format is as follow: Column (1): Source name. Column (2) and (3): flux density-weighted R.A. and uncertainty. Column (4) and (5): flux density-weighted Decl. and uncertainty. Column (6) and (7): integrated source flux density and uncertainty in μJy . Column (8) and (9): peak brightness and uncertainty in $\mu Jy \text{ beam}^{-1}$. Column (10): the local r.m.s. noise. Column (11): number of Gaussian components; S refers to a single-Gaussian source, and M refers to a multi-Gaussian source. Column (12): a flag indicating the resolved parametrization of the source; ‘U’ refers to unresolved sources and ‘R’ to resolved sources.

2.3.8 Source catalog

The final 10 GHz catalog consists of 91 sources and the final 3 GHz catalog consists of 1481 sources. Both catalogs are available as a table in FITS format as part of the online version of this article. Resolved sources are identified as described in Section 2.3.2. Errors given in the catalog are the nominal fit errors reported by PyBDSF. A sample of the 3 GHz catalog is shown in Table 2.3.

2.4 Results

In this section, we report two results based on the produced catalogs: the 10 and 3 GHz faint source counts. Further analysis of these data will be presented in future publications.

2.4.1 Radio source counts

We use the 10 and 3 GHz catalogs to compute the source counts down to integrated flux densities $\sim 2 \mu\text{Jy}$ and $\sim 2.5 \mu\text{Jy}$ respectively.

The source counts are computed using the integrated flux densities (which means peak brightness for unresolved and integrated flux density for resolved), but sources are detected based on their measured peak brightness over the local noise level. The completeness of the source counts will thus depend both on the variation of the noise in the image and on the relation between integrated flux densities and peak brightness. In the following, we discuss these effects and how we correct for them in deriving the source counts.

Multi-component sources

Source counts need to take into account that sources may be made up of multiple components. For example, radio sources associated with radio galaxies can be made up of a nucleus with hot spots along, or at the end of, one or two jets. When jets are detected, it is relatively easy to recognize the components belonging to the same source. When a jet is missing, the radio-lobes are detected as two separated sources. We apply the statistical technique described by Magliocchetti et al. (1998) and White et al. (2012) to find these double component sources. We consider the separation of the nearest neighbor of each component and the summed flux density of the source and its neighbor. Multi-components are combined as single sources if the ratio of their flux densities is between 0.25 and 4 and their separation is less than a critical value dependent on their integrated flux density given by:

$$\theta_{\text{crit}} = 100 \left(\frac{S_{\text{sum}}}{10} \right)^{0.5}, \quad (2.2)$$

where S_{sum} is in mJy and θ_{crit} is in arcsec. This maximum separation is shown in Fig. 2.12. We analyzed both the 10 and 3 GHz image but only found multi-component

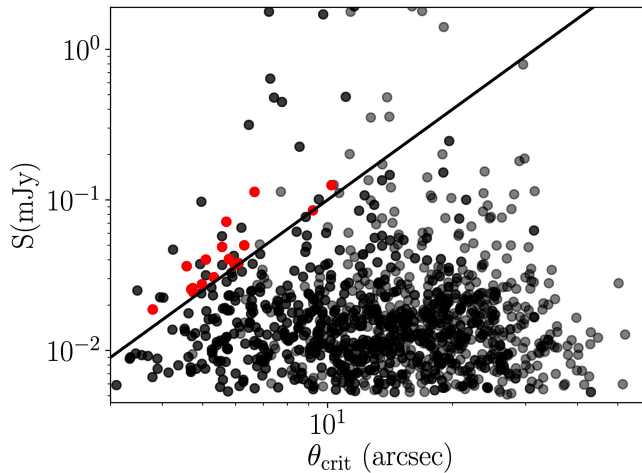


Figure 2.12: Sum of the flux densities of nearest neighbor pairs as a function of their separation. Source pairs that have separation less than the critical value given by the solid line and flux densities that differ by less than a factor of 4 are considered as double source candidates. 17 sources are identified as multi-component sources and are indicated with red points.

sources for the 3 GHz image. The 3 GHz sources that meet both requirements are shown in Fig. 2.12 as red circles. From this analysis we could identify 17 multi-component sources. See also Fig. 2.A.1 for an example of a multi-component source.

Completeness and reliability

We consider a correction for the completeness of the catalog as derived in Section 2.3.6. Using the derived completeness corrections we can calculate the source counts ($n(S)$) in each flux density bin using

$$n(S) = \frac{1}{A} \sum_{i=1}^N \frac{1}{C_{\text{compl}}(S_i)}, \quad (2.3)$$

where $A \sim 350 \text{ arcmin}^2$ is the solid angle considered for the source counts, N is the number of sources in the flux density bin and $C_{\text{compl}}(S_i)$ is the derived completeness for the given flux density.

Additionally, we make a correction for the reliability for the source counts at 3 GHz by applying the false-detection rate derived in Section 2.3.7. This correction acts in the opposite direction to the completeness correction and can be added to Equation 2.3:

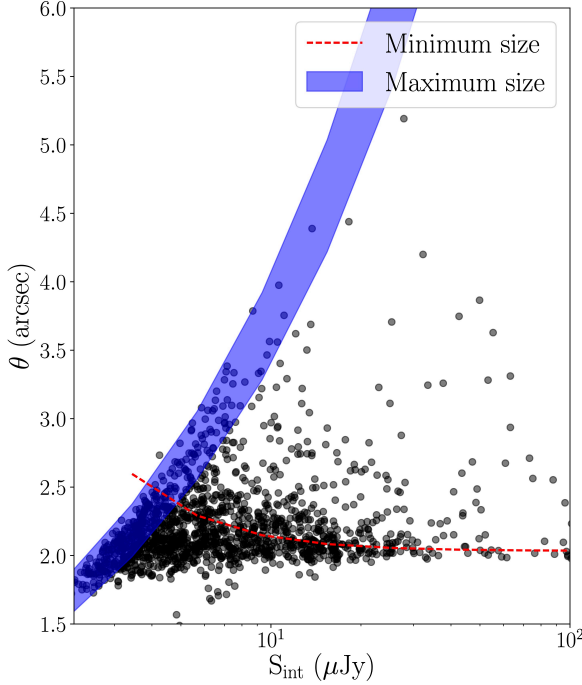


Figure 2.13: The fitted angular size, θ (geometric mean), as a function of integrated flux density at 3 GHz. Unresolved sources fall below the red dotted line giving the minimum size of a source. The minimum size was derived using the envelope from Section 2.3.2. The blue shaded region shows the maximum size a source of a given integrated flux density can have before dropping below the peak brightness detection threshold where the range reflects the range of r.m.s. noise in the 3 GHz image.

$$n(S) = \frac{1}{A} \sum_{i=1}^N (1 - F_{\text{false-det}}(S_i)) \frac{1}{C_{\text{compl}}(S_i)}, \quad (2.4)$$

where A is the solid angle considered for the source counts, N is the number of sources in the flux density bin, $C_{\text{compl}}(S_i)$ is the derived completeness for the given flux density and $F_{\text{false-det}}(S_i)$ is the correction for the false-detection rate for the given flux density bin.

Resolution bias

Sources in our image are found by identifying peaks of emission above a given threshold. This means that a resolved source of a given integrated flux density will be

missed more easily than a point source of the same integrated flux density. This incompleteness is called the resolution bias and causes the number of sources to be underestimated, particularly near the detection limit of the survey. We correct for the resolution bias by utilizing the analytic method as used in Prandoni et al. (2001) and Williams et al. (2016).

The following relation can be used to calculate the maximum angular size that a source can have and still be detected for a given integrated flux density:

$$S_{\text{int}}/5\sigma = \frac{\theta_{\text{min}}\theta_{\text{maj}}}{b_{\text{min}}b_{\text{maj}}}, \quad (2.5)$$

where θ_{min} and θ_{maj} are the fitted source axes as measured by PyBDSF, b_{min} and b_{maj} are the synthesized beam axes and 5σ is the peak brightness detection limit (where σ is the local r.m.s. in the image). We use this relation to calculate the maximum size that a source can have and still be detected. This relation is shown in Fig. 2.13, where the range reflects the range of r.m.s. noise in the image. Fig. 2.13 also shows the distribution of θ , the geometric mean of the source major and minor axes, as a function of integrated flux density for all sources in the 3 GHz catalog. Also shown is the minimum size a source can have before it is deemed to be unresolved. We use the maximum size to calculate the fraction of sources expected to be larger than this value, following Windhorst, Mathis & Neuschaefer (1990), using

$$h(> \theta_{\text{max}}) = \exp \left[-\ln(2) \left(\frac{\theta_{\text{max}}}{\theta_{\text{med}}} \right)^{0.62} \right], \quad (2.6)$$

where θ_{max} is the maximum angular size and θ_{med} the median angular size. θ_{max} can be calculated by rewriting Equation 2.5:

$$\theta_{\text{max}} = \sqrt{b_{\text{min}}b_{\text{maj}} \times \frac{S_{\text{int}}}{5\sigma}} \quad (2.7)$$

We use two different versions of θ_{med} for comparison; the first, given by Windhorst et al. 1990,

$$\theta_{\text{med}} = 2(S_{1.4\text{GHz}})^{0.3}'' \quad (2.8)$$

with $S_{1.4\text{GHz}}$ in mJy (flux densities are scaled from 10 GHz and 3 GHz to 1.4 GHz using a spectral index of -0.7), and the second used a constant size of $0''.35$ below 1 mJy (based on recent results from Cotton et al. 2018 and Bondi et al. 2018) as follows:

$$\theta_{\text{med}} = \begin{cases} 0''.35, & \text{for } S_{1.4\text{GHz}} < 1 \text{ mJy,} \\ 2(S_{1.4\text{GHz}})^{0.3}'', & \text{otherwise.} \end{cases} \quad (2.9)$$

We can calculate the resolution-bias correction factor to be applied to the source counts using:

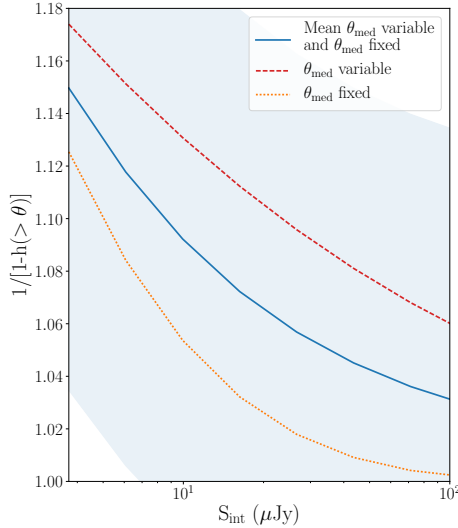


Figure 2.14: Resolution bias correction $1/[1 - h(> \theta_{\max})]$ for the fraction of sources with angular size larger than θ_{\max} at a given integrated flux density at 3 GHz. For the faintest sources, three curves are shown: the red dashed curve shows θ_{med} as a function of S_{int} , the orange dotted curve shows the result assuming $\theta_{\text{med}} = 0''.35$ at these flux densities, and the blue solid curve shows the mean of the two curves. The range reflects the assumed 10% uncertainty following Windhorst et al. (1990). The resolution bias correction is found to be 1.15 for the lowest flux bin.

$$c = 1/[1 - h(> \theta_{\max})]. \quad (2.10)$$

The correction factors calculated using the two different size distributions are plotted as a function of 3 GHz S_{int} in Fig. 2.14. We use the mean of the two correction factors to correct the source counts in this paper, and this correction is calculated and applied for both the 10 and 3 GHz sources. We use the uncertainty in the forms of θ_{med} and in θ_{\max} to estimate the uncertainty in the resolution bias correction. We further include an overall 10% uncertainty following Windhorst et al. (1990) which dominates the error budget. We correct the resolution bias in the source counts measurements by using the following to calculate the source counts in each flux density bin

$$n(S) = \frac{1}{A} \sum_{i=1}^N (1 - F_{\text{false-det}}(S_i)) c(S_i) \frac{1}{C_{\text{compl}}(S_i)}, \quad (2.11)$$

where A is the solid angle considered for the source counts, N is the number of sources in the bin, $C_{\text{compl}}(S_i)$ is the derived completeness and $c(S_i)$ is the resolution bias correction for the given flux density bin.

Table 2.4. Euclidean-normalized differential source counts for the 3 GHz catalog.

ΔS_ν [μJy]	S_ν [μJy]	Counts [$\text{Jy}^{1.5}$ sr^{-1}]	Error [$\text{Jy}^{1.5}$ sr^{-1}]	N	$F_{\text{false-det}}$	C_{compl}	c
2.82 – 4.61	3.72	0.56	0.12	161	0.0	0.17	1.14
4.61 – 7.55	6.08	0.84	0.12	287	0.02	0.4	1.11
7.55 – 12.35	9.95	1.13	0.14	349	0.01	0.74	1.09
12.35 – 20.2	16.27	1.55	0.19	292	0.02	0.91	1.07
20.2 – 33.04	26.62	1.97	0.25	184	0.02	0.93	1.05
33.04 – 54.04	43.54	2.23	0.36	101	0.02	0.94	1.04
54.04 – 88.41	71.22	2.25	0.44	48	0.0	0.94	1.03
88.41 – 144.62	116.51	2.33	0.59	24	0.0	0.94	1.03

Notes. The format is as follows: Column (1): flux interval. Column (2): bin center. Column (3): differential counts normalized to a non evolving Euclidean mode. Column(4): error on differential counts. Column (5): number of sources detected. Column (6): false-detection rate. Column (7): completeness correction. Column (8): resolution bias correction. The listed differential counts were corrected for completeness and resolution bias (C_{compl} and c), as well as false detection fractions ($F_{\text{false-det}}$), by multiplying the raw counts by the correction factor which is equal to $(c(S_i) * (1 - F_{\text{false-det}}(S_i)))/C_{\text{compl}}(S_i)$. The source count errors take into account the Poissonian errors and completeness and bias correction uncertainties (see text for details).

2.4.2 The sub- μJy source counts at 3 GHz compared to observations

The Euclidean-normalized counts are shown in Fig. 2.15(a) and tabulated in Table 2.4. Uncertainties on the final normalized source counts are propagated from the errors on the correction factors and the Poisson errors on the raw counts per bin. For the uncorrected data points, these errors are only the Poisson errors. Fig. 2.15(a) illustrates our results compared to other observational results, including the 3 GHz surveys by Condon et al. (2012), Vernstrom et al. (2014), Smolčić et al. (2017a).

Condon et al. (2012) used the $P(D)$ (probability distribution of peak flux densities) analysis technique to statistically estimate the radio number counts down to $\sim 1 \mu\text{Jy}$ from VLA 3 GHz observations. $P(D)$ analysis tends to be less prone to resolution effects as it studies the statistical properties of sources well below the confusion limit of the survey. This approach results in statistical estimates of the source counts that are much fainter than the faintest sources that can be counted individually. Vernstrom et al. (2014) also used the $P(D)$ analysis technique to re-analyze the 3 GHz observations from Condon et al. (2012) and estimate the radio number counts down to $\sim 50 \text{ nJy}$. They used a different approach from Condon et al. (2012) that allowed

for more flexibility in accurately modelling the true source counts. Our completeness-corrected points are slightly higher than the Condon et al. (2012) results and more consistent with the Vernstrom et al. (2014) results.

Smolčić et al. (2017a) derived source counts from 3 GHz observations of the 2 deg² COSMOS field in the VLA-COSMOS 3 GHz Large Project. For comparison we show both the uncorrected number counts and number counts corrected for completeness, resolution bias and false detections. Our completeness corrected points lie consistently a factor ~ 1.4 above the source counts from Smolčić et al. (2017a).

One possible cause for the offset between our source counts and those of Smolčić et al. (2017a) is an underestimated correction for the resolution bias. In particular, our survey has a lower resolution than the Smolčić et al. (2017a) observation ($2''$ versus $0''.75$) and is therefore less likely to miss sources due to the resolution bias (see also the small correction derived in Section 2.4.1). Smolčić et al. (2017a) performed extensive Monte Carlo simulations to account for the resolution bias. They modeled the intrinsic angular sizes of mock sources using a simple power-law parametrization distribution of the angular sizes as a function of their total flux density, as derived by Bondi et al. (2008). They apply a minimum angular size for faint mock sources to ensure the modelled angular size distribution matched the observed size distribution. We tested whether the difference in resolution bias correction methods between Smolčić et al. (2017a) and that used here (described in Section 2.4.1) is significant, finding that when applied to the same data, our method results in a higher normalization than their method by a factor of ~ 1.1 (i.e., $\sim 25\%$ of the observed difference). Therefore, the difference in resolution bias correction method may partly explain the offset between our number counts and those reported in Smolčić et al. (2017a).

To attempt to gain some additional insight, we also compare our results with those from recent 1.4 GHz (or similar) observations in Fig. 2.15(a). We scale those flux densities to the 3 GHz observed frame assuming a spectral index of -0.84 .⁶ Bondi et al. (2008) derive their counts in the inner 1 deg² region of the COSMOS field from the VLA-COSMOS 1.4 GHz Large Project (Schinnerer et al. 2007) catalog, which requires a somewhat uncertain correction for the effect of bandwidth smearing, while Prandoni et al. (2018) derived their counts from 1.4 GHz mosaic observations obtained with the Westerbork Synthesis Radio Telescope (WSRT). Because the latter cover an area of 6.6 deg², the source catalog contains ~ 6000 sources (note that the error-bars in Fig. 2.15(a) are smaller than the symbols). Finally, Mauch et al. (2020) used the $P(D)$ analysis technique to derive source counts from $0.25 \mu\text{Jy}$ to $10 \mu\text{Jy}$ using confusion-limited 1.28 GHz MeerKAT observations. They further derive the source counts between $10 \mu\text{Jy}$ and 2.5 mJy from individual detected sources. The direct source counts (scaled to 3 GHz) are shown in Fig. 2.15(a).

With the spectral index assumed (-0.84), we find that the source counts of Bondi et al. (2008), Prandoni et al. (2018), and Mauch et al. (2020) generally fall between those of Smolčić et al. (2017a) and those seen here, and are on average lower than our source counts (particularly the Mauch et al. (2020) counts, which also extend to

⁶ Smolčić et al. (2017a) found this spectral index by performing a Gaussian fit to the spectral index distribution of 3 GHz sources which were also detected at 1.4 GHz. This spectral index is different from the value derived using a survival analysis which takes non-detections into account. The difference can be explained by selection effects as discussed in Condon (1984).

the lowest flux densities). As already noted by Smolčić et al. (2017a), the comparison between the 1.4 and 3 GHz source counts is complicated by the potentially overly simplistic scaling of the 3 GHz counts to 1.4 GHz using a single spectral index value (in addition to the varying resolution bias and bandwidth smearing effects present). We therefore investigate one final effect that may influence the measured source counts in the following section.

Cosmic variance

A final source of uncertainty that may affect the measured source counts is cosmic variance. In particular, if we observe over-densities in our single pointing, the resulting number counts will be higher than the number counts averaged over a larger area (as done in Smolčić et al. 2017a).

Heywood et al. (2013) developed a method to assess the influence of source clustering on radio source counts. They extracted a series of independent samples from the models of Wilman et al. (2008). We used a similar approach with both the Wilman et al. (2008) simulation and the Bonaldi et al. (2019) simulation, which are further discussed in the next section, to estimate the uncertainty induced by sample variance on a survey with the properties of our survey.

Following Heywood et al. (2013), we extract multiple non-overlapping sky patches with areas of $0.31 \times 0.31 \text{ deg}^2$ from the Wilman et al. (2008) simulation (comparable to the effective area of our observations). We used a simulated area of $4 \times 4 \text{ deg}^2$. This process resulted in 169 source catalogs. For each of these simulated source subsets, we compute the Euclidean-normalized differential source counts. Fig. 2.15(b) shows the mean value of the simulated counts from the independent distributions in each bin with the solid purple line. The shaded regions surrounding this correspond to one, three and five times the standard deviation of the count measurements. Fig. 2.15(b) shows that count fluctuations found in our observed survey area are significant enough to dominate the observed scatter at flux densities above $100 \mu\text{Jy}$, and contribute significantly below this.

A similar approach was used to produce the shaded regions in Fig. 2.16(a). Here, we extract multiple non-overlapping sky patches with areas of $0.31 \times 0.31 \text{ deg}^2$ from the simulation of Bonaldi et al. (2019). We used a simulated area of 25 deg^2 . This process results in 289 source catalogs. For each of these simulated source subsets, we compute the Euclidean-normalized differential source counts. The shaded regions in Fig. 2.15(b) and Fig. 2.16(a) show that the offset between our number counts and the Smolčić et al. (2017a) counts could be at least partly explained by cosmic variance.

We are able to test this further using the fact that the Smolčić et al. (2017a) counts are derived from an area that also covers our pointing. By counting the sources in the Smolčić et al. (2017a) catalog within the area of our pointing and assuming the completeness corrections described in Smolčić et al. (2017a), we can compare their source density directly with our number counts. This comparison is shown in Fig. 2.15(a). The number counts in the Smolčić et al. (2017a) catalog over our pointing are noisy due to the small number statistics in this (shallower) sample, but indicate a slightly higher source density (on average) within the area of our survey. We conclude that the systematic offset observed between our 3 GHz number

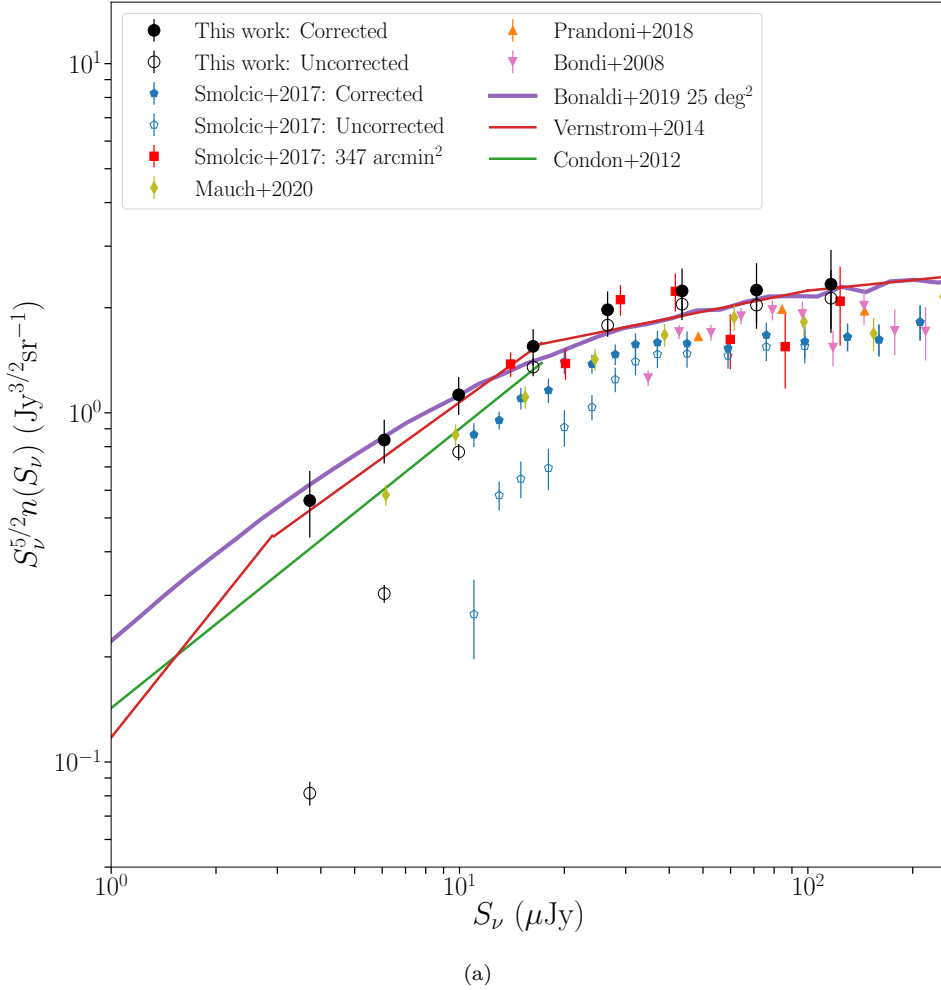


Figure 2.15: Euclidean-normalized radio source counts at 3 GHz (filled black circles). Open black circles show the source counts without corrections. Error bars correspond to the Poisson error for the uncorrected points. For the corrected points the errors are propagated from the errors on the correction factors and the Poisson errors on the raw counts per bin. Corrected (closed) and uncorrected (open) VLA-COSMOS 3 GHz measurements from Smolčić et al. (2017a) are shown with blue points. Panel (a) also shows the number counts from $P(D)$ analysis by Condon et al. (2012, green line) and Vernstrom et al. (2014, red line). The purple line shows the results from the simulation of Bonaldi et al. (2019). The red filled squares show the source counts for sources in the Smolčić et al. (2017a) catalog within the area of our pointing. Panel (a) also shows the results from 1.4 GHz observations from Bondi et al. (2008, filled pink downward triangles) and Prandoni et al. (2018, filled orange upward triangles) and 1.28 GHz observations from Mauch et al. (2020, filled olive diamonds). The flux densities are shifted to the 3 GHz observed frame using a spectral index of -0.84 .

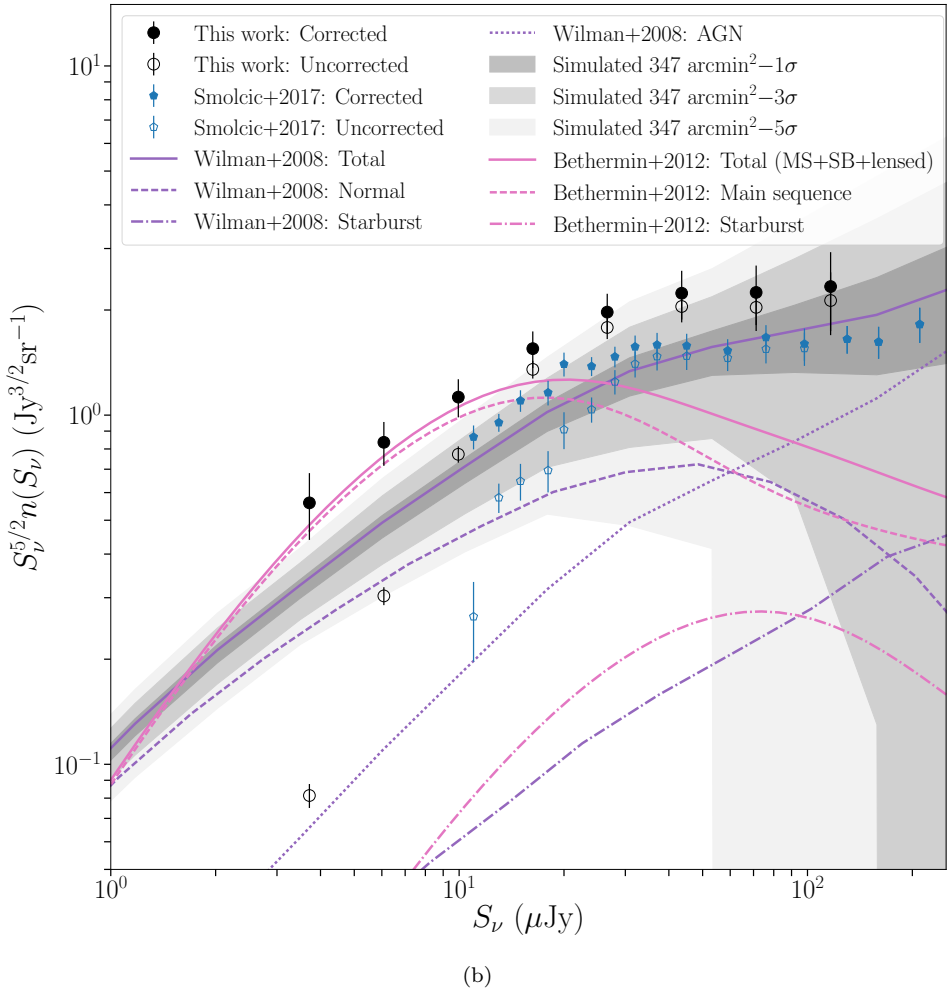


Figure 2.15: Continued. Panel (b) shows the comparison to the number counts from the simulation of Wilman et al. (2008, purple lines) and Béthermin et al. (2012, pink lines). Different line styles correspond to different source types as defined in the legend. The solid lines show the total source counts. The shaded region demonstrates the effect of cosmic variance and correspond to 1, 3 and 5 standard deviations in the source counts measurements of the simulations by Wilman et al. (2008).

counts and the 3 GHz direct detections from Smolčić et al. (2017a) can most likely be explained by a combination of cosmic variance in our pointing and an underestimated resolution bias correction in Smolčić et al. (2017a).

In summary, we find that our 3 GHz source counts agree with those at both 3 and 1.4 GHz within the various uncertainties, while extending down to typically lower flux densities than previous direct detections. In the following section, we will therefore explore the implications of our derived source counts on the modeling of the ultra-faint radio population.

2.4.3 The sub- μ Jy source counts at 3 GHz compared to simulations

In Fig. 2.15(b) we compare our number counts with semi-analytical models from Wilman et al. (2008) and Béthermin et al. (2012). Wilman et al. (2008) developed a semi-empirical simulation that used observed and extrapolated luminosity functions to populate an evolving dark matter skeleton with various galaxy types (normal, starburst and AGN). The distribution of sources on the underlying dark matter density is done with biases which reflects their measured large-scale clustering. The Béthermin et al. (2012) model uses two main ingredients to predict the number counts: the evolution of main-sequence galaxies and starburst galaxies based on the 2-Star-Formation-Mode framework of Sargent et al. (2012) and main-sequence and starburst SEDs to predict the shape of the IR luminosity function at $z \leq 2$. Béthermin et al. (2012) also included dust attenuation and strong lensing in their model. To get to 1.4 GHz radio source counts, they assumed a non-evolving IR-radio correlation and a synchrotron spectral slope of $\alpha = -0.8$.

Our derived source counts deviate from those predicted by the Wilman et al. (2008) model. In particular, they tend to be higher than the predicted model from $\sim 40 \mu\text{Jy}$ downward (and we note that the Smolčić et al. (2017a) counts are also systematically above this model at low flux densities despite a possibly underestimated resolution bias correction; See Section 2.4.2). On the other hand, our 3 GHz source counts are in good agreement with the Béthermin et al. (2012) model below $\sim 10 \mu\text{Jy}$. The AGN population is not included in the Béthermin et al. (2012) model and this explains the decrease in the source counts above $20 \mu\text{Jy}$ as AGN start contributing significantly at these flux densities. Below $20 \mu\text{Jy}$ the star-forming population dominates the number counts, as can be seen from Fig. 2.16(a) and Fig. 2.15(b). Béthermin et al. (2012) model this population using a framework that uses more recent results to predict the LF of SFGs at $z \leq 2$ compared to the Wilman et al. (2008) model. Béthermin et al. (2012) use a combination of mid-IR, UV data (Daddi et al. 2007; Elbaz et al. 2007; Noeske et al. 2007), FIR data (Elbaz et al. 2011; Pannella et al. 2015), and radio continuum imaging (Karim et al. 2011). Wilman et al. (2008) assume pure luminosity evolution out to $z = 1.5$ of the local LF derived from the IRAS 2-Jy sample by Yun et al. (2001). Our results suggest that the Wilman et al. (2008) model could be improved by using the most recent observations to derive a model for the LF for SFGs.

Bonaldi et al. (2019) developed an improved simulation in the spirit of that of

Wilman et al. (2008): the Tiered Radio Extragalactic Continuum Simulation (T-RECS). Bonaldi et al. (2019) model the radio sky in terms of two main populations, AGNs and SFGs, and use these to populate an evolving dark matter skeleton. To describe the cosmological evolution of the LF of AGNs, they adopted an updated model of Massardi et al. (2010), with the revision of Bonato et al. (2017). The LF of SFGs is derived from the evolving SFR function as the radio continuum emission is correlated with the SFR. The SFR function gives the number density of galaxies per logarithmic bin of SFR at a given redshift z . The evolution of the synchrotron-SFR relation accounts for the evolving radio-FIR correlation. Bonaldi et al. (2019) use the SFR function with redshift derived by Cai et al. (2013) and Cai et al. (2014) with an extension derived by Mancuso et al. (2015). The resulting SFR function extends now up to $z \sim 10$ and includes effects from strong gravitational lensing.

We compare the 3 GHz source counts to the simulation from Bonaldi et al. (2019) using the medium tier catalog of 25 deg² containing 3 GHz flux densities. Our number counts, shown in Fig. 2.16(a), match the total number counts from the simulations.

Fig. 2.16(a) also shows the comparison between our source counts and those from the model by Mancuso et al. (2017). This model includes three populations: radio-loud (RL) AGN, radio-quiet (RQ) AGN and SFG. Using the same prescriptions as Bonaldi et al. (2019), they convert SFRs into 10 and 3 GHz luminosities. The SFR function used is, however, slightly different from the function used in Bonaldi et al. (2019) (see Section 2.4.4). The RL AGNs are modeled the same way as in Bonaldi et al. (2019). To model RQ AGNs, the SFR function is mapped into the AGN luminosity function. The obtained AGN bolometric luminosity is subsequently converted to X-ray luminosity. The AGN radio power is then derived using the observed relation between rest-frame X-ray and 1.4 GHz radio luminosity for RQ AGNs.

The Mancuso et al. (2017) model uses an intrinsic SFR function and therefore claims to be less sensitive to dust extinction effects. The derived intrinsic SFR function implies a heavily dust-obscured galaxy population at high redshifts ($z > 4$) and at large SFRs ($10^2 M_{\odot} \text{ yr}^{-1}$) (Mancuso et al. 2016). Our number counts, shown in Fig. 2.16(a), fall well above the total number counts predicted by Mancuso et al. (2017) at the faint end. In addition, there is a clear difference between the Bonaldi et al. (2019) simulations and the Mancuso et al. (2017) model, which is surprising as they use similar assumptions. The difference between the two simulations is further discussed in Section 2.4.4.

To summarize, Wilman et al. (2008) models SFGs assuming pure luminosity evolution out to $z = 1.5$ for the local LF. Thereafter there is no evolution for the LF. This model reproduces the sources in the local universe as it matches the observed number density. These sources dominate flux densities at $> 2 \text{ mJy}$. However, for flux densities $< 40 \mu\text{Jy}$ we find that the Béthermin et al. (2012) model and the Bonaldi et al. (2019) simulation are in better agreement with our observations. These models are able to produce the observed excess with respect to the source counts predicted by the Wilman et al. (2008) simulation. Our number counts support the steeper LF evolution for SFGs that is used in these models.

Table 2.5. Euclidean-normalized differential source counts for the 10 GHz catalog.

ΔS_ν [μJy]	S_ν [μJy]	Counts [$\text{Jy}^{1.5}$ sr^{-1}]	Error [$\text{Jy}^{1.5}$ sr^{-1}]	N	$F_{\text{false-det}}$	C_{compl}	c
2.71 – 8.36	5.53	0.53	0.1	52	0.0	0.53	1.1
8.36 – 25.8	17.08	0.97	0.22	31	0.0	0.9	1.06
25.8 – 79.66	52.73	1.2	0.65	7	0.0	0.88	1.04

Notes. The format as follows: Column (1): flux interval. Column (2): bin center. Column (3): differential counts normalized to a non evolving Euclidean mode. Column(4): error on differential counts. Column (5): number of sources detected. Column (6): false-detection rate. Column (7): completeness correction. Column (8): resolution bias correction. The listed differential counts were corrected for completeness and resolution bias (C_{compl} and c), as well as false detection fractions ($F_{\text{false-det}}$), by multiplying the raw counts by the correction factor which is equal to $(c(S_i) * (1 - F_{\text{false-det}}(S_i))) / C_{\text{compl}}(S_i)$. The source count errors take into account the Poissonian errors and completeness and bias correction uncertainties (see text for details).

2.4.4 The sub- μJy source counts at 10 GHz

The Euclidean-normalized counts at 10 GHz are shown in Fig. 2.16(b). Uncertainties on the final normalized source counts are propagated from the errors on the correction factors and the Poisson errors on the raw counts per bin. The source counts are tabulated in Table 2.5.

With an observing frequency of 10 GHz, we measure flux densities closer to the rest-frame frequencies $\nu \geq 30$ GHz where the total radio emission is dominated by free-free radiation (e.g., Condon 1992; Murphy et al. 2011; Klein et al. 2018). The calibration of the free-free radiation and SFR in the Bonaldi et al. (2019) simulations follows Mancuso et al. (2015) and Murphy et al. (2011). The Mancuso et al. (2017) model used the same calibration for SFGs.

We can compare the 10 GHz source counts to the simulation from Bonaldi et al. (2019) by interpolating between the flux densities of their simulated sources given at 9.2 GHz and 12.5 GHz. Our number counts fall slightly above the total number counts from the simulations. The discrepancy is however within the σ derived for the cosmic variance, shown with gray shaded regions in Fig. 2.16(b). The shaded regions are derived in the same way as described in Section 2.4.2 by extracting sky patches of $0.09 \times 0.09 \text{ deg}^2$ from the Bonaldi et al. (2019) simulations. This process results in 3025 source catalogs.

Our number counts are systematically higher than those predicted by Mancuso et al. (2017) at 10 GHz, especially at the faint end. This would indicate that Mancuso et al. (2017) underestimates the flux density produced at 10 GHz, especially by SFGs,

as these contribute most at low flux densities as can be seen in Fig. 2.16(b).

As seen in Fig. 2.16(a) and Fig. 2.16(b), the Bonaldi et al. (2019) and Mancuso et al. (2017) simulations predict roughly the same general shape of the number counts, but they predict a different normalization. The Mancuso et al. (2017) model includes the specific modeling of RQ AGN. In the Bonaldi et al. (2019) simulations, RQ AGN are not specifically modeled, and Bonaldi et al. (2019) mention that RQ AGNs would contribute part of the flux density of those sources that, in T-RECS, are modelled as SFGs. This could thus not explain the difference in normalization between the total source counts.

Instead, the difference in normalization may be partially explained by how the two models treat the evolution of the radio-FIR correlation. Bonato et al. (2017) already showed that source counts support an evolving radio-FIR correlation. In their study, the source counts found without an evolving radio-FIR correlation are found to be substantially below the observational determinations. The Mancuso et al. (2017) model does not include the increase of the ratio between synchrotron luminosity and FIR luminosity as was recently reported by Delhaize et al. (2017) and Magnelli et al. (2015) and falls thus below the observed source counts. Bonaldi et al. (2019) evolve the synchrotron-SFR relation to account for the evolving radio-FIR correlation, yielding a very good fit to the observational estimates of the radio luminosity function of SFGs (Novak et al. 2017).

In addition to their different treatment of the radio-FIR correlation, both the Mancuso et al. (2017) and Bonaldi et al. (2019) studies also use a slightly different SFR function to make number counts predictions. In particular, both studies use a smooth, analytic representation of the SFR function derived from IR and dust-extinction-corrected UV, Ly α and H α data. However, Mancuso et al. (2017) use a standard Schechter shape characterized by three evolving parameters: the normalization, the characteristic SFR and the faint-end slope. Meanwhile, Bonaldi et al. (2019) use the modified Schechter function introduced by Aversa et al. (2015), with two evolving characteristic slopes. Our observed number counts are in better agreement with the SFR function used by Bonaldi et al. (2019), which was derived by Mancuso et al. (2015), although the function used in Mancuso et al. (2017) was derived using the most recent IR and UV data.

In summary, as seen in Sections 2.4.3 and 2.4.4, models typically assume either an evolving LF or an evolving SFR function to make number counts predictions at the μ -Jy level. We find that our source counts are in agreement with the Bonaldi et al. (2019) model that uses an evolving radio-FIR relation and the modified Schechter function to describe the SFR function. We also find that the source counts predictions from the evolving LF for SFGs used by Béthermin et al. (2012) result in a good match with the observed number counts below 10 μ -Jy.

The relation between the LF and the SFR functions will be investigated and presented in a future publication. The luminosity-SFR relation is of crucial importance for measuring the cosmic SFH, which will also be studied in a future publication. In addition, we can utilize the multi-wavelength information available in the COSMOS region to determine the composition of the faint radio population responsible for the measured number counts. This will be fully discussed and presented in a companion paper (Algera et al. 2020a).

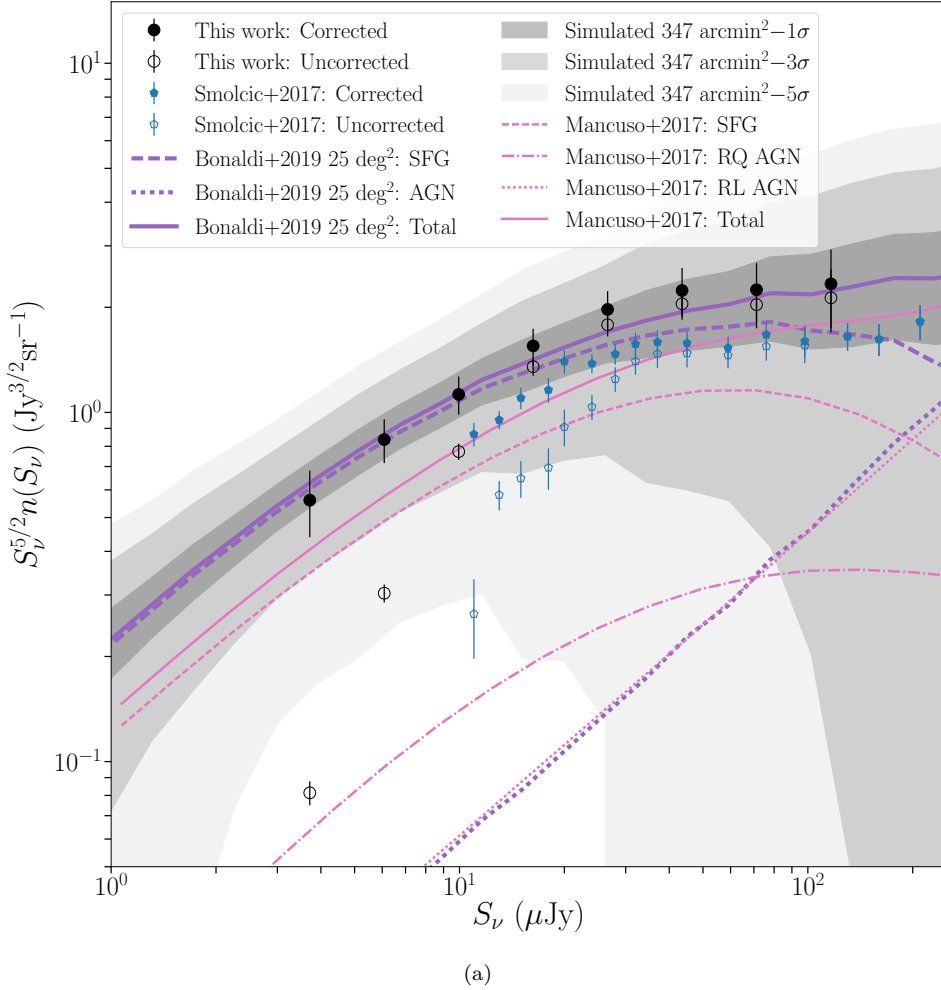
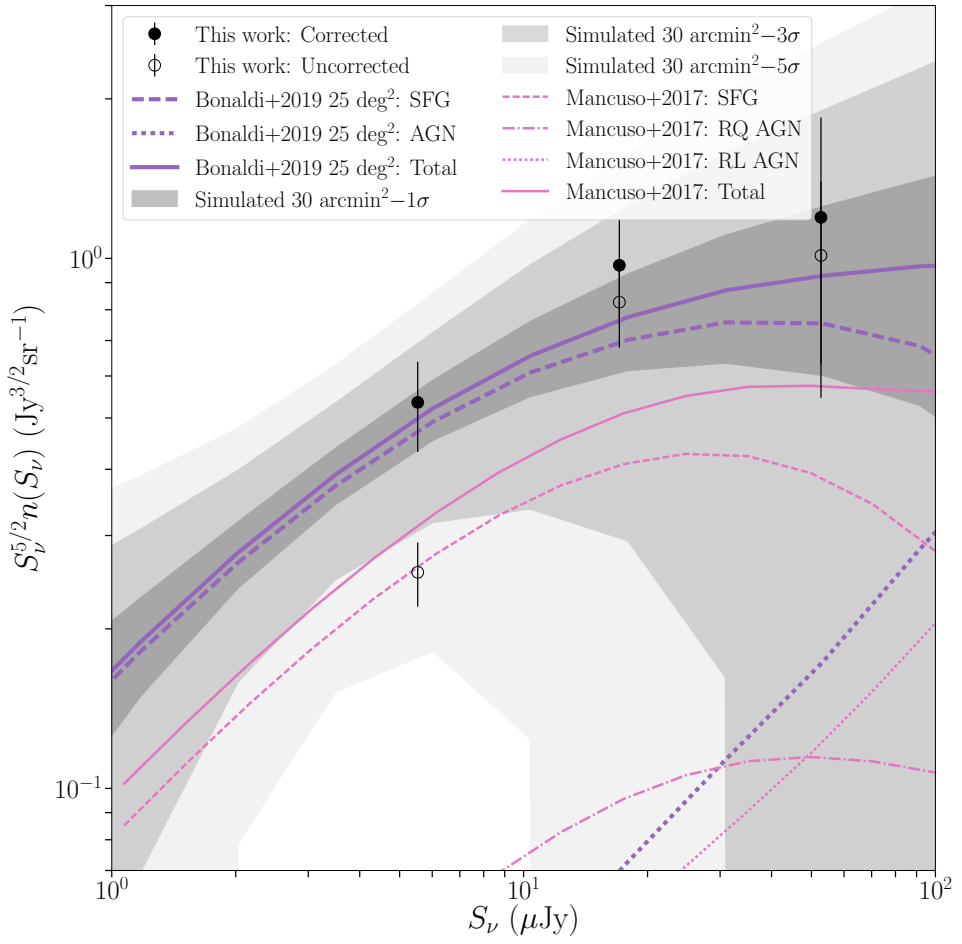


Figure 2.16: Euclidean-normalized radio source counts at 3 GHz (panel (a)) and 10 GHz (panel (b)). The filled black circles show the source counts from COSMOS-XS. Open black circles show the source counts without corrections. Error bars correspond to the Poisson error for the uncorrected points. For the corrected points the errors are propagated from the errors on the correction factors and the Poisson errors on the raw counts per bin. Corrected (closed) and uncorrected (open) VLA-COSMOS 3 GHz measurements from Smolčić et al. (2017a) are shown with blue points. The number counts from the simulation of Bonaldi et al. (2019) and predictions from Mancuso et al. (2017) are shown in purple and pink lines, respectively. Different line styles corresponding to different source types as defined in the legend. The solid lines show the total source counts from the simulation. The shaded regions demonstrate the effect of cosmic variance and correspond to 1, 3 and 5 standard deviations in the source counts measurements of the simulations by Bonaldi et al. (2019).



(b)

Figure 2.16: Continued.

2.5 Summary & Conclusions

In this paper, we presented the details of the COSMOS-XS survey: an ultra-deep pointing in the COSMOS field at 10 and 3 GHz with the Karl G. Jansky VLA. The final 10 and 3 GHz images have a resolution of $\sim 2''$ and reach a median r.m.s. at the phase center of $0.41 \mu\text{Jy beam}^{-1}$ and $0.53 \mu\text{Jy beam}^{-1}$, respectively. The two radio catalogs contain sources detected within 20% of the peak primary beam sensitivity with peak brightness exceeding 5σ . The 10 GHz catalog contains 91 sources and the 3 GHz catalog contains 1498 sources.

Comparing the positions of our 3 GHz sources with those from the high-resolution VLBA imaging at 1.4 GHz, we estimated that the astrometric uncertainties are negligible. Completeness corrections are calculated using Monte Carlo simulations whereby the effect of the primary beam is taken into account. We find that the completeness is above $\sim 85\%$ at $10 \mu\text{Jy}/15 \mu\text{Jy}$ for the 10 GHz/3 GHz source catalogs, respectively. We correct for the resolution bias by utilizing an analytic method as used in Prandoni et al. (2001) and Williams et al. (2016).

The deep 10 and 3 GHz observations enable us to investigate the Euclidean-normalized source counts down to the μJy level. Our corrected radio counts at 3 GHz with direct detections down to $\sim 2.8 \mu\text{Jy}$ are consistent within the uncertainties with other results at 3 and 1.4 GHz, but extend to fainter flux densities than previous direct detections.

In comparison to simulations developed in the framework of the SKA Simulated Skies project (Wilman et al. 2008), our source counts show an excess which cannot be accounted for by cosmic variance. Our measured source counts suggest a steeper LF evolution for SFGs for low flux densities ($< 2 \text{ mJy}$). The T-RECS simulations (Bonaldi et al. 2019) and the Béthermin et al. (2012) model both produce this steeper evolution and are in better agreement with our measured source counts.

Our corrected radio counts at 10 GHz with direct detections down to $\sim 2.7 \mu\text{Jy}$ are systematically higher than those predicted by the T-RECS simulations (Bonaldi et al. 2019), but we demonstrate that this falls within the expected variations from cosmic variance. The more significant offset observed between our counts and Mancuso et al. (2017) support an evolving radio-FIR relation and a modified Schechter function to describe the SFR function, as done in Bonaldi et al. (2019).

The COSMOS-XS survey is one of the deepest radio continuum surveys to-date, providing valuable information for next-generation facilities, such as the ngVLA and SKA, which will achieve much deeper imaging. These radio data, in conjunction with the vast panchromatic COSMOS data sets, will allow us to study the dust-unbiased SFH, place critical constraints on dust attenuation and conduct a study of the long-wavelength spectra of faint radio sources.

Acknowledgments

We thank the anonymous referee for helpful comments and suggestions that significantly improved this work. We thank Preshanth Jagannathan, Huib Intema and

Reinout van Weeren for the useful discussions that helped improve the imaging with `wSclean`; Chris Carilli for the useful discussions while preparing the proposal and for his help planning the observations; Mara Salvato for providing us with the COSMOS spectroscopic master catalog; Ian Smail for his comments; Andrea Lapi for providing the evolutionary track shown in Fig. 2.16(a) and Fig. 2.16(b), which refers to the model discussed in Mancuso et al. (2017); and Paolo Ciliegi and Gianni Zamorani for useful discussion on previous 1.4 GHz source counts. The National Radio Astronomy Observatory is a facility of the National Science Foundation operated under cooperative agreement by Associated Universities, Inc. H.A., D.vdV. and J.H. acknowledge support of the VIDI research programme with project number 639.042.611, which is (partly) financed by the Netherlands Organisation for Scientific Research (NWO). D.R. acknowledges support from the National Science Foundation under grant number AST-1614213. D.R. also acknowledges support from the Alexander von Humboldt Foundation through a Humboldt Research Fellowship for Experienced Researchers. This research made use of `ASTROPY`, a community developed core Python package for astronomy (Astropy Collaboration et al. 2013, 2018) hosted at <http://www.astropy.org/>, `matplotlib` (Hunter 2007), `numpy` (van der Walt et al. 2011), `scipy` (Jones et al. 2001), and of `TOPCAT` (Taylor 2005).

Appendices

2.A Postage stamp images

Examples of extended, multi-component and compact sources are shown in Fig. 2.A.1.

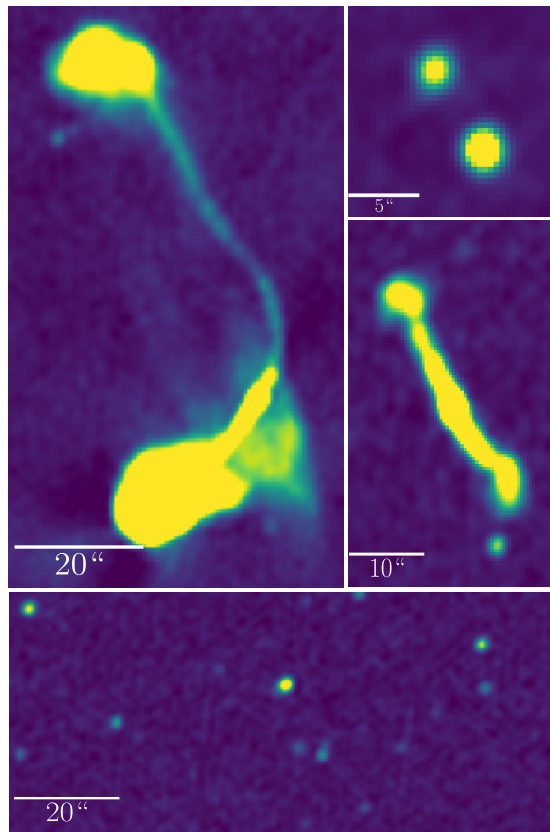


Figure 2.A.1: Stamps from the 3 GHz continuum map showing examples of extended (left and lower right image), multi-component (upper right) and compact (lower panel) radio sources. The color-scale shows the flux density from $-3 \sigma_{\text{local}}$ to $50\sigma_{\text{local}}$, where σ_{local} is the local r.m.s. noise.

3 | New constraints on the cosmic star formation history

Abstract

We make use of ultra-deep 3 GHz Karl G. Jansky Very Large Array observations of the COSMOS field from the multi-band COSMOS-XS survey to infer radio luminosity functions (LFs) of star-forming galaxies (SFGs). Using ~ 1300 SFGs with redshifts out to $z \sim 4.6$, and fixing the faint and bright end shape of the radio LF to the local values, we find a strong redshift trend that can be fitted by pure luminosity evolution with the luminosity parameter given by $\alpha_L \propto (3.40 \pm 0.11) - (0.48 \pm 0.06)z$. We then combine the ultra-deep COSMOS-XS data-set with the shallower VLA-COSMOS 3 GHz large project data-set over the wider COSMOS field in order to fit for joint density+luminosity evolution, finding evidence for significant density evolution. By comparing the radio LFs to the observed far-infrared and ultraviolet (UV) LFs, we find evidence of a significant underestimation of the UV LF by $22\% \pm 14\%$ at high redshift ($3.3 < z < 4.6$, integrated down to $0.03 L_{z=3}^*$). We derive the cosmic star formation rate density (SFRD) by integrating the fitted radio LFs and find that the SFRD rises up to $z \sim 1.8$ and then declines more rapidly than previous radio-based estimates. A direct comparison between the radio SFRD and a recent UV-based SFRD, where we integrate both LFs down to a consistent limit ($0.038 L_{z=3}^*$), reveals that the discrepancy between the radio and UV LFs translates to a significant (~ 1 dex) discrepancy in the derived SFRD at $z > 3$, even assuming the latest dust corrections and without accounting for ‘optically dark’ sources.

3.1 Introduction

Over the past two decades, impressive progress has been made in constraining the star formation rate density (SFRD) over cosmic time using a multitude of star formation rate (SFR) tracers (e.g., review by Madau & Dickinson 2014), providing vital information for understanding galaxy evolution. There is a reasonable consensus regarding the shape of the SFRD in recent history ($z < 2$). However, above $z \sim 3$, the differences in the SFRD still encompass very different predictions from galaxy evolution models (e.g., Gruppioni et al. 2015; Henriques et al. 2015; Lacey et al. 2016; Rowan-Robinson et al. 2016; Casey et al. 2018; Moster et al. 2018; Behroozi et al. 2019). An accurate measurement of the evolution of the SFRD is thus vital for the understanding of galaxy evolution.

Several tracers can be used to trace the SFRD. In principle, ultraviolet (UV) light is the most direct tracer of SFR in dust-free environments which originates mainly from massive stars. UV light thus directly traces young stellar populations and can be used to constrain the unobscured star formation out to very high redshifts ($z \simeq 9$; e.g., McLure et al. 2013; Bouwens et al. 2015; Bowler et al. 2015; Finkelstein et al. 2015; McLeod et al. 2015; Bouwens et al. 2016; Parsa et al. 2016; Mehta et al. 2017; Ono et al. 2018; Oesch et al. 2018; Bouwens et al. 2021). However, UV observations need significant and uncertain corrections for dust obscuration and are unable to detect the most extreme star-forming galaxies (SFGs) in which star formation is known to be enshrouded in dust (e.g., Smail et al. 1997; Lutz et al. 2011; Riechers et al. 2013; Casey et al. 2014a; Dudzevičiūtė et al. 2020). Therefore, knowledge on how the dust attenuation evolves with redshift is mandatory to study the redshift evolution of the SFRD, particularly as the cosmic epoch $z \gtrsim 4$ may be dominated by dust-obscured star formation (Casey et al. 2018; Bouwens et al. 2020).

Dust, heated by young massive stars, re-emits the absorbed UV light at longer wavelengths and can thus be studied in the far-infrared (FIR) or sub-millimeter (sub-mm) to trace the SFR. Current FIR observations are able to constrain the dust content and SFRD up to a redshift $z < 6$ (e.g., Rodighiero et al. 2010; Gruppioni et al. 2013; Rowan-Robinson et al. 2016; Koprowski et al. 2017; Dudzevičiūtė et al. 2020; Lim et al. 2020). However, the constraints beyond $z \simeq 3$ are uncertain as the measurement of the FIR LF becomes more challenging. Source confusion and blending limit the ability to detect faint objects in low resolution *Herschel*/SPIRE observations at $z \simeq 3 - 4$. Such observations are thus biased towards an unrepresentative population of bright sources. In addition, these observations can be significantly contaminated by active galactic nuclei (AGN) as these sources are more numerous at high redshift (Gruppioni et al. 2013; Symeonidis & Page 2021).

Ground-based sub-mm/mm continuum observations of dusty galaxies can help to overcome some of the problems in FIR observations (e.g., Chapman et al. 2005; Hodge et al. 2013; Swinbank et al. 2014; Dunlop et al. 2017; Dudzevičiūtė et al. 2020; Zavala et al. 2021). In particular, ground-based interferometer arrays (e.g., ALMA) offer high-resolution observations and hence do not suffer from source blending. Sub-mm surveys are also less susceptible to AGN contamination as they are predominantly sensitive to the cool-dust in the star-forming population at high redshift (Hodge &

da Cunha 2020). In addition, the dust-unbiased tracer [CII] was recently used in several studies conducted with ALMA to study the SFR (Gruppioni et al. 2020; Khusanova et al. 2021; Loiacono et al. 2021). But even with these advantages, sub-mm observations are still impractical to carry out large surveys that would overcome cosmic variance, which can have a strong impact on any counting statistic (e.g., Moster et al. 2011; Simpson et al. 2019; Gruppioni et al. 2020; Loiacono et al. 2021), because of the small field of view. Cosmic variance in sub-mm can be overcome by combining a wide-field single dish observation with expensive interferometric follow-up observations (Simpson et al. 2020).

Radio continuum emission is also an end-product of the formation of the most massive stars. Synchrotron radiation originates from the shocks produced by the supernova explosions (e.g., Sadler et al. 1989; Condon 1992; Clemens et al. 2008; Tabatabaei et al. 2017). Radio emission triggered by star formation is empirically found to correlate well with the FIR emission of SFGs: the FIR-radio correlation. Radio-SFR calibrations most often rely on this empirical FIR-radio correlation, which appears to hold across more than five magnitudes in luminosity and persists out to high redshifts (e.g., Helou et al. 1985; Yun et al. 2001; Bell 2003), albeit with ill-constrained redshift evolution (e.g., Sargent et al. 2010; Magnelli et al. 2015; Calistro Rivera et al. 2017a; Delhaize et al. 2017). However, there is some discussion whether the redshift evolution can be ascribed to selection biases (Sargent et al. 2010; Algera et al. 2020b; Smith et al. 2021; Molnár et al. 2021; Delvecchio et al. 2021). In addition, AGN activity will cause strong deviation from the local FIR-radio correlation (Molnár et al. 2018) as accreting supermassive black holes (SMBH) in AGN also accelerate the electrons that produce synchrotron emission.

Radio emission is a tracer of star formation which is, unlike UV, not attenuated by dust. In contrast to FIR observations, radio observations have a high spatial resolution and can cover larger areas of the sky than interferometric sub-mm observations with high angular resolution. Radio observations in the synchrotron regime (\sim GHz frequencies) therefore offer a unique opportunity to study the star formation history of the Universe (e.g., Seymour et al. 2008; Smolčić et al. 2009b; Jarvis et al. 2015; Calistro Rivera et al. 2017b; Novak et al. 2017; Leslie et al. 2020; Matthews et al. 2021).

Besides being used to calibrate radio luminosity as a tracer of SFR, the FIR-radio correlation is also often used for the classification of galaxies. A sample used for constraining the SFRD should only consist of sources with radio emission originating from star formation. Therefore one would ideally quantify the emission coming from SF and AGN in all sources. It is, however, easier to simply remove sources that show an excess in radio emission compared to what is expected from the FIR-radio correlation (radio-excess AGN, e.g., Del Moro et al. 2013; Delvecchio et al. 2017; Algera et al. 2020a). Radio-loud AGN are easily removed by this method, as these sources show a large offset from the FIR-radio correlation. A major uncertainty is the ability to distinguish composite sources, which emit low-level AGN emission, from SFGs (e.g., Padovani et al. 2009; Bonzini et al. 2013).

Radio studies to date have observed radio LFs but struggled to reach the knee of the LF (L_*) at $z > 1$. Because these studies are most sensitive to the SFG population above the knee, the density and luminosity evolution parameters may become

degenerate preventing a precise estimate of the knee location. The radio studies from Smolčić et al. (2009b) and Novak et al. (2017) thus assumed pure luminosity evolution rather than luminosity and density evolution (Condon & Mitchell 1984) in order to fit the radio LF out to $z \sim 5$. Recently, Malefahlo et al. (2022) used a Bayesian approach to reach below the 5σ detection limit of Novak et al. (2017) but only constrained pure luminosity evolution. Enia et al. (2022) used 1.4 GHz-selected sample to constrain the evolution of the radio LF up to $z \sim 3.5$ by fitting a modified Schechter function (equivalent to fitting both luminosity and density evolution).

We have taken advantage of the upgraded capabilities of the Karl G. Jansky Very Large Array (VLA) to conduct an ultra-deep, matched-resolution survey in both X- and S-band (10 GHz and 3 GHz, van der Vlugt et al. 2021, hereafter Paper I). In Algera et al. (2020a, hereafter Paper II), the radio catalogs obtained from Paper I were matched with the rich multi-wavelength data available in the COSMOS field (Scoville 2007) to distinguish between AGN and SFG. In this work, we use the 3 GHz star-forming sample to constrain the faint end of the LF with the faintest SFGs that can currently be probed at high redshift with radio surveys. We also leverage the combined power of the COSMOS-XS survey and the 3 GHz VLA-COSMOS Large Project (Smolčić et al. 2017a), which covers a larger 2 deg^2 area to a shallower depth of $\sigma \sim 2.3 \mu\text{Jy beam}^{-1}$, in order to increase our dynamic range and constrain the form and evolution of the LF – and thus ultimately the dust-unbiased SFRD – out to a redshift of $z \sim 4.6$.

This paper is organized as follows: in Section 3.2 we summarize the data and selection methods. In Section 3.3, we present the method of constraining the LFs with redshift. We compare our derived radio LFs to the literature in Section 3.4. In Section 3.5 we discuss possible biases that need to be taken into account in the derivation of the LF. In Section 3.6 we use the most appropriate LF to calculate the evolution of the cosmic star formation rate density. Finally, Section 3.7 summarizes and concludes this work. Throughout this paper, the spectral index, α , is defined as $S_\nu \propto \nu^\alpha$, where S_ν is the source flux density, and ν is the observing frequency. We use a Λ CDM cosmology with parameters $H_0 = 70 \text{ km s}^{-1} \text{ Mpc}^{-1}$, $\Omega_m = 0.3$, $\Omega_\Lambda = 0.7$ (Bennett et al. 2013). We assume a radio spectral index of -0.7 unless otherwise stated. We assume the Chabrier (2003) initial mass function (IMF) to calculate SFRs.

3.2 Data and sample selection

3.2.1 Radio data

The COSMOS-XS survey consists of two overlapping ultra-deep single VLA pointings in the COSMOS field at 3 and 10 GHz of, respectively, $\simeq 90$ and $\simeq 100$ h of observation time. Further details on these observations can be found in Paper I but a short summary of the survey follows. The 3 and 10 GHz observations reach a depth of 0.53 and $0.41 \mu\text{Jy beam}^{-1}$ at their respective pointing centers over an effective area of, respectively, ~ 350 and $\sim 30 \text{ arcmin}^2$. Both frequencies have a near-equal resolution of $\sim 2''0$ ($2''14 \times 1''81$ at 3 GHz and $2''33 \times 2''01$ at 10 GHz) which is large enough

to avoid resolving out faint SF sources.

Details on how the source extraction was performed in both images can be found in Paper I and Paper II. Sources were identified by PYBDSF (Mohan & Rafferty 2015) in the 3 GHz image and resulted in identification of 1540 radio sources.

3.2.2 Counterparts

The counterpart matching method to cross-match the radio sources is fully described in Paper II and briefly summarized below. Counterparts of radio sources were found using a symmetric nearest neighbor algorithm. Counterparts were assigned within a given matching radius. This matching radius was determined through cross-matching with mock versions of the appropriate catalog containing the same sources with randomized sky coordinates.

Radio counterparts

The 10 and 3 GHz data were cross-matched using a matching radius of $0''.9$, which yields 91 matches with a false match rate (FMR) of $\lesssim 0.7\%$. The radio sample was also matched to the VLA COSMOS 1.4 GHz catalog (Schinnerer et al. 2007) using a matching radius of $1''.2$ (FMR $\lesssim 0.1\%$). This generated 185 matches, with 12 sources being detected at all three frequencies (1.4, 3 and 10 GHz).

Optical and near-infrared counterparts

As described in Paper II, the radio observations were complemented with near-UV (NUV) to FIR-data from various multi-wavelength catalogs: i) the Super-deblended mid-infrared to FIR catalog (Jin et al. 2018) containing photometry ranging from IRAC $3.6 \mu\text{m}$ to 20 cm (1.4 GHz) radio observations. Blended galaxies in low-resolution FIR images are partly disentangled using priors on sources' positions from high-resolution images and point spread function fitting; ii) the $z^{++}YJHK_s$ -selected catalog compiled by Laigle et al. (2016, hereafter COSMOS2015) and iii) the i -band selected catalog by Capak et al. (2007).

For each source, we searched for a counterpart in the Super-deblended catalog with a matching radius of $0''.9$. To complement the Super-deblended matches with optical and near-IR (NIR) photometry, we also matched with the COSMOS2015 catalog followed by the i -band catalog with matching radii of $0''.7$ and $0''.9$, respectively. Sources not in the Super-deblended catalog were matched with the COSMOS2015 catalog using a matching radius of $0''.7$. Since the publication of Paper II an updated COSMOS catalog was released: COSMOS2020 (Weaver et al. 2022). For consistency with Paper II, we will use COSMOS2015 but we have verified that updating the redshifts with the COSMOS2020 redshifts does not change the conclusions from this paper. In addition, we computed the reliability of the redshifts, defined as $\sigma = |z_{C2015} - z_{C2020}| / (1 + z_{C2020})$, for the sources that have redshift information in both catalogs. The normalised median absolute deviation (Hoaglin et al. 1983), defined as 1.48 times the median of σ is found to be 0.022, indicating a good overall consistency between the two redshifts. In addition, the fraction of sources

with $\sigma > 0.15$, the threshold for catastrophic failures, equals 6.6%. Sources which still lacked a counterpart were matched with the the *i*-band-selected catalog with a matching radius of $0''.9$. A flowchart of the matching process can be found in Fig. 3 of Paper II. Overall, 70 sources (4.5%) did not have any optical and NIR counterparts. These sources are not included in the subsequent analysis. An analysis on the properties of these sources can be found in Section 5.3 of Paper II. 1470 sources could be matched to a counterpart in at least one multi-wavelength catalog. Based on the matching radii used, we expect a false match rate of $\lesssim 3\%$, corresponding to ~ 40 sources.

Spectroscopic redshifts were obtained from the COSMOS master catalog (M. Salvato et al.; available internally in the COSMOS collaboration). A spectroscopic redshift with a quality factor $Q_f > 3$ was available for 584 radio sources. If a source could be matched within $1''.4$ to an X-ray source, the photometric redshift from the *Chandra* X-ray catalog was used (Civano et al. 2016). Otherwise photometric redshifts from the Super-deblended catalog were used. If a Super-deblended redshift is unavailable, we instead used the photometric redshift from COSMOS2015 or the *i*-band-selected catalog, in that order. 1437 sources have a counterpart and a reliable redshift. 33 sources have no redshift information and are removed from the sample. Out to $z \sim 1$, nearly two-thirds of our redshifts are spectroscopic. This fraction drops dramatically toward higher redshift (Fig. 4 in Paper II shows the distribution of the photometric and spectroscopic redshift).

The accuracy of photometric redshifts is estimated by comparing the photometric and spectroscopic redshift of the 584 sources with a spectroscopic redshift. The median of this comparison is $\sigma(z) = |z_{\text{spec}} - z_{\text{phot}}|/(1 + z_{\text{spec}}) = 0.008$ at all redshifts. The catastrophic failure rate ($\sigma(z) > 0.15$) is found to be 4.8%.

3.2.3 Sample selection

To estimate the LF of SFGs, we need to select sources with their radio emission originating solely from star formation. As radio emission can also originate from accreting black holes, we thus need to remove sources that have their radio emission dominated by an AGN. We use the FIR-radio correlation to select the SFGs, where sources with their radio emission dominated by an AGN will be offset from the FIR-radio correlation. The method to remove AGN from the sample is fully described in Paper II and briefly summarized below.

The FIR-radio correlation is defined as the logarithmic ratio of a galaxy's total FIR-luminosity L_{FIR} , measured between (rest-frame) $8 - 1000 \mu\text{m}$, and its monochromatic radio luminosity at rest-frame 1.4 GHz ($L_{1.4 \text{ GHz}}$, following e.g., Bell 2003; Magagnoli et al. 2015; Delhaize et al. 2017; Calistro Rivera et al. 2017a):

$$q_{\text{TIR}} = \log_{10} \left(\frac{L_{\text{FIR}}}{3.75 \times 10^{12} \text{ W}} \right) - \log_{10} \left(\frac{L_{1.4 \text{ GHz}}}{\text{W Hz}^{-1}} \right). \quad (3.1)$$

The factor 3.75×10^{12} is the central frequency of the total-FIR continuum ($8 - 1000 \mu\text{m}$) in Hz and serves as the normalization. Each galaxy in the sample is fitted

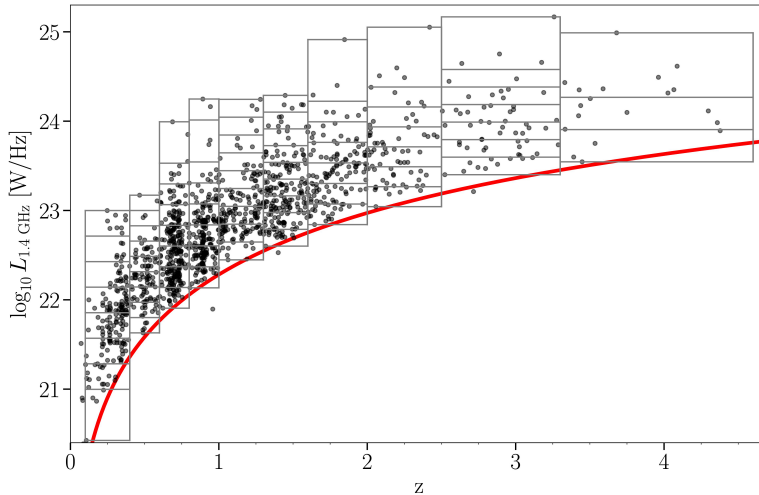


Figure 3.1: The coverage in the COSMOS-XS survey of the luminosity-redshift plane. The gray solid lines depict the redshift and luminosity bins used in the LF analysis. The red line indicates the detection limit of 5σ , where $\sigma = 0.53 \mu\text{Jy beam}^{-1}$ at 3 GHz and a fixed spectral index of $\alpha = -0.7$ is assumed. Sources that fall below the detection limit exist within a region with a low local r.m.s. or have a shallower spectral index.

using the SED fitting code MAGPHYS (da Cunha et al. 2008, 2015), and the total FIR-luminosities are obtained from the best-fitted SEDs.

Rest-frame 1.4 GHz luminosities are determined in Paper II using the measured spectral index for the required K-corrections if available. When only a single radio flux is available, a spectral index of $\alpha = -0.7$ is assumed instead. The luminosities are then calculated through

$$L_{1.4 \text{ GHz}} = \frac{4\pi D_L^2}{(1+z)^{1+\alpha}} \left(\frac{1.4 \text{ GHz}}{3 \text{ GHz}} \right)^\alpha S_{3 \text{ GHz}}. \quad (3.2)$$

Here D_L is the luminosity distance at redshift z and $S_{3 \text{ GHz}}$ is the observed flux density at 3 GHz. The luminosities calculated as a function of redshift are shown in Fig. 3.1.

In order to quantify the FIR-radio correlation and find outliers, we adopt the redshift and mass-dependent $q_{\text{TIR}}(M_*, z)$ determined by Delvecchio et al. (2021). In order to use this $q_{\text{TIR}}(M_*, z)$, we need to have a mass for the sample. We used the mass given by the COSMOS2015 catalog for the sources that could be matched with this catalog. For sources without a mass, we used the derived mean mass per redshift bin, ranging from $10^{10.18} M_\odot$ to $10^{10.70} M_\odot$. When the $q_{\text{TIR}}(M_*, z)$ of a source deviates more than 3σ from the relation from Delvecchio et al. (2021), it is defined as

a radio-excess source, i.e.,

$$q_{\text{TIR}}(M_*, z) < 2.646 \times (1+z)^{-0.023} - 0.148 \times \left(\log_{10} \frac{M_*}{M_{\odot}} - 10\right) - (3 \times \sigma). \quad (3.3)$$

where $\sigma = 0.22$. Such a cut identifies 130 radio-excess sources in total. Recent studies suggest a different evolution, including even a non-evolving $q_{\text{TIR}}(z)$, may be more appropriate (Molnár et al. 2018; Smith et al. 2021; Molnár et al. 2021) and we test the effect of such an assumption in Section 3.5.1.

An additional criterion to identify radio-excess sources is established in Paper II, as only 50% of our sample is detected in the far-infrared at $\geq 3\sigma$. For *Herschel*-undetected sources, a conservative FIR-luminosity at the 2σ level is calculated, assuming the FIR-radio correlation as determined by Delhaize et al. (2017). The calculated FIR-luminosity is compared with the empirically determined detection threshold of *Herschel*. Sources with a calculated FIR-luminosity above the threshold are then identified as ‘inverse radio-excess’ AGN, as they should have been observed with *Herschel* if their radio emission originated solely from star formation. The additional criterion enables us to identify 62 ‘inverse radio-excess’ sources, of which only 17 were not already identified by the threshold in Eq. 3.3. We thus find 147 radio-excess sources in total, leaving a total star-forming galaxy sample consisting of 1290 radio sources. The redshift distribution of the sample is shown in Fig. 3.1.¹

3.2.4 VLA-COSMOS 3 GHz Large Project

Novak et al. (2017) studied the SFRD using the VLA-COSMOS 3 GHz Large Project data. This project provided data over the entire 2 deg^2 COSMOS field allowing for the detection of typical SFGs ($\text{SFR} \lesssim 100 M_{\odot} \text{ yr}^{-1}$) out to $z \sim 1.5$. The COSMOS-XS survey is ~ 5 times deeper than the VLA-COSMOS 3 GHz Large Project and when we combine the VLA-COSMOS 3 GHz Large Project data set over the whole field with our deep COSMOS-XS pointing, we obtain a survey ‘wedding-cake’ with sufficient dynamic range to enable a meaningful measurement of the form and evolution of the LF.

The radio-excess diagnostics by Novak et al. (2017) and Paper II are similar; the overall number of radio-excess sources identified is very similar and the overlap between these two samples is substantial. However, there are a few differences that are addressed in the appendix of Paper II and will be summarized below. Firstly, Paper II used the improved FIR photometry from the Super-deblended catalog (Jin et al. 2018) with a more detailed deblending technique and photometry up to 1.2 mm. Secondly, Novak et al. (2017) used the method from Delvecchio et al. (2017), which uses $\log_{10}(L_{1.4 \text{ GHz}}/\text{SFR}_{\text{IR}})$ to separate radio-excess sources from SF sources. The SFR_{IR} is correlated with the $L_{1.4 \text{ GHz}}$ because the SFR_{IR} is calculated with SED fitting from the L_{IR} and owing to the FIR-radio correlation. Therefore $\log_{10}(L_{1.4 \text{ GHz}}/\text{SFR}_{\text{IR}})$

¹ Sources with $z > 4.6$ like AzTEC-3 are not included because there are too few to give meaningful constraints on the LF.

is equal to q_{TIR} up to a constant.

Delvecchio et al. (2017) then define radio-excess sources when the $\log_{10}(L_{1.4\text{GHz}}/\text{SFR}_{\text{IR}})$ of a source deviates by more than 3σ from the peak of the distribution as a function of redshift. Although this results in a small difference in the total number of radio-excess sources identified in both surveys, we decided to use a consistent criterion for radio-excess sources. We used our threshold which is the $q_{\text{TIR}}(M_{\star}, z)$ determined by Delvecchio et al. (2021) minus 3σ , as described in Section 3.2.3, to select SFGs using the $L_{1.4\text{GHz}}$, $L_{\text{IR,SF}}$ and M_{\star} from the 3 GHz radio catalog (Delvecchio et al. 2017). This results in a data-set with 5822 star-forming sources.

3.3 Analyses

The LF describes the volume density of galaxies as a function of their intrinsic luminosity. We first discuss the method of determining the rest-frame 1.4 GHz LF from the COSMOS-XS survey. We then show how the data can be fitted with a modified-Schechter function assuming different ‘fixed parameters’. Finally, we will consider the addition of the VLA-COSMOS 3 GHz Large Project data to constrain the LF over a larger dynamic range.

3.3.1 Estimating the LF

The radio LFs are derived using the $1/V_{\text{max}}$ method (Schmidt 1968). In each redshift bin, we have computed the co-moving volume available to each source in that bin, defined as $V_{\text{max}} = V_{z_{\text{max}}} - V_{z_{\text{min}}}$, where z_{min} is the lower boundary of the redshift bin and z_{max} is the maximum redshift at which the source could be seen given the flux density limit of the sample. The maximum value of z_{max} corresponds to the upper limit of the redshift bin. For each luminosity bin, the LF is then given by:

$$\Phi(L, z) = \frac{1}{\Delta \log_{10} L} \sum_i \frac{1}{\frac{\Omega}{4\pi} \times V_{\text{max},i} \times w_i(z)}, \quad (3.4)$$

where V_{max} is the co-moving volume over which the i th galaxy could be observed, Ω is the observed area of 350 arcmin^2 , $\Delta \log_{10} L$ is the size of the luminosity bin, and w_i is the completeness correction factor of the i th galaxy. The parameter w_i takes into account the observed area and sensitivity limit and mitigates completeness issues

$$w_i(z) = f_{\text{flux}}(S_{\nu_i}(z)) \times f_{\text{res}}(S_{\nu_i}(z)) \times f_{\text{ctrpt}}(S_{\nu_i}(z)) \times o_i(z), \quad (3.5)$$

where f_{flux} is the flux density completeness of our radio catalog, f_{res} is a correction for resolution bias and f_{ctrpt} is the fraction of sources, which we have obtained reliable non-radio counterparts, for i th galaxy with flux density S_{ν_i} . $o_i(z)$ is the over/under-density factor derived as discussed in Appendix 3.A.

The completeness (f_{flux}) of the COSMOS-XS radio catalog is shown and tabulated in Paper I. The completeness is based on Monte Carlo simulations where mock sources were inserted and extracted from the image. These simulations take into account the effect of the primary beam and the non-uniform r.m.s.. To correct for the resolution bias, we take the values tabulated in Paper I. These resolution bias corrections (f_{res}) were calculated using the analytic method as used in Prandoni et al. (2001) assuming a radio size for faint sources. As discussed in Paper II, 6.7% of our radio sources were not assigned a counterpart. To correct for this incompleteness, we use the counterpart completeness (f_{ctrpt}) of the COSMOS-XS radio catalog which is shown as a function of flux density in Fig 5 from Paper II. The completeness in all bins is upwards of 90%, and no trend with radio flux density can be seen, indicating that the association of counterparts to our radio sources is not limited by the depth of the multi-wavelength photometry.

The error of the LF in each redshift and luminosity bin is calculated as in Marshall (1985):

$$\sigma_{\Phi}(L, z) = \frac{1}{\Delta \log_{10} L} \sqrt{\sum_i \left(\frac{1}{\frac{\Omega}{4\pi} \times V_{\text{max},i} \times w_i(z)} \right)^2}. \quad (3.6)$$

If there are ≤ 10 sources in a luminosity bin, the error is calculated using the tabulated values from Gehrels (1986); we take the tabulated upper and lower 84% confidence interval as σ_N and calculate the upper and lower error on the LF as $\sigma_{\Phi}(L, z) = \Phi(L, z) \times \sigma_N$. We take the average value of the upper and lower error as the final error on the sparsely populated bins.

3.3.2 Constraining the LF

In order to study the evolution of the radio LF, we derive a parametric estimate of the LF at different redshifts. We assume a modified-Schechter function (e.g., Saunders et al. 1990; Smolčić et al. 2009b; Gruppioni et al. 2013) for the shape of the LF:

$$\Phi_0(L) d(\log_{10} L) = \Phi_{\star} \left(\frac{L}{L_{\star}} \right)^{1-\alpha} \exp \left[-\frac{1}{2\sigma^2} \log^2 \left(1 + \frac{L}{L_{\star}} \right) \right] d(\log_{10} L). \quad (3.7)$$

This function behaves as a power-law for $L < L_{\star}$ and as a Gaussian in $\log_{10} L$ for $L > L_{\star}$. Four parameters are used to describe the shape of the LF: L_{\star} describes the position of the turnover of the distribution, Φ_{\star} is used for the normalization and α and σ are used to fit, respectively, the faint and bright end of the distribution. Following

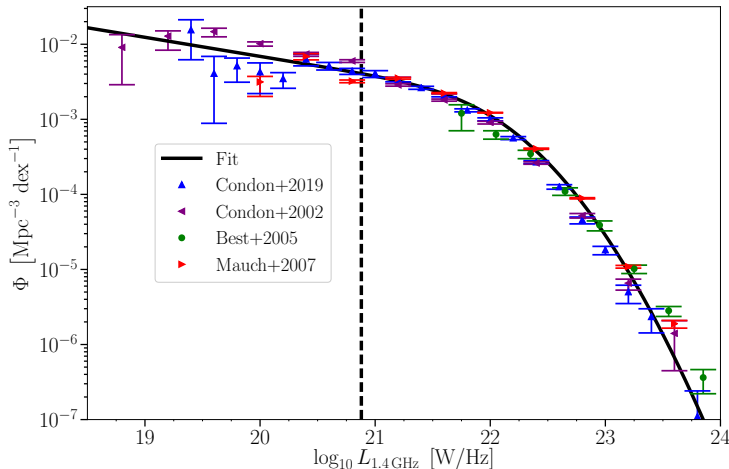


Figure 3.2: Local radio LF of SF galaxies from several surveys with different observed areas and sensitivities. Our modified-Schechter function fit to the combined data is shown with the solid line. The dashed line indicates the depth of the COSMOS-XS survey at $0.1 < z < 0.4$.

previous work (e.g., Novak et al. 2017), the values of α and σ will be frozen at the values found for the local LF. In reality, α and σ may both change with redshift.

To find the parameters of the local LF, we used the Markov chain Monte Carlo (MCMC) algorithm, available in the Python package EMCEE (Foreman-Mackey et al. 2013) to fit a modified-Schechter function to data of the local SFGs from Condon et al. (2002); Best et al. (2005); Mauch & Sadler (2007); Condon et al. (2019). The fit is shown in Fig. 3.2. The obtained best fit parameters are: $L_* = 2.93^{+0.21}_{-0.20} \times 10^{21} \text{ W Hz}^{-1}$, $\Phi_* = 2.93^{+0.10}_{-0.11} \times 10^{-3} \text{ Mpc}^{-3} \text{ dex}^{-1}$, $\alpha = 1.25^{+0.01}_{-0.02}$ and $\sigma = 0.57^{+0.01}_{-0.01}$. These values lie close to the values assumed in the studies from Gruppioni et al. (2013) and Novak et al. (2017).

3.3.3 COSMOS-XS: Pure luminosity evolution

When we fit the LF to the COSMOS-XS data, we only assume the position of the turnover (L_* , characteristic luminosity) to change with redshift. As we are not able to constrain both L_* and Φ_* for the higher redshift bins ($z > 0.4$), we choose to keep Φ_* at the local LF value. In reality, Φ_* may also change with redshift. We assume the shape of the LF to remain unchanged. This pure luminosity evolution can be expressed as

$$\Phi(L, z, \alpha_L) = \Phi_0 \left(\frac{L}{(1+z)^{\alpha_L}} \right), \quad (3.8)$$

where α_L corresponds to the pure evolution parameter and Φ_0 is given in Eq. 3.7.

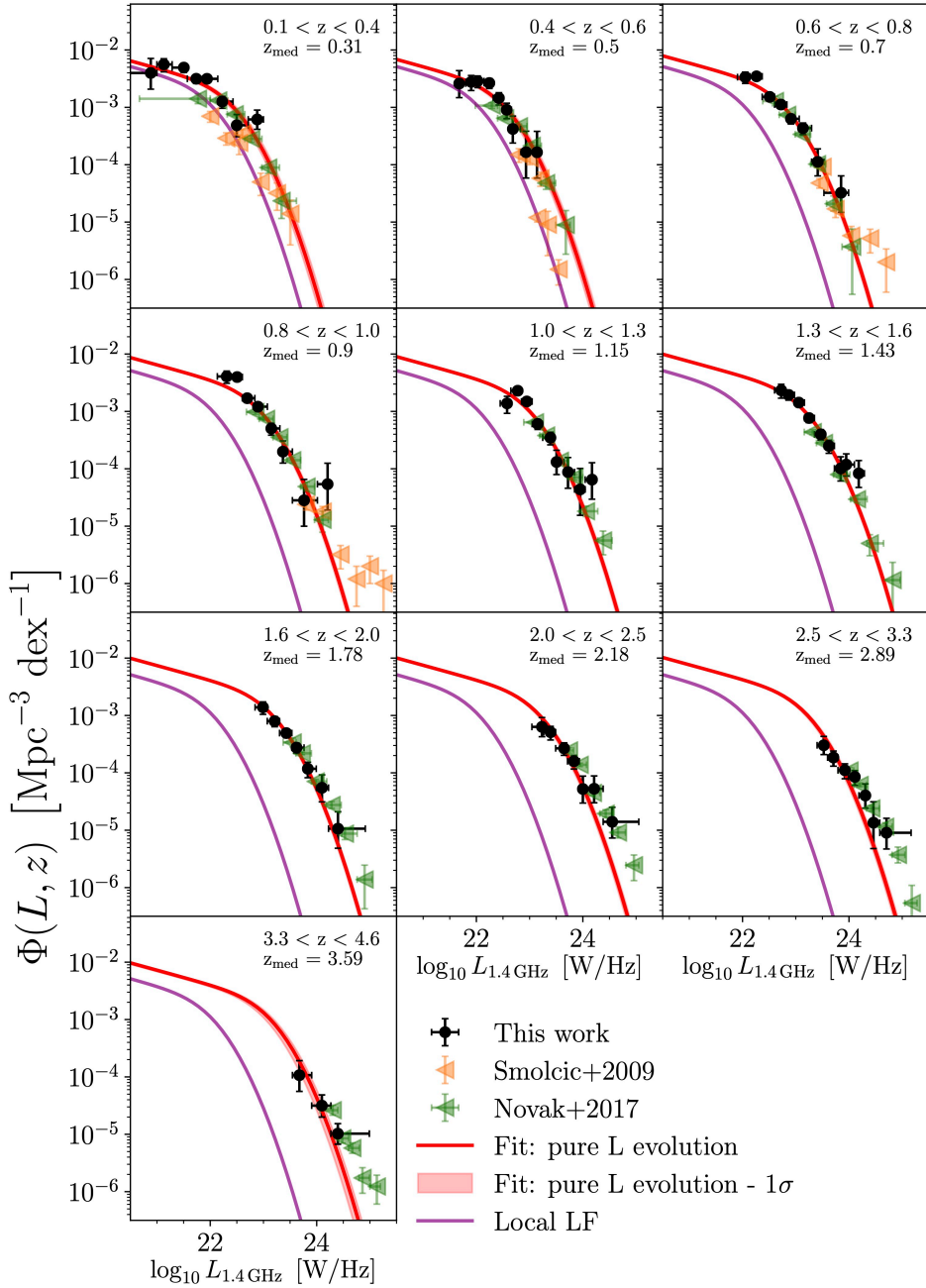


Figure 3.3: Radio LFs of SFGs in COSMOS-XS in different redshift bins. The best-fit pure luminosity function in each redshift bin is shown by the red lines, and the shaded area shows the 1σ confidence interval. The local radio LF is shown for reference as a solid purple line. We compare our data with the radio LFs from Smolčić et al. (2009b) and Novak et al. (2017). The redshift range and median redshift are given in each panel.

Table 3.1. Parameter values describing the pure luminosity evolution fit and the density+luminosity evolution fits.

Redshift range	COSMOS-XS ^a		COSMOS-XS + VLA-COSMOS 3 GHz ^b	
	α_L		α_L	[α_L α_D]
0.1 < z < 0.4	3.26 ^{+0.51} _{-0.52}		1.53 ^{+0.17} _{-0.18}	[4.36 ^{+0.36} _{-0.35} -2.41 ^{+0.28} _{-0.28}]
0.4 < z < 0.6	2.73 ^{+0.31} _{-0.32}		2.39 ^{+0.09} _{-0.09}	[3.27 ^{+0.27} _{-0.28} -1.0 ^{+0.29} _{-0.29}]
0.6 < z < 0.8	3.17 ^{+0.14} _{-0.15}		2.78 ^{+0.05} _{-0.05}	[2.46 ^{+0.21} _{-0.21} 0.45 ^{+0.29} _{-0.29}]
0.8 < z < 1.0	3.2 ^{+0.13} _{-0.13}		3.13 ^{+0.04} _{-0.04}	[3.17 ^{+0.2} _{-0.2} -0.05 ^{+0.26} _{-0.25}]
1.0 < z < 1.3	2.86 ^{+0.1} _{-0.11}		2.75 ^{+0.03} _{-0.03}	[3.19 ^{+0.16} _{-0.17} -0.64 ^{+0.24} _{-0.22}]
1.3 < z < 1.6	2.91 ^{+0.08} _{-0.08}		2.68 ^{+0.03} _{-0.03}	[2.59 ^{+0.15} _{-0.14} 0.16 ^{+0.24} _{-0.24}]
1.6 < z < 2.0	2.52 ^{+0.07} _{-0.07}		2.63 ^{+0.02} _{-0.02}	[2.87 ^{+0.11} _{-0.11} -0.4 ^{+0.18} _{-0.18}]
2.0 < z < 2.5	2.27 ^{+0.07} _{-0.08}		2.48 ^{+0.02} _{-0.02}	[2.99 ^{+0.13} _{-0.12} -0.87 ^{+0.2} _{-0.2}]
2.5 < z < 3.3	1.99 ^{+0.06} _{-0.07}		2.25 ^{+0.02} _{-0.02}	[2.96 ^{+0.12} _{-0.12} -1.24 ^{+0.2} _{-0.2}]
3.3 < z < 4.6	1.63 ^{+0.1} _{-0.15}		1.83 ^{+0.03} _{-0.04}	[2.76 ^{+0.21} _{-0.2} -1.77 ^{+0.35} _{-0.34}]

Notes.

^a Parameter value describing the pure luminosity evolution fit to the COSMOS-XS data.

^b Parameter values describing the pure luminosity evolution fit (third column) and the density+luminosity evolution fits (right two columns) to the combined COSMOS-XS + VLA-COSMOS 3 GHz data-sets. The parameters α_L and α_D shown in the table within brackets are fitted simultaneously.

The range of luminosities and redshifts for which the LFs were calculated were determined from the coverage of the luminosity-redshift plane shown in Fig. 3.1. All sources are distributed into equally spaced luminosity bins spanning the observed luminosity range. Bins which contain fewer than two sources are merged with the lower L consecutive bin. The gray solid lines in Fig. 3.1 show the redshift and luminosity bins used. The LFs calculated with the V_{\max} method are shown in Fig. 3.3 and tabulated in Table 3.B.1 in Appendix 3.B. As noted in Section 3.3.1, the LFs are calculated using the 1.4 GHz rest-frame luminosity for easier comparison with previous studies. The black circles show the median luminosity of all sources in the corresponding luminosity bin. The horizontal error bars show the width of the bin. The vertical errors correspond to the errors calculated using Eq. 3.6. The data points were fitted with the analytical form from Eq. 3.8 using the MCMC algorithm assuming flat priors.² The redshift used in this expression is the median redshift of all the sources in the redshift bin. This value is given in the panels of Fig. 3.3. The best-fit values for α_L are tabulated in Table 3.1 and the best-fit pure luminosity evolved function is shown with the red line in Fig. 3.3. Fig. 3.4 shows α_L as a function of redshift. We find that α_L remains roughly constant at $z < 1.8$; thereafter α_L decreases with z .

² $\alpha_L \in [1.0, 7.0]$ and $\alpha_D \in [-7.0, 7.0]$

3.3.4 COSMOS-XS + VLA-COSMOS 3 GHz samples: Luminosity and density evolution

Up until now, we have been considering pure luminosity evolution as we lacked sensitivity to constrain both the luminosity and density evolution. To constrain a LF with both luminosity and density evolution, we need both the contribution of the brightest and faintest sources to the LF; otherwise the two evolution parameters become degenerate. As shown in Fig. 3.3, the LF data from Novak et al. (2017) is more sensitive to the most luminous SFGs, whereas our data extend to the low-luminosity sources. Novak et al. (2017) found that significant density evolution could not be properly constrained by their observations alone as the faint end was not well-sampled. However, combining the two data-sets offers the possibility of jointly constraining the luminosity and density evolution. To combine the VLA-COSMOS 3 GHz Large Project data with the COSMOS-XS survey, we select the SFGs from the VLA-COSMOS 3 GHz Large Project data, as discussed in Section 3.2.4 using the criterion described in Section 3.2.3. We then treat the two data-sets as two separate regions. This means we mask out the observed area of COSMOS-XS in the VLA-COSMOS 3 GHz Large Project. We then combine the two data-sets by means of the Avni & Bahcall (1980) method for coherent analysis of independent data-sets. The depth of the whole sample is not constant throughout the region, as COSMOS-XS is ~ 5 times deeper than the VLA-COSMOS 3 GHz Large Project. A source in the VLA-COSMOS 3 GHz Large Project area will therefore be detectable over the whole joint area, while fainter sources detected in COSMOS-XS are only detectable in the COSMOS-XS area. This means that the maximum volume of space ($V_{\max,i}$) available for an object in the joint sample is defined by

$$V_{z_{\max},i} = \begin{cases} \frac{\Omega_V}{4\pi} V_{z_{\max}}^V + \frac{\Omega_{XS}}{4\pi} V_{z_{\max}}^{XS} & (\text{if } z_{\max,i} \leq z_{\max}^V) \\ \frac{\Omega_{XS}}{4\pi} V_{z_{\max}}^{XS} & (\text{if } z_{\max}^V < z_{\max,i} \leq z_{\max}^{XS}), \end{cases} \quad (3.9)$$

where $V_{z_{\max}}^{\text{fld}}$ (with fld = V, XS corresponding to VLA-COSMOS 3 GHz Large Project and COSMOS-XS, respectively) is the co-moving volume available to each source in that field, in a given redshift bin, while Ω_{fld} is the area observed (1.673 deg^2 and 0.097 deg^2 for VLA-COSMOS 3 GHz Large Project and COSMOS-XS, respectively).

We do not expect cosmic variance to have a big impact on the VLA-COSMOS 3 GHz Large Project as it consist of a considerably larger field of view than the COSMOS-XS survey. Driver et al. (2018) estimated the cosmic variance to be ~ 0.35 dex at $z \sim 0.3$ and ~ 0.18 dex above $z > 0.8$ for the G10-COSMOS field, a 1 deg^2 sub-region of the HST COSMOS survey. The cosmic variance is thus negligible compared to the error given by Eq. 3.6. Therefore, for each luminosity and redshift bin, the LF is given by Eq. 3.4 with $o_i = 1$ for the VLA-COSMOS 3 GHz Large Project sources. The completeness correction w_i for these sources consists of a completeness correction for the radio catalog and a counterpart completeness correction. These corrections are derived and described in, respectively, Smolčić et al. (2017a) and Novak et al. (2017).

For comparison, we first fit the LF described by the analytical expression from Eq. 3.8 (i.e., pure luminosity evolution) to the joint COSMOS-XS + VLA-COSMOS 3 GHz data points using the method described in Section 3.3.2. The best-fit values for α_L are tabulated in Table 3.1 and the best-fit pure luminosity evolved function is shown with the red line in Fig. 3.5. Fig. 3.4 shows α_L as a function of redshift. At $z > 1.8$, we find that α_L decreases similarly to what was found when pure luminosity evolution was fitted to the COSMOS-XS data-set alone.

With the larger dynamic range probed by the combination of the COSMOS-XS + VLA-COSMOS 3 GHz data-sets, we can now fit not only the position of the turnover with redshift, but also the normalization. This luminosity and density evolution can be described as

$$\Phi(L, z, \alpha_L, \alpha_D) = (1+z)^{\alpha_D} \Phi_0 \left(\frac{L}{(1+z)^{\alpha_L}} \right). \quad (3.10)$$

Because the joint COSMOS-XS + VLA-COSMOS 3 GHz data-sets constrain both the high and low luminosity ends, the evolution parameters (α_D and α_L) are less degenerate. The fit with luminosity and density evolution is shown in Fig. 3.5. Fig. 3.C.1, shown in Appendix 3.C, shows the two dimensional posterior probability distributions of α_L and α_D at each redshift. Fig. 3.4 shows the fitted parameters α_L and α_D as a function of redshift. We find that, when allowing for both luminosity and density evolution, α_L decreases and α_D increases to $z \sim 1$, above which α_L is constant with z while α_D decreases.

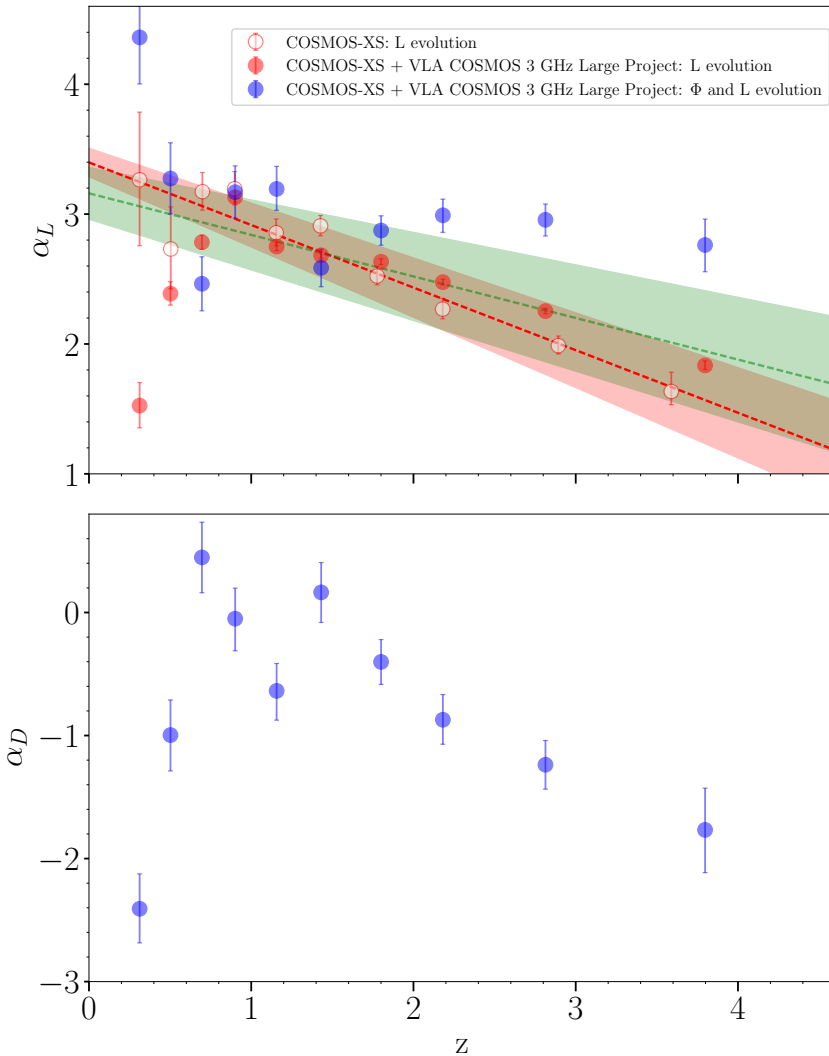


Figure 3.4: The best-fit parameters for the luminosity functions as a function of redshift. The upper panel shows the evolution of the luminosity parameter α_L . The lower panel shows the evolution of the density parameter α_D . Open circles correspond to pure luminosity evolution for the COSMOS-XS survey. The red dashed line shows the fitted evolution to these points of the form $\alpha_L + z\beta$. The green dashed line shows the simple pure luminosity evolution model described by Novak et al. (2017). The luminosity parameter shows a similar evolution as the evolution that Novak et al. (2017) described.

The filled symbols correspond to the joint COSMOS-XS + VLA-COSMOS 3 GHz data. The red and blue filled symbols correspond to the best-fit parameters found for, respectively, the pure luminosity evolution and the luminosity and density evolution fitted to the joint sample. The density parameter shows a strong evolution while we observe little evolution in the luminosity parameter.

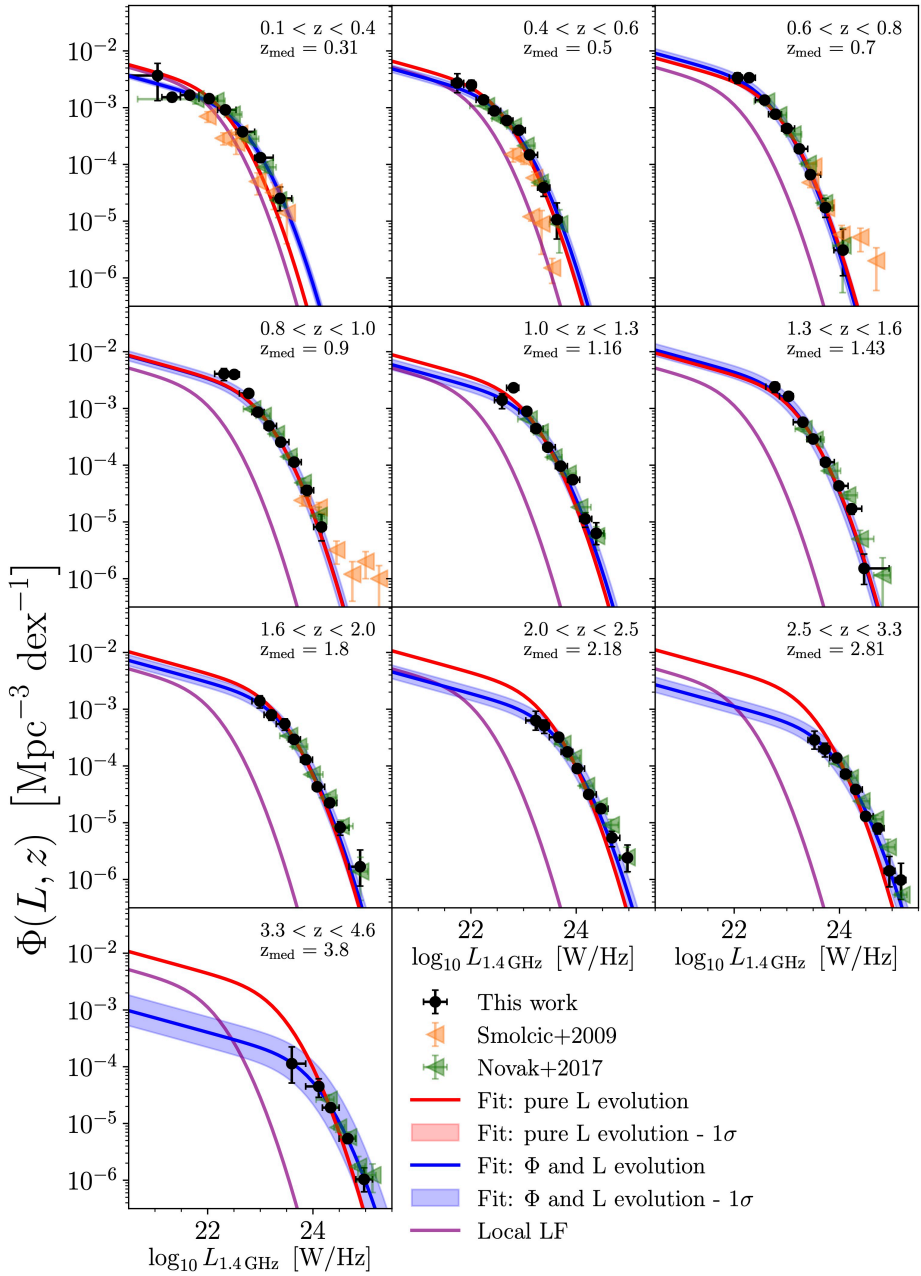


Figure 3.5: Radio LFs of SFGs in different redshift bins from the combined sample of the COSMOS-XS + VLA-COSMOS 3 GHz data-sets compared with the radio LFs from Smolčić et al. (2009b) and Novak et al. (2017). Our best-fit pure luminosity function and best-fit density + luminosity function in each redshift bin are shown with solid red and blue lines, respectively, where the shaded areas show the 1σ confidence interval for the best-fit functions. The local radio luminosity function is shown as the purple line for reference. The redshift range and median redshift are given in each panel.

3.4 A comparison with luminosity functions from the literature

In the following section we compare our results to literature LFs derived from radio, FIR and UV observations.

3.4.1 Radio

Fig. 3.3 and Fig. 3.5 show the determination of the radio LF of Smolčić et al. (2009b) and Novak et al. (2017). Smolčić et al. (2009b) derived the radio LF up to $z < 1.3$ using 340 galaxies from the VLA-COSMOS 1.4 GHz survey conducted over the 2 deg^2 COSMOS field (Schinnerer et al. 2007). Our data generally lies slightly above the data from Smolčić et al. (2009b), which could be due to the different selection criteria. Specifically, Smolčić et al. (2009b) only used rest-frame optical colors to select SFGs. However, at $z > 0.6$, the high luminosity bins ($\log_{10} L_{1.4 \text{ GHz}} \gtrsim 24 \text{ W Hz}^{-1}$) from Smolčić et al. (2009b) lie above our data. This could be due to contamination of their sample from AGN (Smolčić et al. 2009b), as they used a different AGN selection method.

The VLA-COSMOS 3 GHz Large Project (Smolčić et al. 2017a) was also conducted over the COSMOS field and yielded about four times more radio sources compared to the 1.4 GHz data of Schinnerer et al. (2007). This resulted in LFs up to $z \lesssim 5.7$ using 5915 SFGs selected as described in Section 3.2.4. Overall, our radio LFs generally agree very well with those derived by Novak et al. (2017) based on this data-set. Because of the large field of view of the VLA-COSMOS 3 GHz Large Project, the LF data from Novak et al. (2017) is more sensitive to the most luminous SFGs, especially for $z < 1.6$. On the other hand, as Fig. 3.3 shows, the COSMOS-XS data extends towards lower luminosity and adds in almost every redshift bin two low-luminosity data points. Given the good agreement between the COSMOS-XS and VLA-COSMOS 3 GHz data-sets and the larger constraining power of the combination (Section 3.3.4), we use the radio LFs derived from the combined COSMOS-XS + VLA-COSMOS 3 GHz data-sets for the comparison with the LFs derived from the IR and UV in the following sections.

3.4.2 Far-infrared

If the FIR-radio correlation is linear (see Section 3.2.3), both FIR and radio LFs should follow each-other well. In Fig. 3.6, we compare our results with the FIR LFs from Gruppioni et al. (2013), Koprowski et al. (2017), Gruppioni et al. (2020) and Lim et al. (2020). To adapt their results to our redshift bins, we simply plot the value of Φ for which the mean z is within our redshift bin.

Gruppioni et al. (2013) used the data-sets from the *Herschel* PEP Survey, in combination with the HerMES imaging data, resulting in a field of view of $\sim 380 \text{ deg}^2$, to derive the evolution of the FIR LFs up to $z \sim 4$. Koprowski et al. (2017) found their total FIR LF measurements based on SCUBA-2 $850 \mu\text{m}$ observations with a field of view of 1.58 deg^2 . Gruppioni et al. (2020) determined the total FIR

LF using the non-target ALPINE sources observed with ALMA. These 56 sources were blindly detected at $860\ \mu\text{m}$ within the fields of targeted galaxies of the ALPINE survey giving an effective area of $24.92\ \text{arcmin}^2$. The total FIR was derived using SED fitting using semi-empirical templates. Finally, Lim et al. (2020) used a SCUBA-2 $450\ \mu\text{m}$ survey in the COSMOS field, called STUDIES (Wang et al. 2017), covering a area of $300\ \text{arcmin}^2$ to construct the FIR LF.

To convert the total FIR LF given by Gruppioni et al. (2013), Gruppioni et al. (2020) and Lim et al. (2020) to a radio LF, we use the FIR-radio correlation as described in Eq. 3.1, with q_{TIR} as the FIR-radio correlation from Delhaize et al. (2017) and rewritten as follows:

$$\begin{aligned}\log_{10} L_{1.4\ \text{GHz}} &= \log_{10} \left(\frac{L_{\text{FIR}}}{3.75 \times 10^{12}\ \text{W}} \right) - q_{\text{TIR}}(z); \\ \log_{10} L_{1.4\ \text{GHz}} &= \log_{10} \left(\frac{L_{\text{FIR}}}{3.75 \times 10^{12}\ \text{W}} \right) \\ &\quad - (2.88 \times (1+z)^{-0.19}).\end{aligned}\tag{3.11}$$

To find the total FIR LF for Koprowski et al. (2017), we used the $L_{250\ \mu\text{m}}/L_{\text{FIR}}$ ratio given by the Michałowski et al. (2010) template to convert the rest-frame $250\ \mu\text{m}$ LF from the SCUBA-2 data to total FIR LF, which is then converted to a radio LF using Eq. 3.11.

Similar to what Novak et al. (2017) found, our data agree well with these FIR surveys. However, at $z > 2$, our LFs are systematically lower than Gruppioni et al. (2013). We find that the more recent studies from Gruppioni et al. (2020) and Lim et al. (2020) are also higher than our data, although these data-sets are more uncertain due to the low number of sources per bin. The offset between our data and the studies from Gruppioni et al. (2013), Gruppioni et al. (2020) and Lim et al. (2020) at $z > 2$ may be partly attributed to the presence of AGN in the FIR selected sample. While we start from a radio sample that excludes AGNs, as described in Section 3.2, Gruppioni et al. (2013) and Gruppioni et al. (2020) derive the total FIR LF and thus include sources powered by AGN. In addition, the fraction of AGN is found to increase with redshift: Gruppioni et al. (2013) find that AGN largely dominate the FIR luminosity density at $z \gtrsim 2.5$. However, the ALPINE survey (Gruppioni et al. 2020) finds that the large majority of the SEDs of their sources are best fitted by star-forming or composite templates. In contrast, the Lim et al. (2020) study excludes sources identified as AGN based on their X-ray, mid-IR or radio-emission and finds a low AGN fraction compared to literature studies due to their deep observations. These probe a faint sub-mm galaxy (SMG) population which is less likely to host an AGN. The difference can thus not solely be explained by the presence of AGN. Some of the difference could therefore be due to the evolving $q_{\text{TIR}}(z)$ used in the conversion from FIR to radio. This will be discussed in more depth in Section 3.6.3. In addition, there are a lot of uncertainties in measuring the FIR luminosity from a few data points which is reinforced by discussion of Gruppioni & Pozzi (2019) on the study of Koprowski et al. (2017). We find that the Koprowski et al. (2017) LFs are systematically lower

than the other FIR studies over the whole luminosity range and match our data at $z > 2$. Gruppioni & Pozzi (2019) explained the discrepancy to other FIR studies by attributing the difference to a choice of sub-mm SED and sample incompleteness.

In Fig. 3.6 we also compare our results with the observationally motivated sub-mm LF models from Casey et al. (2018). They developed an evolutionary model based on existing measurements of sub-mm number counts, redshift distributions, and multi-band flux information to study the shape and behavior of the FIR LF out to high redshift ($z > 4$). They considered two extreme cases: a dust-poor model, where the abundance of very dust-rich dusty star-forming galaxies (DSFGs) relative to UV-bright galaxies is low ($< 10\%$ at $z = 4$), and a dust-rich model, where DSFGs dominate and contribute $> 90\%$ to the star formation at $z = 4$. Both models include a ‘turning point’ redshift at which the knee of the LF (L_*) and the characteristic number density of the LF (Φ_*) are transitioning in their evolution. For example, Φ_* might evolve like $(1+z)^{-2.8}$ up to $z \sim 1.5$, and then gradually transition to $(1+z)$ by a redshift of $z \sim 3.5$. The turning point for the dust-poor and dust-rich model lies at, respectively, $z = 2.1$ and $z = 1.8$. Before this redshift the models use the same evolution parameters. Thereafter, they will evolve at different rates.

The dust-poor model is similar to the often-adopted evolutionary scenario in the rest-frame UV literature. It represents the model that the dust-formation timescale is longer than the timescale for the formation of UV-bright galaxies. This means that DSFGs are rare at $z > 4$ in this model and only dominate the star formation at $z \sim 2$. The dust-rich model is quite extreme and suggests that most star formation at high redshift was isolated to rare starbursts with very high SFR and that DSFGs would dominate the star formation at $z > 1.5$. Casey et al. (2018) showed that both models were consistent with the sub-mm data that existed at that time.

The predictions of the FIR LFs by Casey et al. (2018) shown in Fig. 3.6 are converted as discussed above. The converted LFs are roughly consistent with our measurements at $z < 2.5$ although the LFs differ at the low luminosity end at $1.3 < z < 2.5$ which is more uncertain due to the large completeness corrections. From $z > 2.5$ the models start to deviate from each other. At $z > 2.5$ the dust-rich model over-predicts our data, while the dust-poor model matches quite well, as also seen with the VLA-COSMOS 3 GHz Large Project data alone (Novak et al. 2017).

In summary, we find that our radio LFs are roughly consistent, within the error bars, with the FIR LFs. At $z > 2$ our LFs are systematically lower than Gruppioni et al. (2013), which we attribute at least partly due to AGN contamination. In addition, we find that the radio data is most consistent with the dust-poor model from Casey et al. (2018) at $z \sim 4$.

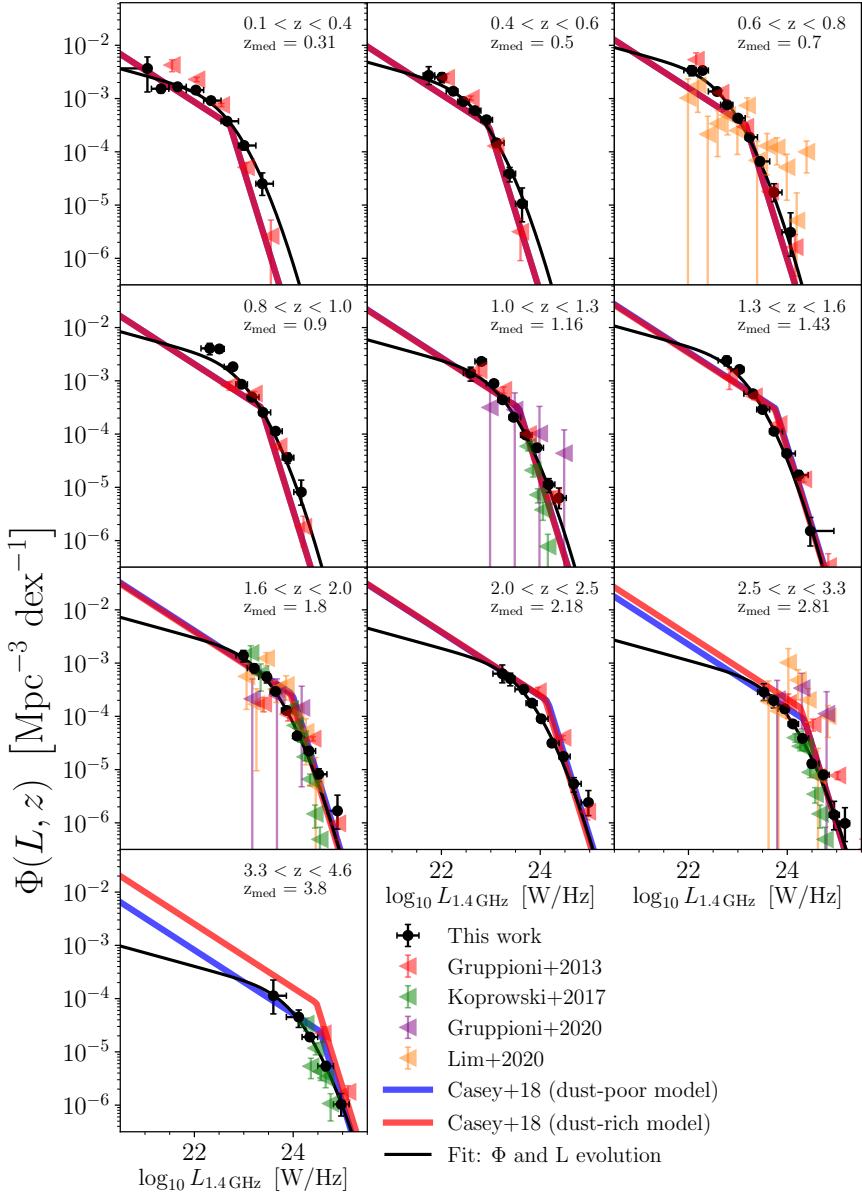


Figure 3.6: Radio LFs of SFGs in different redshift bins for the combined COSMOS-XS + VLA-COSMOS 3 GHz data-sets compared to various FIR LFs from the literature. Our best-fit luminosity + density function in each redshift bin is shown with the black lines. We show FIR LFs from Gruppioni et al. (2013), Koprowski et al. (2017), Gruppioni et al. (2020) and Lim et al. (2020). The LFs of the theoretical study by Casey et al. (2018) for the dust-poor model and the dust-rich model are also shown. The redshift range and median redshift are given in each panel. Our best-fit luminosity + density function is roughly consistent, within the error bars, with the FIR LFs. At $z > 2$ our LFs are systematically lower than the FIR studies expect for the result from Koprowski et al. (2017). Our best-fit function is most consistent with the dust-poor model from Casey et al. (2018) at $z \sim 4$.

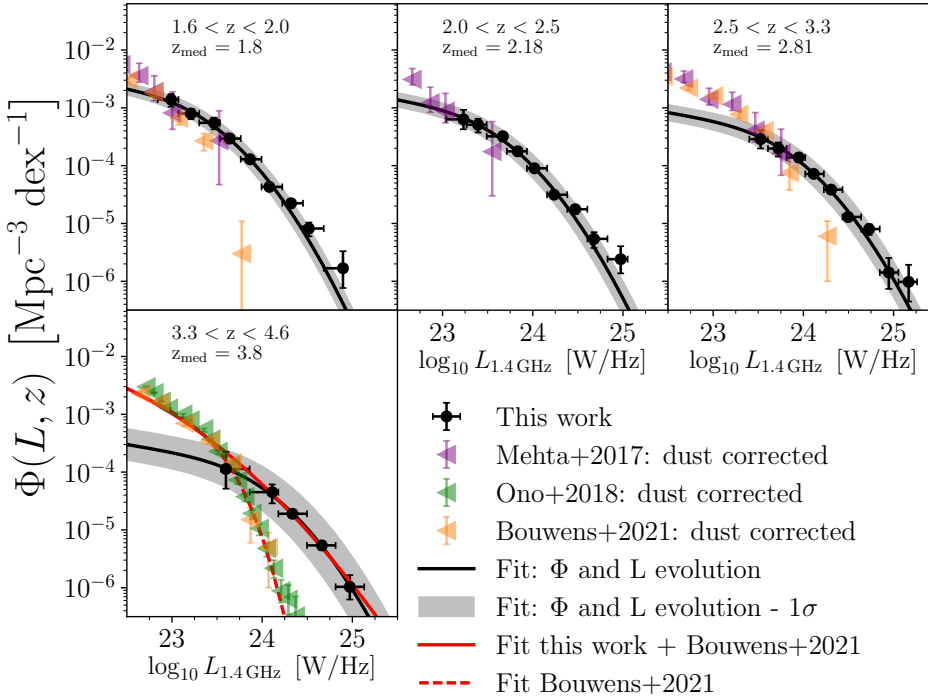


Figure 3.7: Radio LFs of SFGs in different redshift bins compared to UV LFs from the literature. Our best-fit luminosity + density function in each redshift bin is shown with the solid black line. The shaded areas shows the 1σ confidence interval for the best-fit functions. We compare our data with the UV LFs from Mehta et al. (2017), Ono et al. (2018) and Bouwens et al. (2021). The redshift range and median redshift are given in each panel. The best-fit pure local LF for the data from Bouwens et al. (2021) at $z \sim 4.6$ is shown with the dashed red line, while the solid red line shows the joint fit to the UV+radio data discussed in Section 3.4.3. The comparison of these two fits in the last panel suggests that at the highest redshifts probed here ($3.3 < z < 4.6$), the UV data underestimate the integrated LF by at least $22\% \pm 14\%$ where the LF is integrated from $L_{z=3}^*$, to ∞ .

3.4.3 UV

It is also interesting to compare our radio LFs with previous UV LFs studies. The UV probes fainter sources at higher redshift and therefore offers a comparison sample complementary to that of FIR-based studies. In addition, the SFR calibrations from Kennicutt (1998) are self-consistent which means that all SFR tracers should result in roughly the same SFR estimate. The UV and radio both trace SF where radio is mostly sensitive to SFGs with a high SFR and UV is probing emission from SF not obscured by dust. The UV and radio LFs should thus follow each-other well if the UV can be fully corrected for dust extinction. In Fig. 3.7 we compare our results with the UV LFs from Mehta et al. (2017), Ono et al. (2018) and Bouwens et al. (2021).

Mehta et al. (2017) used deep NUV imaging data as part of the *Hubble* Ultra-Violet Ultra Deep Field program to find the rest-frame 1500Å UV LF at $z \sim 1.7, 2.2$ and 3.0 . Ono et al. (2018) conducted the GOLDRUSH project with the optical images taken by the HSC-SSP which cover a large area of $\sim 100 \text{ deg}^2$. The sample is constructed using the so-called drop-out technique. In this case the sample consisted of a total of $\sim 580,000$ Lyman break galaxies at $z \sim 4 - 7$. The UV LF is then derived by combining the LFs from the HSC Subaru program with the LFs from the ultra-deep *Hubble* Space Telescope legacy surveys. Bouwens et al. (2021) derived UV LFs at $z \sim 2 - 10$ based on the *Hubble* data from various legacy fields covering an area of $\sim 0.3 \text{ deg}^2$ which contains $> 24,000$ sources.

The conversion needed to compare LFs at radio and UV wavelengths is derived by Novak et al. (2017) following Kennicutt (1998):

$$L_{1.4 \text{ GHz}} = 16.556 - 0.4(M_{1600, \text{AB}} - A_{\text{UV}}) - q_{\text{TIR}}, \quad (3.12)$$

where $M_{1600, \text{AB}}$ is rest-frame UV absolute magnitude, A_{UV} is the extinction given by $4.43 - 1.99\beta$ with β the UV spectral slope and q_{TIR} is the FIR-radio correlation defined by Delhaize et al. (2017). To correct the UV data for dust extinction, we used the UV spectral slope β as tabulated as a function of magnitude by Bouwens et al. (2009) ($z \sim 2.5 - 4$) and Bouwens et al. (2014b) ($z \sim 4 - 8.5$). Following Viironen et al. (2018), we added a small correction of $\Delta M_{\text{UV}} = +0.035$ to the luminosity values of Mehta et al. (2017), in order to scale them from 1500 Å to 1600 Å. This was done by roughly defining the average β -slopes for the sources ($\beta \sim -1.7$) and deriving the correction from there.

To adapt the UV LF results to our redshift bins, we simply plot the value of Φ for which the mean z is within our redshift bin. We find that our LFs predict an excess of bright sources compared to Bouwens et al. (2021), Mehta et al. (2017) and Ono et al. (2018) at $z \sim 2.9$ and $z \sim 3.6$. The excess is especially striking at high luminosity at $z \sim 3.6$, where the UV dust correction is most severe. Although the UV LFs have been corrected for dust extinction, they still seem to miss a part of the galaxies with dust-obscured SF, as previously noted by Novak et al. (2017) and Viironen et al. (2018). Based on their radio LFs, Novak et al. (2017) estimated that Bouwens et al. (2014b) underestimated the obscured SFR observed in UV by 15%–20%.

To determine the UV underestimation of the obscured SFR suggested by our data, we fitted the local LF, as described in Eq. 3.7, to the dust corrected data from Bouwens et al. (2021) with all parameters unconstrained. The obtained best fit parameters are tabulated in Table 3.2. The fit is shown in Fig. 3.7. We then fitted the local LF in the same way to a combination of the radio data and the dust corrected data from Bouwens et al. (2021). It is known that the UV dust corrections are more severe at high luminosities and that UV observations miss the most massive and dusty galaxies (e.g., Casey et al. 2014a; Dudzevičiūtė et al. 2020). Radio emission traces these galaxies well as it does not suffer from dust extinction. In addition, the radio data span a higher range in luminosity than the UV observations. Therefore, we disregarded the three most luminous LF points from Bouwens et al. (2021) and took the radio data points instead. The obtained best fit parameters are tabulated in Table 3.2 and the fit is shown in Fig. 3.7. We then integrated the two fits from $L_{z=3}^*$, as defined by Bouwens

Table 3.2. Best fit parameters of the local luminosity function, as described in Eq. 3.7, fitted to the luminosity function from Bouwens et al. (2020) and to our radio luminosity function + the luminosity function from Bouwens et al. (2020).

	Bouwens+2021	This work + Bouwens+2021
$L_\star (\times 10^{23}$ [W Hz $^{-1}$])	3.79 $^{+2.44}_{-1.50}$	0.22 $^{+0.13}_{-0.09}$
$\Phi_\star (\times 10^{-4}$ [Mpc $^{-3}$ dex $^{-1}$])	4.76 $^{+2.52}_{-1.61}$	39.0 $^{+17.63}_{-12.27}$
α	1.71 $^{+0.03}_{-0.03}$	1.67 $^{+0.04}_{-0.05}$
σ	0.21 $^{+0.07}_{-0.06}$	0.94 $^{+0.06}_{-0.06}$

Note. Both fits are shown in Fig 3.7.

et al. (2021), which corresponds to $\log_{10} L_{1.4\text{GHz}} = 21.14 \text{ W Hz}^{-1}$ to ∞ , to find the difference between the two. We find the UV data presented in Bouwens et al. (2021) underestimate the integrated LF by $22\% \pm 14\%$ at these redshifts ($3.3 < z < 4.6$). We can interpret this estimate as a lower limit, as the mean redshift of the UV sample presented in the last panel of Fig. 3.7 is 3.8, slightly higher than the median redshift of the radio sample and we expect the UV LF to increase between $z = 3.7$ and $z = 3.8$.

We additionally note that the radio LFs displayed in Fig. 3.7 do not include any of the ‘optically dark’ sources as described in Paper II. These 70 sources were not matched to a counterpart in any of the catalogs used in the counterpart matching as described in Section 3.2.2. Some of these sources could be spurious detections but most of these ‘optically dark’ sources are expected to be real; we expect only ~ 20 spurious sources. As discussed in Section 3.3.1, we do correct for the counterpart completeness with f_{ctrpt} . This small correction as a function of flux density is done over the whole redshift range. However, the method used in Paper II, which finds 29 robust ‘optically dark’ sources, shows that these sources are likely to have a redshift of $z \gtrsim 4$, similar to what was found in ALMA follow up of sources without an optical counterpart (e.g., Dudzevičiūtė et al. 2020; Smail et al. 2021). The LF at $z \sim 4$ including these ‘optically dark’ sources will be higher than shown in Fig. 3.7.

Different works have already identified ‘optically dark’ sources, extreme SFGs heavily obscured by dust which lack an optical or NIR counterpart, out to high redshift ($z \simeq 5$) (e.g., Dannerbauer et al. 2008; Walter et al. 2012; Riechers et al. 2020). Wang et al. (2019) reported the results from the ALMA follow-up of a population of ‘optically dark’ galaxies, and found a fraction of them to be massive dusty galaxies at high-redshift. They concluded that this population constitutes a significant fraction of the SFRD at $z > 3$. In addition, Talia et al. (2021) estimated that dust-obscured star-forming galaxies, found based on their emission at radio wavelengths and the lack of optical counterparts, have a contribution to the SFRD which can be as high as

40% of the previously known UV-SFRD. More recently, Enia et al. (2022) estimated the contribution of ‘optically dark’ sources (H -dark galaxies; not detected in the H -band) to the SFRD using 8 ‘optically dark’ galaxies found at $z \sim 3$, and finding they contribute 7% – 58% to the UV-based SFRD. The discrepancy between our radio LF and the UV LFs will thus also be greater with the inclusion of the ‘optically dark’ sources. The derivation of the radio LF including these sources and implications that follow will be further discussed in a future paper.

In summary, we find our radio observations show an excess above the UV LFs for $z > 2.9$ even without including the ‘optically dark’ sources. Although the UV LFs have been corrected for dust extinction, we estimate that they miss at least $22\% \pm 14\%$ of the star formation traced by the integrated radio LF.

3.4.4 Radio vs. FIR vs. UV

As discussed above, the LF can be constrained by using different tracers: radio, FIR and UV. Each tracer may be affected by different biases. Radio observations can be contaminated by AGN. FIR and sub-mm observations lack, respectively, high resolution and large field of view observations. In addition, these bands have a limited sensitivity to galaxies at $z > 3$ and FIR observations can be significantly affected by AGN. UV observations need significant corrections for dust obscuration and are unable to uncover the most extreme SFGs. By comparing all three tracers, we are able to find which bias is most impactful.

As discussed in Section 3.4.2, the radio data presented here are roughly in agreement with the FIR observations. In addition, Fig. 3.7 shows that our radio observations show an excess above the UV observations at $z > 2.9$. The current radio data thus confirm a discrepancy that exists between the FIR and UV data. This was already suggested by the work of Novak et al. (2017), and the new analysis of the combined data strengthens the evidence for the discrepancy and suggest an underestimation of the UV LF. Although radio and FIR observations share the risk of AGN contamination, these AGN are observed at different wavelengths and thus have different methods of removal. Seeing that the radio and FIR observations are moderately consistent suggests that the most significant issue is with UV observations and their dust corrections

The IRX- β relation (Meurer et al. 1999) is used in UV studies to attempt to correct for dust extinction. Their relation consists of the ratio of total FIR to UV luminosity ($L_{\text{FIR}}/L_{\text{UV}} = \text{IRX}$), a proxy for extinction, and the UV spectral slope (β), which depends on the column density along the line of sight that is attenuating the UV light. The relation is therefore sensitive to a range of interstellar medium (ISM) properties including dust geometries, dust-to-gas ratios, dust grain properties, and the spatial distribution of dust.

Mancuso et al. (2016) have built an intrinsic SFR function and find that, even when corrected for dust absorption with the IRX- β relation, UV observations underestimate the intrinsic SFR for galaxies with a $\text{SFR} > 30M_{\odot}\text{yr}^{-1}$. Their result suggests a galaxy population at $z \gtrsim 4$ with large dust-obscured SFR of $\gtrsim 100M_{\odot}\text{yr}^{-1}$, the higher redshift counterparts to the dusty SF population observed by FIR observations at $z \lesssim 3$. In addition, several studies have already shown that low redshift luminous infrared

galaxies – so-called luminous and ultra-luminous galaxies ($10^{11} \leq L_{\text{IR}} < 10^{13} L_{\odot}$, LIRGs and ULIRGs) and high redshift dusty SFGs ($L_{\text{IR}} \geq 10^{12-13} L_{\odot}$, DSFGs) – are offset from the nominal UV spectral slope (Goldader et al. 2002; Howell et al. 2010; Casey et al. 2014b; Bourne et al. 2017). Furthermore, Khusanova et al. (2020) recently concluded that the brightest Ly α emitters at $z > 5$ are very diverse and found that these galaxies have large scatter in observed β values. These studies show that UV observations miss a part of the galaxies with dust-obscured SF and question the existing IRX- β relation as a method of dust correction.

In particular, we know the reliability of the IRX- β relation for high-redshift galaxies has several issues. Firstly, the shape of the FIR SED at high-redshift is poorly constrained due to a lack of sampling of the SED peak. This means that the FIR luminosity is derived from FIR SED models that are fitted at lower redshift. We also know that the dust temperature (T_{dust}) is crucial for the derivation of L_{IR} , with an incorrectly assumed T_{dust} changing the L_{IR} by as much as an order of magnitude (e.g., Hodge & da Cunha 2020). Unfortunately, T_{dust} is typically highly uncertain for lower luminosity high-redshift galaxies and might depend on various galaxy properties (e.g., Chapman et al. 2003; Magnelli et al. 2014). In addition, the distribution of dust could be more patchy in high-redshift galaxies due to their turbulent nature. The UV slope is then dominated by the least obscured part of the galaxies, leading to an under-prediction of the necessary correction (Faisst et al. 2017). Lastly, there is debate that IRX-beta might be evolving for $z > 3$ (e.g., Fudamoto et al. 2020a,b). These issues indicate that different dust corrections for bright and highly star-forming galaxies at high redshift are necessary, and we may thus need a different approach to correctly estimate dust corrections for these galaxies.

3.4.5 Evolution parameters

In this section, we compare the implied evolution of our LF parameters (Fig. 3.4) with previous multi-wavelength works from the literature. The FIR studies from Gruppioni et al. (2013), Koprowski et al. (2017) and Lim et al. (2020), and the UV study from Bouwens et al. (2021), describe the position of the turnover in the FIR and UV LF with L^* and M^* , respectively. The normalization of the LF is described by Φ^* . In these studies, L^*/M^* and Φ^* are simultaneously fitted. The FIR studies find the position of the turnover to evolve to higher luminosities. Bouwens et al. (2021) also find the characteristic luminosity M^* to increase to $z \sim 3$, but thereafter they find it to remain relatively fixed over the redshift range $z \sim 3 - 8$. This kind of evolution can also be seen in the study by Gruppioni et al. (2013), who describe the luminosity evolution of L^* up to $z \sim 1.85$ as $L^* \propto (1+z)^{3.55 \pm 0.10}$. Thereafter they find a somewhat slower evolution of $L^* \propto (1+z)^{1.62 \pm 0.51}$ up to $z \sim 4$. The normalization of the LF was found to decrease with redshift by Gruppioni et al. (2013), Koprowski et al. (2017) and Bouwens et al. (2021). Lim et al. (2020) also found this once the faint-end slope α was fixed. Gruppioni et al. (2013) describe the normalization evolution again with a break. They find Φ^* to slowly decrease as $\Phi^* \propto (1+z)^{-0.57 \pm 0.22}$ up to $z \sim 1.1$, followed by a quick decrease $\Phi^* \propto (1+z)^{-3.92 \pm 0.34}$ up to $z \sim 4$.

As shown in Fig. 3.4, we find a strong evolution of the luminosity parameter, with a clear break at $z \sim 1$, when we fit the COSMOS-XS survey and the combined data-

sets for pure luminosity evolution. The evolution at $z > 1$ can roughly be fitted with $(3.40 \pm 0.11) - (0.48 \pm 0.06) \times z$, shown with the red dashed line in Fig. 3.4. This agrees with the evolution that was found by Novak et al. (2017). The green dashed line in Fig. 3.4 shows the simple pure luminosity evolution model described by Novak et al. (2017), where they fit an evolution of $(3.16 \pm 0.2) - (0.32 \pm 0.07) \times z$. In addition, we clearly see an increase of the position of the turnover, as seen before in UV, FIR, and radio studies.

When we instead fit simultaneously for luminosity and density evolution, we find a strong evolution of the density evolution parameter, whereas the evolution in the luminosity parameter remains relatively fixed. While the evolution of these parameters could be influenced by the need to fix the bright and faint end shapes of the distribution to the local values (Section 3.3.2), we note that the same caveat applies to all studies, regardless of the LF form fitted, that fix these parameters (e.g., Novak et al. 2017; Enia et al. 2022). We will see that this density+luminosity evolution has an effect on the cosmic star formation history in Section 3.6.

3.5 Potential biases and additional caveats

Before we discuss the implications of our derived radio LFs for the cosmic star formation rate history, we first discuss the possible biases and additional caveats that need to be taken into account when deriving and interpreting the radio LF.

3.5.1 AGN contamination

A recent paper by Symeonidis & Page (2021) investigated the difference between the flatter high luminosity slope seen in the FIR LF compared to the UV LF. They constrained the AGN LF using X-ray observations and then converted the X-ray AGN LF to the FIR AGN LF. This AGN LF was then compared to the total FIR LF, which corresponds to emission from dust heated by stars and AGN. Symeonidis & Page (2021) claim that at $z < 2.5$, the high luminosity tail of the AGN FIR LF and total FIR LF converge, suggesting that the most-FIR-luminous galaxies are AGN-powered. They conclude from this that the flatter high-luminosity slope seen in the FIR LF compared to that in the UV and optical can be attributed to the increasing fraction of AGN-dominated galaxies with increasing total FIR luminosity. The AGN FIR LF and total FIR LF can be used to find the maximum value of SFR that would be believable if computed from the FIR luminosity. The range of maximum SFRs is between 1000 and 4000 $M_{\odot} \text{yr}^{-1}$ at the peak of cosmic star formation history ($1 < z < 3$). When converted to radio luminosities, this gives a range of $\log_{10} L_{1.4 \text{ GHz}} \sim 23.6 - 24.1$. This suggests that the brightest bins in the radio LF in this redshift range could be contaminated with sources powered by AGN.

To assess to what extent our SFG sample is contaminated by AGN, we divide our data into four equally populated redshift bins and stack the X-ray images. The stacking is done with the online available tool CSTACK, which utilizes a mean-stacking method³ (Miyaji et al. 2008). X-ray luminosities are calculated from the

³ CSTACK was developed by Takamitsu Miyaji and can be found at <http://cstack.ucsd.edu/>.

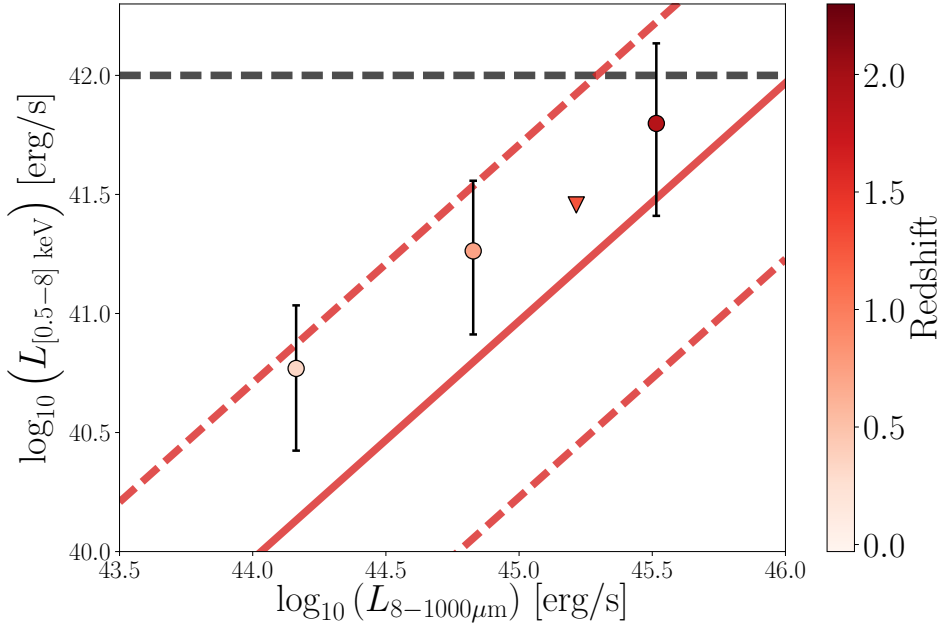


Figure 3.8: X-ray luminosity derived via X-ray stacking versus FIR-luminosity, a proxy for star formation rate, for the star-forming sample, binned in four redshift bins. Circles represent detections whereas the second highest data point is an upper limits indicated with the upside down triangle. The solid line represents the $L_X - L_{\text{IR}}$ relation from Symeonidis et al. (2014). The dashed line shows the 2σ scatter around this relation. The binned data fall within the scatter range from the trend from Symeonidis et al. (2014), indicating no appreciable contribution from AGN.

stacks assuming a power law spectrum with a slope of $\Gamma = 1.4$. Fig. 3.8 shows the X-ray luminosities as a function of FIR-luminosities, where the error-bars represent the bootstrapped spread on the median. The solid line shows the median trend found by Symeonidis et al. (2014), and the dashed line constitutes the 2σ scatter. We find little excess in the X-ray compared to the typical X-ray – star formation relations; the stacked data matches the trend from Symeonidis et al. (2014) within the scatter. Thus, we conclude that our star-forming sample is not substantially contaminated by AGN.

In addition to our examination of the contamination of unidentified AGN in our radio LFs, we want to assess the influence of our SFG selection criteria. As discussed in Section 3.2.3, we used the following selection criterion to select SF sources:

$$q_{\text{TIR}}(M_*, z) > 2.646 \times (1 + z)^{-0.023} - 0.148 \times \left(\log_{10} \frac{M_*}{M_{\odot}} - 10 \right) - (3 \times 0.22). \quad (3.13)$$

These sources do not show an excess in radio emission with respect to their FIR emission and are likely powered by SF. To assess the impact of this criterion, we also investigated using a non-evolving local value as defined by Bell (2003):

$$q_{\text{TIR}}(z) > 2.64 - (3 \times \sigma), \quad (3.14)$$

where $\sigma = 0.26$ is the 1σ scatter in FIR-radio relation as found by Bell (2003). This resulted in a sample containing 187 fewer SFGs than the original sample. The number of sources excluded by this new criterion is thus not much larger than excluded by Eq. 3.13. This can also be seen in Fig. 3.9, where the difference between the original sample and the sample derived with the new criterion is small. The biggest impact can be seen in the last two redshift bins, where the high luminosity points differ slightly in the new sample. We thus conclude that the influence of our selection criterion used to select SFGs is small.

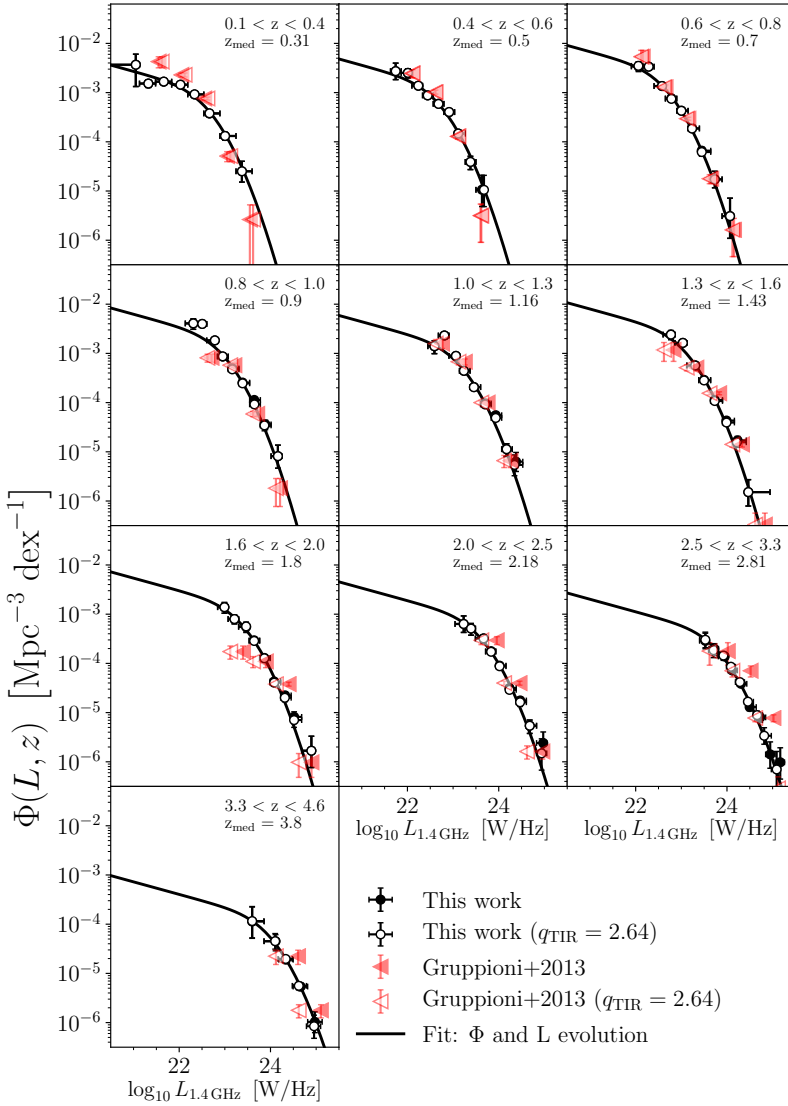


Figure 3.9: Radio LF of SFGs in different redshift bins for the combined COSMOS-XS + VLA-COSMOS 3 GHz data-sets derived using SFGs selected with an evolving FIR-radio correlation. Our best-fit density+luminosity function in each redshift bin is shown with solid lines. The redshift range and median redshift are given in each panel. The open circles show the radio LF of SFGs selected with a constant FIR-radio correlation. The small difference between the open and closed circles shows that the influence of our selection criterion used to select SFGs on the derived LF is small.

We also show the LFs from Gruppioni et al. (2013), converted as described in Section 3.4.2 to radio LFs. The open symbols are converted assuming a constant FIR-radio correlation of 2.64 (Bell 2003) and the filled symbols are converted assuming an evolving FIR-radio correlation. The difference between the open and filled symbols shows the influence of the FIR-radio correlation on the comparison between the radio LF and FIR LF. The FIR-radio correlation remains the largest uncertainty in this comparison.

3.5.2 Radio spectral indices

Where possible, we calculate the spectral index of our sources using the other radio data available over the field. In particular, we find that 8% and 6% of our sources have a spectral index calculated with the 1.4 GHz data and the 10 GHz data, respectively. However, we were unable to measure the spectral index for 86% of our sample, as these sources were only detected at 3 GHz. Because our survey is ~ 19 times deeper than the 1.4 GHz survey ($\sigma \sim 10 \mu\text{Jy beam}^{-1}$, Schinnerer et al. 2010), this induces a bias towards steeper spectra. Sources at the limit of our survey would need to have a spectral index of $\alpha = -3.9$ to be observed in the 1.4 GHz survey. The median spectral index of sources matched at 1.4 GHz is $\alpha = -0.91$. Because the 3 GHz survey is matched in depth with the 10 GHz survey, this bias does not exist for sources matched with the 10 GHz data. The median spectral index of these sources is $\alpha = -0.63$. For the bulk of our sample, we therefore assume a standard spectral index of $\alpha = -0.7$, which is consistent with that typically found for SFGs (Condon 1992; Kimball & Ivezić 2008; Murphy 2009; Smolčić et al. 2017a).

An uncertainty in the spectral index of $\Delta\alpha = 0.1$ would change $L_{1.4\text{GHz}}$ by 0.08 dex and 0.11 dex at $z = 2$ and $z = 5$, respectively (Novak et al. 2018). Assuming the canonical spectral index of $\alpha = -0.7$ thus adds a large uncertainty to the measured LF. However, the observed spread in spectral indices is symmetric ($\sigma \approx 0.35$; e.g., Kimball & Ivezić 2008; Smolčić et al. 2017a) and therefore expected to cancel out statistically.

When we derive spectral indices, we assume the radio SED to be well described by a single power-law. However, there are processes which can alter the shape of the radio spectrum. For example, if thermal free-free emission substantially contributes to the radio emission (e.g., Tabatabaei et al. 2017; Tisanić et al. 2019) the spectrum will flatten and the single power-law will not hold. Recent work by Algera et al. (2021) using COSMOS-XS and COLDz on the radio spectra of high-redshift star-forming galaxies finds thermal fractions and synchrotron spectral indices typical of local star-forming galaxies, suggesting this is not a major source of uncertainty. Future deep, multi-frequency radio observations of larger samples will be necessary to study the radio SEDs of SFGs and understand the physical processes shaping them across cosmic redshift.

3.6 Cosmic star formation rate history

In this section, we first discuss how to calculate the SFRD from the radio LFs (Section 3.6.1). We then discuss how the form of the LF fitted and FIR-radio conversion can affect the results (Sections 3.6.2 and 3.6.3, respectively). Finally, we compare our results to literature results derived from radio, FIR and UV observations (Section 3.6.4).

3.6.1 Calculating the SFRD

Having constructed the rest-frame 1.4 GHz LF, it is now possible to establish the redshift evolution of the star formation rate density. To convert luminosity density

into a star formation rate density, we use the functional form given in Delvecchio et al. (2021):

$$\text{SFR}(L_{1.4\text{ GHz}}) = f_{\text{IMF}} 10^{-24} 10^{q_{\text{TIR}}(z)} L_{1.4\text{ GHz}}, \quad (3.15)$$

where SFR is the star formation rate in units of $M_{\odot}\text{yr}^{-1}$, f_{IMF} is a factor accounting for the IMF ($f_{\text{IMF}} = 1$ for a Chabrier IMF and $f_{\text{IMF}} = 1.7$ for a Salpeter IMF) and $L_{1.4\text{ GHz}}$ is the rest-frame 1.4 GHz luminosity in units of W Hz^{-1} . Novak et al. (2017) stresses that since low-mass stars do not contribute significantly to the total light of the galaxy, only the mass-to-light ratio is changed when the Chabrier IMF is used. Following Novak et al. (2017), we therefore used the Chabrier IMF.

The SFRD can then be estimated by taking the luminosity-weighted integral of the analytical form of the fitted LF and converting the luminosity in the integral to SFR. The integral of the SFRD can thus be written as:

$$\text{SFRD} = \int_{L_{\text{min}}}^{L_{\text{min}}} \Phi(L, z, \alpha_L) \times \text{SFR}(L_{1.4\text{ GHz}}) d \log_{10} L. \quad (3.16)$$

This integral gives the SFRD of a given epoch. Unless stated otherwise, all results show the SFRD obtained by integrating the fitted LF from 0.0 to $\rightarrow \infty$. Our errors are estimated from the fitting parameters uncertainties through bootstrapping whereby the uncertainties in $q_{\text{TIR}}(z)$ are taken into account. The quoted errors do not account for any systematic errors due to cosmic variance.

3.6.2 Luminosity evolution vs. density and luminosity evolution

Fig. 3.10(a) shows the SFRD computed using the different fits to the radio LF discussed in Section 3.3.3 and Section 3.3.4, and using only the COSMOS-XS data compared to the combination of the COSMOS-XS + VLA-COSMOS 3 GHz data-sets. The combination enables us to fit not only pure luminosity evolution, but also to constrain the joint density+luminosity evolution.

When we compare all three results, we find that they all roughly agree up to $z \sim 1.8$. At that point, both pure luminosity evolution model fits show an elevated SFRD at high redshift compared to the Madau & Dickinson (2014) curve (as also seen for the VLA-COSMOS 3 GHz data alone; Novak et al. 2017). However, when we fit density+luminosity evolution to the combined data-sets, as favored by the data (Fig. 3.5), we instead find that the SFRD falls below the Madau & Dickinson (2014) curve at $z \gtrsim 1.8$. In the following sections, we will use the SFRD derived from the combined COSMOS-XS + VLA-COSMOS 3 GHz data-sets using density+luminosity evolution for the comparison with the SFRD derived from radio, FIR and UV observations.

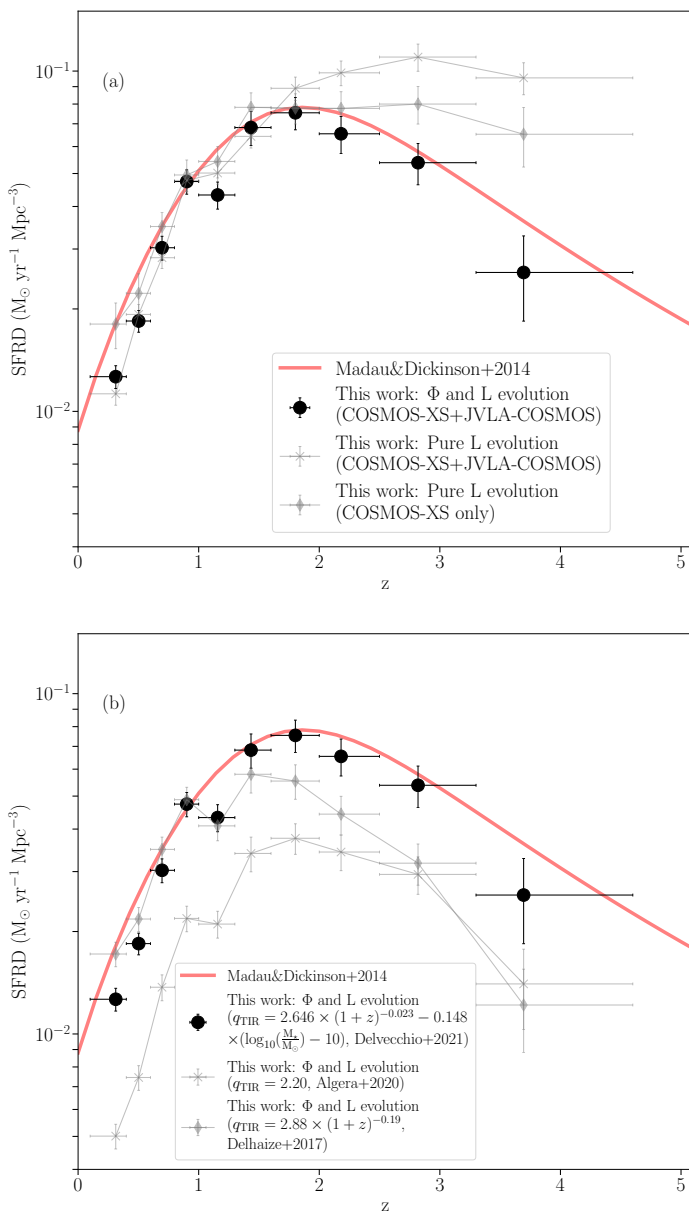


Figure 3.10: The impact of the fitted LF form and assumed FIR-radio correlation on the derived cosmic star formation rate density (SFRD). The upper panel shows the effect of fitting pure luminosity evolution compared to the preferred model of density+luminosity evolution (assuming the same FIR-radio correlation).

The lower panel shows the SFRD obtained from the combined COSMOS-XS + VLA-COSMOS 3 GHz data-sets (assuming density+luminosity evolution) but for different assumed FIR-radio correlations. This gives an indication of the impact an assumed FIR-radio correlation has. The study of Madau & Dickinson (2014) is shown as a red line in both panels. In the remainder of the paper, we convert our radio LFs to SFRD using the Delvecchio et al. (2021) FIR-radio correlation.

3.6.3 FIR-radio conversion

As Eq. 3.15 shows, the calibration of the SFR depends on $q_{\text{TIR}}(z)$ (see Section 3.2.3). Therefore not only is the FIR-radio correlation one of the uncertainties in the conversion from FIR luminosities to radio luminosities, as discussed in Section 3.4.2, but it is also one of the main uncertainties in the SFRD calculation. Current observations do not favor a constant $q_{\text{TIR}}(z)$ (Magnelli et al. 2015; Delhaize et al. 2017; Calistro Rivera et al. 2017a), although there is some discussion as to whether this evolution can be ascribed to AGN activity (Molnár et al. 2018) or selection biases such as the sampling of high mass galaxies at high redshift (Smith et al. 2021) and/or a redshift-dependent sampling of different parts of a non-linear FIR/SFR relation (Molnár et al. 2021). To illustrate the impact of the assumed FIR-radio correlation on the comparison between the FIR LF and radio LF, we show in Fig. 3.9 the data from Gruppioni et al. (2013) converted using an evolving $q_{\text{TIR}}(z)$ (Eq. 3.11) and using the local constant value for the FIR-radio correlation: $q_{\text{TIR}} = 2.64$ (Bell 2003). The difference between the two samples increases with redshift as expected due to the growing difference between the evolving and non-evolving q_{TIR} . Fig. 3.9 also shows that if we assume $q_{\text{TIR}}(z)$ to be constant at the local value of 2.64, our radio LFs would match the FIR LFs better. This comparison shows also that the FIR-radio correlation remains the largest uncertainty in the comparison between the radio LF and FIR LF.

The impact of the $q_{\text{TIR}}(z)$ on the SFRD derived from the radio LFs is shown in Fig. 3.10(b). All three curves show density+luminosity evolution fitted to the combined COSMOS-XS + VLA-COSMOS 3 GHz sample, but with different values of $q_{\text{TIR}}(z)$. These values are derived by Delhaize et al. (2017), Algera et al. (2020b) and Delvecchio et al. (2021). Fig. 3.10(b) also shows the fit from Madau & Dickinson (2014) based on a collection of previously published UV and FIR data. The first FIR-correlation we consider is from Delhaize et al. (2017). They constrained the evolution $q_{\text{TIR}}(z)$ using a doubly censored survival analysis on $\sim 10,000$ SFGs. To prevent from biases towards low and high average $q_{\text{TIR}}(z)$ measurements, these star-forming sources are jointly-selected in radio observations at 3 GHz and FIR observations. Assuming an average spectral index of -0.7 , Delhaize et al. (2017) find that $q_{\text{TIR}}(z)$ decreases with redshift as:

$$q_{\text{TIR}}(z) = (2.88 \pm 0.03) \times (1 + z)^{-0.19 \pm 0.01}. \quad (3.17)$$

Fig. 3.10(b) shows that this adopted $q_{\text{TIR}}(z)$ has a large impact on the evolution of the SFRD due to the steep evolution of $q_{\text{TIR}}(z)$ with redshift. The SFRD matches the fit from Madau & Dickinson (2014) at $z < 1$ well, after which there is an increasing and systematic discrepancy with redshift toward low implied SFRD values.

We next consider the FIR-radio relation from the recent study by Delvecchio et al. (2021). They calibrated $q_{\text{TIR}}(z)$ with a stacking analysis in the radio/FIR of a mass-selected sample of more than 400,000 SFGs in the COSMOS field. Delvecchio et al. (2021) find that $q_{\text{TIR}}(z)$ evolves primarily with M_* . A secondary, weaker dependence on redshift is also observed. The $q_{\text{TIR}}(M_*, z)$ is quantified as:

$$q_{\text{TIR}}(M_{\star}, z) = (2.646 \pm 0.024) \times (1 + z)^{-0.023 \pm 0.008} - (0.148 \pm 0.013) \times \left(\log_{10} \frac{M_{\star}}{M_{\odot}} - 10 \right). \quad (3.18)$$

In order to use Eq. 3.18 to derive the SFRD, we need to have a mass for the sample used to derive the radio LF as shown in Fig. 3.5. We used the mass given by the COSMOS2015 catalog for the sources that could be matched with this catalog. We then derived the mean mass per redshift bin, ranging from $10^{10.18} M_{\odot}$ to $10^{10.70} M_{\odot}$, to find $q_{\text{TIR}}(M_{\star}, z)$. Fig. 3.10(b) shows that the SFRD derived with $q_{\text{TIR}}(M_{\star}, z)$ described in Eq. 3.18 has a weaker dependence on redshift compared to Delhaize et al. (2017) and results in the best match with the compilation from Madau & Dickinson (2014) over the whole redshift range.

Lastly, we consider the FIR-radio correlation from Algera et al. (2020b), which focuses on a luminosity-limited sample of SMGs. They find $q_{\text{TIR}}(z) = 2.20 \pm 0.03$, where they have addressed the incompleteness in the radio observations through a stacking analysis, and they find no evidence of evolution between $1.5 \leq z \leq 4.0$. We note that the SMG sample is not well matched to the radio sample observed by the COSMOS-XS survey and the VLA-COSMOS 3 GHz Large Project. However, at $z \gtrsim 2$ the sample would be a better match as our sample traces SFGs with a high SFR. In addition, the derived $q_{\text{TIR}}(z)$ is free from some of the biases that come into play in $q_{\text{TIR}}(z)$ estimates from studies based on radio-selected samples. As expected, Fig. 3.10(b) shows that the SFRD calculated with $q_{\text{TIR}}(z) = 2.20$ does not match the fit from Madau & Dickinson (2014) at $z < 1$, and we see that the SFRD values are in fact systematically low at all redshifts.

In summary, we show that the assumed FIR-radio relation has a significant impact and remains one of the biggest uncertainties in the comparison between the radio LF and FIR LF. In addition, the assumed relation has a significant impact on the derived SFRD. We find that the recent study by Delvecchio et al. (2021), which constitutes the first calibration of the FIR-radio correlation as a function of both stellar mass and redshift, shows the best agreement with the multi-wavelength compilation from Madau & Dickinson (2014), while the other two FIR-radio relations explored result in under-predicted SFRDs at high redshift. To be consistent with our sample selection described in Section 3.2.3 and given that the Delvecchio et al. (2021) result was also derived with a large unbiased sample using some of the deepest radio and FIR images available over the same field as our observations, we will use the FIR-radio correlation from Delvecchio et al. (2021) to convert our radio LFs to SFRD in the following.

3.6.4 Comparison with the literature

In Fig. 3.11, we show the redshift evolution of the cosmic star formation density derived from this work compared with work in the literature derived at different wavelengths. The study of Madau & Dickinson (2014) is shown in all panels for ease of comparison. Below $z < 2$, our data agree well with the compilation from Madau & Dickinson (2014), although we observe some scatter in our SFRD estimates around

$z \sim 0.9$ which is likely due to cosmic variance (see Appendix 3.A). Our SFRD turns over at $z \sim 1.8$ and falls more rapidly than Madau & Dickinson (2014) out to high-redshift.

In Fig. 3.11(a) we show our derived SFRD compared to radio observations. Smolčić et al. (2009b) derived the SFRD out to $z = 1.3$ from VLA imaging at 1.4 GHz. They assumed pure luminosity evolution for the local LF, a non-evolving FIR-radio correlation established by Bell (2003) and integrated over the full luminosity range. We find a good match with the SFRD derived by Smolčić et al. (2009b) despite the different assumptions; though we note that they are only sensitive to lower redshifts ($z \lesssim 1$) where the different assumptions have a smaller effect. Karim et al. (2011) performed stacking on mass selected galaxies and find a rise up to $z \sim 3$. This rise is mainly due to the fact that they use a non-evolving FIR-radio correlation established by Bell (2003). Because this correlation does not evolve towards a lower q_{TIR} value at high redshift, the resulting SFRD will be higher at higher z as discussed in Section 3.6.3. Finally, as discussed in Section 3.2.4, Novak et al. (2017) used the VLA-COSMOS 3 GHz Large Project to derive the SFRD up to $z = 6$. They assumed pure luminosity evolution and an evolving FIR-radio correlation $q_{\text{TIR}}(z)$ derived by Delhaize et al. (2017). Below $z \sim 2$, our data agree well with the SFRD derived by Novak et al. (2017). However, our SFRD declines towards a much lower value than Novak et al. (2017) found for $z \gtrsim 2.2$. This is due to the fitted density evolution, as discussed in Section 3.4.5, and can also be seen from Fig 3.10(a). The offset would be even larger if we would have used a similar FIR-radio correlation as Novak et al. (2017) used. This can be seen from Fig. 3.10(b), which shows the large offset between the SFRD we calculate assuming the FIR-radio correlation from Delhaize et al. (2017) compared to that of Delvecchio et al. (2021).

In Fig. 3.11(b), we compare our measurement of the SFRD to results from recent FIR observations from Gruppioni et al. (2020) and Lim et al. (2020). Gruppioni et al. (2020) derive the dust-obscured SFRD using the serendipitously detected sources in the ALPINE survey. In this case, the SFRD is derived from an extrapolation of the FIR LF, where the LF (shown in Fig. 3.6) is integrated down to $\log_{10}(L_{\text{IR}}/L_{\odot}) = 8$. Lim et al. (2020) derive the SFRD by integrating the FIR LF shown in Fig. 3.6 inferred using SCUBA-2 450 μm observations. They used the integration limits of $L_{\text{min}} = 0.03L_{\star}$ and $L_{\text{max}} = 10^{13.5}L_{\odot}$. This integration is necessary in both studies since the data only constrains a small part of the LF, as can be seen in Fig. 3.6.

The first thing that stands out from Fig. 3.11(b) are the large error bars found in the studies of Gruppioni et al. (2020) and Lim et al. (2020), which are due to the small sample of sources considered in these studies. The observations by Lim et al. (2020) are still in agreement with our observations within these error margins. The next thing to note is that both FIR studies find a higher SFRD over the whole redshift range compared to the radio SFRD. This cannot be explained by the different integration limits, which should result in a higher radio SFRD as this is computed over the full luminosity range. However, Zavala et al. (2021) suggest that the SFRD found by Gruppioni et al. (2020) may be unusually high due to possible clustering of the serendipitous targets.

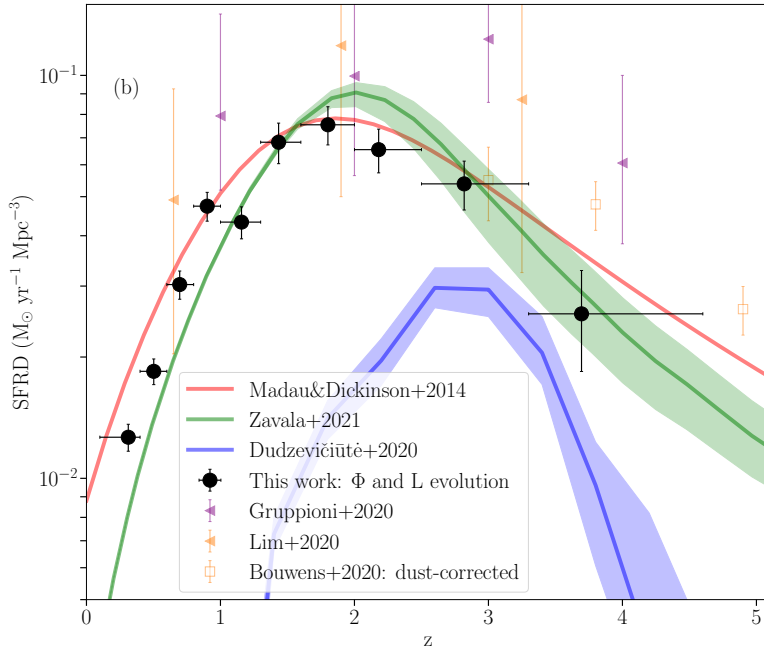
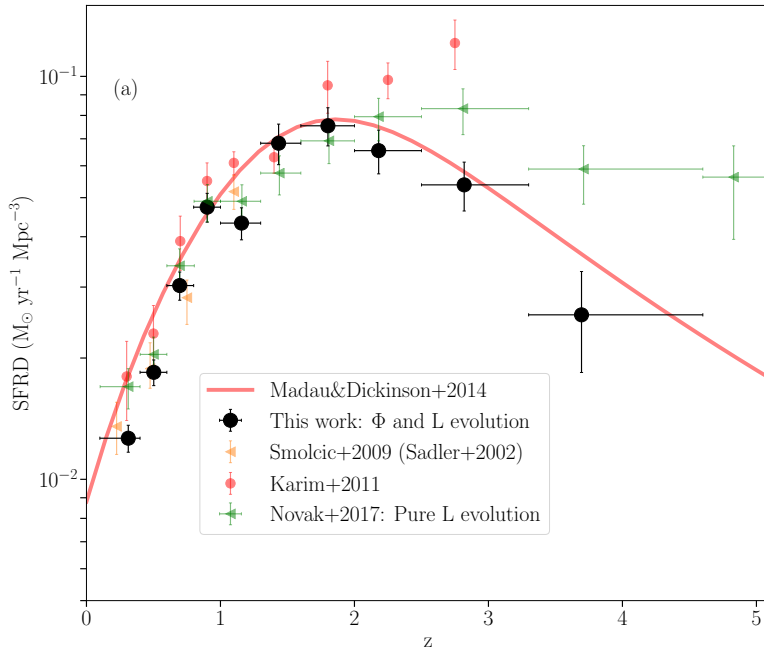


Figure 3.11: Cosmic star formation rate density (SFRD) history. Our SFRD history is shown with filled circles in all panels and is obtained from the combined COSMOS-XS + VLA-COSMOS 3 GHz data-sets (assuming density+luminosity evolution). The study of Madau & Dickinson (2014) is shown as a red line in all panels. All data shown for comparison are indicated in the legend of each panel; see text for details.

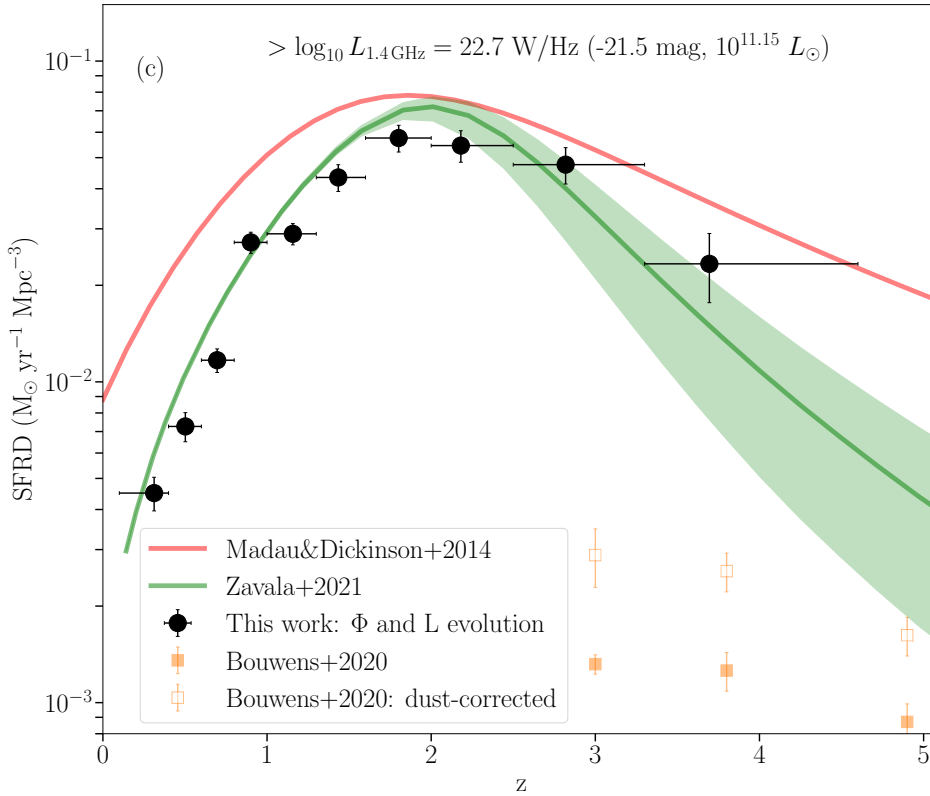


Figure 3.11: Continued. The comparison of radio- and UV-based SFRDs, integrated down to the same limit, in panel (c), shows that the UV-based SFRD from Bouwens et al. (2020) falls ~ 1 dex below the radio SFRD at $z \gtrsim 2.8$. This suggests that the bulk of the star formation contributed by high-luminosity sources at high redshifts is not accounted for by dust corrections.

Fig. 3.11(b) also shows results from recent sub-mm observations from Dudzevičiūtė et al. (2020) and Zavala et al. (2021). Dudzevičiūtė et al. (2020) used the AS2UDS sample from the $\sim 1\text{deg}^2$ SCUBA-2 survey to derive the SFR from MAGPHYS fits. The SFRD is then found from an extrapolation of the $870\mu\text{m}$ flux limit of 3.6 to 1 mJy (equivalent to $L_{\text{IR}} \approx 10^{12} L_{\odot}$) using the slope from the sub-millimeter counts in Hatsukade et al. (2018). Because of the area covered by this survey, it is likely to be much more representative than smaller volume studies such as Gruppioni et al. (2020). The curve from Dudzevičiūtė et al. (2020) does not match our radio SFRD at $z \lesssim 3$ because this curve does not represent the total SFRD but shows the SMG contribution. The study by Dudzevičiūtė et al. (2020) demonstrates that the activity of SMGs peaks at $z \sim 3$, suggesting that more massive and obscured galaxies are more active at earlier times. At $z \sim 4$ the curve is roughly consistent with our data. Zavala et al. (2021) used the results from the MORA survey to search for DSFGs at

2 mm. The number counts from the survey are combined with the number counts at 1.2 and 3 mm to place constraints on the evolution of the FIR LF by making use of the evolution model of Casey et al. (2018). The SFRD is then found by integrating the best-fit FIR LF with an integration interval of $\log_{10}(L_{\text{IR}}/L_{\odot}) = [9, 13.8]$. The curve from Zavala et al. (2021) is consistent with our data despite the different integration limits.

In addition, Fig. 3.11(b) shows the results from the UV observations from Bouwens et al. (2020). They make use of ALMA observations for a sample of galaxies in the HUDF at $1.5 < z < 10$ to provide improved constraints on the IRX- β relation. Bouwens et al. (2020) integrate their UV LFs from $0.03 \times L_{\star}$ to $\rightarrow \infty$ in order to derive the SFRD. The radio SFRD matches the UV SFRD at $z \sim 3$ and at $z > 3$ the UV SFRD rises above the radio SFRD. However, it is important to realize that the UV SFRD and radio SFRD compared in Fig. 3.11(b) are derived using different integration limits.

Differing integration limits will have a more substantial effect for the comparison between our radio-based study and UV-based studies, given the different shapes of the derived LFs evident in Fig. 3.7. To investigate the impact of the integration limits, in Fig. 3.11(c), we compare our radio-based results with the FIR-based study from Zavala et al. (2021) and the UV-based study from Bouwens et al. (2020), but now using a consistent integration limit across all studies except for the compilation from Madau & Dickinson (2014) which remains unchanged for ease of comparison. In particular, Bouwens et al. (2020) originally integrate their UV LFs from $0.03 \times L_{\star}$ to $\rightarrow \infty$ in order to derive the SFRD. However, a fairer comparison of the radio- and UV-based SFRDs necessitates that they be integrated down to the same limit. As the radio observations do not reach the faint luminosities the UV observations reach, we have chosen the integration limit as the luminosity limit reached by the radio observations between $z = 1.15$ and $z = 1.43$, which is $\log_{10} L_{1.4\text{GHz}} = 22.7 \text{ W Hz}^{-1}$. This corresponds to a luminosity limit of -21.5 mag ($0.038 L_{z=3}^{\star}$) for the UV LF. For the Zavala et al. (2021) FIR-based study, this corresponds to an FIR luminosity limit of $10^{11.15} L_{\odot}$.

Below $z < 2$, Fig. 3.11(c) shows that the radio data now falls below the SFRD from Madau & Dickinson (2014), which can be explained by the limit that has been set for the integration of the radio LF. For $z \gtrsim 2.2$, the difference between our radio-based SFRD and Madau & Dickinson (2014) becomes similar to what was found in Fig. 3.11(a) and Fig. 3.11(b). The Zavala et al. (2021) curve appears similarly affected by the new integration limits, now falling below the Madau & Dickinson (2014) compilation, but continuing to follow the radio-based SFRD reasonably well.

In contrast, the UV-based SFRD from Bouwens et al. (2020) falls ~ 1 dex below the radio SFRD at $z \gtrsim 2.8$. This result is very different from a naive comparison between the radio and UV-based SFRDs using their respective nominal integration limits, which would result in a reasonable match of the SFRDs even at the high redshift end. However, this can be explained by a ‘conspiracy’ between the amount in which different sources contribute to the LFs at the different wavelengths. Observations in the UV find that the faint-end slope of the UV LF at high redshift is very steep, and the bulk of the luminosity at high redshift is thus coming from faint sources, as can be seen in Fig. 3.7. Our radio observations, on the other hand, suggest a much shallower

faint-end slope, but they instead find a significant amount, even without including the ‘optically dark’ sources, of star formation in high-luminosity sources that is missed by UV observations. When the integration limit is thus fixed to avoid extrapolating the radio LFs significantly below our detection limit, we find a significant discrepancy in the resulting SFRDs. Fig. 3.11(c) shows that this is true even when UV observations are corrected for dust. In particular, Bouwens et al. (2020) make use of improved constraints on the IRX- β relation. This ~ 1 dex discrepancy in the resulting SFRDs therefore suggests that the bulk of the star formation contributed by high-luminosity sources at high redshifts is not accounted for by dust corrections. As discussed in Section 3.4.3, including ‘optically dark’ sources would only increase this discrepancy further.

3.7 Summary & Conclusions

We studied a 3 GHz-selected sample of star-forming galaxies (SFGs) identified in the ultra-deep, multi-band COSMOS-XS survey. Using the deep multi-wavelength data available in the COSMOS field, and selecting SFGs based on the FIR-radio correlation, we identify ~ 1300 SFGs with redshifts out to $z \sim 4.6$. We use this SFG sample to study the evolution of the radio LF with redshift.

We fit our radio LFs with a modified-Schechter function evolved in luminosity (pure luminosity evolution). By fixing the faint and bright end shape of the radio LFs to the local values, we find a strong trend in redshift for the luminosity parameter of $\alpha_L \propto (3.40 \pm 0.11) - (0.48 \pm 0.06)z$. This evolution agrees with what has been reported in previous radio-based studies (e.g., Novak et al. 2017).

We then combined the ultra-deep COSMOS-XS data-set with the shallower VLA-COSMOS 3 GHz large project data-set over the wider COSMOS field. This combination increases our dynamic range to include both the faintest and brightest sources, allowing us to simultaneously constrain the density and luminosity evolution. Doing so, we find evidence for significant density evolution over the observed redshift range.

In order to compare our radio LFs to FIR LFs, we converted FIR luminosities to radio luminosities using a redshift-dependent FIR-radio correlation. We find that our LFs agree well with the FIR LFs at $z < 2$. At $z > 2$ our LFs are systematically lower than Gruppioni et al. (2013), which we attribute at least partly to AGN contamination and the FIR-radio correlation. In addition, we find that the radio data is most consistent with the dust-poor model from Casey et al. (2018) at $z \sim 4$.

We also compare the radio LFs to the UV LFs of Mehta et al. (2017), Ono et al. (2018) and Bouwens et al. (2021), which are based on UV rest-frame observations of Lyman break galaxies. By fitting the local LF to the UV and UV+radio LFs and integrating down to $0.03 L_{z=3}^*$, we find evidence for a significant underestimation of the UV LF by $22\% \pm 14\%$ at high redshift ($3.3 < z < 4.6$). We attribute this underestimation to appreciable star formation in highly dust-obscured galaxies.

We integrate the derived radio LFs with joint density+luminosity evolution to determine the cosmic SFRD. We find the radio-derived SFRD to be consistent with the established behavior at low redshift, where it increases strongly with redshift out to $z \sim 1.8$. The radio-based SFRD then declines more rapidly out to high-redshift

than previous radio-based estimates, and is more consistent with the recent FIR-based estimated from Zavala et al. (2021).

In order to more directly compare the radio-based SFRD derived here with the recent UV-based SFRD from Bouwens et al. (2020), and to avoid extrapolating far below the radio detection limit, we integrate both LFs down to a consistent limit ($0.038 L_{z=3}^*$). This direct comparison reveals that the discrepancy between the radio and UV LFs discussed above translates to an even more significant (~ 1 dex) discrepancy between the radio- and UV-based SFRDs at high redshifts ($z > 3$). This discrepancy persists even when the UV observations are corrected for dust obscuration assuming the latest dust corrections. The discrepancy would only increase with the inclusion of ‘optically dark’ sources, which will be discussed further in a future paper.

Acknowledgments

The authors wish to thank Mara Salvato for providing us with the COSMOS spectroscopic master catalog. We thank Ivan Delvecchio, Mara Salvato and Vasily Kokorev for helpful comments on the manuscript. The National Radio Astronomy Observatory is a facility of the National Science Foundation operated under cooperative agreement by Associated Universities, Inc. D.vdV. and J.H. acknowledge support of the VIDI research programme with project number 639.042.611, which is (partly) financed by the Netherlands Organisation for Scientific Research (NWO). H.S.B.A. acknowledges support from NAOJ ALMA Scientific Research Grant Code 2021-19A. I.S. acknowledges support from STFC (ST/T000244/1). D.R. acknowledges support from the National Science Foundation under grant number AST-1614213. D.R. also acknowledges support from the Alexander von Humboldt Foundation through a Humboldt Research Fellowship for Experienced Researchers. This research made use of ASTROPY, a community developed core Python package for astronomy (Astropy Collaboration et al. 2013, 2018) hosted at <http://www.astropy.org/>, matplotlib (Hunter 2007), numpy (van der Walt et al. 2011), scipy (Jones et al. 2001), and of TOPCAT (Taylor 2005).

Appendices

3.A Cosmic variance

We need to consider whether our single pointing of 350 arcmin^2 covers over- or under-densities that will affect our LF measurements. In particular, the COSMOS field contains a very complex structure located in an extremely narrow redshift slice at $z \sim 0.73$ (Iovino et al. 2016). This structure includes a rich X-ray cluster (Finoguenov et al. 2007) and a number of groups (Knobel et al. 2012). Our field of view covers part of this structure and this can also be seen in Fig. 3.1 from the large number of sources detected in the redshift slice $0.6 < z < 0.8$. In other redshift slices we also cover several X-ray clusters and groups. At $z \sim 0.5$, $z \sim 0.9$, and $z \sim 1.25$ our field of view covers X-ray clusters described by Finoguenov et al. (2007) and at $z \sim 0.35$, $z \sim 0.5$, and $z \sim 0.8$ our field of view covers groups described by Knobel et al. (2012). We also cover part of an under-density or void at $2.0 < z < 2.5$ as found by Krolewski et al. (2018).

Scoville et al. (2013) studied the large-scale structures using a K_s -band selected sample of galaxies in the COSMOS field. They estimated the environmental densities within 127 redshift slices out to $z < 3$ using a Voronoi-based algorithm. Using the established density maps, we are able to estimate the median density in our pointing in the redshift ranges considered. Fig. 3.A.1 shows the density maps as a function of redshift in the COSMOS-XS field of view. The images were made by summing the derived densities measured from the individual redshift slices. Table 3.A.1 lists the over- and under-density factors defined as the surface density normalized to the median surface density in that redshift range. The over-densities are corrected with $o_i > 1$ where the under-densities are corrected with $o_i < 1$. If we assume radio galaxies follow the distribution of the K_s -band selected galaxies, we can use the over/under-density factors calculated to scale the measured LFs. Cosmic variance affects, to first order, the measured overall number density and will thus move the radio LF up and down relative to the full COSMOS field. The shape of the LF would be left unchanged. We introduce the over-density factor in Eq. 3.4 as:

$$\Phi(L, z) = \frac{1}{\Delta \log_{10} L} \sum_i \frac{1}{V_{\text{max},i} \times w_i(z) \times o_i(z)}, \quad (3.19)$$

where V_{max} is the co-moving volume over which the i th galaxy could be observed, $\Delta \log_{10} L$ is the size of the luminosity bin, w_i is the completeness correction factor of the i th galaxy and o_i is the over-density correction factor of the i th galaxy as tabulated in Table 3.A.1. The equation of the error of the LF in each redshift and luminosity bin (Eq. 3.6) then becomes:

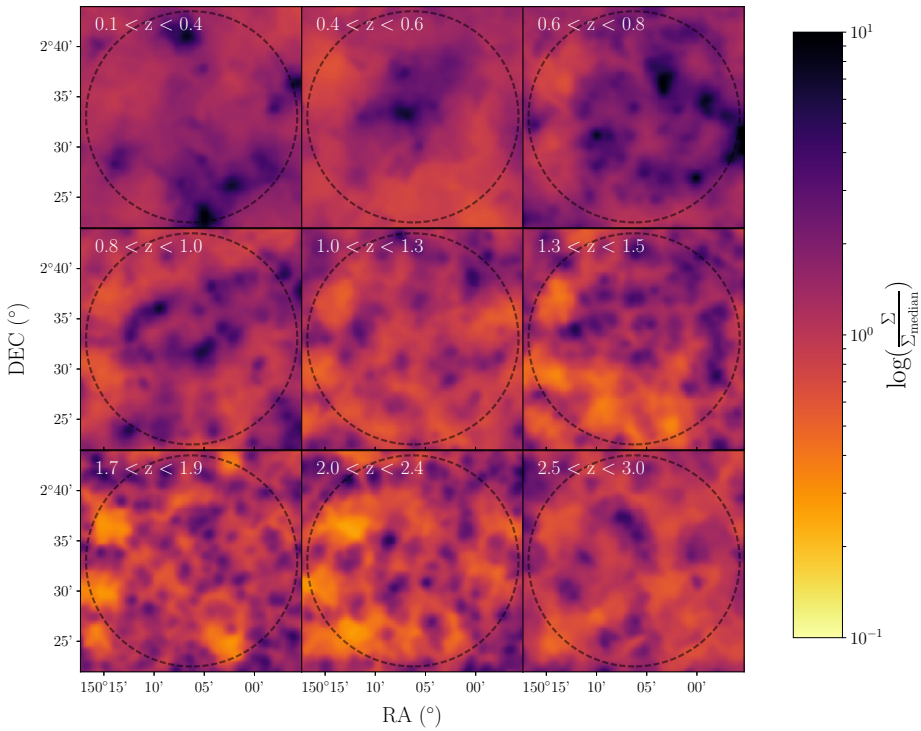


Figure 3.A.1: Density maps as a function of redshift in the COSMOS-XS field of view constructed by Scoville et al. (2013) with the Voronoi technique. The images were made by summing the derived densities measured from the individual redshift slices. The color-bar corresponds to the density unit per Mpc^2 divided by the median density over the whole COSMOS field. The redshift range is given in each panel and the COSMOS-XS area is shown with the dashed circle.

Table 3.A.1. Median density over the COSMOS-XS survey area.

Redshift range	o
$0.1 < z < 0.4$	1.56 ± 0.006
$0.4 < z < 0.6$	1.25 ± 0.004
$0.6 < z < 0.8$	2.04 ± 0.007
$0.8 < z < 1.0$	1.30 ± 0.007
$1.0 < z < 1.3$	1.02 ± 0.004
$1.3 < z < 1.6$	1.22 ± 0.007
$1.6 < z < 2.0$	1.10 ± 0.004
$2.0 < z < 2.5$	0.89 ± 0.005
$2.5 < z < 3.0$	0.99 ± 0.003

Note. The over/under-density parameter o is defined as the surface density normalized to the median surface density in that redshift range. The error margins are derived via a bootstrap analysis.

$$\sigma_{\Phi}(L, z) = \frac{1}{\Delta \log_{10} L} \sqrt{\sum_i \left(\frac{1}{\frac{\Omega}{4\pi} \times V_{\max,i} \times w_i(z) \times o_i(z)} \right)^2}. \quad (3.20)$$

The derived density corrections are subsequently applied to the derived LF in each redshift and luminosity bin. As the environmental densities are only constrained to $z < 3$, we do not apply any correction factor for the last redshift bin considered ($3.3 < z < 4.6$).

3.B Luminosity functions of star-forming galaxies

Table 3.B.1 gives the luminosity functions of SFGs in the COSMOS-XS survey obtained with the V_{\max} method.

Table 3.B.1. Luminosity functions of star-forming galaxies obtained with the V_{\max} method.

Redshift	$\log_{10}(L_{1.4 \text{ GHz}}/\text{W Hz}^{-1})$	$\log_{10}(\Phi/\text{Mpc}^{-3} \text{dex}^{-1})$
$0.1 < z < 0.4$	20.88 $^{+0.11}_{-0.46}$	-2.4 $^{+0.21}_{-0.34}$
	21.13 $^{+0.16}_{-0.13}$	-2.25 $^{+0.11}_{-0.11}$
	21.5 $^{+0.07}_{-0.22}$	-2.31 $^{+0.08}_{-0.08}$
	21.74 $^{+0.12}_{-0.17}$	-2.5 $^{+0.07}_{-0.07}$
	21.94 $^{+0.2}_{-0.08}$	-2.5 $^{+0.07}_{-0.07}$
	22.23 $^{+0.2}_{-0.08}$	-2.9 $^{+0.1}_{-0.1}$
	22.5 $^{+0.22}_{-0.07}$	-3.31 $^{+0.16}_{-0.23}$
	22.88 $^{+0.12}_{-0.17}$	-3.21 $^{+0.14}_{-0.2}$
$0.4 < z < 0.6$	21.68 $^{+0.12}_{-0.05}$	-2.58 $^{+0.19}_{-0.29}$
	21.9 $^{+0.07}_{-0.1}$	-2.56 $^{+0.13}_{-0.13}$
	22.02 $^{+0.12}_{-0.05}$	-2.54 $^{+0.1}_{-0.1}$
	22.24 $^{+0.07}_{-0.1}$	-2.58 $^{+0.09}_{-0.09}$
	22.42 $^{+0.06}_{-0.11}$	-2.84 $^{+0.11}_{-0.11}$
	22.57 $^{+0.09}_{-0.08}$	-3.04 $^{+0.13}_{-0.13}$
	22.68 $^{+0.14}_{-0.03}$	-3.38 $^{+0.19}_{-0.29}$
	22.93 $^{+0.07}_{-0.1}$	-3.78 $^{+0.28}_{-0.57}$
23.14 $^{+0.03}_{-0.14}$	-3.78 $^{+0.28}_{-0.57}$	
$0.6 < z < 0.8$	22.05 $^{+0.09}_{-0.15}$	-2.47 $^{+0.1}_{-0.1}$
	22.26 $^{+0.11}_{-0.12}$	-2.46 $^{+0.06}_{-0.06}$
	22.51 $^{+0.09}_{-0.14}$	-2.82 $^{+0.06}_{-0.06}$
	22.72 $^{+0.11}_{-0.12}$	-2.95 $^{+0.06}_{-0.06}$
	22.91 $^{+0.16}_{-0.08}$	-3.2 $^{+0.08}_{-0.08}$
	23.14 $^{+0.16}_{-0.07}$	-3.36 $^{+0.1}_{-0.1}$
	23.41 $^{+0.12}_{-0.12}$	-3.95 $^{+0.19}_{-0.29}$
	23.85 $^{+0.14}_{-0.32}$	-4.49 $^{+0.24}_{-0.42}$
$0.8 < z < 1.0$	22.31 $^{+0.06}_{-0.18}$	-2.39 $^{+0.1}_{-0.1}$
	22.51 $^{+0.1}_{-0.14}$	-2.4 $^{+0.06}_{-0.06}$
	22.69 $^{+0.14}_{-0.09}$	-2.77 $^{+0.07}_{-0.07}$

Table 3.B.1. Luminosity functions of star-forming galaxies obtained with the V_{\max} method.

Redshift	$\log_{10}(L_{1.4\text{GHz}}/\text{W Hz}^{-1})$	$\log_{10}(\Phi/\text{Mpc}^{-3}\text{dex}^{-1})$
	22.9 ^{+0.18} _{-0.06}	-2.92 ^{+0.07} _{-0.07}
	23.15 ^{+0.16} _{-0.07}	-3.3 ^{+0.1} _{-0.1}
	23.37 ^{+0.18} _{-0.06}	-3.7 ^{+0.16} _{-0.23}
	23.76 ^{+0.25} _{-0.22}	-4.55 ^{+0.28} _{-0.57}
	24.21 ^{+0.04} _{-0.19}	-4.27 ^{+0.28} _{-0.57}
<hr/>		
1.0 < z < 1.3	22.58 ^{+0.07} _{-0.13}	-2.86 ^{+0.14} _{-0.14}
	22.78 ^{+0.07} _{-0.13}	-2.64 ^{+0.07} _{-0.07}
	22.95 ^{+0.1} _{-0.1}	-2.83 ^{+0.07} _{-0.07}
	23.15 ^{+0.09} _{-0.11}	-3.22 ^{+0.09} _{-0.09}
	23.39 ^{+0.05} _{-0.15}	-3.46 ^{+0.11} _{-0.11}
	23.51 ^{+0.14} _{-0.06}	-3.88 ^{+0.17} _{-0.26}
	23.72 ^{+0.12} _{-0.08}	-4.06 ^{+0.21} _{-0.34}
	23.95 ^{+0.09} _{-0.11}	-4.36 ^{+0.28} _{-0.57}
	24.17 ^{+0.07} _{-0.13}	-4.19 ^{+0.24} _{-0.42}
<hr/>		
1.3 < z < 1.6	22.73 ^{+0.06} _{-0.13}	-2.63 ^{+0.12} _{-0.12}
	22.87 ^{+0.11} _{-0.08}	-2.71 ^{+0.08} _{-0.08}
	23.06 ^{+0.11} _{-0.08}	-2.85 ^{+0.07} _{-0.07}
	23.25 ^{+0.1} _{-0.09}	-3.12 ^{+0.07} _{-0.07}
	23.47 ^{+0.07} _{-0.12}	-3.4 ^{+0.09} _{-0.09}
	23.62 ^{+0.1} _{-0.08}	-3.6 ^{+0.11} _{-0.11}
	23.84 ^{+0.07} _{-0.12}	-3.99 ^{+0.17} _{-0.26}
	23.95 ^{+0.15} _{-0.03}	-3.93 ^{+0.16} _{-0.23}
	24.18 ^{+0.11} _{-0.08}	-4.08 ^{+0.19} _{-0.29}
<hr/>		
1.6 < z < 2.0	22.99 ^{+0.08} _{-0.15}	-2.86 ^{+0.11} _{-0.11}
	23.21 ^{+0.09} _{-0.14}	-3.1 ^{+0.09} _{-0.09}
	23.43 ^{+0.1} _{-0.13}	-3.31 ^{+0.08} _{-0.08}
	23.62 ^{+0.14} _{-0.09}	-3.56 ^{+0.09} _{-0.09}
	23.83 ^{+0.16} _{-0.07}	-3.93 ^{+0.13} _{-0.13}

Table 3.B.1. Luminosity functions of star-forming galaxies obtained with the V_{\max} method.

Redshift	$\log_{10}(L_{1.4\text{ GHz}}/\text{W Hz}^{-1})$	$\log_{10}(\Phi/\text{Mpc}^{-3}\text{dex}^{-1})$
	24.1 $^{+0.12}_{-0.11}$	-4.26 $^{+0.19}_{-0.29}$
	24.4 $^{+0.51}_{-0.18}$	-4.97 $^{+0.24}_{-0.42}$
<hr/>		
$2.0 < z < 2.5$	23.23 $^{+0.03}_{-0.19}$	-3.2 $^{+0.14}_{-0.2}$
	23.39 $^{+0.1}_{-0.13}$	-3.29 $^{+0.12}_{-0.12}$
	23.65 $^{+0.06}_{-0.16}$	-3.57 $^{+0.11}_{-0.11}$
	23.83 $^{+0.1}_{-0.12}$	-3.8 $^{+0.12}_{-0.12}$
	24.0 $^{+0.16}_{-0.06}$	-4.28 $^{+0.19}_{-0.29}$
	24.21 $^{+0.17}_{-0.05}$	-4.28 $^{+0.19}_{-0.29}$
	24.55 $^{+0.5}_{-0.17}$	-4.85 $^{+0.21}_{-0.34}$
<hr/>		
$2.5 < z < 3.3$	23.53 $^{+0.07}_{-0.13}$	-3.52 $^{+0.14}_{-0.19}$
	23.71 $^{+0.09}_{-0.11}$	-3.73 $^{+0.13}_{-0.13}$
	23.92 $^{+0.07}_{-0.13}$	-3.95 $^{+0.13}_{-0.13}$
	24.11 $^{+0.08}_{-0.12}$	-4.07 $^{+0.13}_{-0.13}$
	24.31 $^{+0.07}_{-0.12}$	-4.39 $^{+0.17}_{-0.26}$
	24.46 $^{+0.12}_{-0.08}$	-4.87 $^{+0.28}_{-0.57}$
	24.7 $^{+0.46}_{-0.13}$	-5.04 $^{+0.21}_{-0.34}$
<hr/>		
$3.3 < z < 4.6$	23.67 $^{+0.23}_{-0.13}$	-3.97 $^{+0.21}_{-0.34}$
	24.1 $^{+0.17}_{-0.19}$	-4.5 $^{+0.16}_{-0.23}$
	24.4 $^{+0.59}_{-0.13}$	-4.99 $^{+0.15}_{-0.21}$

3.C Posterior distributions

Fig. 3.C.1 shows the two dimensional posterior probability distributions of α_L and α_D for the density+luminosity evolution fitted to the combination of the COSMOS-XS survey and the VLA-COSMOS 3 GHz large project. The marginalized distributions for each parameter is shown independently in the histograms.

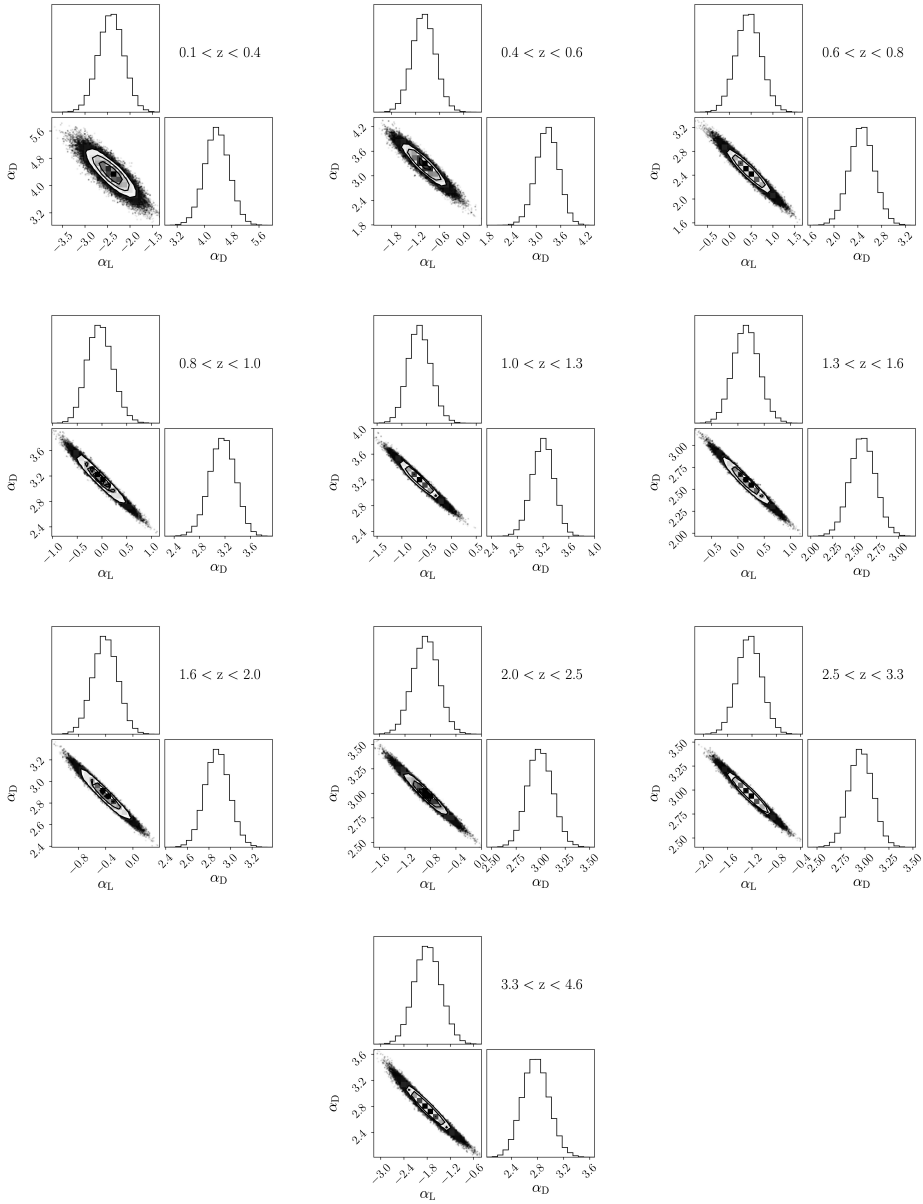


Figure 3.C.1: Corner plots showing the two dimensional posterior probability distributions of α_L and α_D for the density+lumosity evolution fitted to the COSMOS-XS + VLA-COSMOS 3 GHz samples. The marginalized distributions for each parameter is shown independently in the histograms. For all redshift bins the parameters have well-defined peaks.

4 | New constraints on the optically dark population

Abstract

Attempts to trace star formation with rest-frame UV/optical observations at redshifts $z > 2$ are affected by the presence of potentially substantial, yet uncertain, dust attenuation. Recent studies have demonstrated the existence of a population of galaxies that are virtually invisible in the observed optical/near-IR due to dust obscuration, but which could contribute substantially to the star formation history at $2 < z < 6$. Here, we make use of ultra-deep 3 GHz Karl G. Jansky Very Large Array observations from the COSMOS-XS survey to investigate the contribution of radio-selected ‘optically dark’ galaxies (undetected to a depth of $K_S \sim 25.9$ mag) to the cosmic star formation rate density (SFRD). We identify 19 such ‘optically dark’ sources, and utilize recent deblended far-infrared photometry to determine photometric redshifts based on IR and radio information for 11 of them. Through stacking, we infer that the remaining 8 sources reside predominantly at high-redshift ($z > 4$). Therefore, we conservatively assume these sources lie between $z = 2$ and $z = 5$. We derive the radio luminosity function (LF) for the sample with and without ‘optically dark’ sources by fixing the faint and bright end shape of the radio LF to the local values and allowing for luminosity evolution. By integrating both LFs, we estimate the contribution of the ‘optically dark’ galaxies to the radio SFRD to be $\sim 15^{+7}_{-7}\%$ at $z \sim 5$. This is consistent with constraints from NIR-dark and UV-dark sources while being in disagreement with some estimates using H -dropouts. This result implies that ‘optically dark’ sources play a non-negligible role at high redshift.

4.1 Introduction

For the last 20 years, pioneering work in the optical/UV has continued to push the frontier of our knowledge of galaxy evolution to higher and higher redshift. Deep surveys with Hubble Space Telescope (*HST*) and the development of color selection techniques (e.g., Lyman-break galaxies (LBGs); Steidel et al. 1996), allowed for measurements of the cosmic star formation rate density (SFRD) well beyond the era of peak galaxy assembly ($1 \lesssim z \lesssim 3$) and even into the epoch of re-ionization (e.g., Bouwens et al. 2020). However, rest-frame optical/UV observations only accurately constrain dust-unobscured star formation, potentially biasing such studies against galaxies with significant dust obscuration (e.g. Madau & Dickinson 2014).

The contribution of galaxies without observable rest-frame optical/UV emission – the ‘optically dark’ population – remains unconstrained by such observations. Samples of optical and near-infrared (NIR)-dark sources have been detected by observing deep CO line emission (Riechers et al. 2020) and via high angular resolution Atacama Large Millimeter/sub-millimeter Array (ALMA) studies (e.g., Simpson et al. 2014; Franco et al. 2018; Dudzevičiūtė et al. 2020; Gruppioni et al. 2020; Gómez-Guijarro et al. 2022; Shu et al. 2022; Xiao et al. 2023), suggesting that the classically single-dish-selected sub-millimeter galaxies (SMGs) that have long been known to be ‘optically dark’ based on pre-ALMA-era observations (e.g., Downes et al. 1999; Smail et al. 1999; Frayer et al. 2004) may be the tip of the iceberg. Most recently, several studies have observed this elusive population with the James Webb Space Telescope (*JWST*; Barrufet et al. 2023; Pérez-González et al. 2023).

Current simulations under-predict the number density of ‘optically dark’ sources (e.g., Wang et al. 2019). However, different observational studies have also reached varying conclusions about the relative contribution of ‘optically dark’ population to the cosmic SFRD. While Wang et al. (2019) find that ALMA-observed H -dropouts correspond to $\sim 10\%$ of the SFRD from LBGs at similar redshifts ($3 < z < 6$), Talia et al. (2021) report a contribution of $\sim 10\% - 25\%$ at $z \sim 3.8$ to the UV-SFRD for their sample of radio-selected ‘optically dark’ galaxies, rising to $\sim 25\% - 40\%$ at $z > 4.5$. Meanwhile, Gruppioni et al. (2020) report that the contribution of their *HST*+NIR dark sample of galaxies is nearly equal to the total extinction-corrected contribution from all the known UV-selected galaxies at $z \sim 5$.

Radio observations have been shown to identify ‘optically dark’ galaxies that contribute most significantly to the cosmic SFRD (Talia et al. 2021; Enia et al. 2022). Radio synchrotron emission provides a complementary way to trace star formation owing to its insensitivity to dust obscuration and strong correlation with far-infrared (FIR) emission and star formation rate (SFR) (FIR-radio correlation; e.g., Helou et al. 1985; Delvecchio et al. 2021) although it lacks the benefit of the negative K-correction in the FIR/sub-mm.

Recently, the COSMOS-XS survey has been carried out in the COSMOS field over an area of ~ 350 arcmin² at 3 GHz (van der Vlugt et al. 2021, hereafter Paper I). This ultra-deep, multi-band radio survey has been matched with the extensive multi-wavelength data in the COSMOS field (Algera et al. 2020a, hereafter Paper II), providing redshift information and enabling improved constraints on the radio-derived SFRD (van der Vlugt et al. 2022, hereafter Paper III). This matching has

also revealed a population of radio-detected ‘optically dark’ sources (Paper II) which are likely to be at high-redshift ($z > 3$). This sample offers the possibility to study the ‘optically dark’ population uncovered in this ultra-deep radio survey and derive the impact on the cosmic SFRD.

Throughout this paper, the spectral index, α , is defined as $S_\nu \propto \nu^\alpha$, where S_ν is the source flux density, and ν is the observing frequency. We use a Λ CDM cosmology with parameters $H_0 = 70 \text{ km s}^{-1} \text{ Mpc}^{-1}$, $\Omega_m = 0.3$, $\Omega_\Lambda = 0.7$ (Bennett et al. 2013). We assume a radio spectral index of -0.7 unless otherwise stated. We assume the Chabrier (2003) initial mass function (IMF) to calculate SFRs.

4.2 Data and sample selection

In this work we focus on the radio-selected sample in the COSMOS field obtained from the COSMOS-XS survey.

4.2.1 COSMOS-XS

The COSMOS-XS survey consists of two overlapping ultra-deep single VLA pointings in the COSMOS field at 3 and 10 GHz, respectively. Further details on these observations can be found in Paper I. Summarizing briefly: the 3 and 10 GHz observations reach a depth of $0.53 \mu\text{Jy beam}^{-1}$ and $0.41 \mu\text{Jy beam}^{-1}$ at their respective pointing centers. Both maps have a near-equal resolution of $\sim 2''.0$ ($2''.14 \times 1''.81$ at 3 GHz and $2''.33 \times 2''.01$ at 10 GHz).

4.2.2 Counterparts and sample selection

The method to cross-match the radio sources from the COSMOS-XS survey with their counterparts is fully described in Paper II. We have updated the method slightly as summarized below (and see the flowchart in Fig. 4.1).

We start by taking the 1540 COSMOS-XS 3 GHz sources detected at $\geq 5\sigma$ and matching them with the Super-deblended photometric catalog (Jin et al. 2018). We then match the resulting catalog with the latest $z^{++}YJHK_s$ -selected catalog compiled by Weaver et al. (2022) (hereafter COSMOS2020). For sources with multiple redshift estimates, we prioritize spectroscopic redshifts obtained from the COSMOS master catalog (M. Salvato et al. (2023); priv. comm.). For sources without spectroscopic redshifts, we prioritize the photometric redshift from the Super-deblended catalog, followed by the photometric redshift from COSMOS2020 or the i -band-selected catalog (Capak et al. 2007) (in that order). However, if a source could be matched within $1''.4$ to an X-ray source, the photometric redshift from the *Chandra* X-ray catalog was used (Civano et al. 2016) because these redshifts have been determined through SED fitting with the inclusion of AGN templates. The COSMOS-XS survey has 1408 sources that could be matched to a counterpart in at least one multi-wavelength catalog. The number of radio sources with spectroscopic redshifts is 584.

We select the star-forming galaxies (SFGs) from the COSMOS-XS survey, as discussed in Paper III, using the radio-FIR correlation determined by Delvecchio et al.

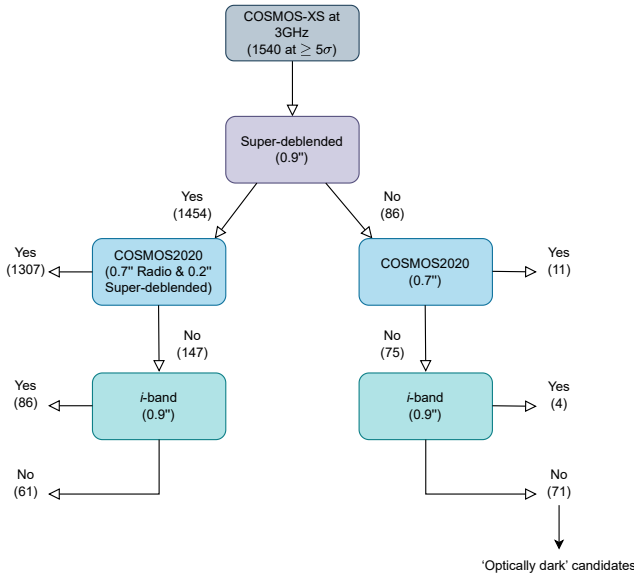


Figure 4.1: Flowchart of the multi-wavelength counterpart matching process used to identify ‘optically dark’ sources, with numbers of sources and matching radii shown in parentheses. In total, we find 71 sources without counterparts in the optical or NIR catalogs. These sources form the basis of this work.

(2021, $q_{\text{TIR}}(M_{\star}, z)$). As this relation includes stellar mass, we used the mass given by COSMOS2020 for the sources that could be matched with this catalog. For sources without a mass, we used the derived mean mass per redshift bin, ranging from $10^{10.31} M_{\odot}$ to $10^{10.64} M_{\odot}$. When the $q_{\text{TIR}}(M_{\star}, z)$ of a source deviates by more than 3.0σ from the relation, it is defined as a radio-excess source. This criterion identifies 153 radio-excess sources in total, which are removed from the SFG sample. In addition, following Papers II and III, we remove 62 ‘inverse radio-excess’ sources from the COSMOS-XS survey (of which only 16 were not already identified).

4.2.3 ‘Optically dark’ sources

We find 71 ‘optically dark’ source candidates with no counterpart in the optical or NIR catalogs (5% of the whole COSMOS-XS sample; Fig. 4.1). Based on a similar analysis from Paper II, we expect only ~ 20 may be spurious radio sources. From these 71 ‘optically dark’ source candidates, a ‘robust’ sub-sample was compiled by removing sources meeting any of the following criteria: 1) a S/N below 6 at 3 GHz; 2) located near a bright radio source; 3) located near a bright optical/NIR source. The first two criteria are adopted to remove potential spurious radio sources, the last criterion ensures we do not add sources with potential optical counterparts. This results in a sample of 19 robust ‘optically dark’ sources invisible to a depth of $K_{\text{S}} \sim 25.9$ mag (none of which have a counterpart in the *Chandra* X-ray catalog). Previously, Paper II reported the discovery of 70 ‘optically dark’ source candidates with no counter-

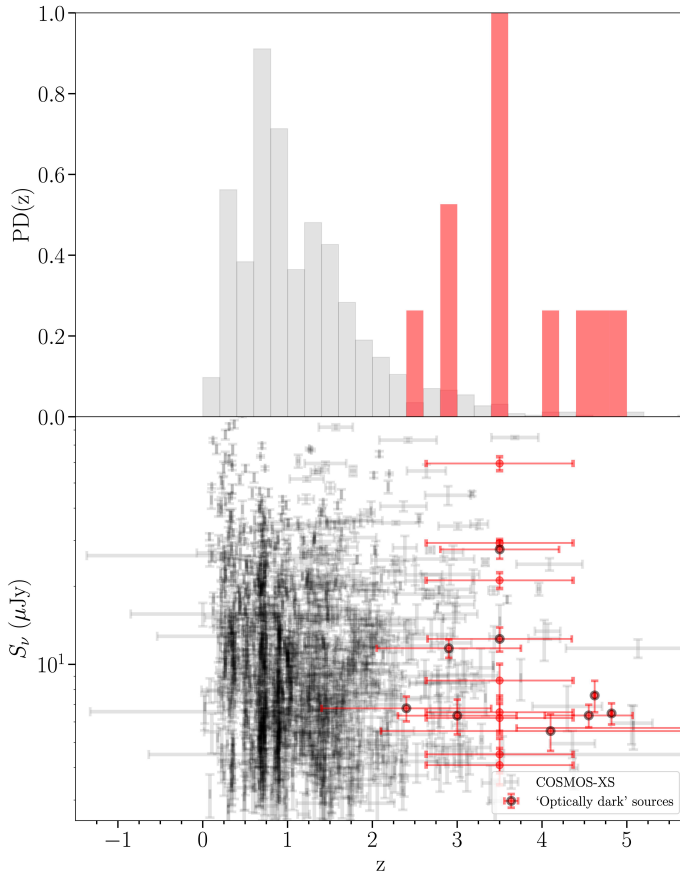


Figure 4.2: The upper panel shows a histogram of the redshift distribution of the COSMOS-XS sample compared to the 19 ‘optically dark’ sources. All but one of these sources are found to be SFGs. The lower panel shows the total flux density vs. redshift distributions of the COSMOS-XS sample compared to the ‘optically dark’ sources. $\sim 68\%$ of the ‘optically dark’ sources fall below $10 \mu Jy$. The FIR-based photometric redshifts of the ‘optically dark’ population are found using SED fitting on the new Super-deblended photometry. The sources without a black edge consist of the sample of 8 ‘optically dark’ sources with a FIR detection of $S/N_{FIR} < 5$. The error bar of these sources represents the standard deviation of the distribution. Their redshift is sampled from a uniform distribution between $z = 2$ and $z = 5$.

part in the optical or NIR catalogs, with the main difference being the use of the COSMOS2015 catalog. They found 29 robust sources using outlined criteria above.

By adding the COSMOS-XS sources to a prior catalog based on the COSMOS2020 catalog (Weaver et al. 2022), we adopted the ‘Super-deblending’ technique (Jin et al. 2018; Liu et al. 2018) and deblended FIR/(sub-)mm to radio data in COSMOS-XS on the priors’ positions. For the 19 robust ‘optically dark’ sources in the new Super-deblended catalog in COSMOS (Jin et al. in prep.), we have deblended photometry in MIPS $24\mu\text{m}$, *Herschel*, SCUBA-2, AzTEC, MAMBO, VLA 1.4 & 3GHz and MeerKAT 1.28 GHz band, in which 11 of them are detected in FIR with combined $S/N_{\text{FIR}} > 5$, providing FIR-luminosity (L_{FIR}) values.

In total, 2/19 sources have a spectroscopic redshift from the COSMOS master catalog. For the $S/N_{\text{FIR}} > 5$ sources without spectroscopic redshifts, we then used the FIR-based photometric redshifts based on the method described in Jin et al. (2018) and shortly summarized below. Four distinct SED components are used in the fitting procedure: (1) a stellar component (Bruzual & Charlot 2003) with a Small Magellanic Cloud dust attenuation law; (2) a mid-infrared AGN torus component (Mullaney et al. 2011); (3) dust continuum emission from the Magdis et al. (2012) library with the more updated $L_{\text{IR}}/M_{\text{dust}}$ -redshift evolution taken from Béthermin et al. (2015); and (4) a power-law radio continuum with an evolving q_{TIR} . Examples of the SED fits and multi-wavelength cutouts of $z > 4$ candidates can be found in Fig. 23 of Jin et al. (2018) and two of these candidates have weak or no detection in the K_S -band similar to the ‘optically dark’ sources. Jin et al. (2018) note that the IR SED-driven photometric redshifts of $z > 3$ are in good agreement with the spectroscopic redshift for galaxies with significant FIR detections, while it is somewhat underestimated for galaxies with significant AGN torus emission. We find that the FIR-based photometric redshifts for the two ‘optically dark’ sources found within the spectroscopic COSMOS master catalog agree with their spectroscopic redshift within 1σ uncertainty. Additionally, recent ALMA spectral scans of a similarly selected population find that 7/9 sources with lines detected have spectroscopic redshifts that agree with their FIR photometric redshifts within $< 2\sigma$ (project 2022.1.00863.S, PI: Hodge). Despite the dispersion, the spectroscopic redshifts confirm that all of the ‘optically dark’ sources targeted are at $z \gtrsim 3$ as suggested by their estimated FIR photometric redshifts.

Finally, for the 8/19 sources with $S/N_{\text{FIR}} < 5$, we estimated the redshift probability distribution from the stacking analysis as described in Section 5.3 in Paper II. The final SED and redshift probability distribution showed that a sample of ‘optically dark’ sources without counterparts predominantly consists of high-redshift ($z > 4$) sources, as can be seen in Fig 15 in Paper II. The 8 sources are thus added to the ‘optically dark’ sample with a redshift conservatively sampled from a uniform distribution between $z = 2$ and $z = 5$.

The properties of the 19 robust ‘optically dark’ sources are listed in Table 4.1, and the redshift and total flux density distributions are shown in Fig. 4.2 compared to the redshift and total flux density distribution of the COSMOS-XS sample. In addition, Table 4.2 shows the number of ‘optically dark’ sources+non-dark sources in the four bins compared to the non-dark sources in the bin. The four bins range from $z = 2$ to $z = 5.7$, and we note that changing the bins does not change our results.

Table 4.1. ‘Optically dark’ sources with their Super-deblended redshifts.

R.A.	Decl.	Total flux density at 3 GHz [μJy]	$S/N_{\text{FIR}}^{\text{a}}$	Redshift ^b
10h00m04.8463s	2d35m59.5056s	6.21 \pm 0.85	4.50	3.50 \pm 0.87 ^c
10h00m05.4573s	2d30m03.7998s	5.53 \pm 0.89	5.92	4.10 \pm 2.00
10h00m07.3881s	2d42m03.2196s	59.45 \pm 3.69	3.52	3.50 \pm 0.87 ^c
10h00m08.6347s	2d32m50.8604s	4.50 \pm 0.68	0.45	3.50 \pm 0.87 ^c
10h00m10.5157s	2d39m24.9492s	21.08 \pm 1.48	1.53	3.50 \pm 0.87 ^c
10h00m14.6954s	2d28m01.7486s	5.69 \pm 0.91	7.33	6.75 \pm 3.05 ^d
10h00m17.1643s	2d25m19.1251s	12.53 \pm 1.34	6.48	3.50 \pm 0.85
10h00m24.0435s	2d29m48.5492s	6.47 \pm 0.61	7.64	4.82 \pm 0.00 ^e
10h00m24.4352s	2d37m49.3438s	6.77 \pm 0.74	5.24	2.40 \pm 1.00
10h00m24.5641s	2d39m11.5684s	6.34 \pm 0.97	10.55	3.00 \pm 0.70
10h00m25.3726s	2d26m05.3135s	7.59 \pm 1.05	10.24	4.62 \pm 0.00
10h00m28.9934s	2d29m37.5088s	6.35 \pm 0.63	3.85	4.55 \pm 0.52
10h00m35.3442s	2d28m26.6779s	5.83 \pm 0.77	19.42	8.55 \pm 1.35 ^f
10h00m37.2974s	2d30m39.9243s	4.09 \pm 0.65	1.08	3.50 \pm 0.87 ^c
10h00m38.999s	2d30m40.1547s	29.37 \pm 0.94	0.64	3.50 \pm 0.87 ^c
10h00m39.2093s	2d40m52.7322s	27.73 \pm 2.20	18.57	3.50 \pm 0.70
10h00m48.4633s	2d36m41.2455s	6.54 \pm 1.01	3.03	3.50 \pm 0.87 ^c
10h00m48.7159s	2d30m17.9943s	11.54 \pm 0.94	9.71	2.90 \pm 0.85
10h00m58.2531s	2d32m45.7583s	8.66 \pm 1.36	1.34	3.50 \pm 0.87 ^c

Notes.

^a The FIR+mm combined S/N_{FIR} as described in Eq. 2 from Liu et al. (2018).

^b The spectroscopic/photometric/FIR redshift and uncertainty based on SED fitting. A uncertainty of zero refers to a spectroscopic redshift.

^c This redshift is sampled from a uniform distribution between $z = 2$ and $z = 5$ because $S/N_{\text{FIR}} < 5$. The redshift given here is the median of the distribution and the error is the standard deviation of the distribution.

^d Removed from the ‘optically dark’ sample by the cut on $q_{\text{TIR}}(M_{\star}, z)$.

^e Spectroscopic redshift from recent ALMA observations as determined by Sillaseen et al. in prep.

^f This promising candidate at $z > 6 - 9$ is a target in an ongoing NOEMA line scan project.

We find that the ‘optically dark’ sample makes up $\sim 12\%$ of the total number of sources at $z > 2$. The derived redshift distribution confirms that the bulk of our population of ‘optically dark’ sources is consisting of dusty SFGs at $z > 2$. However, we note that the photometric redshifts contain a large photometric error, with a typical uncertainty of 0.85. The total flux density distribution in Fig. 4.2 shows that $\sim 68\%$ of the ‘optically dark’ sources fall below $10 \mu\text{Jy}$.

Lastly, we select SFGs from the 19 ‘optically dark’ sources with $S/N_{\text{FIR}} > 5$ using the radio-FIR correlation as discussed above (and we also note that the fraction of COSMOS-XS radio sources powered by star formation in general already reaches near-unity below $20 \mu\text{Jy}$ (Paper II)). One of the 19 sources is removed by the cut on $q_{\text{TIR}}(M_*, z)$ where the mass is the derived mean mass per redshift bin and L_{FIR} is found in the Super-deblended FIR catalog. This leaves 18 ‘optically dark’ sources that are classified as SFGs. This sample will be used to estimate the contribution of the ‘optically dark’ galaxies to the radio SFRD.

4.3 Contribution of the ‘optically dark’ population to the SFRD

We measure the impact of ‘optically dark’ sources by constructing the radio luminosity function (LF) with and without these sources. Using these radio LFs, we then derive the SFRD and quantify the contribution of the ‘optically dark’ sources to the radio SFRD.

4.3.1 Constraining the LF

The radio LFs are derived using the same $1/V_{\text{max}}$ (Schmidt 1968) method as described in Paper III. We will shortly summarize the method below.

In each redshift bin, we compute the co-moving volume available to each source in that bin. Following Paper III, this volume is corrected with the completeness correction factor which takes into account the observed area and sensitivity limit. However, we do not correct for counterpart completeness in this work given that we are interested in exactly those sources with no optical/NIR counterparts. We use the parametric estimate of the LF at different redshifts as done in Paper III to fit the LF. We assume a modified-Schechter function (e.g., Saunders et al. 1990) for the shape of the LF where the values of Φ_* , α and σ will be frozen at the values found for the local LF. In reality, Φ_* , α and σ may change with redshift. We use the parameters of the local LF as determined in Paper III. When we fit the LF, we only assume the position of the turnover (L_* , characteristic luminosity) to change with redshift. The reason is we are not able to constrain both L_* and Φ_* for the higher redshifts ($z > 2.0$). All sources are distributed into equally spaced luminosity bins spanning the observed luminosity range. The LFs calculated with the V_{max} method are shown in Fig. 4.3. The LFs are calculated using the 1.4 GHz rest-frame luminosity for easier comparison with previous studies.

In order to take the uncertainties on the photometric redshifts into account, we

Table 4.2. Parameter values describing the luminosity evolution fits to the COSMOS-XS data-set and to the COSMOS-XS data-set + ‘optically dark’ sources.

Redshift range	Median redshift	COSMOS-XS		COSMOS-XS + ‘optically dark’ sources		SFRD ^a [$M_{\odot} \text{ yr}^{-1}$ Mpc ⁻³]
		α_L	Number of sources	SFRD ^a [$M_{\odot} \text{ yr}^{-1}$ Mpc ⁻³]	α_L	
2.0 < z < 2.5	2.18	2.20 ^{+0.08} _{-0.09}	69	0.075 ^{+0.009} _{-0.009}	2.21 ^{+0.08} _{-0.08}	0.075 ^{+0.010} _{-0.009}
2.5 < z < 3.3	2.89	1.72 ^{+0.07} _{-0.09}	58	0.057 ^{+0.008} _{-0.007}	1.76 ^{+0.07} _{-0.08}	0.059 ^{+0.009} _{-0.008}
3.3 < z < 4.6	3.52	1.60 ^{+0.13} _{-0.19}	18	0.056 ^{+0.013} _{-0.015}	1.70 ^{+0.11} _{-0.16}	0.065 ^{+0.014} _{-0.015}
4.6 < z < 5.7	5.06	1.47 ^{+0.15} _{-0.21}	7	0.071 ^{+0.023} _{-0.023}	1.57 ^{+0.14} _{-0.23}	0.082 ^{+0.026} _{-0.029}

Note.

^a Obtained by integrating the fitted LF from $L_{\min} = 0.0$ to $L_{\max} = \infty$.

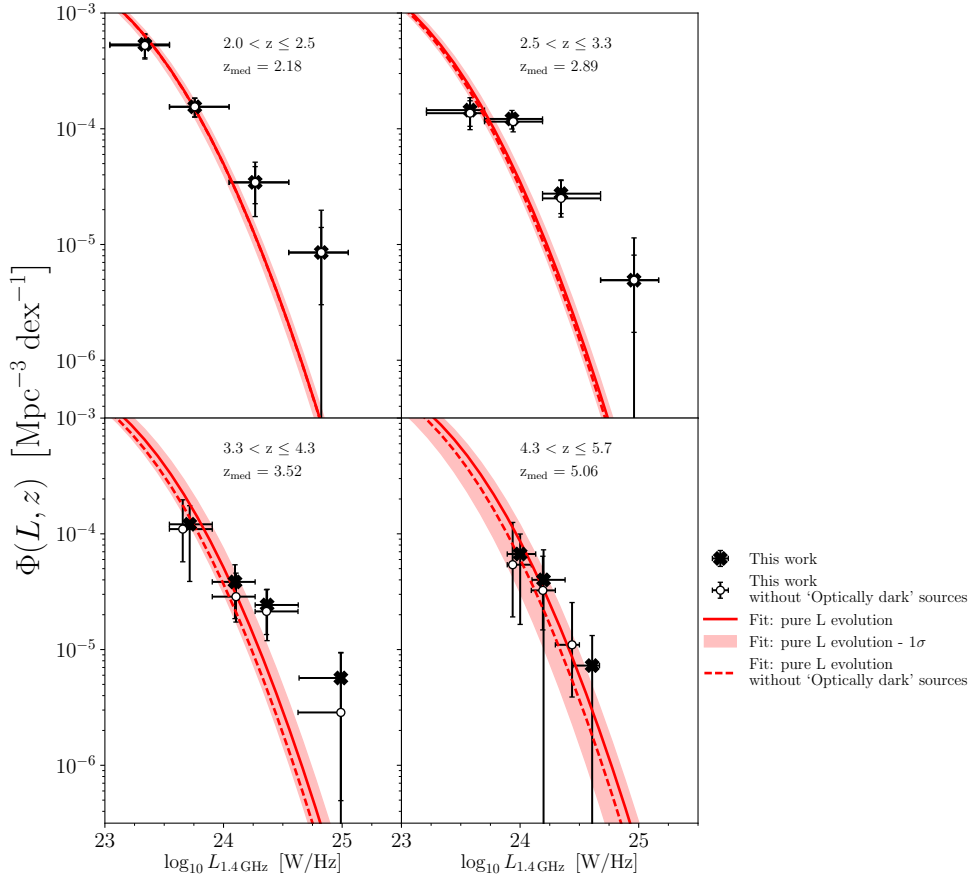


Figure 4.3: Radio LFs of SFGs in four redshift bins from the COSMOS-XS survey. Our best-fit pure luminosity function, fitted to the black points, in each redshift bin are shown with solid red where the shaded area shows the 1σ confidence interval for the best-fit function. The dotted red line is the best-fit pure luminosity function fitted to the open symbols. The redshift range and median redshift are given in each panel. The open symbols show the LF without the contribution of ‘optically dark’ sources and the filled symbols show the LF including ‘optically dark’ sources. The difference between the open and filled symbols shows the impact of the contribution of the ‘optically dark’ sources which is especially notable in the highest-redshift bin.

measure the luminosity function for 1000 different realizations of z and $\log L$, extracted from their probability density distributions. The distributions are taken to be Gaussian. The error is defined as the 16th and 84th percentile of the final distribution added to median error as calculated with Eq. 6 in Paper III in quadrature.

The black filled circles show the median luminosity of all sources, including the ‘optically dark’ sources, in the corresponding luminosity bin. The black open circles are a reference as they consist of the COSMOS-XS data-set without ‘optically dark’ sources. The horizontal error bars show the width of the bin. The vertical errors correspond to the errors calculated using Eq. 6 in Paper III. The data points were fitted with the analytical form from Eq. 4.1 using the MCMC algorithm assuming flat priors¹:

$$\Phi(L, z, \alpha_L) = \Phi_0 \left(\frac{L}{(1+z)^{\alpha_L}} \right), \quad (4.1)$$

where α_L corresponds to the pure evolution parameter and Φ_0 is given in Eq. 7 in Paper III.

The redshift used in Eq. 4.1 is the median redshift of all the sources in the redshift bin. This value is given in the panels of Fig. 4.3. The best-fit values for α_L are tabulated in Table 4.2 and the best-fit pure luminosity evolved function is shown with the red line in Fig. 4.3. The difference between the open and filled symbols shows the impact of the contribution of the ‘optically dark’ sources which is especially notable in the highest redshift bin.

4.3.2 SFRD

The radio SFRD is derived using the same method as described in Paper III. We will shortly summarize the method below. The SFRD is estimated by taking the luminosity-weighted integral of the analytical form of the fitted LF and converting the luminosity in the integral to SFR. The integral of the SFRD is given by Eq. 16 in Paper III. This integral gives the SFRD of a given epoch. The results of the SFRD shown in Fig. 4.4 are obtained by integrating the fitted LF from 0.0 to $\rightarrow \infty$. Our errors are estimated from the fitting parameter uncertainties through bootstrapping whereby the uncertainties in $q_{\text{TIR}}(M_*, z)$ are taken into account. The error is defined as the 16th and 84th percentile of the final distribution. The quoted errors do not account for any systematic errors due to cosmic variance. The total SFRD for the COSMOS-XS sample and the COSMOS-XS sample including ‘optically dark’ sources are shown in Table 4.2. We find that at $z \sim 2.9$ ‘optically dark’ sources account for $\sim 2_{-0.4}^{+0.4}\%$ of the total radio SFRD derived from the full radio-sample. This fraction rises with redshift until $z \sim 3.5$, reaching $\sim 17_{-6}^{+5}\%$ at $z \sim 3.5$ and $\sim 15_{-7}^{+7}\%$ at $z \sim 5.1$. Their contribution to the SFRD is shown in Fig. 4.4. As the radio observations do not constrain the location of the knee and the faint-end slope, we have also integrated the LF using the luminosity limit reached by the radio observations in the range $z = 2.0$ and $z = 2.5$, which is $\log_{10} L_{1.4\text{GHz}} = 23.0 \text{ W Hz}^{-1}$. This does not change the results significantly and we find at $z \sim 2.9$ a contribution of $\sim 0.3_{-0.3}^{+0.3}\%$,

¹ $\alpha_L \in [1.0, 7.0]$

reaching $\sim 33_{-17}^{+16}\%$ at $z \sim 3.5$ and $\sim 21_{-14}^{+14}\%$ at $z \sim 5.1$. The sky density of star-forming ‘optically dark’ sources is approximately $185 \pm 44 \text{ deg}^{-2}$. This is within the error of the potential surface density found by Smail et al. (2021) of $450_{-300}^{+750} \text{ deg}^{-2}$ for NIR-faint SMGs. It is lower than the ALMA-selected H -dropout surface density corrected for incompleteness of 530 deg^{-2} (Wang et al. 2019).

4.3.3 Discussion

Different works have already identified ‘optically dark’ sources, extreme SFGs heavily obscured by dust which lack an optical or NIR counterpart, out to high redshift ($z \simeq 5$; e.g., Simpson et al. 2014; Wang et al. 2019; Dudzevičiūtė et al. 2020; Gruppioni et al. 2020; Talia et al. 2021; Enia et al. 2022; Shen et al. 2022). Fig. 4.4 shows the results from a number of recent observational and theoretical studies compared to this work. The definitions and depths of the observational studies are listed in Table 4.3. For reference, Fig. 4.4 also shows the SMG contribution for a complete dust-mass-selected sample to the SFRD from Dudzevičiūtė et al. (2020).

Most observational studies show that the contribution of ‘optically dark’ sources increases up to $z \sim 3.5$ and thereafter decreases. However, the observations still span a wide range of SFRD values over an order of magnitude at $3 \lesssim z \lesssim 6$. Part of the difference among observational studies could be due to the different selection criteria for these various optical and NIR ‘dark’ samples, leading Talia et al. (2021) to suggest a possible diversity of galaxy populations under the common ‘dark’ label. Fig. 4.4 includes two other studies of radio-selected ‘optically dark’ galaxies: Talia et al. (2021) used radio sources without counterparts in the COSMOS2015 catalog (Laigle et al. 2016) and Enia et al. (2022) selected radio galaxies lacking a counterpart in the *HST*/WFC3 H -band. Fig. 4.4 also shows ‘optically dark’ sources that were selected from *Spitzer*/IRAC imaging or as serendipitous sources in ALMA sub-mm continuum data. Wang et al. (2019) reported ALMA follow-up observations of a population of H -dropouts, while Shu et al. (2022) reported ALMA and JCMT/SCUBA-2 follow-up of 12 strongly lensed galaxies also selected as H -dropouts, and Gruppioni et al. (2020) utilized serendipitous ALMA continuum detections around main-sequence galaxies. Recently, Barrufet et al. (2023) presented a *JWST* study of *HST*-dark galaxies which were selected with similar color cuts to select the H -dropout galaxies. Finally, Xiao et al. (2023) extended the H -dropout criterion, using multi-wavelength observations ranging from *HST* to ALMA, to select normal star-forming galaxies with lower stellar masses ($\log(M_*/M_\odot) = 9.5 - 10.5$).

Compared to these non-radio-based studies, our results are most consistent with Gruppioni et al. (2020) and Xiao et al. (2023) at $z \sim 4$, and somewhat higher than the results of Wang et al. (2019), Shu et al. (2022) and Barrufet et al. (2023). This might be due to the selection criteria used in these studies to select the H -dropout population. Xiao et al. (2023) showed that Wang et al. (2019) selected only extremely dust-obscured massive galaxies with a median mass of $\log(M_*/M_\odot) = 10.6$. Meanwhile, Barrufet et al. (2023) used similar color cuts to Wang et al. (2019) to identify their sample. Studies using radio emission are less likely to be biased toward these extreme objects because of the lack of dependence on dust temperature, but are more likely to be biased by radio emission originating from AGN.

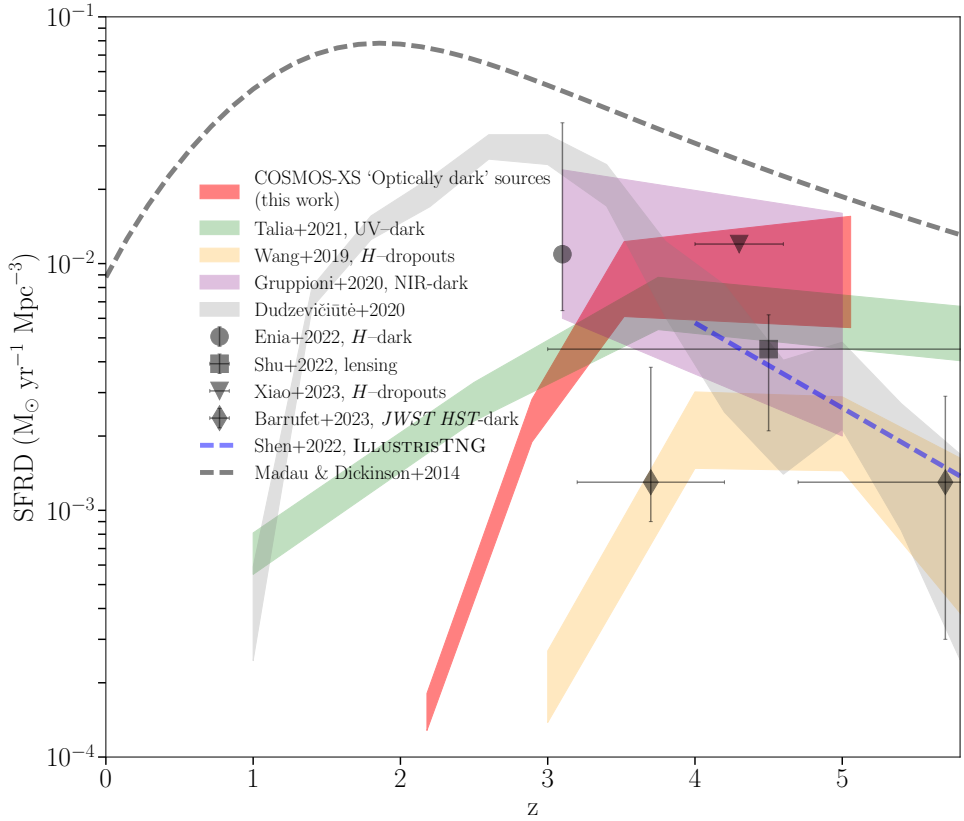


Figure 4.4: The cosmic star formation rate density (SFRD) history. The black dotted curve represents the study of Madau & Dickinson (2014). The red shaded area shows the 1σ confidence interval for the contribution of ‘optically dark’ COSMOS-XS sources to the SFRD. The green area and the black point show the SFRD from radio-selected UV-dark galaxies from Talia et al. (2021) and Enia et al. (2022), respectively. The yellow area is the SFRD from the H -dropouts in Wang et al. (2019) and the purple region shows the sub-sample of NIR-dark galaxies in the ALPINE fields (Gruppioni et al. 2020). The black square, triangle and diamond give the SFRD from the recent studies by, respectively, Shu et al. (2022), Xiao et al. (2023) and Barrufet et al. (2023). The blue dashed line shows the results from the ILLUSTRISTNG simulations (Shen et al. 2022). The gray area shows, for reference, the SMG contribution for a complete dust-mass-selected sample to the SFRD from Dudzevičiūtė et al. (2020). Our estimate of the ‘optically dark’ contribution stays constant for $3.5 \lesssim z \lesssim 5.0$ and the ‘optically dark’ sources contribute $\sim 15^{+7}_{-7}\%$ of the total radio-derived SFRD at $z \sim 5$.

Table 4.3. Criteria for ‘optically dark’ sources.

Study	Definition ‘optically dark’	$L_{1.4}$ GHz at $z=4$ limit [W Hz^{-1}]	SFRD at $z = 4$ [$M_{\odot} \text{ yr}^{-1}$ Mpc^{-3}]
Our study	No counterpart in COSMOS2020 and Super-deblended ($K_S = 25.9$ mag)	4.29×10^{23}	$0.010^{+0.013}_{-0.006}$
Talia et al. (2021)	No counterpart in NIR-for-FIR bands ($K_S = 24.5 - 24.9$ mag)	1.86×10^{24}	0.007 ± 0.002
Wang et al. (2019)	No counterpart in the H -band ($H > 27$ mag, $[4.5] < 24$ mag)	6.28×10^{23a}	0.002 ± 0.007
Grupponi et al. (2020)	No counterpart in HST or NIR ($K_S = 24.9$ mag)	8.31×10^{22a}	0.01 ± 0.008
Enia et al. (2022)	No counterpart in $HST/WFC3$ H -band ($H = 27.3$ mag)	1.04×10^{24}	0.01 ± 0.004^b
Jin et al. (2022)	No counterpart in ($K_S = 24.9$ mag)	6.28×10^{23a}	0.0026
Xiao et al. (2023)	No counterpart in $HST/WFC3$ H -band ($H > 26.5$ mag) and IRAC ($[4.5] = 25$ mag)	9.53×10^{23}	0.012^c
Barrufet et al. (2023)	HST -dark galaxies selected on $H - F444W$ colors ($H - F444W > 2.3$, $H > 27$ mag, $F444W > 26.4$ mag)	2.05×10^{22a}	$0.0013^{+0.0024}_{-0.0005}$
Shu et al. (2022)	No counterpart in $HST/WFC3$ H -band ($H > 27.5$ mag)	9.60×10^{22a}	$0.0045^{+0.0017d}_{-0.0024}$

Notes.

^a Converted to radio luminosity at 1.4 GHz using the radio-FIR correlation determined by Delvecchio et al. (2021). As this relation includes stellar mass, we use the mean mass at $z = 4$ found for the COSMOS-XS sample ($10^{10.41} M_{\odot}$).

^b SFRD at $z = 3$ since Enia et al. (2022) do not derive the SFRD at $z = 4$.

^c SFRD at $z = 4.3$ since Xiao et al. (2023) do not derive the SFRD at $z = 4$.

^d SFRD at $z = 4.5$ since Shu et al. (2022) do not derive the SFRD at $z = 4$.

Our selection criteria are closest to the studies by Talia et al. (2021) and Enia et al. (2022) as they both used radio surveys to identify their ‘optically dark’ sources. Indeed, we find general agreement with Talia et al. (2021) at $z \sim 3$, though the behavior at lower and higher redshift is somewhat different. The remaining differences between these radio-based observational studies (and their associated uncertainties) could be partly explained by the redshifts assumed for the ‘optically dark’ sources. Talia et al. (2021) estimated redshifts using SED fitting for sources with one FIR and one NIR-to-MIR photometric point from COSMOS2015 and the Super-deblended catalogs (comprising $\sim 50\%$ of their sample), and they estimated the photometric distribution for the other sources from a stacked SED. As Enia et al. (2022) did not have redshift constraints for $\sim 50\%$ of their ‘optically dark’ sample, they assumed those sources to be at $z \sim 3$. For the other sources, they estimated their photometric redshift from SED fitting. In this study, we have attempted to mitigate some of this uncertainty by using the latest Super-deblended FIR catalog to determine FIR-based photometric redshifts for our individual sources, though we caution that the uncertainties are still significant as shown in Fig. 4.2. Precise redshifts for the ‘optically dark’ sources would help us to place more robust constraints on the relative contribution of ‘optically dark’ sources to the SFRD.

A final consideration, at least in observational studies like ours, is the effect of small number statistics and cosmic variance. Our small observed area is likely to suffer from cosmic variance, as was also discussed in Paper III, and might explain some of the discrepancies with other observational studies. Observing larger areas to the depth achieved here would help to place more precise constraints.

Forming dusty galaxies at high redshift in simulations while simultaneously matching constraints from other low or high redshift galaxy populations has been surprisingly problematic for theorists (e.g., Casey et al. 2014a). To illustrate the difference between observations and simulations, Fig. 4.4 also shows the result from the recent theoretical study by Shen et al. (2022). They used post-processed galaxies in the ILLUSTRISTNG simulation and find a strongly decreasing trend at $z > 4$, where their predicted obscured SFRD becomes subdominant (i.e., contributes less than 50% to the total SFRD) at $z \gtrsim 5$ and diminishes at higher redshift. This is also an upper limit as they assume that all the galaxies with $L_{\text{IR}} = 10^{12} L_{\odot}$ are optical and NIR dark. This discrepancy between the observations and the ILLUSTRISTNG simulation is related to the under-prediction of luminous IR galaxies in the model.

4.4 Summary & Conclusions

We make use of ultra-deep 3 GHz Karl G. Jansky Very Large Array observations of the COSMOS field from the multi-band COSMOS-XS survey to infer the contribution of ‘optically dark’ sources to the cosmic SFRD. Approximately 5% of all COSMOS-XS radio sources are found to be optically and NIR dark (to a depth $K_S \sim 25.9$ mag). Using redshift estimates either from newly deblended FIR photometry or informed by stacking, we estimate the contribution of these ‘optically dark’ sources to the SFRD by deriving the radio LF for the sample with and without this population.

We identify a robust sub-sample of 19 ‘optically dark’ sources between $2 < z < 5$

and derive their contribution to the radio SFRD. We conclude that ‘optically dark’ sources contribute $\sim 15_{-7}^{+7}\%$ of the total radio-derived SFRD at $z \sim 5$. In addition, we find the contribution stays constant for $3.5 \lesssim z \lesssim 5.0$. Our derived contribution at $z \sim 5$ is in agreement with some previous observational results from NIR- and UV-dark sources by Gruppioni et al. (2020), Talia et al. (2021) and Xiao et al. (2023), but higher than some estimates based on H-dropouts. This result highlights that ‘optically dark’ sources possibly play a non-negligible role at high redshift. In addition, it shows the advantage of deep radio imaging in observing the ‘optically dark’ population, which will be even more feasible with future deep and wide radio surveys, such as the SKA, ngVLA and MeerKAT.

Acknowledgments

We wish to thank the anonymous referee for their comments and suggestions which greatly improved this work. The authors wish to thank Ian Smail for the useful discussions that helped improve this work and Mara Salvato for providing us with the COSMOS spectroscopic master catalog. The National Radio Astronomy Observatory is a facility of the National Science Foundation operated under cooperative agreement by Associated Universities, Inc. D.vdV. and J.H. acknowledge support of the VIDI research programme with project number 639.042.611, which is (partly) financed by the Netherlands Organisation for Scientific Research (NWO). H.S.B.A. acknowledges support from NAOJ ALMA Scientific Research Grant Code 2021-19A. S.J. is supported by the European Union’s Horizon Europe research and innovation program under the Marie Skłodowska-Curie grant agreement No. 101060888. This research made use of ASTROPY, a community developed core Python package for astronomy (Astropy Collaboration et al. 2013, 2018) hosted at <http://www.astropy.org/>, matplotlib (Hunter 2007), numpy (van der Walt et al. 2011), scipy (Jones et al. 2001), and of TOPCAT (Taylor 2005).

5 | ALMA confirms optically dark population at $z > 3$

Abstract

Using ALMA spectral scan observations covering 84–108 GHz, we report observations of 10 radio-selected star-forming galaxies at $z \gtrsim 3$ in the COSMOS field which are unseen in deep imaging from the ultraviolet to the near-infrared. With the addition of an archival and a recent additional ALMA observation for two of the sources, we securely detect CO emission lines in eight sources. For the other two sources, we find tentative line detections. The redshifts are unambiguously identified for six sources. The remaining four sources have two possible redshift solutions, and we use the $L'_{\text{CO}(5-4)}\text{-}L_{\text{IR}}$ correlation to identify the most likely redshift solution for each source. We find that the redshifts of the observed sources lie between $z = 3.1$ and $z = 5.0$, with a median redshift of $z = 3.95 \pm 0.62$. This confirms that the ‘optically dark’ sources targeted lie at $z \gtrsim 3$. We derive that the ‘optically dark’ sources contribute $5.42 \pm 0.41 \times 10^{-4} \text{ M}_{\odot} \text{ yr}^{-1} \text{ Mpc}^{-3}$ to the cosmic star formation rate density at $z \sim 4$ and show that it validates some previous estimates relying on photometric redshifts. This study confirms the cosmic importance of these sources at high ($z > 3$) redshift.

5.1 Introduction

For the last 20 years, our knowledge of galaxy evolution has been based mainly on ultraviolet (UV) selected galaxy populations such as, e.g., Lyman-break galaxies (LBGs; Steidel et al. 1996) observed with deep surveys with the Hubble Space Telescope (*HST*). The Lyman break selection is biased towards young star-forming galaxies (SFGs) with little dust attenuation, leading to a significant number of dusty SFGs at high redshift missed by rest-frame UV surveys (e.g., Wang et al. 2009; Franco et al. 2018; Smail et al. 2021). This means measurements of the cosmic star formation rate density (SFRD) well beyond the era of peak galaxy assembly ($1 \lesssim z \lesssim 3$) (e.g., Bouwens et al. 2020) are biased against galaxies with significant dust obscuration (e.g., Madau & Dickinson 2014).

The discovery of sub-millimeter galaxies (SMGs) (e.g., Downes et al. 1999; Smail et al. 1999; Frayer et al. 2004) highlighted the importance of a more complete census of the star formation history across cosmic time. Since these galaxies are heavily attenuated in the rest-frame UV (e.g., Simpson et al. 2014; Franco et al. 2018; Dudzevičiūtė et al. 2020), they are generally missed in LBGs studies. Via high angular resolution Atacama Large Millimeter/sub-millimeter Array (ALMA) observations, we can now uncover faint SMGs missed by UV/optical-surveys: also classified as ‘optically dark’ sources (e.g., Gruppioni et al. 2020; Gómez-Guijarro et al. 2022; Shu et al. 2022; Xiao et al. 2023). Different observational studies conducted with ALMA have reached varying conclusions about the relative contribution of ‘optically dark’ population to the cosmic SFRD. For example, Franco et al. (2018) found that $20\% \pm 10\%$ of the 1.1mm sources are not detected with *HST* down to a depth of $H \sim 28$ mag. However, Wang et al. (2019) and Gruppioni et al. (2020) determined that the contribution of their ‘dark’ samples ranged from, respectively, $10^{+2.3}_{-5.1}\%$ of the SFRD contributed by LBGs at similar redshifts, to almost equal ($48\% \pm 37\%$) to the total extinction-corrected contribution from all the known UV-selected galaxies at $z \sim 5$. Recently, observations of ‘optically dark’ sources have also been conducted with James Webb Space Telescope (*JWST*; Barrufet et al. 2023; Pérez-González et al. 2023), determining that these sources are mostly dusty star-forming galaxies and finding a similar contribution ($\sim 10\%$) to the SFRD as determined by Wang et al. (2019). Some of the discrepancy in the derived contributions to the SFRD may be due to the different methods of selecting the various optical/UV ‘dark’ samples.

Radio surveys are also powerful tools to help uncover the nature and contribution to the SFRD of ‘optically dark’ sources. Radio observations have been shown to identify ‘optically dark’ galaxies that contribute most significantly to the cosmic SFRD (Talia et al. 2021; Enia et al. 2022). Radio synchrotron emission provides a complementary way to trace star formation owing to its insensitivity to dust obscuration and strong correlation with far-infrared (FIR) emission and star formation rate (SFR) (FIR-radio correlation; e.g., Helou et al. 1985; Delvecchio et al. 2021) although it lacks the benefit of the negative K-correction in the FIR/sub-millimeter (sub-mm). In addition, radio observations offer high spatial resolution over larger areas than interferometric sub-mm observations. However, one of the major uncertainties in all of the above mentioned studies, including the radio-based studies, is the lack of reliable redshifts. For example, Talia et al. (2021) used the photometric redshift derived from

a stacked SED for 50% of their radio selected sample from the VLA-COSMOS 3 GHz Large Project (Smolčić et al. 2017a).

Recently, the COSMOS-XS survey has been carried out in the COSMOS field over an area of ~ 350 arcmin² at 3 GHz (van der Vlugt et al. 2021). Since the study by van der Vlugt et al. (2021), the COSMOS-XS pointing has been additionally observed with the VLA L-band (1.4 GHz; Algera et al. in prep.). The ultra-deep, multi-band COSMOS-XS survey has been matched with the extensive multi-wavelength data in the COSMOS field (Algera et al. 2020a), enabling improved constraints on the radio-derived SFRD (van der Vlugt et al. 2022). The multi-wavelength matching of the COSMOS-XS data has also revealed a population of radio-detected ‘optically dark’ sources. van der Vlugt et al. (2023) showed the contribution of the ‘optically dark’ galaxies to the radio SFRD to be $\sim 15_{-7}^{+7}\%$ at $z \sim 5$, and they improved on previous studies (e.g., Talia et al. 2021; Enia et al. 2022) by making use of the new Super-deblended FIR-derived redshifts for sources with high S/N_{FIR}. The FIR-based redshifts suggested that these sources all lie at $z > 2$. However, they still had a significant uncertainty due to the redshift–T_{dust} degeneracy (e.g., Pope & Chary 2010).

In this paper, we present ALMA follow-up observations of 10 $S_{1.1\text{mm}} > 3.5$ mJy ‘optically dark’ sources in the COSMOS-XS survey observed over the L-band area. Following van der Vlugt et al. (2023), the redshifts for these sources have been determined using the Super-deblending technique (Liu et al. 2018; Jin et al. 2019). With the follow-up observations, we are then able to use a blind line scanning technique with to derive their spectroscopic redshifts. Finally, we place constraints on the relative contribution of such ‘optically dark’ sources to the cosmic SFRD. Throughout this paper, the spectral index, α , is defined as $S_\nu \propto \nu^\alpha$, where S_ν is the source flux density, and ν is the observing frequency. We use a Λ CDM cosmology with parameters $H_0 = 70$ km s⁻¹Mpc⁻¹, $\Omega_m = 0.3$, $\Omega_\Lambda = 0.7$ (Bennett et al. 2013). We assume a radio spectral index of -0.7 unless otherwise stated. We assume the Chabrier (2003) initial mass function (IMF) to calculate SFRs.

5.2 Data and sample selection

5.2.1 Selection of dark sources

The sample consists of 10 ‘optically dark’ radio & sub-mm-bright sources, which were selected via three criteria: (1) covered by the primary beam (0.48 deg²) of the COSMOS-XS L-band image and detected in either COSMOS-XS or JVLA-COSMOS 3 GHz images (van der Vlugt et al. 2021; Smolčić et al. 2017a); (2) no counterpart is found in the COSMOS2020 catalog (Weaver et al. 2022); and (3) the 1mm flux, $S_{1.1\text{mm}} > 3.5$ mJy, using derived fluxes from FIR SED fitting in the Super-deblended catalog (Jin et al. 2018; Jin et al. in prep.). Of the 10 sources, two sources (ID: 600000037, 600000055) were only detected in the deep COSMOS-XS S-band image, while the remaining sources were also detected in the VLA-COSMOS 3GHz catalog (Smolčić et al. 2017a).

Following Dudzevičiūtė et al. (2020), $S_{1.1\text{mm}} = 3.5$ mJy corresponds to a 870 μm

Table 5.1. Properties of ALMA-targeted ‘optically dark’ sources.

ID	R.A.	Decl.	$S_{3\text{ GHz}}$ [mJy]	$z_{\text{FIR}}^{\text{a}}$
20003080/COSBO-7	10h00m23.96s	2d17m50.03s	28.6 ± 2.8	4.0 ± 0.35
20004275	9h59m35.36s	2d19m20.14s	22.3 ± 2.6	5.6 ± 0.85
20004337	9h59m21.43s	2d22m40.07s	28.4 ± 2.7	3.2 ± 0.4
20004728	10h01m35.67s	2d45m24.81s	20.4 ± 2.5	3.3 ± 0.95
20004824	9h59m01.96s	2d24m29.25s	19.9 ± 2.5	3.5 ± 0.5
20005887	9h58m53.63s	2d30m04.57s	25.0 ± 2.6	3.1 ± 0.8
20006212	10h00m54.49s	2d43m36.21s	16.2 ± 2.4	8.9 ± 2.6
20007237	10h00m00.39s	2d41m45.17s	14.7 ± 2.4	4.0 ± 1.3
60000037	10h00m05.24s	2d37m54.18s	15.3 ± 1.7	6.6 ± 2.65
60000055	10h00m24.04s	2d29m48.55s	6.4 ± 1.0	6.2 ± 2.4

Notes.

^a The new Super-deblended FIR-derived redshift and uncertainty based on SED fitting using the procedure from Liu et al. (2018) and Jin et al. (2018).

flux density of 6.3 mJy (adopting $S_{870\mu\text{m}}/S_{1.1\text{mm}} = 1.8$, equivalent to a $\nu \sim 2.5$ spectral index based on the average flux ratio of AS2UDS SMGs from Ikarashi et al. 2017). This is ~ 7 times higher than the flux range probed by Smail et al. (2021), who probed NIR-faint SMGs. All targeted sources have a FIR+mm combined detection with $S/N_{\text{FIR}} > 5$, calculated as described in Eq. 2 from Liu et al. (2018). The properties of the selected ‘optically dark’ sources can be found in Table 5.1. Fig. 5.1 shows the S-band radio observations with contours from the ALMA observations overlaid.

5.2.2 ALMA follow-up observations and data reduction

The ALMA Band-3 spectral scans of 10 ‘optically dark’ galaxies were performed at end of January and early March 2023 (project 2022.1.00863.S, PI: Hodge). The observations were centered on the positions with a spectral configuration using three frequency tunings to cover 84-108 GHz with resolution of 7.8 MHz. The spectral configuration is shown in Fig. 5.2 where also can be seen which lines can be detected with this setup. The three separate tunings cover the frequency range with 5 narrow gaps, indicated with the white horizontal lines in Fig. 5.2 and the gray shaded area in the spectra presented in Appendix 5.A. The observations were carried out with the array configuration C4 giving a synthesized beam of $1''$. The 10 galaxies were observed in track sharing mode, and each source was observed for 0.5 hr of on-source time in each tuning, reaching typical r.m.s. noise level of 0.12 mJy per 600 km s^{-1} .

The ALMA 3mm data are calibrated and reduced with CASA6.4 (McMullin et al. 2007). We converted the data into uvfits format to perform further analysis with the IRAM GILDAS tool working on the u-v space (visibility) data. The spectra are extracted by fitting models in the u-v space with fixed positions using point source

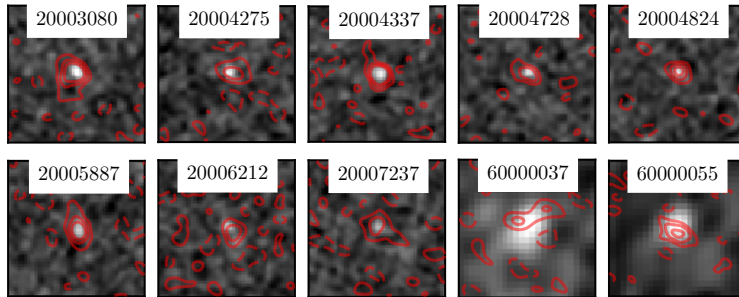


Figure 5.1: Radio images of ALMA-targeted ‘optically dark’ sources with ALMA contours overlaid. Images are $10'' \times 10''$, centered at the centroid of the new Super-deblended catalog entry (Jin et al. in prep.). The gray-scale images are the radio images the S-band VLA-COSMOS 3 GHz Large Project (Smolčić et al. 2017a) and the S-band COSMOS-XS VLA imaging, for 20003080, 20004275, 20004337, 20004728, 20004824, 20005887, 20006212, 20007237 and 60000037 and 60000055, respectively. The red solid contours are the ALMA line imaging for detected CO lines with contours starting at 2σ and increasing as 4σ and 6σ . Negative contours at the same significance are shown with red dashed lines. 2000612, 20007237, 60000037 and 60000055 do not show a significant line detection.

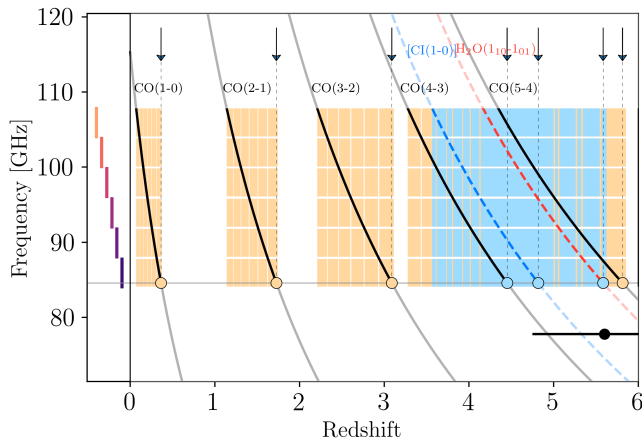


Figure 5.2: Graphic showing the full redshift space probed by the frequency coverage of the ALMA spectral scan observations covering 84-108 GHz. This figure was made using the method from Bakx & Dannerbauer (2022). Assuming the observed bandwidths, the filled regions show redshifts where single (orange) and multiple lines ([CI](1-0) in blue and H₂O(1₁₀-1₀₁) in red) would be detected for the observed source 20004275. The horizontal line marks the observed line at ~ 84.6 GHz, indicating the potential redshift solutions with circles and the top arrows. The black error bar marks the FIR redshift determined for 20004275, see also Table 5.1, using SED fitting.

models. Given that most sources are not detected in 3mm continuum maps, we adopted the radio positions from COMSOS-XS and Smolčić et al. (2017a) catalogs for extracting spectra. We searched iterative for evidence of resolved emission either in the continuum, in the emission-line candidates, and found that only the lensed source 20003080 is resolved and we calibrated for the total line flux using an $3''$ aperture. The spectra with the line detections indicated in green are shown in the figures presented in Appendix 5.A. For sources with two possible redshift solutions, we present the spectrum for each of the solution indicating the different line detections. The velocity averaged maps for the detected CO lines can be seen overlaid on the radio images in Fig. 5.1.

5.2.3 Multi-wavelength photometry

The multi-wavelength data used to estimate the 1.1mm flux for the 10 ‘optically dark’ sources are from the latest Super-deblended catalog (Jin et al. in prep.), which adopted the Super-deblending technique (Jin et al. 2018; Liu et al. 2018) by adding priors from the COSMOS-XS sources from the COSMOS-XS catalog (van der Vlugt et al. 2021) and the COSMOS2020 catalog (Weaver et al. 2022). The new Super-deblended catalog in COSMOS (Jin et al. in prep.) has deblended photometry in MIPS $24\mu\text{m}$, *Herschel*, SCUBA-2 $450\mu\text{m}$ & $850\mu\text{m}$ (Wang et al. 2017; Simpson et al. 2019), AzTEC (Aretxaga et al. 2011), MAMBO (Bertoldi et al. 2007), VLA 1.4 & 3 GHz and MeerKAT 1.28 GHz data sets (Schinnerer et al. 2007, 2010; Smolčić et al. 2017a; Jarvis et al. 2016). Fig. 5.3 shows the optical images from the ACS I-band, UltraVISTA K_S -band images and IRAC $3.6\mu\text{m}$ and $4.5\mu\text{m}$ images. All sources have been detected in MIPS, *Herschel*/PACS, at $250\mu\text{m}$, $350\mu\text{m}$ and $500\mu\text{m}$, SCUBA-2 and AzTEC. Two sources are also detected in SCUBA-2 at $450\mu\text{m}$. Additionally, three sources have counterparts in IRAC.

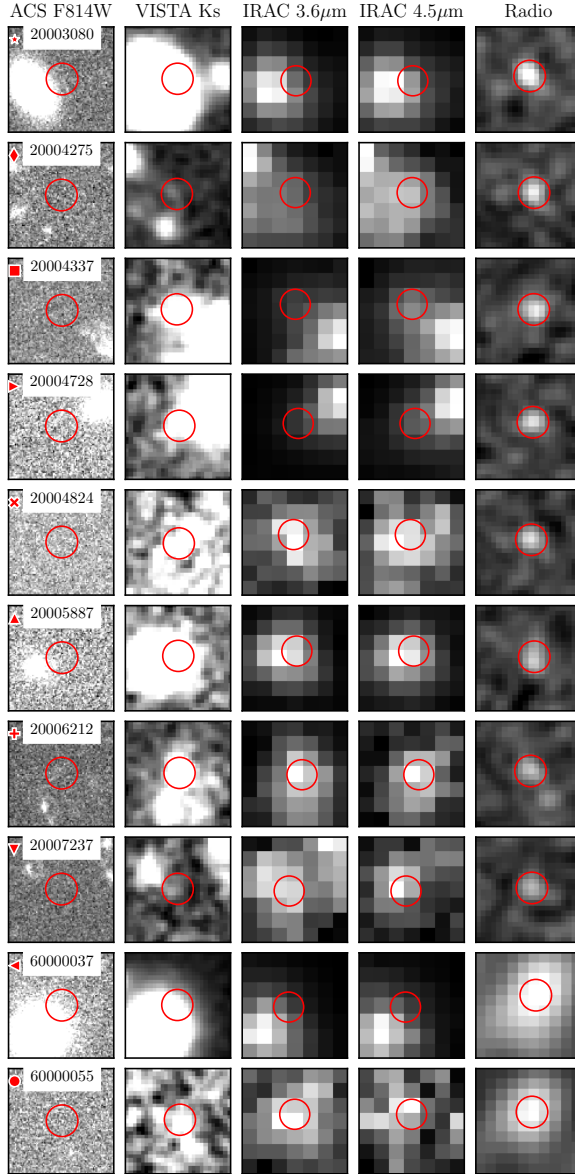


Figure 5.3: Postage-stamp images of 10 ‘optically dark’ galaxies targeted with ALMA. From left to right, the optical images from the ACS I-band, UltraVISTA K_S -band images and IRAC $3.6\mu\text{m}$ and $4.5\mu\text{m}$ images and the radio images from the S-band VLA-COSMOS 3 GHz Large Project (Smolčić et al. 2017a) and the S-band COSMOS-XS VLA imaging for 20003080, 20004275, 20004337, 20004728, 20004824, 20005887, 20006212, 20007237 and 60000037 and 60000055, respectively. Each panel has a size of $4'' \times 4''$, centered at the centroid of the new Super-deblended catalog entry (Jin et al. in prep.). The red circle marks the target galaxies with $0''.6$ in radius. The markers next to the source IDs are used throughout the paper to indicate the respective sources.

Table 5.2. Line detections.

ID	S/N _{1st} ^a	I_{1st} ^b [Jy km s ⁻¹]	S/N _{2nd} ^a	I_{2nd} ^b [Jy km s ⁻¹]
20003080	11.6 (CO(5-4))	1.43 ± 0.20
20004275	4.1 (CO(3-2))	0.68 ± 0.26
20004337	14.9 (CO(4-3))	1.86 ± 0.31
20004728	8.4 (CO(4-3))/ (CO(5-4))	0.45 ± 0.10	2.3 ([CI](1-0))	0.43 ± 0.24
20004824	6.3 (CO(4-3))	0.76 ± 0.18	3.6 ([CI](1-0))	0.38 ± 0.19
20005887	6.9 (CO(4-3))/ (CO(5-4))	0.98 ± 0.40	1.4 (H ₂ O(1 ₁₀ -1 ₀₁))	0.17 ± 0.20
20006212 ^c	4.6 (CO(5-4))	0.93 ± 0.40
20007237	2.9 (CO(4-3))/ (CO(5-4))	0.49 ± 0.18	2.6 ([CI](1-0))	0.46 ± 0.26
60000037	3.3 (CO(3-2))/ (CO(4-3))	0.33 ± 0.12	1.1 (H ₂ O(1 ₁₀ -1 ₀₁))	0.11 ± 0.15
60000055 ^d	4.0 (CO(5-4))	0.49 ± 0.18	1.4 ([CI](1-0))	0.12 ± 0.2

Notes.^a Signal-to-noise ratio of the 1st/2nd line.^b Flux density of the 1st/2nd line.^c This line is confirmed by a [CII] 158 μ m detection in ALMA archival data (ID: 2021.1.00280.L, PI: R. Herrera-Camus).^d This line is confirmed by the recent observations from Sillaseen et al. (in prep.).

5.3 Properties of the galaxies

5.3.1 Line identification

To search for emission line features in the observed ALMA 3mm blind line scans, we follow the technique described by Jin et al. (2019). We search for the single emission-line feature with the highest signal-to-noise ratio for each galaxy, following the same line-searching algorithm applied in Daddi et al. (2015), Coogan et al. (2018), and Puglisi et al. (2019). The found lines are then fitted with a Gaussian profile and the Gaussian fits are shown in the figures presented in Appendix 5.C. The flux of the lines is found by integrating over the full width at zero intensity (FWZI) range (e.g., Emonts et al. 2014; Coogan et al. 2018; Jin et al. 2019). The signal-to-noise ratio is given by the weighted mean of the channels over the FWZI range. The signal-to-noise ratio and flux density are given in Table 5.2.

After a detection of a line which we assume to be CO, we searched for additional matching lines: [CI](1-0) or H₂O(1₁₀-1₀₁). We know that the secondary lines are typically fainter than CO lines (e.g., Walter et al. 2011; Yang et al. 2019). We use the redshift solutions and velocity range as determined by the primary line. A tentative second line is detected for two sources with one redshift solution: 20004824 and 60000055. A tentative second line is detected for all sources with two redshift solutions: 20004728, 20005887, 20007237 and 60000037. The spectra with the line detections indicated in green are shown in the figures presented in Appendix 5.A. For

sources with two redshift solutions two spectra are given for both redshift solutions indicating all possible line detections.

In six sources we are able to determine the redshift unambiguously with the observed line transitions. The line detections are shortly summarized below and the spectra can be found in Appendix 5.A. First we will discuss 20003080/COSBO-7. The source was originally selected from the IRAM MAMBO 1.2mm survey by Bertoldi et al. (2007) and identified as a lensing system by (Jin et al. 2018), in which the high- z sub-mm galaxy is lensed by a foreground elliptical galaxy at $z_{\text{spec}} = 0.36$ by a factor of 3.6 (Jin et al. in prep.). In 20003080/COSBO-7 we observe a strong CO line at ~ 95.4 GHz. Since we do not detect [CI](1-0) at ~ 102 GHz, which is inconsistent with [CI](1-0)/CO(4-3) numbers in the literature (Bothwell et al. 2017; Jin et al. 2022), we are able to determine this is the CO(5-4) line and the source lies at $z = 5.042$. The ortho-H₂O(1₁₀-1₀₁) is not detected, because (1) it is on the edge of spectral window; and (2) this line is expected to be absorbed by the cosmic background at $z = 5$ from the models in Riechers et al. (2013). A detailed study of COSBO-7 with JWST data will be carried out by Jin et al. (in prep.). For 20004275, we detect just one line at the low end of the spectrum at ~ 84.6 GHz. The only line we are able to detect at this end of the spectrum which also matches the photometric redshift best is CO(3-2) as is shown in Fig. 5.2. The redshift of this source is thus determined to be $z = 3.087$. Similarly, for 20004337, we detect just one line at the high end of the spectrum at ~ 107.5 GHz. The only single line we are able to detect at this end of the spectrum is CO(4-3) and the redshift of this source is thus determined to be $z = 3.285$. One line detection and one tentative line detection with S/N = 3.6 are determined for 20004824 at ~ 93 GHz and ~ 99.5 GHz, respectively. The only two lines that can be observed this close are CO(4-3) and [CI](1-0). The redshift of this source is thus determined to be $z = 3.955$. In 20006212 we detect one line close to the gap in the frequency coverage. However, we are able to determine the redshift to be $z = 4.539$ since it has [CII] 158 μ m detection in ALMA archival data (ID: 2021.1.00280.L, PI: R. Herrera-Camus). The detected line thus corresponds to CO(5-4). For 60000055 we are able to, with the addition of the recent observations from Sillaseen et al. in prep., detect a line at ~ 99 GHz. With the tentative detection of [CI](1-0) at ~ 84.5 GHz, we are able to determine the redshift for 60000055 at $z = 4.820$.

For four sources with line transitions, we find two redshift solutions. In 20004728 we find a tentative line with S/N = 2.3 close to the gap in the frequency coverage at ~ 88 GHz. In addition, we detect a significant line at ~ 103 GHz. Because the line close to the frequency gap is only a tentative detection, the line detected at ~ 103 GHz can be CO(4-3) or CO(5-4). The redshift for 20004728 can thus be either $z = 3.485$ or $z = 4.606$. For 20005887, we find one CO line at ~ 93.5 GHz. In addition, we find one tentative line with S/N = 1.4 at ~ 91.5 GHz which could be H₂O(1₁₀-1₀₁) if the CO transition corresponds to CO(5-4). The [CI](1-0) line that would be observed if the CO transition corresponds to CO(4-3) lies close to the frequency gap at ~ 93 GHz and can thus not be detected. Because of the frequency gap and the tentative line detection, we can not find a single redshift solution. The redshift for 20005887 can thus be either $z = 3.934$ or $z = 5.167$. For 20007237, we find one tentative CO line with S/N = 2.9 at ~ 98 GHz. The [CI](1-0) line that would be observed if the CO transition corresponds to CO(5-4) lies close to the low end of the frequency range at

~ 84 GHz and can thus not be detected. In addition, we find one tentative line at ~ 104.5 GHz with $S/N = 2.6$ which could be [CI](1-0) if the CO transition corresponds to CO(4-3). Because of the frequency range and the tentative line detection, we can not find one redshift solution. The redshift solutions for 20007237 that also match the photometric redshift ($z_{\text{FIR}} = 4.0 \pm 1.3$) can be either $z = 3.7$ if the tentative CO transition corresponds to CO(4-3) or $z = 4.868$ if the tentative CO transition corresponds to CO(5-4). Lastly, for 60000037, we do not detect any significant CO line, the signal-to-noise ratio of the line at ~ 86.8 GHz is $S/N = 3.3$. In addition, we can find one tentative line with $S/N = 1.1$ at ~ 105 GHz if the CO transition corresponds to CO(4-3) which could be H₂O(1₁₀-1₀₁). We therefore have two redshift solutions with $z = 2.08$ and $z = 4.3$.

The sky density of the 8 ALMA-confirmed ‘optically dark’ sources with $S_{1.1\text{mm}} > 3.5$ mJy and a line detection is $16.7 \pm 5.9 \text{ deg}^{-2}$. As expected this sky density is lower than the potential surface density found by Smail et al. (2021) of $450^{+750}_{-300} \text{ deg}^{-2}$ for NIR-faint SMGs with $S_{870\mu\text{m}} \geq 1$ mJy which is equivalent to $S_{1\text{mm}} \geq 0.56$ mJy. Smail et al. (2021) thus probe a flux range ~ 7 times lower than the range probed by this study as discussed in Section 5.2.1. Three sources from the sub-sample discussed by Smail et al. (2021) have $S_{870\mu\text{m}} \geq 6.3$ mJy in the AS2UDS catalog (Stach et al. 2019) and would thus be selected from the 0.96 deg^2 field with the flux cut of $S_{1.1\text{mm}} > 3.5$ mJy. This gives a sky density of $3.125 \pm 1.8 \text{ deg}^{-2}$, significantly below the sky density found in this study. Similarly, our sky density is also significantly lower than the ALMA-selected H -dropout surface density corrected for incompleteness of 530 deg^{-2} (Wang et al. 2019) with $S_{870\mu\text{m}} \geq 0.6$ mJy which is equivalent to $S_{1\text{mm}} \geq 0.33$ mJy.

5.3.2 Redshifts

For the 10 sources in the sample, the median redshift, including the low- z solutions for the sources with two redshift solutions, is $z = 3.82$, with a 16-84th percentile range of $z = (3.2 - 4.7)$. The median redshift, including the high redshift for the sources with two redshift solutions, is $z = 4.57$, with a 16-84th percentile range of $z = (3.6 - 5.0)$. 7/10 sources agree with their found spectroscopic redshift to their estimated FIR photometric redshift within $< 2\sigma$. Hence the spectroscopic redshifts confirm that all of the ‘optically dark’ sources targeted are at $z \gtrsim 3$ as suggested by their estimated FIR photometric redshifts. The estimated redshifts are presented in Table 5.3. The comparison between the FIR-based photometric redshifts and the redshifts derived using ALMA 3mm line scans are shown in Fig. 5.4.

5.3.3 SED fitting

We collected the new Super-deblended FIR/(sub-)millimeter photometry together with the ALMA 3mm continuum measurements and redshifts as determined above to fit the full SEDs. For the four sources for which we find two redshift solutions, we fit for both of the solutions. In the SED fitting four distinct SED components are used: (1) a stellar component (Bruzual & Charlot 2003) with a Small Magellanic Cloud dust attenuation law (indicated in blue); (2) a mid-infrared AGN torus component (Mul-

Table 5.3. Derived properties of ‘optically dark’ sources.

ID	$z_{\text{ALMA}}^{\text{a}}$	SFR_{FIR} [$M_{\odot} \text{ yr}^{-1}$]	L_{IR} [$10^{12} L_{\odot}$]
20003080 ^b	5.041	220.2 ± 64.4	2.2 ± 0.6
20004275	3.087	412.2 ± 3.6	4.1 ± 0.04
20004337	3.285	701.7 ± 4.3	7.0 ± 0.04
20004728	3.485 /4.606	579.6 \pm 58.5 /1187.8 \pm 62.4	5.8 \pm 0.6 /11.9 \pm 0.6
20004824	3.955	789.3 ± 175.6	7.9 ± 1.8
20005887	3.943 /5.167	804.2 \pm 159.1 /1583.0 \pm 52.2	8.0 \pm 1.6 /15.8 \pm 0.5
20006212	4.539	617.9 ± 318.7	6.2 ± 3.2
20007237	3.7 /4.868	481.9 \pm 4.5 /995.4 \pm 145.1	4.8 \pm 0.04 /10.0 \pm 1.5
60000037	2.98/ 4.3	253.2 ± 2.0 / 487.4 \pm 87.1	2.5 ± 0.02 / 4.9 \pm 0.9
60000055	4.82	358.4 ± 6.0	3.6 ± 0.06

Notes.

^a The ‘best’ redshift solutions for sources with two redshift solutions as determined in Section 5.3.4 are indicated in bold.

^b 20003080 is lensed by a factor of 3.6 (Jin et al. in prep.), therefore the physical parameters noted here are divided by 3.6.

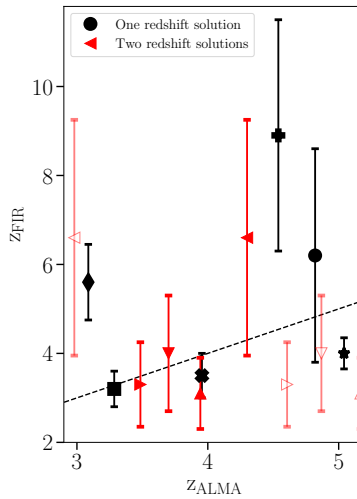


Figure 5.4: Comparison between the FIR-based photometric redshifts from the new Super-deblended catalog (Jin et al. in prep.) and the redshifts derived using ALMA 3mm line scans. Black and red symbols indicate sources with one and two redshift solutions, respectively. The markers refer to individual sources as shown in Fig. 5.3. Closed red symbols indicate the ‘best’ redshift solutions for sources with two redshift solutions as determined in Section 5.3.4.

laney et al. 2011, indicated in red); (3) dust continuum emission (indicated in green) from the Magdis et al. (2012) library with the more updated $L_{\text{IR}}/M_{\text{dust}}$ -redshift evolution taken from Béthermin et al. (2015); and (4) a power-law radio continuum with an evolving radio-FIR correlation (q_{TIR}). Extra details on the SED fitting procedure can be found in Liu et al. (2018) and Jin et al. (2018). The results for the fitted SEDs for the 10 sources can be found in Appendix 5.B.

5.3.4 Far-infrared luminosity

Using the derived SEDs, the IR luminosities (L_{IR}) are taken as the pure dust component L_{IR} over 8–1000 μm , excluding any AGN torus components. For the sample, the median FIR luminosity, including the low redshift solutions for the sources with two redshift solutions, is $L_{\text{IR}} = (5.3 \pm 0.3) \times 10^{12} L_{\odot}$, with a 16-84th percentile range of $L_{\text{IR}} = (3.8 - 7.9) \times 10^{12} L_{\odot}$. The median FIR luminosity, including the high redshift solutions for the sources with two redshift solutions, is $L_{\text{IR}} = (6.6 \pm 0.6) \times 10^{12} L_{\odot}$, with a 16-84th percentile range of $L_{\text{IR}} = (4.5 - 11.0) \times 10^{12} L_{\odot}$. 8 sources from the sample are classified as ULIRGs with $L_{\text{IR}} = 1 - 10 \times 10^{12} L_{\odot}$. None of the sources are LIRGs with $L_{\text{IR}} < 1 \times 10^{12} L_{\odot}$ and 2 sources can be determined to be HyLIRGs with $L_{\text{IR}} > 1 \times 10^{13} L_{\odot}$ assuming their highest redshift solution lying at $z \sim 4.6$ and $z \sim 5.2$. Local ULIRGs have considerably lower FIR luminosities as derived by Dudzevičiūtė et al. (2020) for the GAMA local ULIRG sample (Driver et al. 2018) with a median of $L_{\text{IR}} = (1.41 \pm 0.03) \times 10^{12} L_{\odot}$ and a 16-84th percentile range of $L_{\text{IR}} = (1.1 - 2.4) \times 10^{12} L_{\odot}$. We can thus conclude that the observed sample is comparable to SMGs as they have some FIR luminosities higher or similar to local ULIRGs. In addition, we find that the redshifts of these sources form the high-redshift tail as all observed sources have a redshift $z \gtrsim 3$ (Simpson et al. 2014). The FIR luminosities determined for the sample are somewhat higher than the median FIR luminosity of the 1.1mm selected SMG sample from Miettinen et al. (2017), who derive a median of $L_{\text{IR}} = (4.0 \pm 0.3) \times 10^{12} L_{\odot}$ for a sample with an flux density range of 0.83-11.1 mJy which is close to the selection criterion of $S_{1.1\text{mm}} > 3.5$ mJy. The median FIR luminosity determined in this study is also higher compared to the FIR luminosities Dudzevičiūtė et al. (2020) derived for their sample of 707 SMGs with flux densities in the range $S_{870\mu\text{m}} = 0.6 - 13.6$ mJy. They find a median FIR luminosity of $L_{\text{IR}} = (2.88 \pm 0.09) \times 10^{12} L_{\odot}$.

Correlation between $L'_{\text{CO}(5-4)}$ and L_{IR}

The CO(5-4) transition is believed to be a good tracer of the star-forming gas, resulting in an almost linear $L'_{\text{CO}(5-4)}$ - L_{IR} correlation. Daddi et al. (2015) find that this linear correlation between $L_{\text{CO}(5-4)}$ and L_{IR} can be described by $\log L'_{\text{CO}(5-4)} = \log L_{\text{IR}}/L_{\odot} - 2.52$ with a dispersion of 0.24 dex, which is remarkable for a relation spanning 4 orders of magnitude along either axes. In addition, it holds for normal and starburst galaxies both locally and at high redshift. It is thus interesting to verify where the sources that have a detected CO(5-4) line lie on the $L'_{\text{CO}(5-4)}$ and L_{IR} plane. In addition, we can use this relation to check whether the CO transitions detected in 20004728, 20005887, 20007237 and 60000037 correspond to CO(5-4), CO(4-3) or

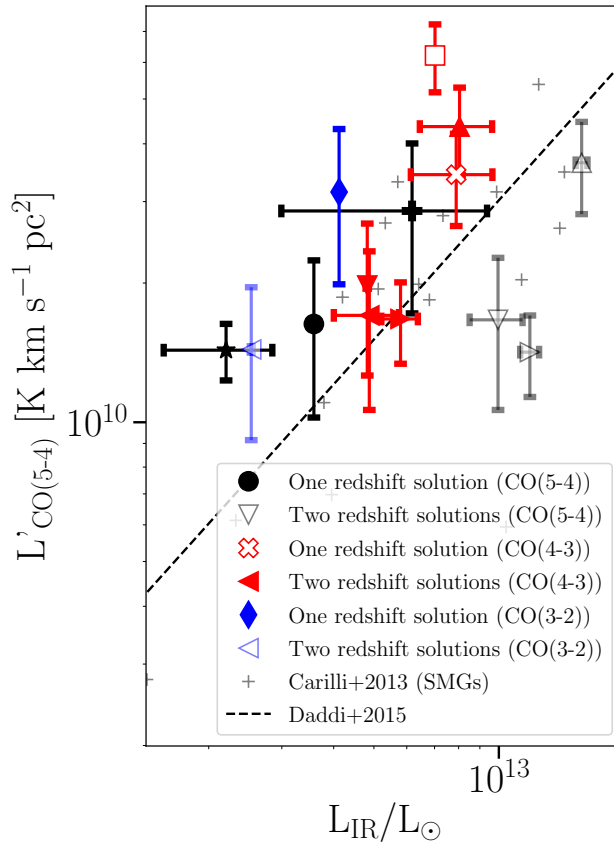


Figure 5.5: The CO(5-4) line luminosity versus the IR luminosity. All sources with a detected CO(5-4) line are indicated with black closed symbols. Sources with a possible CO(5-4) line detection are indicated with black open symbols. The sources with an extrapolated CO(5-4) line luminosity from the measured CO(4-3) line luminosity are indicated with the red closed and open symbols; the open symbols indicate an detected CO(4-3) line and the closed symbols indicate a possible CO(4-3) line detection. The sources with an extrapolated CO(5-4) line luminosity from the measured CO(3-2) line luminosity are indicated with blue symbols; the open symbol for the source with a possible CO(3-2) line detection and the closed symbol for the source with an detected CO(3-2) line detection. The markers refer to individual sources as shown in Fig. 5.3. The dotted line gives the correlation between the CO(5-4) line luminosity with the IR luminosity from Daddi et al. (2015). Crosses indicate literature SMGs from Carilli & Walter (2013).

CO(3-2). When the calculated luminosities ($L'_{\text{CO}(5-4)}$) lie on the linear correlation, they are likely to originate from the CO(5-4) transition.

To obtain the integrated line flux $S_{\text{CO}(5-4)}$, we fit the lines indicated in green in the 1D spectrum, shown in the figures presented in Appendix 5.A, with a Gaussian profile and integrate over the FWZI range. The fitting results can be found in Appendix 5.C. From the line flux we can then determine the luminosity as defined in Solomon et al. (1992):

$$L'_{\text{CO}(5-4)} = 3.25 \times 10^7 \frac{S_{\text{CO}(5-4)} D_L^2}{(1+z)^3 \nu_{\text{obs}}^2}, \quad (5.1)$$

where the CO line luminosity, $L'_{\text{CO}(5-4)}$, is measured in $\text{K km s}^{-1} \text{pc}^2$; $S_{\text{CO}(5-4)}$ is the CO integrated flux density in units of Jy km s^{-1} , D_L to the luminosity distance at redshift z , in Mpc, and ν_{obs} is the observing frequency in GHz. Fig. 5.5 shows the correlation of the CO(5-4) line luminosity with the IR luminosity of all the sources with a detected CO(5-4) line (20003080, 20006212 and 60000055) and the sources with a possible CO(5-4) line detection (20004728, 20005887 and 20007237) together with the best-fitting relations from Daddi et al. (2015). In addition, we compare the sources to $L'_{\text{CO}(5-4)}\text{-}L_{\text{IR}}$ of SMGs taken from the compilation of Carilli & Walter (2013). In addition, Fig. 5.5 shows the correlation of the CO(5-4) line luminosity with the IR luminosity of all the sources with a detected CO(4-3) line (20004337 and 20004824) and the sources with a possible CO(4-3) line detection (20004728, 20005887, 20007237 and 60000037). The CO(5-4) luminosities shown in Fig. 5.5 for these sources are extrapolated as $1.67 \times L'_{\text{CO}(4-3)}$ (assuming $r_{54/10} = 0.7$ and $r_{43/10} = 0.6$; Stanley et al. 2023). Fig. 5.5 also shows the correlation of the CO(5-4) line luminosity with the IR luminosity of the source with a detected CO(3-2) line (20004275) and the source with a possible CO(3-2) line detection (60000037). The CO(5-4) luminosities shown in Fig. 5.5 for these sources are extrapolated as $1.0 \times L'_{\text{CO}(3-2)}$ (assuming $r_{54/10} = 0.7$ and $r_{32/10} = 0.7$; Stanley et al. 2023).

We find all sources fall within the range expected for SMGs. First we will discuss the six sources with a confirmed redshift. We have to note that the line for 20006212 is detected close to the gap in the frequency coverage. Therefore, we only measure about half of the line luminosity and have to extrapolate beyond the gap. This source and 60000055 lie within 0.9σ of the $L'_{\text{CO}(5-4)}\text{-}L_{\text{IR}}$ correlation from Daddi et al. (2015) whereas 20003080 lies within 3.9σ . For the two sources with an extrapolated $L'_{\text{CO}(4-3)}$, 20004337 and 20004824, we find they lie within 4.0σ and 1.3σ , respectively.

For the source with an extrapolated $L'_{\text{CO}(3-2)}$ (20004275) we find it lies within 1.6σ . Next, we will discuss the four sources with two redshift solutions. For 20004728, 20005887 and 20007237 we find they lie within, respectively, 7.5σ , 1.4σ and 2.2σ of the correlation assuming a CO(5-4) line. They lie within, respectively, 0.2σ , 2.0σ and 0.7σ assuming a CO(4-3) line. For 60000037 we find it lies within 0.4σ and 1.3σ assuming a CO(4-3) line and a CO(3-2) line, respectively.

From this analysis, we find that 20004728, 20007237 and 60000037 are most likely to have a CO(4-3) detection implying that these sources would lie at, respectively, $z = 3.5$, $z = 3.7$ and $z = 4.3$. This is also in line with the redshifts derived from SED-fitting shown in Fig. 5.4. For 20005887, the difference between assuming a CO(5-4) line and assuming a CO(4-3) line is only 0.6σ . Since the redshift derived from SED-

fitting ($z_{\text{FIR}} = 3.1 \pm 0.8$) lies closest to the redshift found when assuming the detected line corresponds to CO(4-3) ($z_{\text{ALMA}} = 3.9$), we find that this sources is most likely to have a CO(4-3) detection. We thus determine a ‘best’ redshift for each source, which is indicated in bold in Table 5.3. Assuming these redshifts, the median redshift of the 10 sources is then $z = 3.95 \pm 0.62$, with a 16-84th percentile range of $z = (3.4 - 4.7)$. The median L_{IR} assuming these redshifts is $L_{\text{IR}} = (5.3 \pm 0.6) \times 10^{12} L_{\odot}$, with a 16-84th percentile range of $L_{\text{IR}} = (3.8 - 7.5) \times 10^{12} L_{\odot}$. In the following sections and figures, we will continue to show both solutions since the above test only indicates which redshift would be ‘better’ but does not constrain the redshift with certainty.

5.3.5 Star formation rates

The IR luminosity traces dust-obscured star formation, assuming a Chabrier IMF (Chabrier 2003) and the relation $\text{SFR} = L_{\text{IR}} / (1 \times 10^{10} L_{\odot}) M_{\odot} \text{yr}^{-1}$ (Daddi et al. 2010) we determine a median SFR, including the low redshift solutions for the sources with two redshift solutions, of $\text{SFR} = 530.8 \pm 32.2 M_{\odot} \text{yr}^{-1}$ with a 16-84th percentile range of $\text{SFR} = 299.5 - 750.8 M_{\odot} \text{yr}^{-1}$. The median SFR, including the high redshift solutions for the sources with two redshift solutions, is $\text{SFR} = 659.8 \pm 63.4 M_{\odot} \text{yr}^{-1}$ with a 16-84th percentile range of $\text{SFR} = 382.1 - 1103.1 M_{\odot} \text{yr}^{-1}$. The estimated SFRs are presented in Table 5.3. Assuming the ‘best’ redshifts, as determined in Section 5.3.4, we find a median SFR of $\text{SFR} = 533.5 \pm 61.5 M_{\odot} \text{yr}^{-1}$ with a 16-84th percentile range of $\text{SFR} = 382.1 - 750.8 M_{\odot} \text{yr}^{-1}$.

Since we also have radio detections for all of the observed sources, we are able to compare the SFR calculated from the IR luminosity to the SFR that can be derived from the radio luminosity. Rest-frame 1.4 GHz luminosities are determined using the measured spectral index for the required K-corrections if available. When only a single radio flux is available, a spectral index of $\alpha = -0.7$ is assumed instead. The luminosities are then calculated through

$$L_{1.4 \text{ GHz}} = \frac{4\pi D_L^2}{(1+z)^{1+\alpha}} S_{1.4 \text{ GHz}}. \quad (5.2)$$

Here D_L is the luminosity distance to redshift z and $S_{1.4 \text{ GHz}}$ is the observed flux density at 1.4 GHz. Having the rest-frame 1.4 GHz luminosities, we are now able to estimate the SFRs from radio luminosities. To convert luminosity into a SFR, we follow van der Vlugt et al. (2022):

$$\text{SFR}(L_{1.4 \text{ GHz}}) = f_{\text{IMF}} 10^{-24} 10^{q_{\text{TIR}}(z)} L_{1.4 \text{ GHz}}, \quad (5.3)$$

where SFR is the SFR in units of $M_{\odot} \text{yr}^{-1}$, f_{IMF} is a factor accounting for the IMF ($f_{\text{IMF}} = 1$ for a Chabrier IMF and $f_{\text{IMF}} = 1.7$ for a Salpeter IMF) and $L_{1.4 \text{ GHz}}$ is the rest-frame 1.4 GHz luminosity in units of W Hz^{-1} . For q_{TIR} we use the radio-FIR correlation found by Delvecchio et al. (2021):

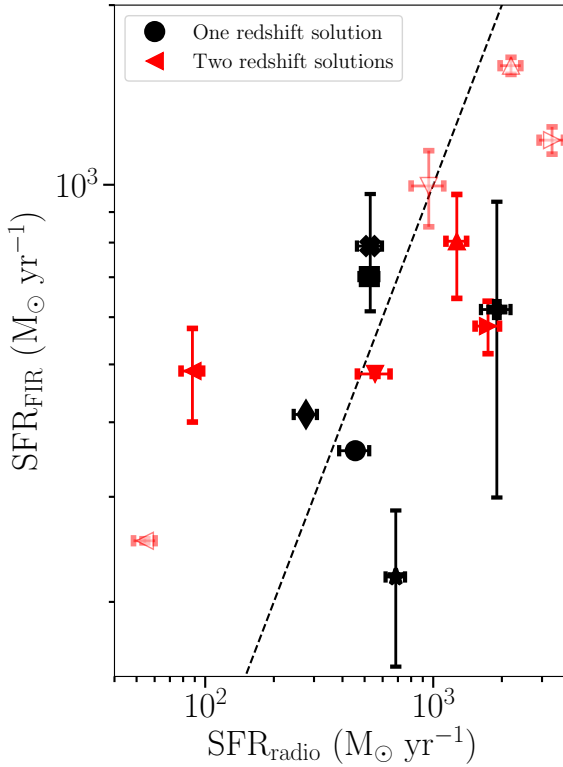


Figure 5.6: Comparison between the star formation rate determined from the infrared luminosity derived by SED fitting and the star formation rate derived from radio luminosity. The dotted line describes the one-to-one relation. Black and red symbols indicate sources with, respectively, one and two redshift solutions. The markers refer to individual sources as shown in Fig. 5.3. Closed red symbols indicate the ‘best’ redshift solutions for sources with two redshift solutions as determined in Section 5.3.4.

$$q_{\text{TIR}}(M_*, z) = 2.646 \times (1 + z)^{-0.023} - 0.148 \times \left(\log_{10} \frac{M_*}{M_\odot} - 10 \right). \quad (5.4)$$

For the mass (M_*), we assume the same mass for every source of $M_* = 2.8 \times 10^{10} M_\odot$ which was the mass for ‘optically dark’/faint galaxies derived by Xiao et al. (2023) from SED fitting with median stacked photometry.

For two sources we find their radio SFR is ~ 3 times higher than what was expected based on the FIR luminosity: 20003080 and 20006212. 20004728 also has a high radio SFR for both redshift solutions, the radio SFR is 3.0 times and 2.8 times higher

than what was expected based on the FIR luminosity. This is likely due to AGN contamination which increases the radio luminosity. Accreting supermassive black holes (SMBHs) in AGN can also accelerate the electrons that produce synchrotron emission. This AGN contribution would also result in a strong deviation from the FIR-radio correlation expected for star-forming sources. This will be discussed in the next section. We do find one outlier located far above the one-to-one line in both redshift solutions at the low end of radio SFR: 60000037. This is a source for which we did not measure a significant line. This shows that the inferred FIR luminosity might be overestimated in the current SED-fit based on the current redshift solutions. It also shows the importance of having spectroscopic redshifts for SED-fitting.

5.3.6 Radio-FIR correlation

Attempts have been made to study the radio-FIR correlation in high- z SMGs at $z > 3$ (e.g., Miettinen et al. 2017; Algera et al. 2020b). These studies found that these sources generally lie significantly below the canonical q_{TIR} ratio of local normal SFGs. Miettinen et al. (2017) studied the physical properties of 16 SMGs in the redshift range of $z = 1.6 - 5.3$ in the COSMOS field. They found a median of $q_{\text{TIR}} = 2.27^{+0.27}_{-0.13}$, shown as the green shaded region in Fig. 5.7, using the radio luminosity derived from 325 MHz and the IR luminosity derived with MAGPHYS. A similar value was found by Algera et al. (2020b). They measured the q_{TIR} of 273 SMGs with 1.4 GHz detections, and found a median $q_{\text{TIR}} = 2.20 \pm 0.03$ independent of redshift, shown as the blue shaded region in Fig. 5.7. We find that the measured q_{TIR} values are broadly in line with Miettinen et al. (2017) and Algera et al. (2020b). Assuming the ‘best’ redshifts, we find a median q_{TIR} of $q_{\text{TIR}} = 2.41 \pm 0.08$ with a 16-84th percentile range of $q_{\text{TIR}} = 2.01 - 2.67$. The q_{TIR} values fall generally close and below the values found for local, typically less strongly star-forming galaxies with an average $q_{\text{TIR}} = 2.64 \pm 0.02$ (Bell 2003) and local ULIRGs with an average $q_{\text{TIR}} = 2.7 \pm 0.06$ (Farrah et al. 2003), indicated with the dashed line in Fig. 5.7. We do find one outlier located far above the q_{TIR} found by Farrah et al. (2003) in both redshift solutions: 60000037. This is a source for which we did not detect a significant line. Since such values are unexpected for SMGs and rare for high redshift radio selected sources (Delvecchio et al. 2021), this shows that the inferred FIR luminosity and following from that q_{TIR} might be overestimated in the current SED-fit. 20003080, 20006212 and 20004728 can be found at the low end of the radio-FIR correlation as we expected based on their radio SFR. However we do not find a significant deviation from the q_{TIR} found by Algera et al. (2020b). If AGN contamination is the cause of the deviation, it is only a small contribution as expected for SMGs. In conclusion, both IR and radio can be used to trace the SFR for dust-obscured star formation. In addition, the q_{TIR} found for these sources are below the local correlation for both normal star-forming galaxies and local ULIRGs.

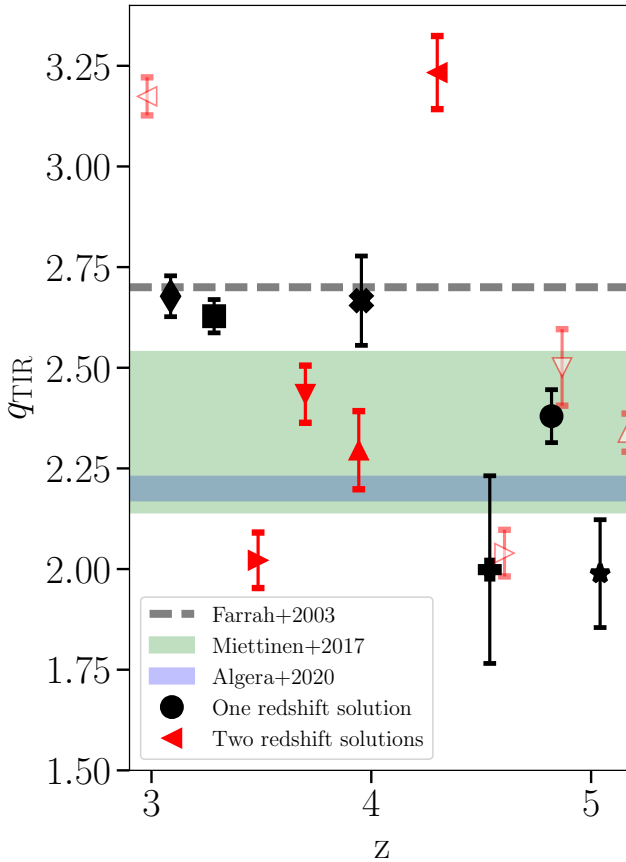


Figure 5.7: The q_{TIR} values for the 10 ‘optically dark’ sources compared to the q_{TIR} for 16 SMGs in the COSMOS field (Miettinen et al. 2017), a sample of radio-detected SMGs from the AS2UDS survey (Algera et al. 2020b) and local ULIRGs (Farrah et al. 2003). Black and red symbols indicate sources with, respectively, one and two redshift solutions. The markers refer to individual sources as shown in Fig. 5.3. Closed red symbols indicate the ‘best’ redshift solutions for sources with two redshift solutions as determined in Section 5.3.4.

5.4 Contribution to the cosmic star formation rate density history

The SFRD is the star formation in galaxies over a given co-moving volume. To estimate the contribution and importance of the $S_{1.1\text{mm}} > 3.5$ mJy selected ‘optically dark’ sources, we calculate their SFRD and compare it to literature data. As the ‘optically dark’ sources were discovered within a radio survey area, we can simply calculate their SFRD by using their total SFR divided by the survey volume. We will use the SFR estimated from the FIR based SED. Since this SFR estimate is derived from a dust component excluding AGN torus components in contrast to the radio SFR which might be contaminated by some contribution from the AGN as discussed in Section 5.3.5. In addition, the FIR-derived SFR should be a good estimate of the total SFR as we expect a low SFR_{UV} contribution. Franco et al. (2020) found the SFR_{UV} contributes only 1% to the total SFR in the 35 galaxies detected at 1mm in the GOODS-ALMA field.

To calculate the SFRD, we need the survey volume. This is the volume between the shells defined by the redshift range of the sources, within a solid angle:

$$\begin{aligned}
 V &= \frac{\Omega}{4\pi} (V_{z_1} - V_{z_0}); \\
 &= \frac{\Omega}{4\pi} \left[\frac{4\pi}{3} (d_{z_1}^3 - d_{z_0}^3) \right]; \\
 &= \frac{\Omega}{3} [(d_{z_1}^3 - d_{z_0}^3)], \tag{5.5}
 \end{aligned}$$

where the solid angle Ω corresponds to the effective area of the L-band observations: 0.48 deg^2 , in units of steradian 1.45×10^{-4} sr; and d_{z_0} and d_{z_1} correspond to the co-moving distances at given redshifts of z_0 and z_1 (Shu et al. 2022; Xiao et al. 2023). Since the sample size is limited, we consider a single redshift bin with a broad redshift range in which all detected sources are included.

The cosmic SFRD for the total sample is:

$$\text{SFRD} = \frac{\sum_i \text{SFR}_i}{V}, \tag{5.6}$$

where the SFR_i is the FIR-based SFR given for each galaxy. The SFRD of the 10 sources, assuming the highest redshift for sources with two redshift solutions, reaches approximately $6.92 \pm 0.39 \times 10^{-4} \text{ M}_\odot \text{ yr}^{-1} \text{ Mpc}^{-3}$ with the mean redshift of $z_{\text{mean}} = 4.37$ (and $z_{\text{median}} = 4.57$). The SFRD of the 10 sources, assuming the lowest redshift for sources with two redshift solutions, reaches approximately $3.90 \pm 0.38 \times 10^{-4} \text{ M}_\odot \text{ yr}^{-1} \text{ Mpc}^{-3}$ with the mean redshift of $z_{\text{mean}} = 3.88$ (and $z_{\text{median}} = 3.82$). The SFRD of the 10 sources, assuming the ‘best’ redshift for sources with two redshift solutions, reaches approximately $5.42 \pm 0.41 \times 10^{-4} \text{ M}_\odot \text{ yr}^{-1} \text{ Mpc}^{-3}$ with the mean redshift of $z_{\text{mean}} = 4.02$ (and $z_{\text{median}} = 3.95$).

Fig. 5.8 shows the SFRD derived from $S_{1.1\text{mm}} > 3.5$ mJy selected ‘optically dark’ sources. In addition, Fig. 5.8(a) shows a variety of observational studies (Wang et al.

2019; Dudzevičiūtė et al. 2020; Gruppioni et al. 2020; Talia et al. 2021; Enia et al. 2022; Shu et al. 2022; Barrufet et al. 2023; Xiao et al. 2023) determining the contribution of ‘optically dark’ sources. The observations span a wide range of SFRD values over an order of magnitude at $3 \lesssim z \lesssim 6$. A further discussion on the differences of these studies can be found in van der Vlugt et al. (2023). Assuming the ‘best’ redshifts for sources with two redshift solutions, we find that the $S_{1.1\text{mm}} > 3.5$ mJy selected ‘optically dark’ sources make up $\sim 1.7\%$ of the SFRD derived by Madau & Dickinson (2014) at $z = 3.95$.

Due to our flux cut, only sources with $S_{1.1\text{mm}} > 3.5$ mJy have been selected. The found SFRD is thus lower than the SFRD derived by Dudzevičiūtė et al. (2020) using a complete dust-mass-selected sample of SMGs with a flux cut of $S_{870\mu\text{m}} \geq 3.6$ mJy. They find a ~ 4 times higher SFRD of $2.33^{+0.70}_{-0.68} \times 10^{-3} M_{\odot}\text{yr}^{-1}\text{Mpc}^{-3}$ at $z = 3.95$ using the MAGPHYS estimated redshift for 94% of their sample. We can make an estimate of the Dudzevičiūtė et al. (2020) SFRD with a flux cut of $S_{1.1\text{mm}} \geq 3.5$ mJy by scaling down the SFRD using the differential counts at $850\mu\text{m}$ from Geach et al. (2017). We note that this is a crude approximation as there is a relation between redshift and flux density found by Stach et al. (2019) using AS2UDS survey. The found SFRD at $z = 3.95$ is slightly higher than the SFRD found for the $S_{1.1\text{mm}} > 3.5$ mJy selected ‘optically dark’ sources, indicating that the 10 ‘optically dark’ sources are likely to be similar to the SMGs observed by Dudzevičiūtė et al. (2020). This is also in line with the conclusions from Dudzevičiūtė et al. (2020) as they find that $\sim 17\%$ of their sample is ‘optically dark’ since they are undetected at $K \gtrsim 25.7$ mag.

As our estimate is only a lower limit to the total contribution of ‘optically dark’ sources, we also find a much lower contribution than the previous estimate of the contribution of ‘optically dark’ sources selected from radio observations by van der Vlugt et al. (2023) from the COSMOS-XS survey using the (largely) FIR-based photometric redshifts. To determine the van der Vlugt et al. (2023) SFRD using a similar flux cut as used here, we determine the radio luminosity which corresponds to $S_{1.1\text{mm}} = 3.5$ mJy by finding the L_{FIR} using the median $870\mu\text{m}/L_{\text{FIR}}$ ratio from AS2UDS. The L_{FIR} is then converted to $L_{1.4\text{GHz}}$ using the radio-FIR correlation from Delvecchio et al. (2021) at $z = 3.95$ (the median redshift of the sample) and assuming a mass of $M_{\star} = 2.8 \times 10^{10} M_{\odot}$ (see Section 5.3.5). We find the flux limit corresponds to $\log_{10} L_{1.4\text{GHz}} = 24.2 \text{ W Hz}^{-1}$. Integrating the luminosity functions found by van der Vlugt et al. (2023) to this limit, we find a SFRD similar to the SFRD found in this study (albeit with large error bars), as can be seen in Fig. 5.8(b). This confirms the photo-z-based estimates by van der Vlugt et al. (2023) for this subset of sources and suggests that the total contribution of ‘optically dark’ sources to the SFRD would indeed be similar to the fraction derived by van der Vlugt et al. (2023): $\sim 15^{+7}_{-7}\%$ at $z \sim 5$.

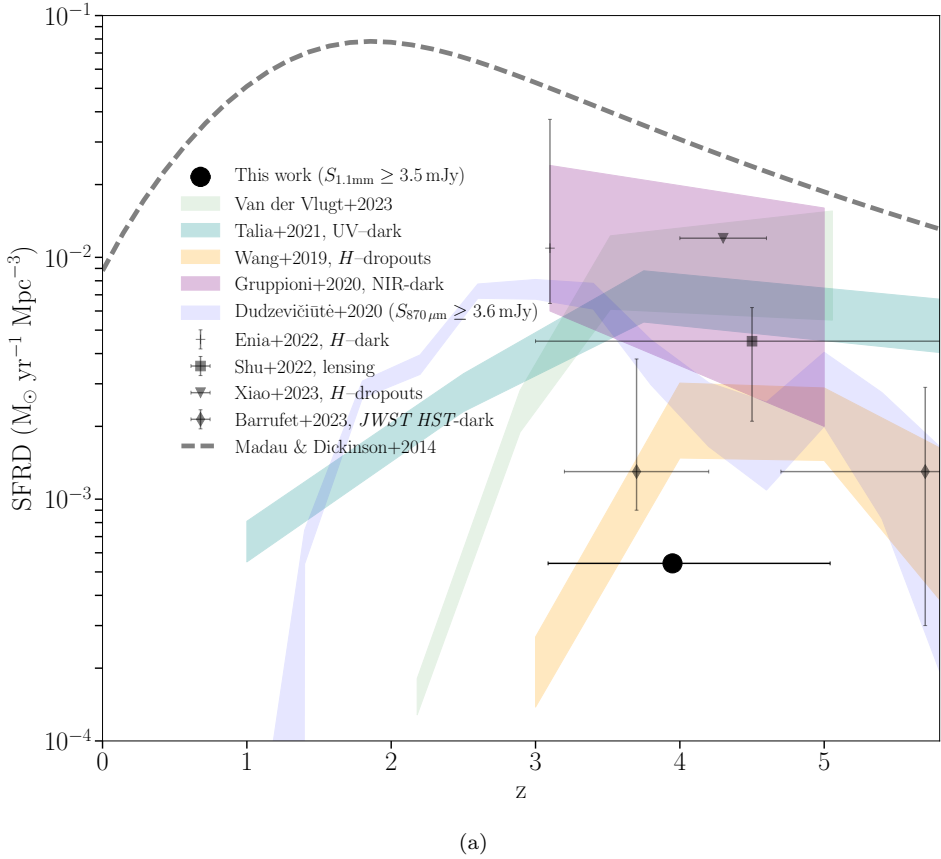
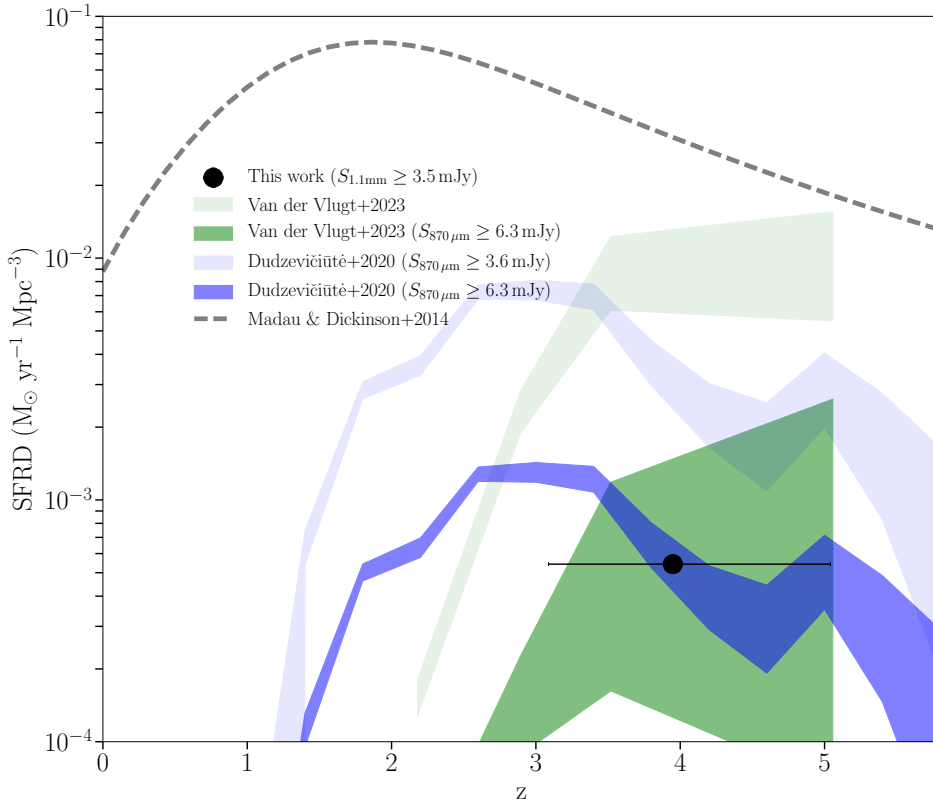


Figure 5.8: The cosmic star formation rate density (SFRD) history. The gray dotted curve in both panels represents the study of Madau & Dickinson (2014). The black closed symbol gives the SFRD derived in this study assuming the ‘best’ redshift for ‘optically dark’ sources with two redshift solutions. The cyan area and the black point in panel (a) show the SFRD from radio-selected UV-dark galaxies from Talia et al. (2021) and Enia et al. (2022), respectively. The yellow area in panel (a) is the SFRD from the H -dropouts in Wang et al. (2019) and the purple region in panel (a) shows the sub-sample of NIR-dark galaxies in the ALPINE fields (Gruppioni et al. 2020). The black square, triangle and diamond in panel (a) give the SFRD from the recent studies by, respectively, Shu et al. (2022), Xiao et al. (2023) and Barrufet et al. (2023). The light green area in both panels shows the SFRD from radio-selected ‘optically dark’ galaxies from van der Vlugt et al. (2023) where the darker green area in panel (b) gives the SFRD with $S_{870\mu\text{m}} \geq 6.3\text{ mJy}$. The lighter blue area in both panels shows the SMG contribution for a complete dust-mass-selected sample to the SFRD from Dudzevičiūtė et al. (2020) and $S_{870\mu\text{m}} \geq 3.6\text{ mJy}$.



(b)

Figure 5.8: Continued. The SFRD contribution with $S_{870\ \mu\text{m}} \geq 6.3\ \text{mJy}$, shown with the dark blue area in panel (b), is found using the relative integrated number counts from Geach et al. (2017).

5.5 Summary & Conclusions

We have used ALMA spectral scan observations to obtain spectroscopic redshifts and investigate the properties of 10 ‘optically dark’ galaxies detected in 3 GHz radio observations with counterparts in newly deblended FIR data (Jin et al. in prep.). With the addition of archival and recent additional ALMA observations for two sources, we securely detect the CO(5-4), CO(4-3) and CO(3-2) transitions for eight sources. For the other two sources, we find tentative line detections. We unambiguously identify the redshifts for six sources and for the remaining four sources we find two possible redshift solutions. Using the $L'_{\text{CO}(5-4)}\text{-}L_{\text{IR}}$ correlation, we find the most likely redshift solutions for each source with two redshift solutions. We find that the redshifts of all sources lie between $z = 3.1$ and $z = 5.0$ and have a median redshift of $z = 3.95 \pm 0.62$. Hence all targeted ‘optically dark’ sources lie at $z \gtrsim 3$.

The derived L_{IR} , $L'_{\text{CO}(5-4)}\text{-}L_{\text{IR}}$ correlation and q_{TIR} ratios of the 10 ‘optically dark’ sources all show that these sources have properties that are comparable to SMGs. The comparison between the FIR-SFR determined from SED-fitting and the radio-SFR calculated from the radio flux density shows roughly the same SFR for all sources. Three sources have a slightly elevated radio-SFR compared to the FIR-SFR which could indicate an additional source for the observed radio luminosity in the form of an AGN. We derive that the ‘optically dark’ sources contribute $5.42 \pm 0.41 \times 10^{-4} M_{\odot}\text{yr}^{-1}\text{Mpc}^{-3}$ to the SFRD at $z \sim 4$. In addition, by integrating the luminosity functions found by van der Vlugt et al. (2023) to the flux limit used to select the ‘optically dark’ sources ($S_{1.1\text{mm}} = 3.5\text{mJy}$), we determine that the SFRD is in agreement with the SFRD found for the 10 ‘optically dark’ sources. This validates the results derived by van der Vlugt et al. (2023), which relied mostly on photometric redshifts, and confirms the importance of ‘optically dark’ sources at high redshift ($z > 3$).

Acknowledgments

The authors wish to thank Mara Salvato for providing us with the COSMOS spectroscopic master catalog. This paper makes use of the following ALMA data: #2022.1.00863.S. ALMA is a partnership of ESO (representing its member states), NSF (USA), and NINS (Japan), together with NRC (Canada), MOST and ASIAA (Taiwan), and KASI (Republic of Korea), in cooperation with the Republic of Chile. The National Radio Astronomy Observatory is a facility of the National Science Foundation operated under cooperative agreement by Associated Universities, Inc. D.vdV. and J.H. acknowledge support of the VIDI research programme with project number 639.042.611, which is (partly) financed by the Netherlands Organisation for Scientific Research (NWO). S.J. is supported by the European Union’s Horizon Europe research and innovation program under the Marie Skłodowska-Curie grant agreement No. 101060888. This research made use of ASTROPY, a community developed core Python package for astronomy (Astropy Collaboration et al. 2013, 2018) hosted at <http://www.astropy.org/>, matplotlib (Hunter 2007), numpy (van der Walt et al. 2011), scipy (Jones et al. 2001), and of TOPCAT (Taylor 2005).

Appendices

5.A ALMA spectra

Here we present the ALMA spectra observed for the 10 targeted sources. Fig. 5.A.1 shows the spectra of sources with one redshift solution and Fig. 5.A.2 to Fig. 5.A.5 show the spectra of sources with two redshift solutions. The spectral configuration uses three frequency tunings to cover 84-108 GHz with a resolution of 7.8 MHz. The three separate tunings cover the frequency range with 5 narrow gaps, indicated with the gray shaded area. The blue dashed line indicates the 1σ r.m.s. noise for each bin. All lines (detected and tentative) identifications are labeled and line detections are highlighted in green. For sources with two redshift solutions, we show the spectra twice where the possible line transitions for both redshifts are indicated.

5.B SED fitting results

Here we present dust SEDs of the 10 galaxies discussed in this work. Fig. 5.A.1 shows the SEDs of sources with one redshift solution and Fig. 5.A.2 to Fig. 5.A.5 show the SEDs of sources with two redshift solutions. For sources with two redshift solutions, we show both SEDs assuming both redshifts. The blue (near-IR wavelengths), red (if present at mid-IR wavelengths) and green (FIR wavelengths) curves represent, respectively, the stellar, mid-infrared AGN (if present) and dust components. Photometries are taken from the new Super-deblended catalog (Jin et al. in prep.) and the ALMA 3mm observations. Arrows mark 3σ upper limits.

5.C Line fitting results

Here we present the Gaussian fits to the CO, [CI](1-0) and H₂O(1₁₀-1₀₁) emission lines for the 10 galaxies discussed in this work. Each emission line is plotted in black and centered at the zero velocity corresponding to the redshift of the source. Fig. 5.C.1 shows the fits to the CO(5-4) line, Fig. 5.C.2 shows the fits to the CO(4-3) line, Fig. 5.C.3 shows the fits to the CO(3-2) line, Fig. 5.C.4 shows the fits to the [CI](1-0) line and Fig. 5.C.5 shows the fits to the H₂O(1₁₀-1₀₁) line. The Gaussian fits to the lines are shown with red curves. The vertical dashed lines give the measured FWHM.

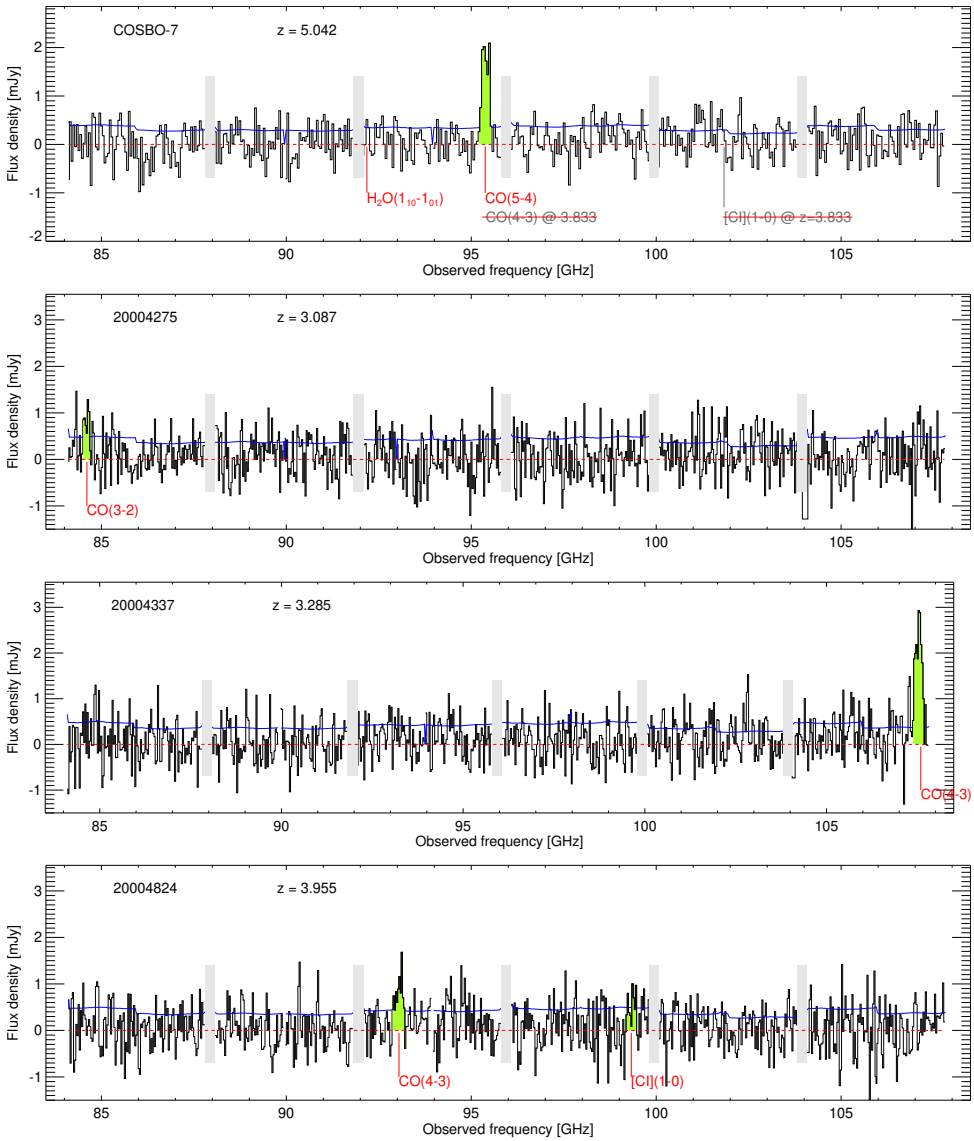


Figure 5.A.1: The ALMA Band-3 spectra in the frequency range 84-108 GHz for all sources with one redshift solution. The three separate tunings cover the frequency range with 5 narrow gaps, indicated with the gray shaded area. The emission lines detected are highlighted with green shaded regions and their identifications are labeled.

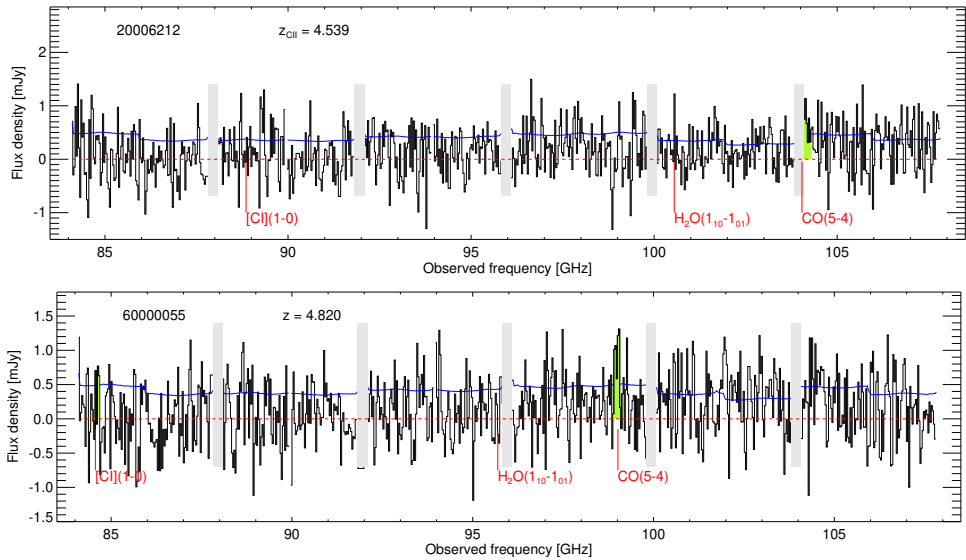


Figure 5.A.1: Continued. The line detected for 20006212 is confirmed by a [CII] $158\mu\text{m}$ detection in ALMA archival data (ID: 2021.1.00280.L, PI: R. Herrera-Camus). The line detected for 60000055 is confirmed by the recent observations from Sillaseen et al. (in prep.).

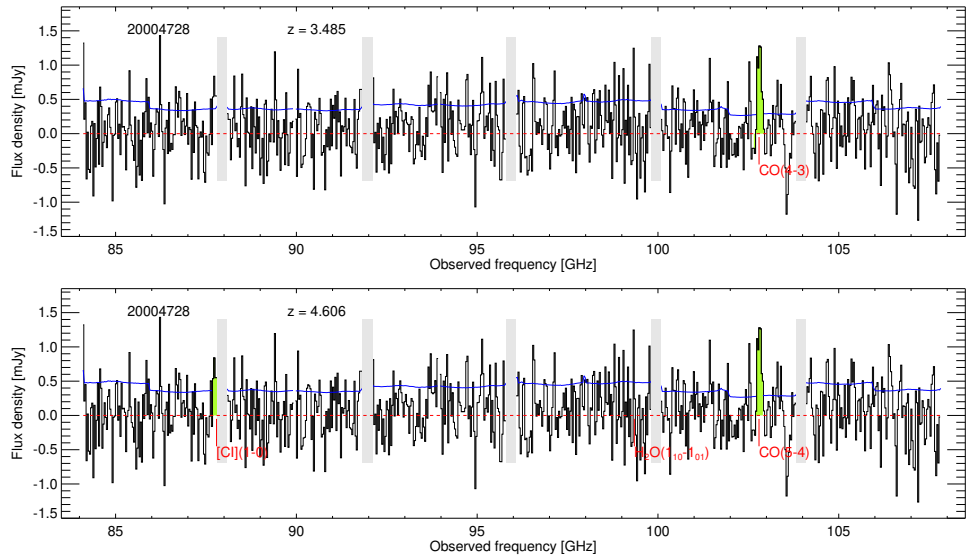


Figure 5.A.2: The ALMA Band-3 spectrum for 20004728 in the frequency range 84–108 GHz. This source has two redshift solutions: $z = 3.49$ and $z = 4.61$. The three separate tunings cover the frequency range with 5 narrow gaps, indicated with the gray shaded area. The emission lines detected are highlighted with green shaded regions and their identifications are labeled.

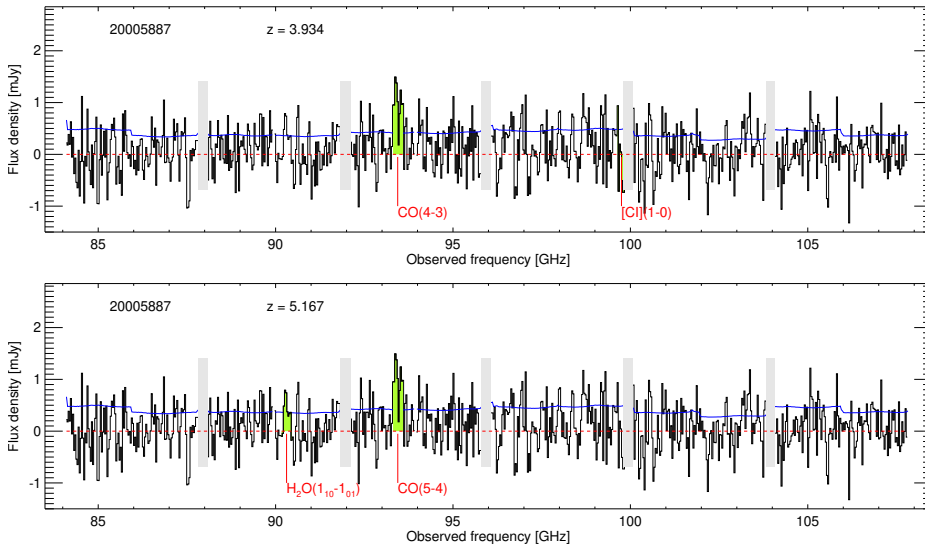


Figure 5.A.3: The ALMA Band-3 spectrum for 20005887 in the frequency range 84–108 GHz. This source has two redshift solutions: $z = 3.93$ and $z = 5.17$. The three separate tunings cover the frequency range with 5 narrow gaps, indicated with the gray shaded area. The emission lines detected are highlighted with green shaded regions and their identifications are labeled.

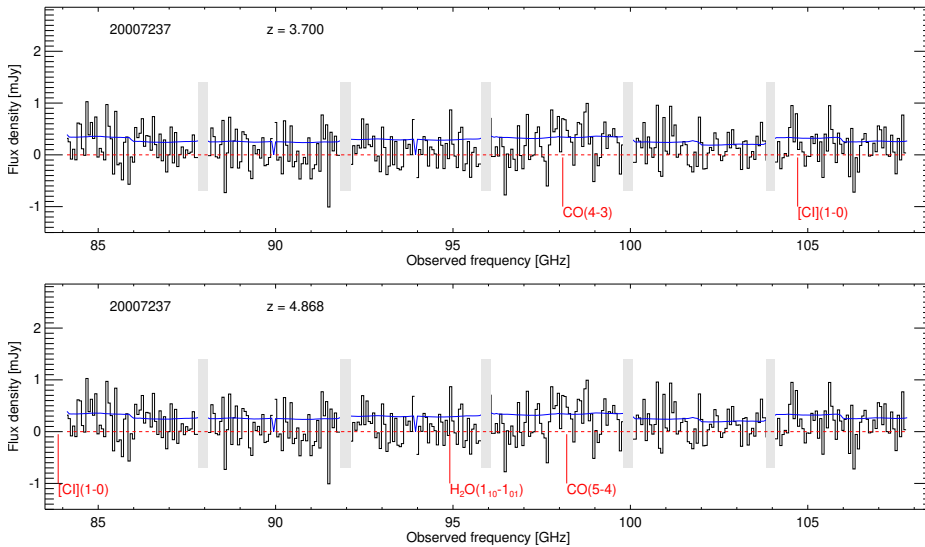


Figure 5.A.4: The ALMA Band-3 spectrum for 20007237 in the frequency range 84–108 GHz. The spectrum shows two tentative emission lines at ~ 98 GHz and ~ 104.5 . The source has two redshift solutions: $z = 3.70$ and $z = 4.87$. The three separate tunings cover the frequency range with 5 narrow gaps, indicated with the gray shaded area.

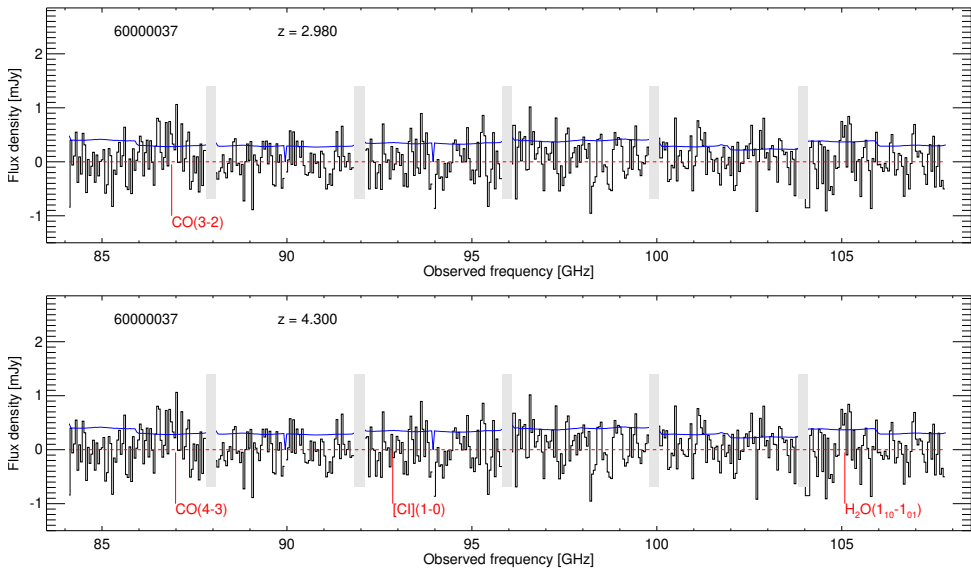


Figure 5.A.5: The ALMA Band-3 spectra for 60000037 in the frequency range 84–108 GHz. The spectrum shows two tentative emission lines at ~ 86.8 GHz and ~ 105 GHz. The source has two redshift solutions: $z = 2.98$ and $z = 4.30$. The three separate tunings cover the frequency range with 5 narrow gaps, indicated with the gray shaded area.

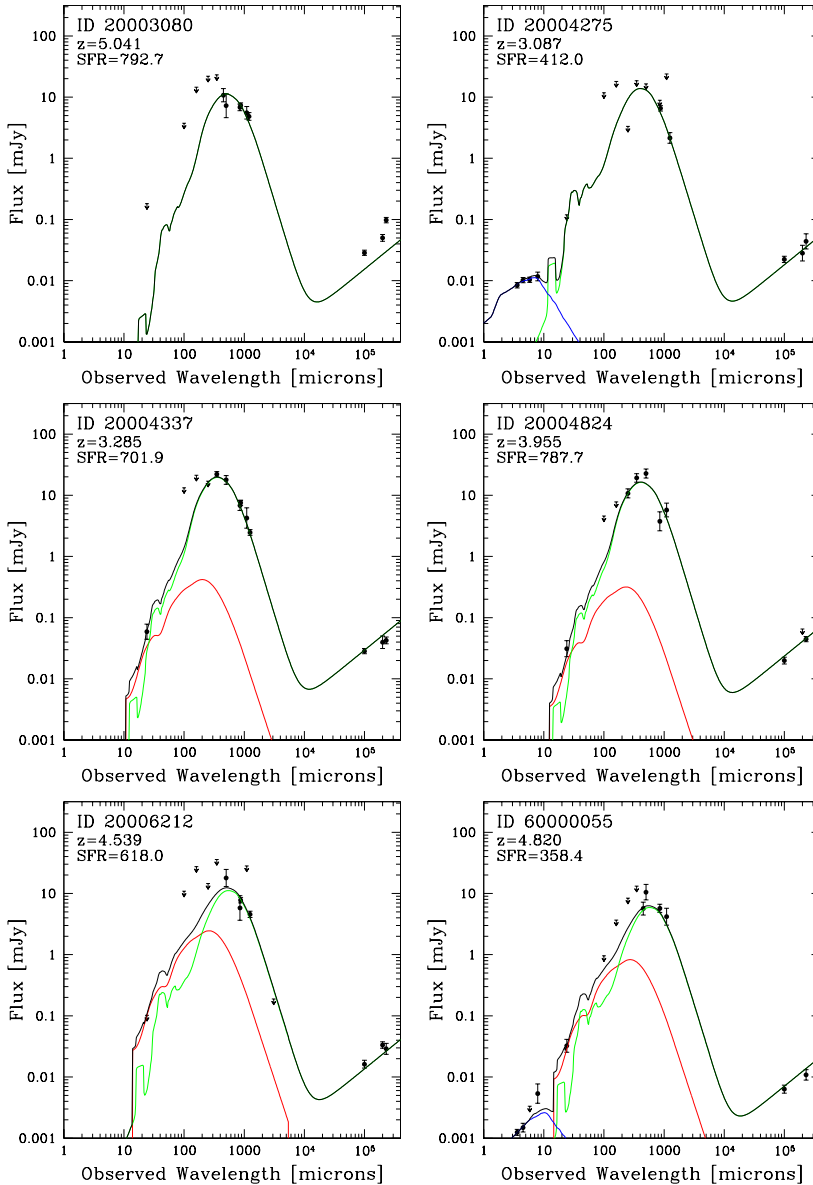


Figure 5.B.1: The observed SEDs and its best-fit models for all sources with one redshift solution. The blue (near-IR wavelengths), red (if present at mid-IR wavelengths) and green (FIR wavelengths) curves represent, respectively, the stellar, mid-infrared AGN (if present) and dust components. Photometries are taken from the new Super-deblended catalog (Jin et al. in prep.) and the ALMA 3mm observations. Arrows mark the 3σ upper limits. The solid curve shows the best fit to the observed SED.

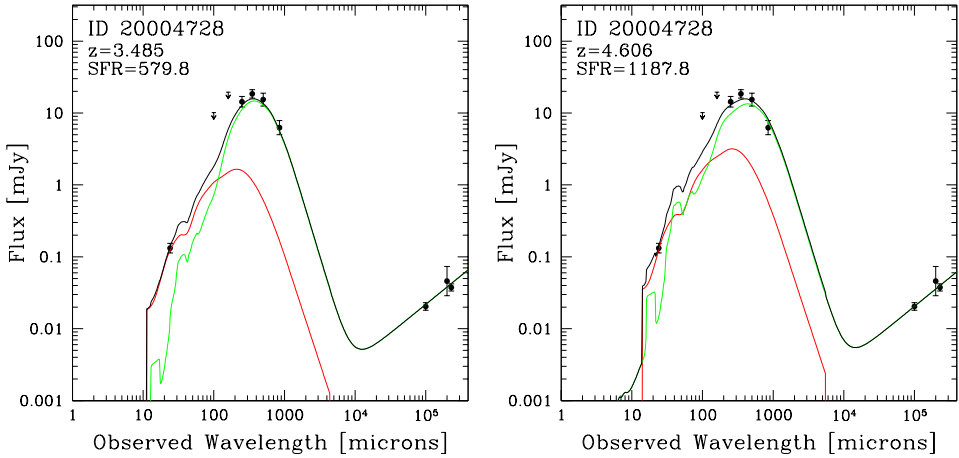


Figure 5.B.2: The observed SED and its best-fit model for 20004728. This sources has two redshift solutions: $z = 3.49$ and $z = 4.61$. The blue (near-IR wavelengths), red (if present at mid-IR wavelengths) and green (FIR wavelengths) curves represent, respectively, the stellar, mid-infrared AGN (if present) and dust components. Photometries are taken from the new Super-deblended catalog (Jin et al. in prep.) and the ALMA 3mm observations. Arrows mark the 3σ upper limits. The solid curve shows the best fit to the observed SED.

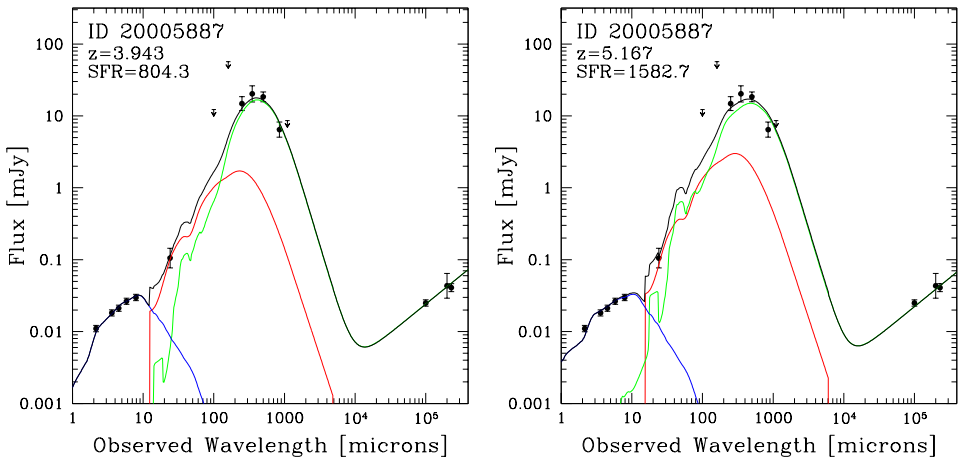


Figure 5.B.3: The observed SED and its best-fit model for 20005887. This sources has two redshift solutions: $z = 3.93$ and $z = 5.17$. The blue (near-IR wavelengths), red (if present at mid-IR wavelengths) and green (FIR wavelengths) curves represent, respectively, the stellar, mid-infrared AGN (if present) and dust components. Photometries are taken from the new Super-deblended catalog (Jin et al. in prep.) and the ALMA 3mm observations. Arrows mark the 3σ upper limits. The solid curve shows the best fit to the observed SED.

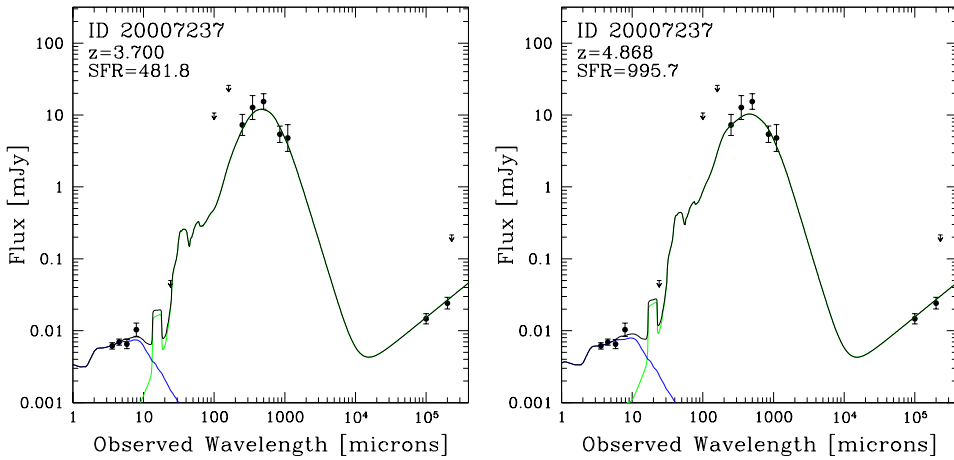


Figure 5.B.4: The observed SED and its best-fit model for 20007237. This sources has two redshift solutions: $z = 3.70$ and $z = 4.87$. The blue (near-IR wavelengths), red (if present at mid-IR wavelengths) and green (FIR wavelengths) curves represent, respectively, the stellar, mid-infrared AGN (if present) and dust components. Photometries are taken from the new Super-deblended catalog (Jin et al. in prep.) and the ALMA 3mm observations. Arrows mark the 3σ upper limits. The solid curve shows the best fit to the observed SED.

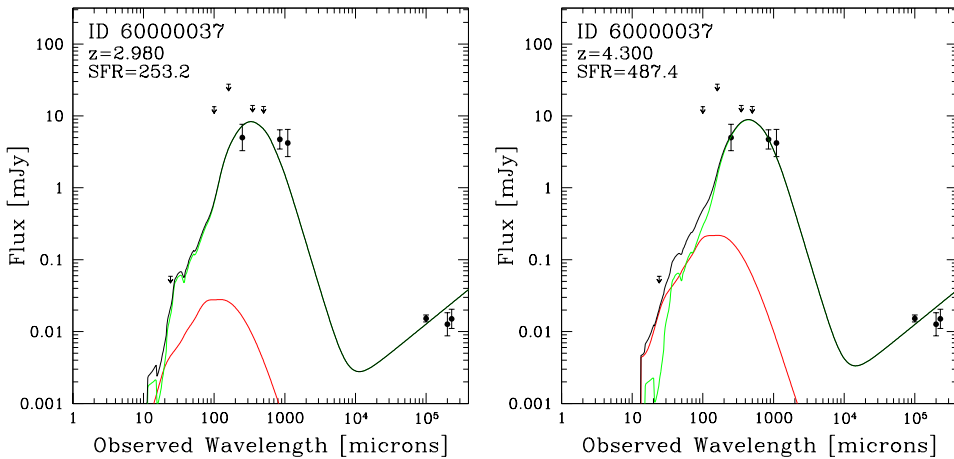


Figure 5.B.5: The observed SED and its best-fit model for 60000037. This sources has two redshift solutions: $z = 2.98$ and $z = 4.30$. The blue (near-IR wavelengths), red (if present at mid-IR wavelengths) and green (FIR wavelengths) curves represent, respectively, the stellar, mid-infrared AGN (if present) and dust components. Photometries are taken from the new Super-deblended catalog (Jin et al. in prep.) and the ALMA 3mm observations. Arrows mark the 3σ upper limits. The solid curve shows the best fit to the observed SED.

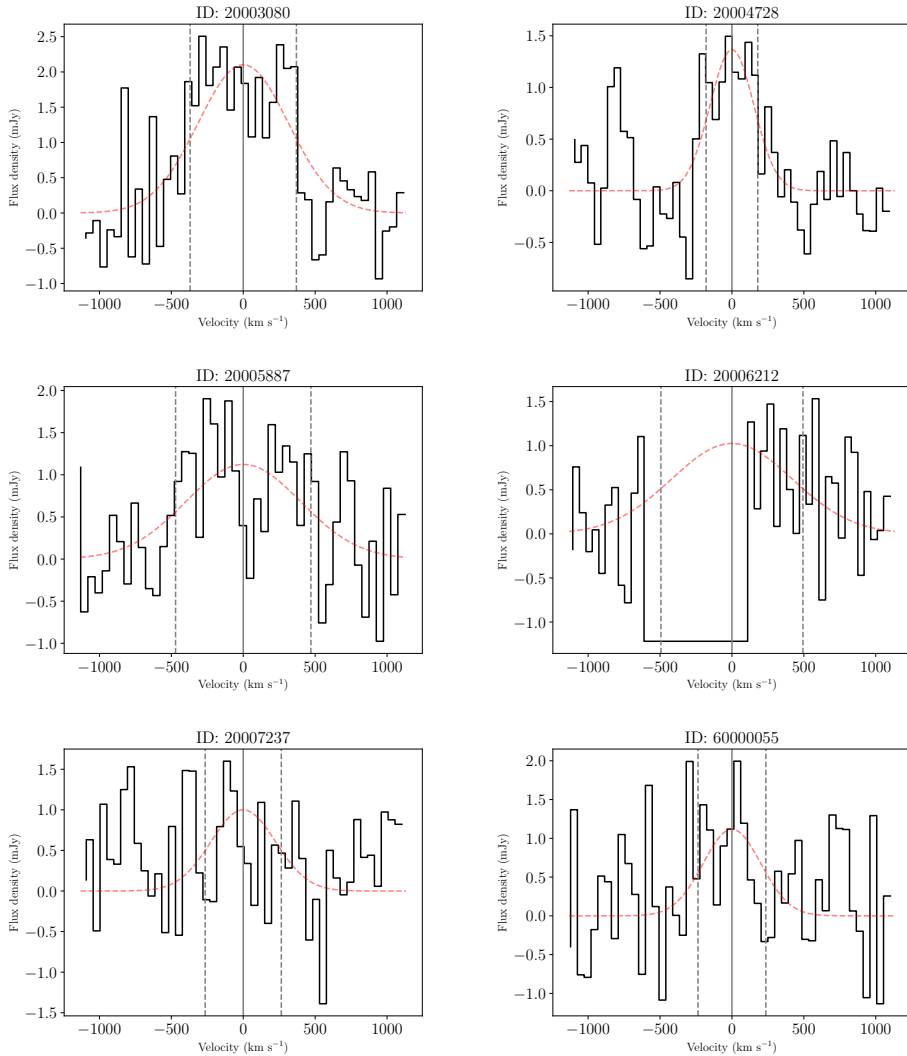


Figure 5.C.1: Spectra of the sources with a detected CO(5-4) line (20003080), tentative CO(5-4) line (2000612) and a potential CO(5-4) tentative detection (20007237 and 60000055) or detection (20004728 and 20005887). The velocity is relative to the redshifts of the sources, respectively, 5.041, 4.606, 5.167, 4.539, 4.868 and 4.82 for 20003080, 20004728, 20005887, 2000612, 20007237 and 60000055. The dashed red line gives the Gaussian fitting result. The vertical dashed lines give the measured FWHM.

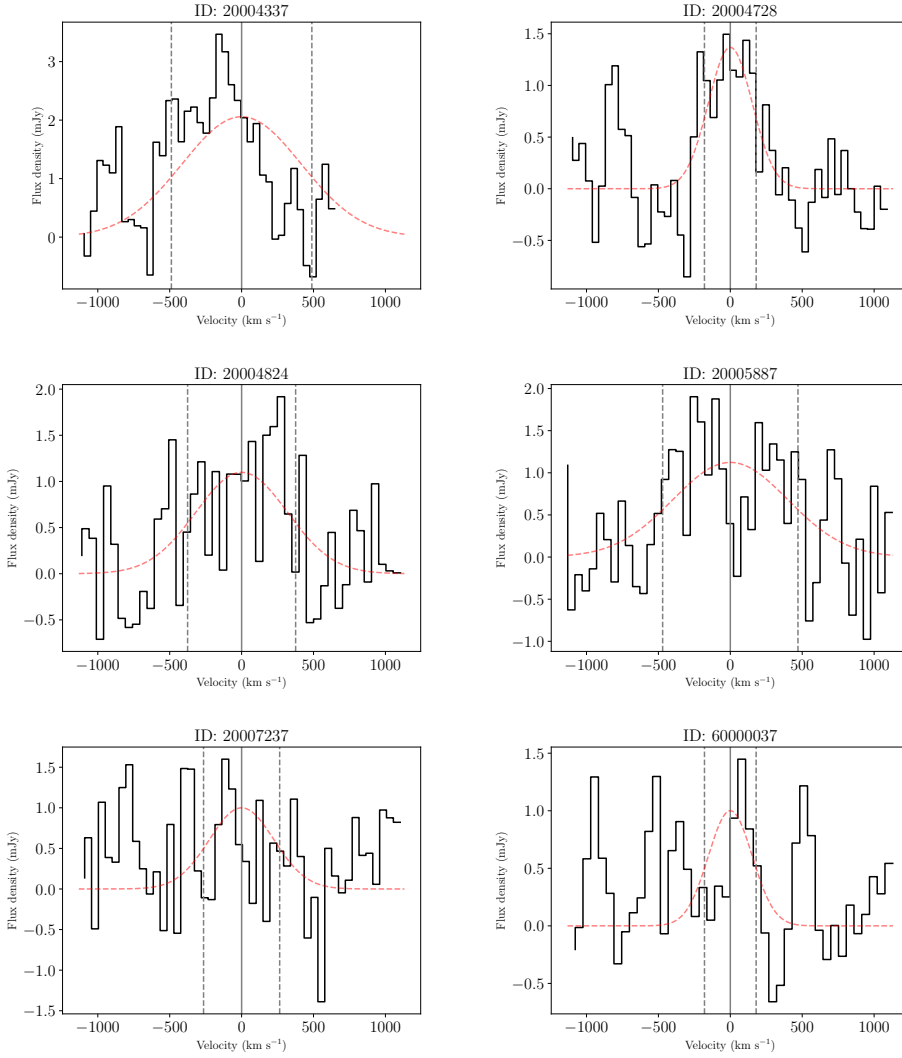


Figure 5.C.2: Spectra of the sources with a detected CO(4-3) line profile (20004337 and 20004824) and a potential CO(4-3) tentative detection (20007237 and 60000037) or detection (20004728 and 20005887). The velocity is relative to the redshifts of the sources, respectively, 3.285, 3.485, 3.955, 3.934, 3.7 and 4.3 for 20004337, 20004728, 20004824, 20005887, 20007237 and 60000037. The dashed red line gives the Gaussian fitting result. The vertical dashed lines give the measured FWHM.

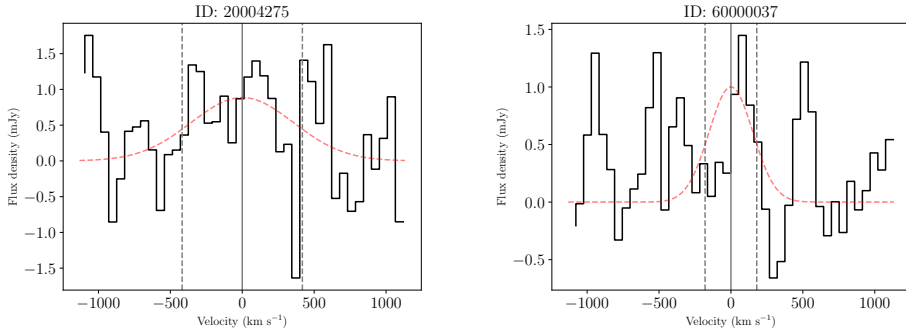


Figure 5.C.3: Spectra of the sources with a detected CO(3-2) line (20004275) and a tentative potential CO(3-2) detection (60000037). The velocity is relative to the redshifts of the sources, respectively, 3.087 and 2.98 for 20004275 and 60000037. The dashed red line gives the Gaussian fitting result. The vertical dashed lines give the measured FWHM.

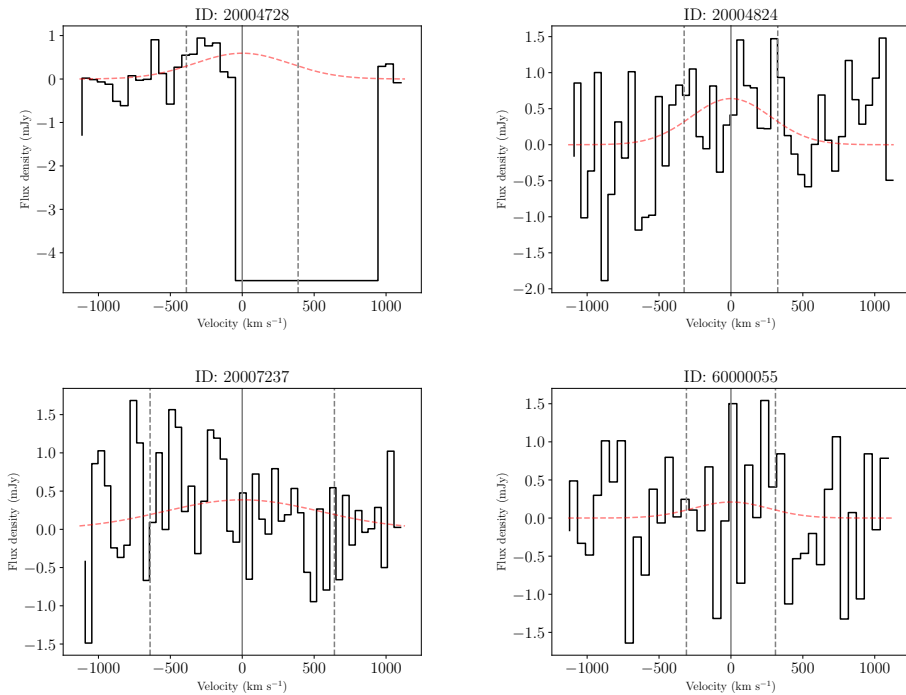


Figure 5.C.4: Spectra of the sources with a potential tentative [CI](1-0) line detection. The velocity is relative to the redshifts of the sources, respectively, 4.606, 3.955, 3.7 and 4.3 for 20004728, 20004924, 20007237 and 60000055. The dashed red line gives the Gaussian fitting result. The vertical dashed lines give the measured FWHM.

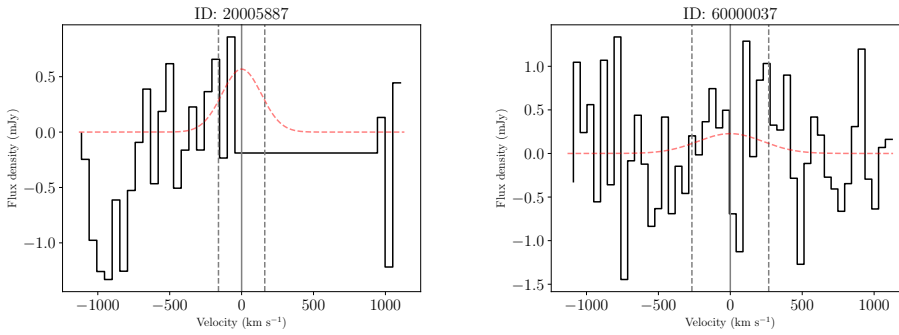


Figure 5.C.5: Spectra of the sources with a potential tentative $\text{H}_2\text{O}(1_{10}-1_{01})$ line detection. The velocity is relative to the redshifts of the sources, respectively, 5.167 and 4.3 for 20005887 and 60000037. The dashed red line gives the Gaussian fitting result. The vertical dashed lines give the measured FWHM.

Bibliography

- Algera, H. S. B., van der Vlugt, D., Hodge, J. A., et al. 2020a, *ApJ*, 903, 139
- Algera, H. S. B., Smail, I., Dudzevičiūtė, U., et al. 2020b, *ApJ*, 903, 138
- Algera, H. S. B., Hodge, J. A., Riechers, D., et al. 2021, *ApJ*, 912, 73
- Algera, H. S. B., Hodge, J. A., Riechers, D. A., et al. 2022, *ApJ*, 924, 76
- Aretxaga, I., Wilson, G. W., Aguilar, E., et al. 2011, *MNRAS*, 415, 3831
- Astropy Collaboration, Robitaille, T. P., Tollerud, E. J., et al. 2013, *aap*, 558, A33
- Astropy Collaboration, Price-Whelan, A. M., Sipőcz, B. M., et al. 2018, *AJ*, 156, 123
- Aversa, R., Lapi, A., de Zotti, G., Shankar, F., & Danese, L. 2015, *ApJ*, 810, 74
- Avni, Y., & Bahcall, J. N. 1980, *ApJ*, 235, 694
- Bakx, T. J. L. C., & Dannerbauer, H. 2022, *MNRAS*, 515, 678
- Barkana, R., & Loeb, A. 2001, *Phys. Rep.*, 349, 125
- Barrufet, L., Oesch, P. A., Weibel, A., et al. 2023, *MNRAS*, 522, 449
- Baumann, D. 2009, *ArXiv e-prints*, arXiv:0907.5424
- Behroozi, P., Wechsler, R. H., Hearin, A. P., & Conroy, C. 2019, *MNRAS*, 488, 3143
- Bell, E. F. 2003, *ApJ*, 586, 794
- Bennett, C. L., Larson, D., Weiland, J. L., et al. 2013, *ApJS*, 208, 20
- Bertoldi, F., Carilli, C., Aravena, M., et al. 2007, *ApJS*, 172, 132
- Best, P. N., Kauffmann, G., Heckman, T. M., & Ivezić, Ž. 2005, *MNRAS*, 362, 9
- Best, P. N., Ker, L. M., Simpson, C., Rigby, E. E., & Sabater, J. 2014, *MNRAS*, 445, 955
- Béthermin, M., Daddi, E., Magdis, G., et al. 2012, *ApJL*, 757, L23
- Béthermin, M., Daddi, E., Magdis, G., et al. 2015, *A&A*, 573, A113
- Biggs, A. D., & Ivison, R. J. 2006, *MNRAS*, 371, 963
- Bolton, J. G., Stanley, G. J., & Slee, O. B. 1949, *Nature*, 164, 101
- Bonaldi, A., Bonato, M., Galluzzi, V., et al. 2019, *MNRAS*, 482, 2
- Bonato, M., Negrello, M., Mancuso, C., et al. 2017, *MNRAS*, 469, 1912
- Bondi, M., Ciliegi, P., Schinnerer, E., et al. 2008, *ApJ*, 681, 1129
- Bondi, M., Zamorani, G., Ciliegi, P., et al. 2018, *A&A*, 618, L8
- Bonzini, M., Padovani, P., Mainieri, V., et al. 2013, *MNRAS*, 436, 3759
- Bothwell, M. S., Aguirre, J. E., Aravena, M., et al. 2017, *MNRAS*, 466, 2825
- Bourne, N., Dunlop, J. S., Merlin, E., et al. 2017, *MNRAS*, 467, 1360
- Bouwens, R., González-López, J., Aravena, M., et al. 2020, *ApJ*, 902, 112
- Bouwens, R. J., Illingworth, G. D., Franx, M., et al. 2009, *ApJ*, 705, 936
- Bouwens, R. J., Illingworth, G. D., Oesch, P. A., et al. 2012, *ApJ*, 754, 83
- Bouwens, R. J., Bradley, L., Zitrin, A., et al. 2014a, *ApJ*, 795, 126
- Bouwens, R. J., Illingworth, G. D., Oesch, P. A., et al. 2014b, *ApJ*, 793, 115
- Bouwens, R. J., Illingworth, G. D., Oesch, P. A., et al. 2015, *ApJ*, 803, 34
- Bouwens, R. J., Oesch, P. A., Labbé, I., et al. 2016, *ApJ*, 830, 67
- Bouwens, R. J., Oesch, P. A., Stefanon, M., et al. 2021, *AJ*, 162, 47
- Bouwens, R. J., Stefanon, M., Brammer, G., et al. 2023, *MNRAS*, 523, 1036
- Bowler, R. A. A., Dunlop, J. S., McLure, R. J., et al. 2015, *MNRAS*, 452, 1817

- Bressan, A., Silva, L., & Granato, G. L. 2002, *A&A*, 392, 377
- Briggs, D. S. 1995, in *American Astronomical Society Meeting Abstracts*, Vol. 187, 112.02
- Brinchmann, J., Charlot, S., White, S. D. M., et al. 2004, *MNRAS*, 351, 1151
- Brout, D., Scolnic, D., Popovic, B., et al. 2022, *ApJ*, 938, 110
- Bruzual, G. 2010, *Philosophical Transactions of the Royal Society of London Series A*, 368, 783
- Bruzual, G., & Charlot, S. 2003, *MNRAS*, 344, 1000
- Cai, Z.-Y., Lapi, A., Bressan, A., et al. 2014, *ApJ*, 785, 65
- Cai, Z.-Y., Lapi, A., Xia, J.-Q., et al. 2013, *ApJ*, 768, 21
- Calistro Rivera, G., Williams, W. L., Hardcastle, M. J., et al. 2017a, *MNRAS*, 469, 3468
- Calistro Rivera, G., Williams, W. L., Hardcastle, M. J., et al. 2017b, *MNRAS*, 469, 3468
- Capak, P., Aussel, H., Ajiki, M., et al. 2007, *ApJS*, 172, 99
- Carilli, C. L., & Walter, F. 2013, *ARA&A*, 51, 105
- Carilli, C. L., Lee, N., Capak, P., et al. 2008, *ApJ*, 689, 883
- Casey, C. M., Narayanan, D., & Cooray, A. 2014a, *Phys. Rep.*, 541, 45
- Casey, C. M., Scoville, N. Z., Sanders, D. B., et al. 2014b, *ApJ*, 796, 95
- Casey, C. M., Zavala, J. A., Spilker, J., et al. 2018, *ApJ*, 862, 77
- Chabrier, G. 2003, *PASP*, 115, 763
- Chapman, S. C., Blain, A. W., Smail, I., & Ivison, R. J. 2005, *ApJ*, 622, 772
- Chapman, S. C., Helou, G., Lewis, G. F., & Dale, D. A. 2003, *ApJ*, 588, 186
- Chapman, S. C., Huber, A. I., Sinclair, A. K., et al. 2022, in *Society of Photo-Optical Instrumentation Engineers (SPIE) Conference Series*, Vol. 12190, *Millimeter, Submillimeter, and Far-Infrared Detectors and Instrumentation for Astronomy XI*, ed. J. Zmuidzinas & J.-R. Gao, 1219005
- Chary, R.-R., & Pope, A. 2010, *ArXiv e-prints*, arXiv:1003.1731
- Civano, F., Marchesi, S., Comastri, A., et al. 2016, *ApJ*, 819, 62
- Clemens, M. S., Vega, O., Bressan, A., et al. 2008, *A&A*, 477, 95
- Clesse, S. 2015, *arXiv e-prints*, arXiv:1501.00460
- Cochrane, R. K., Kondapally, R., Best, P. N., et al. 2023, *MNRAS*, 523, 6082
- Condon, J. J. 1984, *ApJ*, 287, 461
- Condon, J. J. 1992, *ARA&A*, 30, 575
- Condon, J. J., Cotton, W. D., & Broderick, J. J. 2002, *AJ*, 124, 675
- Condon, J. J., Cotton, W. D., Greisen, E. W., et al. 1998, *AJ*, 115, 1693
- Condon, J. J., Matthews, A. M., & Broderick, J. J. 2019, *ApJ*, 872, 148
- Condon, J. J., & Mitchell, K. J. 1984, *AJ*, 89, 610
- Condon, J. J., Cotton, W. D., Fomalont, E. B., et al. 2012, *ApJ*, 758, 23
- Conroy, C. 2013, *ARA&A*, 51, 393
- Coogan, R. T., Daddi, E., Sargent, M. T., et al. 2018, *MNRAS*, 479, 703
- Cotton, W. D., Condon, J. J., Kellermann, K. I., et al. 2018, *ApJ*, 856, 67
- Croton, D. J., Springel, V., White, S. D. M., et al. 2006, *MNRAS*, 365, 11
- da Cunha, E., Charlot, S., & Elbaz, D. 2008, *MNRAS*, 388, 1595
- da Cunha, E., Walter, F., Smail, I. R., et al. 2015, *ApJ*, 806, 110
- Daddi, E., Dickinson, M., Morrison, G., et al. 2007, *ApJ*, 670, 156

- Daddi, E., Elbaz, D., Walter, F., et al. 2010, *ApJL*, 714, L118
- Daddi, E., Dannerbauer, H., Liu, D., et al. 2015, *A&A*, 577, A46
- Dannerbauer, H., Walter, F., & Morrison, G. 2008, *ApJL*, 673, L127
- de Jong, T., Klein, U., Wielebinski, R., & Wunderlich, E. 1985, *A&A*, 147, L6
- De Looze, I., Cormier, D., Leboutteiller, V., et al. 2014, *A&A*, 568, A62
- De Zotti, G., Bonato, M., & Cai, Z.-Y. 2019, in *3rd Cosmology School, Introduction to Cosmology*, ed. K. Bajan, M. Biernacka, & A. Pollo, Vol. 9, 125–150
- Del Moro, A., Alexander, D. M., Mullaney, J. R., et al. 2013, *A&A*, 549, A59
- Delhaize, J., Smolčić, V., Delvecchio, I., et al. 2017, *A&A*, 602, A4
- Delvecchio, I., Gruppioni, C., Pozzi, F., et al. 2014, *MNRAS*, 439, 2736
- Delvecchio, I., Smolčić, V., Zamorani, G., et al. 2017, *A&A*, 602, A3
- Delvecchio, I., Daddi, E., Sargent, M. T., et al. 2021, *A&A*, 647, A123
- Downes, D., Neri, R., Greve, A., et al. 1999, *A&A*, 347, 809
- Driver, S. P., Andrews, S. K., da Cunha, E., et al. 2018, *MNRAS*, 475, 2891
- Dudzevičiūtė, U., Smail, I., Swinbank, A. M., et al. 2020, *MNRAS*, 494, 3828
- Dumas, G., Schinnerer, E., Tabatabaei, F. S., et al. 2011, *AJ*, 141, 41
- Dunlop, J. S., McLure, R. J., Biggs, A. D., et al. 2017, *MNRAS*, 466, 861
- Edler, H. W., de Gasperin, F., & Rafferty, D. 2021, *A&A*, 652, A37
- Elbaz, D., Daddi, E., Le Borgne, D., et al. 2007, *A&A*, 468, 33
- Elbaz, D., Dickinson, M., Hwang, H. S., et al. 2011, *A&A*, 533, A119
- Emonts, B. H. C., Norris, R. P., Feain, I., et al. 2014, *MNRAS*, 438, 2898
- Enia, A., Talia, M., Pozzi, F., et al. 2022, *ApJ*, 927, 204
- Faisst, A. L., Capak, P. L., Yan, L., et al. 2017, *ApJ*, 847, 21
- Farrah, D., Afonso, J., Efstathiou, A., et al. 2003, *MNRAS*, 343, 585
- Finkelstein, S. L., Ryan, Russell E., J., Papovich, C., et al. 2015, *ApJ*, 810, 71
- Finoguenov, A., Guzzo, L., Hasinger, G., et al. 2007, *ApJS*, 172, 182
- Foreman-Mackey, D., Hogg, D. W., Lang, D., & Goodman, J. 2013, *PASP*, 125, 306
- Franco, M., Elbaz, D., Béthermin, M., et al. 2018, *A&A*, 620, A152
- Franco, M., Elbaz, D., Zhou, L., et al. 2020, *A&A*, 643, A30
- Frayer, D. T., Reddy, N. A., Armus, L., et al. 2004, *AJ*, 127, 728
- Frieman, J. A., Turner, M. S., & Huterer, D. 2008, *ARA&A*, 46, 385
- Fudamoto, Y., Oesch, P. A., Magnelli, B., et al. 2020a, *MNRAS*, 491, 4724
- Fudamoto, Y., Oesch, P. A., Faisst, A., et al. 2020b, *A&A*, 643, A4
- Geach, J. E., Dunlop, J. S., Halpern, M., et al. 2017, *MNRAS*, 465, 1789
- Gehrels, N. 1986, *ApJ*, 303, 336
- Gehrz, R. 1989, in *Interstellar Dust*, ed. L. J. Allamandola & A. G. G. M. Tielens, Vol. 135, 445
- Goldader, J. D., Meurer, G., Heckman, T. M., et al. 2002, *ApJ*, 568, 651
- Gómez-Guijarro, C., Elbaz, D., Xiao, M., et al. 2022, *A&A*, 658, A43
- Gruppioni, C., & Pozzi, F. 2019, *MNRAS*, 483, 1993
- Gruppioni, C., Pozzi, F., Rodighiero, G., et al. 2013, *MNRAS*, 432, 23
- Gruppioni, C., Calura, F., Pozzi, F., et al. 2015, *MNRAS*, 451, 3419
- Gruppioni, C., Béthermin, M., Loiacono, F., et al. 2020, *A&A*, 643, A8
- Hatsukade, B., Kohno, K., Yamaguchi, Y., et al. 2018, *PASJ*, 70, 105
- Helou, G., Soifer, B. T., & Rowan-Robinson, M. 1985, *ApJL*, 298, L7
- Henriques, B. M. B., White, S. D. M., Thomas, P. A., et al. 2015, *MNRAS*, 451, 2663

- Herrera Ruiz, N., Middelberg, E., Deller, A., et al. 2017, *A&A*, 607, A132
- Heywood, I., Jarvis, M. J., & Condon, J. J. 2013, *MNRAS*, 432, 2625
- Hickox, R. C., Jones, C., Forman, W. R., et al. 2009, *ApJ*, 696, 891
- Hoaglin, D. C., Mosteller, F., & Tukey, J. W. 1983, *Understanding Robust and Exploratory Data Analysis* (New York: Wiley)
- Hodge, J. A., & da Cunha, E. 2020, *Royal Society Open Science*, 7, 200556
- Hodge, J. A., Karim, A., Smail, I., et al. 2013, *ApJ*, 768, 91
- Howell, J. H., Armus, L., Mazzarella, J. M., et al. 2010, *ApJ*, 715, 572
- Hunter, J. D. 2007, *Computing in Science and Engineering*, 9, 90
- Huynh, M. T., Jackson, C. A., Norris, R. P., & Prandoni, I. 2005, *AJ*, 130, 1373
- Ikarashi, S., Caputi, K. I., Ohta, K., et al. 2017, *ApJL*, 849, L36
- Ilbert, O., McCracken, H. J., Le Fèvre, O., et al. 2013, *A&A*, 556, A55
- Inoue, A. K. 2003, *PASJ*, 55, 901
- Iovino, A., Petropoulou, V., Scodreggio, M., et al. 2016, *A&A*, 592, A78
- Jarvis, M., Seymour, N., Afonso, J., et al. 2015, *Advancing Astrophysics with the Square Kilometre Array (AASKA14)*, 68
- Jarvis, M., Taylor, R., Agudo, I., et al. 2016, in *MeerKAT Science: On the Pathway to the SKA*, 6
- Jarvis, M. J., & Rawlings, S. 2000, *MNRAS*, 319, 121
- Jennison, R. C., & Das Gupta, M. K. 1953, *Nature*, 172, 996
- Jin, S., Daddi, E., Liu, D., et al. 2018, *ApJ*, 864, 56
- Jin, S., Daddi, E., Magdis, G. E., et al. 2019, *ApJ*, 887, 144
- Jin, S., Daddi, E., Magdis, G. E., et al. 2022, *A&A*, 665, A3
- Jones, E., Oliphant, T., Peterson, P., et al. 2001, *SciPy: Open source scientific tools for Python*
- Karim, A., Schinnerer, E., Martínez-Sansigre, A., et al. 2011, *ApJ*, 730, 61
- Kennicutt, Robert C., J. 1998, *ARA&A*, 36, 189
- Kennicutt, R. C., & Evans, N. J. 2012, *ARA&A*, 50, 531
- Khusanova, Y., Le Fèvre, O., Cassata, P., et al. 2020, *A&A*, 634, A97
- Khusanova, Y., Bethermin, M., Le Fèvre, O., et al. 2021, *A&A*, 649, A152
- Kimball, A. E., & Ivezić, Ž. 2008, *AJ*, 136, 684
- Klein, U., & Graeve, R. 1986, *A&A*, 161, 155
- Klein, U., Lisenfeld, U., & Verley, S. 2018, *A&A*, 611, A55
- Klein, U., Wielebinski, R., & Morsi, H. W. 1988, *A&A*, 190, 41
- Knobel, C., Lilly, S. J., Iovino, A., et al. 2012, *ApJ*, 753, 121
- Kobulnicky, H. A., & Johnson, K. E. 1999, *ApJ*, 527, 154
- Koprowski, M. P., Dunlop, J. S., Michałowski, M. J., et al. 2017, *MNRAS*, 471, 4155
- Krolewski, A., Lee, K.-G., White, M., et al. 2018, *ApJ*, 861, 60
- Kroupa, P. 2001, *MNRAS*, 322, 231
- Kurczynski, P., Gawiser, E., Acquaviva, V., et al. 2016, *ApJ*, 820, L1
- Lacey, C. G., Baugh, C. M., Frenk, C. S., et al. 2016, *MNRAS*, 462, 3854
- Lacki, B. C., & Thompson, T. A. 2010, *ApJ*, 717, 196
- Laigle, C., McCracken, H. J., Ilbert, O., et al. 2016, *ApJS*, 224, 24
- Leslie, S. K., Schinnerer, E., Liu, D., et al. 2020, *ApJ*, 899, 58
- Lim, C.-F., Wang, W.-H., Smail, I., et al. 2020, *ApJ*, 889, 80
- Liu, D., Daddi, E., Dickinson, M., et al. 2018, *ApJ*, 853, 172

- Loeb, A., & Barkana, R. 2001, *ARA&A*, 39, 19
- Loiacono, F., Decarli, R., Gruppioni, C., et al. 2021, *A&A*, 646, A76
- Lutz, D., Poglitsch, A., Altieri, B., et al. 2011, *A&A*, 532, A90
- Madau, P., & Dickinson, M. 2014, *ARA&A*, 52, 415
- Magdis, G. E., Elbaz, D., Hwang, H. S., et al. 2010, *ApJL*, 720, L185
- Magdis, G. E., Daddi, E., Béthermin, M., et al. 2012, *ApJ*, 760, 6
- Magliocchetti, M., Maddox, S. J., Lahav, O., & Wall, J. V. 1998, *MNRAS*, 300, 257
- Magnelli, B., Lutz, D., Saintonge, A., et al. 2014, *A&A*, 561, A86
- Magnelli, B., Ivison, R. J., Lutz, D., et al. 2015, *A&A*, 573, A45
- Malefahlo, E. D., Jarvis, M. J., Santos, M. G., et al. 2022, *MNRAS*, 509, 4291
- Mancuso, C., Lapi, A., Shi, J., et al. 2016, *ApJ*, 823, 128
- Mancuso, C., Lapi, A., Cai, Z.-Y., et al. 2015, *ApJ*, 810, 72
- Mancuso, C., Lapi, A., Prandoni, I., et al. 2017, *ApJ*, 842, 95
- Markevitch, M., Gonzalez, A. H., Clowe, D., et al. 2004, *ApJ*, 606, 819
- Marshall, H. L. 1985, *ApJ*, 299, 109
- Massardi, M., Bonaldi, A., Negrello, M., et al. 2010, *MNRAS*, 404, 532
- Matthee, J., Sobral, D., Boogaard, L. A., et al. 2019, *ApJ*, 881, 124
- Matthews, A. M., Condon, J. J., Cotton, W. D., & Mauch, T. 2021, *ApJ*, 914, 126
- Matthews, T. A., & Sandage, A. R. 1963, *ApJ*, 138, 30
- Mauch, T., & Sadler, E. M. 2007, *MNRAS*, 375, 931
- Mauch, T., Cotton, W. D., Condon, J. J., et al. 2020, *ApJ*, 888, 61
- McAlpine, K., Jarvis, M. J., & Bonfield, D. G. 2013, *MNRAS*, 436, 1084
- McCheyne, I., Oliver, S., Sargent, M., et al. 2022, *A&A*, 662, A100
- McLeod, D. J., McLure, R. J., Dunlop, J. S., et al. 2015, *MNRAS*, 450, 3032
- McLure, R. J., Dunlop, J. S., Bowler, R. A. A., et al. 2013, *MNRAS*, 432, 2696
- McMullin, J. P., Waters, B., Schiebel, D., Young, W., & Golap, K. 2007, in *Astronomical Society of the Pacific Conference Series*, Vol. 376, *Astronomical Data Analysis Software and Systems XVI*, ed. R. A. Shaw, F. Hill, & D. J. Bell, 127
- Mehta, V., Scarlata, C., Rafelski, M., et al. 2017, *ApJ*, 838, 29
- Mendez, A. J., Coil, A. L., Aird, J., et al. 2013, *ApJ*, 770, 40
- Meurer, G. R., Heckman, T. M., & Calzetti, D. 1999, *ApJ*, 521, 64
- Mezger, P. G., & Henderson, A. P. 1967, *ApJ*, 147, 471
- Michałowski, M., Hjorth, J., & Watson, D. 2010, *A&A*, 514, A67
- Miettinen, O., Delvecchio, I., Smolčić, V., et al. 2017, *A&A*, 606, A17
- Miyaji, T., Griffiths, R. E., & C-COSMOS Team. 2008, in *AAS/High Energy Astrophysics Division*, Vol. 10, *AAS/High Energy Astrophysics Division #10*, 4.01
- Mohan, N., & Rafferty, D. 2015, *PyBDSF: Python Blob Detection and Source Finder*, *Astrophysics Source Code Library*, ascl:1502.007
- Molnár, D. C., Sargent, M. T., Delhaize, J., et al. 2018, *MNRAS*, 475, 827
- Molnár, D. C., Sargent, M. T., Leslie, S., et al. 2021, *MNRAS*, 504, 118
- Morrison, G. E., Owen, F. N., Dickinson, M., Ivison, R. J., & Ibar, E. 2010, *ApJS*, 188, 178
- Moster, B. P., Naab, T., & White, S. D. M. 2018, *MNRAS*, 477, 1822
- Moster, B. P., Somerville, R. S., Newman, J. A., & Rix, H.-W. 2011, *ApJ*, 731, 113
- Mullaney, J. R., Alexander, D. M., Goulding, A. D., & Hickox, R. C. 2011, *MNRAS*, 414, 1082

- Murphy, E. J. 2009, *ApJ*, 706, 482
- Murphy, E. J., Momjian, E., Condon, J. J., et al. 2017, *ApJ*, 839, 35
- Murphy, E. J., Condon, J. J., Schinnerer, E., et al. 2011, *ApJ*, 737, 67
- Murphy, E. J., Bremseth, J., Mason, B. S., et al. 2012, *ApJ*, 761, 97
- Murphy, E. J., Dong, D., Leroy, A. K., et al. 2015, *ApJ*, 813, 118
- Nayyeri, H., Hemmati, S., Mobasher, B., et al. 2017, *The Astrophysical Journal Supplement Series*, 228, 7
- Nikolic, B., & Bolton, R. C. 2012, *MNRAS*, 425, 1257
- Noeske, K. G., Weiner, B. J., Faber, S. M., et al. 2007, *ApJL*, 660, L43
- Novak, M., Smolčić, V., Schinnerer, E., et al. 2018, *A&A*, 614, A47
- Novak, M., Smolčić, V., Delhaize, J., et al. 2017, *A&A*, 602, A5
- Ocran, E. F., Taylor, A. R., Vaccari, M., et al. 2020, *MNRAS*, 491, 5911
- Oesch, P. A., Bouwens, R. J., Illingworth, G. D., Labbé, I., & Stefanon, M. 2018, *ApJ*, 855, 105
- Offringa, A. R. 2010, *AOFlagger: RFI Software*, *Astrophysics Source Code Library*, ascl:1010.017
- Offringa, A. R., & Smirnov, O. 2017, *MNRAS*, 471, 301
- Offringa, A. R., McKinley, B., Hurley-Walker, N., et al. 2014, *WSClean: Widefield interferometric imager*, *Astrophysics Source Code Library*, ascl:1408.023
- Ono, Y., Ouchi, M., Harikane, Y., et al. 2018, *PASJ*, 70, S10
- Owen, F. N. 2018, *ApJS*, 235, 34
- Owen, F. N., & Morrison, G. E. 2008, *AJ*, 136, 1889
- Padovani, P., Bonzini, M., Kellermann, K. I., et al. 2015, *MNRAS*, 452, 1263
- Padovani, P., Mainieri, V., Tozzi, P., et al. 2009, *ApJ*, 694, 235
- Pannella, M., Carilli, C. L., Daddi, E., et al. 2009, *ApJL*, 698, L116
- Pannella, M., Elbaz, D., Daddi, E., et al. 2015, *ApJ*, 807, 141
- Parsa, S., Dunlop, J. S., McLure, R. J., & Mortlock, A. 2016, *MNRAS*, 456, 3194
- Pavesi, R., Sharon, C. E., Riechers, D. A., et al. 2018, *ApJ*, 864, 49
- Peebles, P. J., & Ratra, B. 2003, *Reviews of Modern Physics*, 75, 559
- Penzias, A. A., & Wilson, R. W. 1965, *ApJ*, 142, 419
- Pérez-González, P. G., Barro, G., Annunziatella, M., et al. 2023, *ApJL*, 946, L16
- Perley, R. A., & Butler, B. J. 2013, *ApJS*, 204, 19
- Planck Collaboration, Akrami, Y., Ashdown, M., et al. 2020, *A&A*, 641, A4
- Pope, A., & Chary, R.-R. 2010, *ApJL*, 715, L171
- Prandoni, I., Gregorini, L., Parma, P., et al. 2001, *A&A*, 365, 392
- Prandoni, I., Guglielmino, G., Morganti, R., et al. 2018, *MNRAS*, 481, 4548
- Puget, J. L., Abergel, A., Bernard, J. P., et al. 1996, *A&A*, 308, L5
- Puglisi, A., Daddi, E., Liu, D., et al. 2019, *ApJL*, 877, L23
- Rau, U., & Cornwell, T. J. 2011, *A&A*, 532, A71
- Rho, J., Kozasa, T., Reach, W. T., et al. 2008, *ApJ*, 673, 271
- Richards, E. A. 2000, *ApJ*, 533, 611
- Riechers, D. A., Bradford, C. M., Clements, D. L., et al. 2013, *Nature*, 496, 329
- Riechers, D. A., Pavesi, R., Sharon, C. E., et al. 2019, *ApJ*, 872, 7
- Riechers, D. A., Hodge, J. A., Pavesi, R., et al. 2020, *ApJ*, 895, 81
- Rigby, E. E., Best, P. N., Brookes, M. H., et al. 2011, *MNRAS*, 416, 1900
- Rodighiero, G., Vaccari, M., Franceschini, A., et al. 2010, *A&A*, 515, A8

- Rowan-Robinson, M., Benn, C. R., Lawrence, A., McMahon, R. G., & Broadhurst, T. J. 1993, *MNRAS*, 263, 123
- Rowan-Robinson, M., Oliver, S., Wang, L., et al. 2016, *MNRAS*, 461, 1100
- Rubin, V. C., & Ford, W. K., J. 1970, in *The Spiral Structure of our Galaxy*, ed. W. Becker & G. I. Kontopoulos, Vol. 38, 61
- Rujopakarn, W., Dunlop, J. S., Rieke, G. H., et al. 2016, *ApJ*, 833, 12
- Ryle, M., & Scheuer, P. A. G. 1955, *Proceedings of the Royal Society of London Series A*, 230, 448
- Sabater, J., Best, P. N., Hardcastle, M. J., et al. 2019, *A&A*, 622, A17
- Sadler, E. M., Jenkins, C. R., & Kotanyi, C. G. 1989, *MNRAS*, 240, 591
- Salim, S., & Narayanan, D. 2020, *ARA&A*, 58, 529
- Salim, S., Rich, R. M., Charlot, S., et al. 2007, *ApJS*, 173, 267
- Salmon, B., Papovich, C., Finkelstein, S. L., et al. 2015, *ApJ*, 799, 183
- Salpeter, E. E. 1955, *ApJ*, 121, 161
- Sargent, M. T., Béthermin, M., Daddi, E., & Elbaz, D. 2012, *ApJL*, 747, L31
- Sargent, M. T., Schinnerer, E., Murphy, E., et al. 2010, *ApJS*, 186, 341
- Saunders, W., Rowan-Robinson, M., Lawrence, A., et al. 1990, *MNRAS*, 242, 318
- Schinnerer, E., Smolčić, V., Carilli, C. L., et al. 2007, *ApJS*, 172, 46
- Schinnerer, E., Sargent, M. T., Bondi, M., et al. 2010, *ApJS*, 188, 384
- Schmidt, M. 1968, *ApJ*, 151, 393
- Schreiber, C., Pannella, M., Elbaz, D., et al. 2015, *A&A*, 575, A74
- Scoville, N. 2007, in *Astronomical Society of the Pacific Conference Series*, Vol. 375, *From Z-Machines to ALMA: (Sub)Millimeter Spectroscopy of Galaxies*, ed. A. J. Baker, J. Glenn, A. I. Harris, J. G. Mangum, & M. S. Yun, 166
- Scoville, N., Arnouts, S., Aussel, H., et al. 2013, *ApJS*, 206, 3
- Seymour, N., McHardy, I. M., & Gunn, K. F. 2004, *MNRAS*, 352, 131
- Seymour, N., Dwelly, T., Moss, D., et al. 2008, *MNRAS*, 386, 1695
- Shakeshaft, J. R., Ryle, M., Baldwin, J. E., Elsmore, B., & Thomson, J. H. 1955, *MmRAS*, 67, 106
- Shen, X., Vogelsberger, M., Nelson, D., et al. 2022, *MNRAS*, 510, 5560
- Shu, X., Yang, L., Liu, D., et al. 2022, *ApJ*, 926, 155
- Shull, J. M., Smith, B. D., & Danforth, C. W. 2012, *ApJ*, 759, 23
- Siana, B., Teplitz, H. I., Chary, R.-R., Colbert, J., & Frayer, D. T. 2008, *ApJ*, 689, 59
- Siana, B., Smail, I., Swinbank, A. M., et al. 2009, *ApJ*, 698, 1273
- Sijacki, D., Springel, V., Di Matteo, T., & Hernquist, L. 2007, *MNRAS*, 380, 877
- Simpson, J. M., Swinbank, A. M., Smail, I., et al. 2014, *ApJ*, 788, 125
- Simpson, J. M., Smail, I., Swinbank, A. M., et al. 2019, *ApJ*, 880, 43
- Simpson, J. M., Smail, I., Dudzevičiūtė, U., et al. 2020, *MNRAS*, 495, 3409
- Smail, I., Ivison, R. J., & Blain, A. W. 1997, *ApJL*, 490, L5
- Smail, I., Ivison, R. J., Kneib, J. P., et al. 1999, *MNRAS*, 308, 1061
- Smail, I., Dudzevičiūtė, U., Stach, S. M., et al. 2021, *MNRAS*, 502, 3426
- Smith, D. J. B., Haskell, P., Gürkan, G., et al. 2021, *A&A*, 648, A6
- Smolčić, V., Zamorani, G., Schinnerer, E., et al. 2009a, *ApJ*, 696, 24
- Smolčić, V., Schinnerer, E., Zamorani, G., et al. 2009b, *ApJ*, 690, 610
- Smolčić, V., Novak, M., Bondi, M., et al. 2017a, *A&A*, 602, A1

- Smolčić, V., Delvecchio, I., Zamorani, G., et al. 2017b, *A&A*, 602, A2
- Solomon, P. M., Downes, D., & Radford, S. J. E. 1992, *ApJL*, 398, L29
- Speagle, J. S., Steinhardt, C. L., Capak, P. L., & Silverman, J. D. 2014, *ApJS*, 214, 15
- Springel, V., White, S. D. M., Jenkins, A., et al. 2005, *Nature*, 435, 629
- Stach, S. M., Dudzevičiūtė, U., Smail, I., et al. 2019, *MNRAS*, 487, 4648
- Stanley, F., Jones, B. M., Riechers, D. A., et al. 2023, *ApJ*, 945, 24
- Steidel, C. C., Giavalisco, M., Dickinson, M., & Adelberger, K. L. 1996, *AJ*, 112, 352
- Sullivan, W. T. 1984, *The early years of radio astronomy - Reflections fifty years after Jansky's discovery* (Cambridge: Cambridge University Press)
- Swinbank, A. M., Simpson, J. M., Smail, I., et al. 2014, *MNRAS*, 438, 1267
- Symeonidis, M., & Page, M. J. 2021, *MNRAS*, 503, 3992
- Symeonidis, M., Georgakakis, A., Page, M. J., et al. 2014, *Monthly Notices of the Royal Astronomical Society*, 443, 3728
- Tabatabaei, F. S., Schinnerer, E., Krause, M., et al. 2017, *ApJ*, 836, 185
- Talia, M., Cimatti, A., Giulietti, M., et al. 2021, *ApJ*, 909, 23
- Taylor, M. B. 2005, in *Astronomical Society of the Pacific Conference Series*, Vol. 347, *Astronomical Data Analysis Software and Systems XIV*, ed. P. Shopbell, M. Britton, & R. Ebert, 29
- Tisanić, K., Smolčić, V., Delhaize, J., et al. 2019, *A&A*, 621, A139
- Tomczak, A. R., Quadri, R. F., Tran, K.-V. H., et al. 2016, *ApJ*, 817, 118
- Turner, J. L., & Ho, P. T. P. 1983, *ApJL*, 268, L79
- Turner, J. L., & Ho, P. T. P. 1985, *ApJL*, 299, L77
- van der Vlugt, D., Hodge, J. A., Algera, H. S. B., et al. 2022, *ApJ*, 941, 10
- van der Vlugt, D., Algera, H. S. B., Hodge, J. A., et al. 2021, *ApJ*, 907, 5
- van der Vlugt, D., Hodge, J. A., Jin, S., et al. 2023, *ApJ*, 951, 131
- van der Walt, S., Colbert, S. C., & Varoquaux, G. 2011, *Computing in Science and Engineering*, 13, 22
- van Haarlem, M. P., Wise, M. W., Gunst, A. W., et al. 2013, *A&A*, 556, A2
- Vernstrom, T., Scott, D., Wall, J. V., et al. 2016, *MNRAS*, 462, 2934
- Vernstrom, T., Scott, D., Wall, J. V., et al. 2014, *MNRAS*, 440, 2791
- Viironen, K., López-Sanjuan, C., Hernández-Monteagudo, C., et al. 2018, *A&A*, 614, A129
- Walter, F., Weiß, A., Downes, D., Decarli, R., & Henkel, C. 2011, *ApJ*, 730, 18
- Walter, F., Decarli, R., Carilli, C., et al. 2012, *ApJ*, 752, 93
- Wang, T., Schreiber, C., Elbaz, D., et al. 2019, *Nature*, 572, 211
- Wang, W.-H., Barger, A. J., & Cowie, L. L. 2009, *ApJ*, 690, 319
- Wang, W.-H., Lin, W.-C., Lim, C.-F., et al. 2017, *ApJ*, 850, 37
- Weaver, J. R., Kauffmann, O. B., Ilbert, O., et al. 2022, *ApJS*, 258, 11
- White, G. J., Hatsukade, B., Pearson, C., et al. 2012, *MNRAS*, 427, 1830
- White, S. D. M., & Rees, M. J. 1978, *MNRAS*, 183, 341
- Williams, W. L., van Weeren, R. J., Röttgering, H. J. A., et al. 2016, *MNRAS*, 460, 2385
- Wilman, R. J., Miller, L., Jarvis, M. J., et al. 2008, *MNRAS*, 388, 1335
- Windhorst, R., Mathis, D., & Neuschaefer, L. 1990, in *Astronomical Society of the Pacific Conference Series*, Vol. 10, *Evolution of the Universe of Galaxies*, ed. R. G.

- Kron, 389–403
- Wise, J. H. 2019, arXiv e-prints, arXiv:1907.06653
- Wootten, A., & Thompson, A. R. 2009, *IEEE Proceedings*, 97, 1463
- Xiao, M. Y., Elbaz, D., Gómez-Guijarro, C., et al. 2023, *A&A*, 672, A18
- Yang, C., Gavazzi, R., Beelen, A., et al. 2019, *A&A*, 624, A138
- Yun, M. S., Reddy, N. A., & Condon, J. J. 2001, *ApJ*, 554, 803
- Zavala, J. A., Casey, C. M., Manning, S. M., et al. 2021, *ApJ*, 909, 165

Summary

The first stars and galaxies formed a few hundred million years after the *Big Bang*, the beginning of the Universe, which occurred some 13 billion years ago. The foundations from which those galaxies formed were established shortly after the Big Bang. To understand how galaxies and star formation evolved from that period to the present day is a challenging and complex question, considering that the processes involved work on very different size scales and time ranges. A group of stars forms on a much smaller scale than a galaxy, for example, while it takes millions of years to build up a galaxy-size population of stars, since the gas from which the stars are formed first has to cool and fall on the galaxy from large distances. Because of the large timescales, the evolution of galaxies cannot be followed in real time, but can be inferred using the finite speed of light. Light emitted by galaxies at great distances from Earth needs time to reach the observing telescopes. Galaxies are thus observed as they appeared when the light was emitted. Furthermore, the wavelength of light emitted increases because of the expansion of the Universe. In other words, the light emitted by galaxies reddens depending on the distance it has to travel to its observers, an effect known as *redshift* (z). Redshift can be measured to precisely determine the distance to a galaxy, thereby establishing the time at which the light was emitted. By observing many different galaxies at different stages in their evolution and across various cosmic epochs, we can attempt to infer and stitch together their evolutionary pathways.

Stars are the most visible constituents of galaxies and can be studied to help us understand how galaxies evolve. Stars are born from molecular clouds and the rate at which they form, the *star formation rate*, is a crucial parameter used to describe the evolution of a galaxy. Since it is not possible to observe single stars in galaxies at great distances, sophisticated techniques are needed to measure the buildup of stars in galaxies. For instance, to obtain as much detail as possible about the galaxies observed, measurements involve not only optical wavelengths of light, but also light emitted at other wavelengths, such as ultraviolet, low-energy infrared, millimeter and radio wavelengths. Ultraviolet light is emitted by young massive stars, such that this wavelength range of the spectrum traces galaxies that are actively star-forming. However, dust obscures ultraviolet light which means star formation can be partly obscured. Additionally, some of the most intense *star-forming galaxies* appear dark when observed at ultraviolet wavelengths and are thus missed in ultraviolet based measurements. The obscuring dust is heated by the young massive stars and re-emits the light absorbed at (longer) infrared wavelengths. Hence, dust-obscured star formation can be observed by means of infrared observations. However, infrared-based measurements also have limitations on their capacity to measure star formation accurately. Infrared telescopes lack the sensitivity to detect galaxies in the very early Universe and have poorer resolution, meaning galaxies are not delimited as sharply and some galaxies may blend together in observations. Ground-based sub-millimeter/millimeter continuum observations can help to overcome some of the problems in infrared observations. They offer high resolution and hence do not suffer from source blending.

However, the field of view of sub-millimeter/millimeter telescopes are typically small which means many expensive observations are needed to overcome cosmic variance. Observations at radio wavelengths provide both high resolution and do not suffer from dust attenuation. In addition, they generally have a large field of view. Radio observations offer therefore an alternative way of studying star formation in galaxies and form the main topic of this thesis.

Measuring star formation with radio observations

Radio observations, carried out with the *Very Large Array* (VLA) in New Mexico, USA, are used in this thesis to trace star formation in galaxies. The VLA constitutes an *interferometer*, which uses 27 antennas to reach the angular resolution and depth needed to study star formation in galaxies at high redshift. Radio emission in star-forming galaxies has two components related to star formation: *free-free emission* and *synchrotron radiation*. Free-free emission is produced directly by young massive stars, while synchrotron radiation arises from *supernova* remnants associated with the death of those young massive stars. Isolating the free-free component and measuring its flux density is difficult since free-free emission is much fainter than synchrotron radiation. Synchrotron emission can therefore be used more easily as a star formation tracer. However, when studying star formation in galaxies using radio observations, it is important to verify that the observed radio emissions are indeed produced by stars. Notably, accreting *supermassive black holes* located in the centers of galaxies, known as *active galactic nuclei*, can also produce synchrotron emission.

Redshifts of a sample of observed radio sources are needed to perform more advanced analysis on the sample, such as measuring the evolution of the star formation rate as function of time. Since the radio spectrum mimics by a featureless power law, radio observations alone cannot constrain the redshift. Multi-wavelength data, either from *photometric* or *spectroscopic* surveys, are thus needed to determine redshifts for radio sources. Photometric surveys give the average brightness of a galaxy over a fixed wavelength band, with a single data point per band, whereas spectroscopic surveys deliver a high-resolution spectrum of a galaxy. Obtaining photometric redshift is cheaper and can be done over larger survey areas, but the redshifts obtained are more uncertain. Spectroscopic redshifts are measured to high precisions by means of time-consuming spectroscopic surveys. Spectroscopic redshifts are therefore more reliable than photometric redshifts. Targeting carbon-monoxide (CO) is a relatively efficient method for obtaining spectroscopic redshifts for radio sources with photometric redshifts. CO is the second most abundant molecule present in the cold gas and dust that fills the space between stars, the *interstellar medium*. The rotational transitions of CO have a very low excitation temperature meaning CO gets easily excited and emits emission even in cold molecular clouds. The CO transitions emit radiation at specific sub-millimeter wavelengths. The *Atacama Large Millimeter/sub-millimeter Array* (ALMA) in the Atacama desert, Chili, is an interferometer comprised of 66 antennae with a frequency coverage and sensitivity which enables it to target CO transitions and thus obtain spectroscopic redshifts for gas/dust-rich sources at high redshift.

A sample of radio sources with determined redshifts and for which radio emissions solely result from star formation can be used to determine the evolution of star formation throughout the history of the Universe. Radio observations probe recent star formation and are especially valuable for probing dust-obscured star formation as even the most extreme star-forming galaxies enshrouded in dust can be observed. However, it is not trivial to use radio observations to determine star formation rates. The processes which link supernova remnants to synchrotron emission are complex and involve taking account of many key factors. Fortunately, the *far-infrared-radio-correlation* can be used. This correlation describes the link between the radio and infrared luminosities of galaxies, which has been observed across a wide variety of galaxy types, as well as out to high redshift. Since infrared luminosity is proportional to star formation rate, the far-infrared-radio-correlation can be used to convert synchrotron luminosities to star formation rates.

With the help of the far-infrared-radio-correlation, radio observations can be used to study the evolution of the star formation rate per unit volume, or the *cosmic star formation rate density*, as a function of redshift. This parameter is one of the most fundamental tools for understanding how star formation proceeds globally across cosmic time. Previous studies have shown that about 10 billion years ago, eight times more stars were formed in the Universe than today. This can be seen in Figure 1.4, which shows the cosmic star formation rate density as a function of redshift. However, most studies measuring the cosmic star formation rate density at high redshift use ultraviolet observations, a wavelength range prone to dust attenuation. This motivates the work presented in this thesis. The first two chapters outline how we obtain our radio observations and use them to measure the cosmic star formation rate density with a dust-unbiased tracer. These radio observations are also used to uncover the ‘*optically dark*’ population: extremely dust-obscured sources that are invisible even in deep ultraviolet imaging. Different studies have examined the contribution of these sources to the cosmic star formation rate density, yet have found constraints that still span more than an order of magnitude in range. The work in chapters three and four provides constraints on the contribution of ‘optically dark’ sources selected from our radio observations to the cosmic star formation rate density.

The COSMOS-XS survey

In this thesis the dust-obscured star formation is studied using the sensitive COSMOS-XS survey. Carried out with the upgraded VLA, COSMOS-XS provides some of the deepest radio observations to date at two frequencies: 10 GHz and 3 GHz (i.e., X- and S-bands). The survey was conducted in the COSMOS field, a 2 deg^2 field which has been observed with all leading ground-based and satellite facilities, yielding a rich multi-wavelength data set. Combining all these sources, the COSMOS-XS survey presents a unique data set that allows us to study the faintest radio populations that can currently be probed. The COSMOS-XS survey also reaches very faint flux densities which gives the ability to trace ‘normal’ galaxies over the epoch at which star formation in the Universe peaked, 10 billion years ago. Analysis of the COSMOS-XS survey and our resulting conclusions regarding the dust-obscured star formation rate

are the subject of this thesis. The chapters of the thesis are summarized below.

This thesis

In this thesis, we present the radio observations from the VLA COSMOS-XS survey and use them to trace dust-unbiased star formation over cosmic time. **Chapter One** introduces the current state of the field and additionally provides the necessary background for the subsequent chapters.

In **Chapter Two**, we discuss the details of the COSMOS-XS survey and present the radio catalogs with the observed radio sources. Counting the number of galaxies or, in other terms, constraining the source counts, is the simplest statistical analysis that can be performed with a flux-limited radio survey. It provides information on the evolutionary properties of sources. The deep 10 and 3 GHz observations enable us to investigate the Euclidean-normalized source counts down to faint flux densities. We show that our observations are consistent within uncertainties with other results at 3 and 1.4 GHz, but extend to fainter flux densities than previous direct detections.

In **Chapter Three**, we use the COSMOS-XS survey to select star-forming galaxies with the far-infrared-radio-correlation. These galaxies are used to constrain the radio luminosity function. The luminosity function gives the cosmic density of sources in bins of luminosity. It can be used to constrain the evolutionary path of star-forming galaxies. We present evidence for significant density evolution over the observed redshift range. We use the radio luminosity functions to derive the dust-unbiased star formation rate density out to $z \sim 4.6$. Using this dust-unbiased survey, we present evidence for a significant underestimation of the star formation rate density based on the ultraviolet luminosity functions at high redshift.

In **Chapter Four**, the focus shifts to ‘optically dark’ galaxies. We use the 3 GHz radio map from the COSMOS-XS survey to identify these sources. We utilize the new ‘Super-deblended’ far-infrared catalog to find the photometric redshifts of the ‘optically dark’ sources. The far-infrared catalog adopts a novel deblending technique to address sources that are blended together. This catalog takes the positions of the sources detected in the COSMOS-XS survey as priors. Using the ‘Super-deblended’ catalog, we derive the far-infrared-based photometric redshifts of the sources to be between $z = 2$ and $z = 5$. We then quantify the contribution of ‘optically dark’ sources to the total star formation rate density using the method described in chapter three, and find that they play a non-negligible role at high redshift.

Building on the results of chapter four, we present new ALMA observations of ‘optically dark’ sources in **Chapter Five**. These ALMA observations comprise a scan of the frequency range 84–108 GHz. In this way the observations are sensitive to CO emission in the cosmic volume without specifically targeting CO lines. With the ALMA scans we can determine the spectroscopic redshifts for a sub-sample of 10 radio-selected ‘optically dark’ galaxies. We find CO-based redshifts that confirm that the ‘optically dark’ sources targeted lie at $z \gtrsim 3$. By integrating the luminosity functions found in chapter four to the flux limit of the targeted sub-sample, we determine that the star formation rate density is in agreement with the star formation rate density found for the 10 ALMA detected ‘optically dark’ sources. This confirms the cosmic importance of ‘optically dark’ sources at high redshift.

Nederlandse samenvatting

Pas een paar honderd miljoen jaar na de *Big bang* – het ontstaan van het universum dat ongeveer 13 miljard jaar geleden plaatsvond – vormden zich de eerste sterren en sterrenstelsels. De basis voor het ontstaan van deze sterrenstelsels werd echter al kort na de Big Bang gelegd. Het begrijpen van de vorming van sterren en sterrenstelsels is complex en uitdagend. Dit omdat deze processen sterk variëren in zowel grootte als tijd. De formatie van een sterrenstelsel vindt plaats op veel grotere schaal dan de vorming van een groep sterren. Bovendien duurt het miljoenen jaren om een populatie sterren op te bouwen met de grootte van een sterrenstelsel. Het gas waar de sterren van gevormd worden moet namelijk eerst afkoelen en van grote afstanden op het sterrenstelsel vallen. Omdat de evolutie van een sterrenstelsel niet in werkelijke tijd gevolgd kan worden, wordt gebruik gemaakt van de eindige lichtsnelheid. Het licht dat wordt uitgezonden door sterrenstelsels heeft namelijk veel tijd nodig om onze telescopen op grote afstand van deze sterrenstelsels te bereiken. Wij zien de sterrenstelsels dus zoals ze waren toen het licht werd uitgezonden. Bovendien wordt de golflengte van het uitgezonden licht langer door de uitdijning van het heelal. Hoe groter de afstand die het door sterrenstelsels uitgezonden licht naar zijn waarnemers moet afleggen, hoe roder dit licht wordt. Dit effect heet *roodverschuiving* (z) en is meetbaar. Aan de hand van de roodverschuiving kan de afstand tot een sterrenstelsel, en dus de tijd waarop het licht werd uitgezonden, precies bepaald worden. Door verschillende sterrenstelsels waar te nemen op verschillende momenten in hun evolutie en tijdens verschillende kosmische perioden proberen we om de ontwikkelingen van sterrenstelsels te beschrijven en aan elkaar te verbinden.

Sterren zijn het meest zichtbare onderdeel van sterrenstelsels en kunnen gebruikt worden om te bestuderen hoe sterrenstelsels zich ontwikkelen. Sterren worden geboren uit moleculaire wolken en de snelheid waarmee ze worden gevormd, de *ster-vormingssnelheid*, is een cruciale parameter die gebruikt wordt om de evolutie van sterrenstelsels te beschrijven. Omdat sterren in sterrenstelsels die zich op grote afstand bevinden niet afzonderlijk kunnen worden waargenomen, zijn er geavanceerde technieken nodig om de vorming van deze sterren te meten. Om zoveel mogelijk informatie te vergaren wordt niet enkel optisch licht, maar ook licht dat wordt uitgezonden op andere golflengten zoals ultraviolet, lage energie infrarood, millimeter en radiogolflengten gebruikt. Ultraviolet licht wordt uitgezonden door jonge, zware sterren. Dit golflengtebereik van het spectrum kan daarom gelinkt worden aan sterrenstelsels die actief sterren vormen. Stof verduistert ultraviolet licht en verhult daarmee een deel van de stervorming. Ook kunnen de meest heftig *stervormende sterrenstelsels* er donker uitzien op ultravioletgolflengten waardoor deze sterrenstelsels niet direct waargenomen worden in ultravioletwaarnemingen. Het verduisterende stof wordt verhit door de jonge, zware sterren en zendt het geabsorbeerde licht opnieuw uit op (langere) infraroodgolflengten. Aan de hand van die infraroodwaarnemingen kan dus de met stof verhulde stervorming bepaald worden. Op hun beurt hebben infraroodmetingen echter ook eigenschappen die het vermogen om accuraat de stervorming

te bepalen beperken. Infrarood telescopen missen bijvoorbeeld de gevoeligheid om sterrenstelsels waar te nemen in het jonge heelal. Door de slechtere resolutie worden sterrenstelsels niet scherp waargenomen waardoor sommige sterrenstelsels mogelijk niet meer te onderscheiden zijn. Aardse submillimeter/millimeter continue waarnemingen hebben een hogere resolutie en kunnen helpen om dit probleem van vermenigving op te lossen. Millimeter waarnemingen kunnen echter slechts een klein deel van de hemel waarnemen waardoor veel dure waarnemingen nodig zijn om het probleem van kosmische variantie te ondervangen. Waarnemingen op radiogolflengten hebben daarentegen geen last van het verduisterende stof en zijn bovendien in hoge resolutie. Ook nemen ze over het algemeen een groot deel van de hemel waar. Omdat radiowaarnemingen een alternatieve manier bieden om de stervorming in sterrenstelsels te bestuderen, vormen zij het hoofdonderwerp van dit proefschrift.

Stervorming bepalen met radiowaarnemingen

Om de stervorming in sterrenstelsels te bepalen wordt in dit proefschrift gebruik gemaakt van radiowaarnemingen van de *Very Large Array* (VLA) in New Mexico in de Verenigde Staten. De VLA is een *interferometer* bestaande uit 27 antennes waarmee de hoge resolutie en de gevoeligheid bereikt kunnen worden die nodig zijn om stervorming in sterrenstelsels op hoge roodverschuiving te kunnen bestuderen. Radiostraling afkomstig van stervormende sterrenstelsels bestaat uit twee componenten die gerelateerd zijn aan stervorming: *remstraling* and *synchrotronstraling*. Remstraling komt direct van jonge, massieve sterren; synchrotronstraling daarentegen komt voort uit de overblijfselen van *supernova's* ontstaan door de dood van deze jonge, massieve sterren. Omdat remstraling gekenmerkt wordt door een lagere flux dan synchrotronstraling, is het isoleren van deze straling en het meten van de bijbehorende fluxdichtheid lastig. Synchrotronstraling kan daarom beter gebruikt worden om stervorming te bepalen. Wel is het bij het bestuderen van stervorming met behulp van radiowaarnemingen belangrijk om te verifiëren dat de radio-emissie daadwerkelijk door sterren geproduceerd wordt. Synchrotronstraling kan namelijk ook geproduceerd worden door *superzwarte zwarte gaten* die materie accrediteren. Deze zwarte gaten die zich in het midden van sterrenstelsels bevinden, worden ook wel *actieve sterrenstelsels* genoemd.

De roodverschuivingen van waargenomen radiobronnen zijn essentieel voor het meten van de evolutie van de stervormingssnelheid als functie van tijd. Het radiospectrum kan echter niet op zichzelf gebruikt worden om de roodverschuiving te achterhalen. Dit omdat de machtsfunctie die dit spectrum beschrijft geen kenmerken heeft. Door metingen op meerdere golflengtes – van *fotometrische* of *spectroscopische* waarnemingsprogramma's – te gebruiken, kunnen de roodverschuivingen van radiobronnen vastgesteld worden. Fotometrische waarnemingsprogramma's meten de gemiddelde helderheid van een sterrenstelsel over een vaste golflengteband, met een enkel meetpunt per band. Het verkrijgen van fotometrische roodverschuivingen is daardoor relatief goedkoop en de waarnemingen beslaan bovendien een groter deel van de hemel. Wel zijn verkregen fotometrische roodverschuivingen minder precies dan spectroscopische, die het spectrum van een sterrenstelsel op hoge resolutie meten. Al-

hoewel spectroscopische waarnemingsprogramma's veel tijd kosten en daardoor kostbaarder zijn, zijn spectroscopische roodverschuivingen dus beduidend betrouwbaarder dan fotometrische. Om spectroscopische roodverschuivingen te verkrijgen voor radiobronnen met fotometrische roodverschuivingen kan gebruik worden gemaakt van de straling die koolstofmonoxide (CO) uitzendt. CO is het tweede meest voorkomende molecuul in het gas en stof dat zich bevindt tussen de sterren in een sterrenstelsel, het *interstellair medium*. De rotationele overgangen van CO worden op lage temperaturen aangeslagen waardoor CO zelfs in koude moleculaire wolken makkelijk wordt aangeslagen en straling uitzendt. Deze straling wordt uitgezonden op specifieke submillimeter golflengten. De *Atacama Large Millimeter/submillimeter Array* (ALMA) in de Atacama woestijn in Chili is een interferometer bestaande uit 66 antennes die door haar golflengtebereik en gevoeligheid gebruikt kan worden voor het waarnemen van deze CO-overgangen. Met ALMA kunnen dus de zo cruciale spectroscopische roodverschuivingen van gas- en/of stofrijke bronnen op hoge roodverschuiving verkregen worden.

Wanneer de radiohelderheid van een groep radiobronnen enkel voortkomt uit stervorming en de roodverschuiving van deze bronnen bekend is, kunnen zij gebruikt worden om de evolutie van stervorming gedurende de geschiedenis van het heelal vast te stellen. Radiowaarnemingen stellen ons in staat om zowel recente stervorming als de meest extreem stervormende sterrenstelsels gehuld in stof te bestuderen. Zij zijn daarom erg waardevol. Toch is het niet geheel triviaal om radiowaarnemingen te gebruiken voor het vaststellen van de stervormingssnelheid. De eerdergenoemde fysische processen die ertoe leiden dat supernova overblijfselen uiteindelijk synchrotronstraling uitstralen zijn complex. Gelukkig biedt de zogenoemde *ver-infrarood-radio-correlatie* uitkomst. Deze correlatie beschrijft de link tussen de radio- en infraroodhelderheid van sterrenstelsels en is waargenomen voor veel verschillende typen sterrenstelsels en tot op hoge roodverschuiving. Omdat de ver-infraroodhelderheid evenredig is met stervorming, kan de ver-infrarood-radio-correlatie ons helpen om de synchrotonhelderheid te vertalen naar stervormingssnelheid.

Met behulp van de ver-infrarood-radio-correlatie kunnen radiowaarnemingen gebruikt worden om de evolutie van de stervormingssnelheid per eenheid van volume – de *kosmische dichtheid van stervormingssnelheid* – als functie van roodverschuiving te bestuderen. Deze parameter maakt inzichtelijk hoe stervorming globaal verloopt over kosmische tijd. Onderzoek toont aan dat ongeveer 10 miljard jaar geleden acht keer meer sterren werden gevormd in het universum dan vandaag de dag. Dit kan ook worden gezien in Figuur 1.4, dat de kosmische dichtheid van de stervormingssnelheid als een functie van roodverschuiving laat zien. De meeste studies die de kosmische dichtheid van stervormingssnelheid meten op hoge roodverschuiving maken echter gebruik van ultravioletwaarnemingen, een golflengte vatbaar voor verduistering door stof. In de eerste twee hoofdstukken van dit proefschrift beschrijven we onze radiowaarnemingen en hoe wij deze gebruiken als een indicator van de kosmische dichtheid van stervormingssnelheid. Deze radiowaarnemingen worden ook gebruikt om de zogenoemde ‘*optisch donkere*’ populatie waar te nemen. Deze extreem door stof omhulde bronnen zijn namelijk onzichtbaar voor zelfs de gevoeligste ultravioletwaarnemingen. De bijdrage van deze ‘optisch donkere’ bronnen aan de kosmische dichtheid van stervormingssnelheid is onderwerp van discussie: verschillende studies

vonden sterk uiteenlopende bijdragen. In hoofdstuk drie en vier stellen we vast wat de bijdrage van de uit onze radiowaarnemingen geselecteerde ‘optisch donkere’ bronnen is aan de kosmische dichtheid van stervormingssnelheid.

Het COSMOS-XS waarnemingsprogramma

In dit proefschrift maken we gebruik van het gevoelige COSMOS-XS waarnemingsprogramma. Dit programma stelt ons in staat om de met stof verduisterde stervorming te bestuderen. Uitgevoerd met de verbeterde VLA biedt het enkele van de gevoeligste radiowaarnemingen tot nu toe op twee golflengten: 10 en 3 GHz (ofwel de X en S band). Deze radiowaarnemingen richtten zich op het COSMOS veld, een veld van 2 deg^2 dat al vaak met behulp van verschillende toonaangevende instrumenten – zowel op aarde als in de ruimte – en op meerdere golflengtes onder de loep genomen werd. Door deze datasets te combineren hebben wij een unieke dataset gecreëerd waarmee zelfs de zwakste radiopopulaties bestudeerd kunnen worden. Het COSMOS-XS waarnemingsprogramma is daarbij een van de gevoeligste radiowaarnemingsprogramma’s tot nu toe. Het meet zwakke fluxdichtheden waarmee ‘normale’ sterrenstelsels kunnen worden waargenomen gedurende het tijdperk dat stervorming in het universum zo’n 10 miljard jaar geleden piekte. De analyse van het COSMOS-XS waarnemingsprogramma en de conclusies over de met stof verduisterde stervorming op hoge roodverschuiving zijn het onderwerp van dit proefschrift. De hoofdstukken worden hieronder samengevat.

Dit proefschrift

In dit proefschrift presenteren we de waarnemingen gedaan binnen het VLA COSMOS-XS waarnemingsprogramma. Onze bevindingen geven een nieuw beeld van de met stof verduisterde stervorming. **Hoofdstuk Een** introduceert de huidige stand van zaken in het bredere vakgebied. Het biedt de nodige achtergrondkennis om de daaropvolgende hoofdstukken te begrijpen.

In **Hoofdstuk Twee** bespreken we het COSMOS-XS waarnemingsprogramma in detail en presenteren we de radiocatalogi van de geobserveerde radiobronnen. Het tellen van het aantal sterrenstelsels of, in andere woorden, het vaststellen van het aantal bronnen, is de eenvoudigst mogelijke statistische analyse. Hoewel dit waarnemingsprogramma door flux gelimiteerd is, geeft het aantal sterrenstelsels informatie over de evolutionaire eigenschappen van deze bronnen. De gevoelige waarnemingen op 10 en 3 GHz geven ons de mogelijkheid om het euclidische genormaliseerde bronnen-aantal tot zwakke fluxdichtheden vast te stellen. We laten zien dat onze waarnemingen consistent zijn met andere resultaten op 3 en 1.4 GHz binnen de onzekerheden maar dat we het bronnen-aantal tot zwakkere fluxdichtheden kunnen vaststellen dan vorige waarnemingen.

In **Hoofdstuk Drie** gebruiken we het COSMOS-XS waarnemingsprogramma om stervormende sterrenstelsels te selecteren met behulp van de ver-infrarood-radio-correlatie. Deze sterrenstelsels worden gebruikt om de radioverdelingsfunctie van

de helderheden van sterrenstelsels te bepalen. De verdelingsfunctie van helderheden laat de verdeling zien van de kosmische dichtheid van bronnen over verschillende klassenbreedten van helderheid. Deze functie kan gebruikt worden om de evolutie van stervormende sterrenstelsels vast te stellen. Wij presenteren bewijs voor significante evolutie van dichtheid over het geobserveerde roodverschuivingsbereik. We gebruiken de radioverdelingsfunctie van helderheden om de met stof verduisterde dichtheid van stervormingssnelheid te meten tot een roodverschuiving van $z \sim 4.6$. Het niet door stof gehinderde waarnemingsprogramma wordt ook gebruikt om te bewijzen dat de dichtheid van stervormingssnelheid wordt onderschat op hoge roodverschuiving door studies die zich baseren op de ultravioletverdelingsfunctie van helderheden.

In **Hoofdstuk Vier** verschuift de focus naar ‘optisch donkere’ sterrenstelsels. We gebruiken het 3 GHz radiobeeld waargenomen in het COSMOS-XS waarnemingsprogramma om deze bronnen te identificeren. Met de nieuwe ‘Super-deblended’ ver-infraroodcatalogus – gecreëerd door een innovatieve ‘deblending’ techniek die met elkaar vermengde bronnen ontwart – achterhalen we de fotometrische roodverschuivingen van de ‘optisch donkere’ bronnen. De catalogus gebruikt de posities van de bronnen die waargenomen zijn met het COSMOS-XS waarnemingsprogramma als initiële informatie. We kunnen vaststellen dat de op de ‘Super-deblended’ catalogus gebaseerde ver-infrarood fotometrische roodverschuivingen tussen $z = 2$ en $z = 5$ liggen. Vervolgens stellen we vast hoeveel de ‘optisch donkere’ bronnen bijdragen aan de totale dichtheid van stervormingssnelheid met de methode beschreven in hoofdstuk drie. We kunnen concluderen dat deze bronnen een niet te verwaarlozen bijdrage hebben op hoge roodverschuiving.

Voortbouwend op de resultaten van hoofdstuk vier kunnen we in **Hoofdstuk Vijf** nieuwe ALMA waarnemingen van ‘optisch donkere’ bronnen presenteren. De ALMA waarnemingen geven een scan over het golflengtebereik van 84–108 GHz. Op deze manier zijn de waarnemingen gevoelig voor alle straling van CO in het kosmische volume zonder van te voren de specifieke CO-lijnen uit te kiezen. Met de ALMA scans kunnen we de spectroscopische roodverschuiving voor een kleine subgroep van 10 uit radiowaarnemingen geselecteerde ‘optisch donkere’ sterrenstelsels vaststellen. We vinden op CO gebaseerde roodverschuivingen die laten zien dat de uitgekozen ‘optisch donkere’ bronnen op roodverschuivingen liggen met $z \gtrsim 3$. We integreren de verdelingsfunctie van helderheden uit hoofdstuk vier tot de fluxlimiet die is gebruikt om de subgroep te selecteren en vinden zo dat de dichtheid van stervormingssnelheid overeenkomt met de dichtheid van stervormingssnelheid die werd gevonden voor de 10 met ALMA gedetecteerde ‘optisch donkere’ bronnen. Dit geeft aan dat deze bronnen van kosmisch belang zijn op hoge roodverschuiving.

Publications

An ultra-deep multi-band VLA survey of the faint radio sky (COSMOS-XS): ALMA confirms optically dark population at $z > 3$

D. van der Vlugt, S. Jin, J.A. Hodge & H.S.B. Algera
to be submitted to The Astrophysical Journal

(Chapter Five)

An ultra-deep multi-band VLA survey of the faint radio sky (COSMOS-XS): New constraints on the optically dark population

D. van der Vlugt, J.A. Hodge, S. Jin, H.S.B. Algera, S.K. Leslie, D. Riechers, H. Röttgering, V. Smolčić & F. Walter
2023, *The Astrophysical Journal*, 51, 131

(Chapter Four)

An Ultra-deep Multi-band VLA Survey of the Faint Radio Sky (COSMOS-XS): New Constraints on the Cosmic Star Formation History

D. van der Vlugt, J.A. Hodge, H.S.B. Algera, I. Smail, S.K. Leslie, J.F. Radcliffe, D. Riechers & H. Röttgering
2022, *The Astrophysical Journal*, 941, 10

(Chapter Three)

An Ultra-deep Multi-band VLA Survey of the Faint Radio Sky (COSMOS-XS): Source Catalog and Number Counts

D. van der Vlugt, H.S.B. Algera, J.A. Hodge, M. Novak, J.F. Radcliffe, D. Riechers, H. Röttgering, V. Smolčić & F. Walter
2021, *The Astrophysical Journal*, 907, 5

(Chapter Two)

A Multi-wavelength Analysis of the Faint Radio Sky (COSMOS-XS): the Nature of the Ultra-faint Radio Population

H.S.B. Algera, **D. van der Vlugt**, J.A. Hodge, I. Smail, M. Novak, J.F. Radcliffe, D. Riechers, H. Röttgering, V. Smolčić & F. Walter
2020, *The Astrophysical Journal*, 903, 139

An ALMA Survey of the SCUBA-2 Cosmology Legacy Survey UKIDSS/UDS Field: The Far-infrared/Radio Correlation for High-redshift Dusty Star-forming Galaxies

H.S.B. Algera, I. Smail, U. Dudzevičiūtė, A.M. Swinbank, S. Stach, J.A. Hodge, A.P. Thomson, O. Almaini, V. Arumugam, A.W. Blain, G. Calistro-Rivera, S.C. Chapman, C.-C. Chen, E. da Cunha, D. Farrah, S.K. Leslie, D. Scott,
D. van der Vlugt, J.L. Wardlow & P. van der Werf

2020, *The Astrophysical Journal*, 903, 138

Compact Star-forming Galaxies as Old Starbursts Becoming Quiescent

C. Gómez-Guijarro, G.E. Magdis, F. Valentino, S. Toft, A.W.S. Man, R.J. Ivison, K. Tisanić, **D. van der Vlugt**, M. Stockmann, S. Martin-Alvarez & G. Brammer
2019, *The Astrophysical Journal*, 886, 88

How AGN feedback drives the size growth of the first quasars

D. van der Vlugt & T. Costa

2019, *Monthly Notices of the Royal Astronomical Society*, 490, 4918

The size and shape of the Milky Way disc and halo from M-type brown dwarfs in the BoRG survey

I. van Vledder, **D. van der Vlugt**, B.W. Holwerda, M.A. Kenworthy, R.J. Bouwens & M. Trenti

2016, *Monthly Notices of the Royal Astronomical Society*, 458, 425

Curriculum Vitae

I was born in Hillegom on January 11th, 1994. After moving to the neighboring town of Lisse, I attended the Atheneum at the Fioretti College high school with a curriculum focused on science and technology. I decided to pursue a bachelor's degree in astronomy at the Leiden University. I undertook my bachelor's research with fellow student and friend Isabel van Vledder. We determined the size and shape of the Milky Way disc and halo using M-type brown dwarfs. We published our findings in *Monthly Notices of the Royal Astronomical Society*. Subsequently, I obtained my BSc in 2015.

I chose to continue onward with a MSc in astronomy at the Leiden University with the cosmology specialization. During this time, I was introduced to radio astronomy and studied the double radio relic system in PSZ1 G108.18-11.53 under the supervision of prof.dr. Francesco de Gasperin. In my master's thesis I learned about cosmological simulations and, under the supervision of dr. Tiago Costa, studied the effect of AGN feedback on the growth in size of the first quasars. This work was later published in *Monthly Notices of the Royal Astronomical Society*. I obtained my MSc from Leiden University in 2017.

In the same year, I was fortunate to secure a place in the PhD program at Leiden University, studying the dust-obscured star formation under the supervision of Dr. Jacqueline Hodge. During my PhD, I have written four scientific articles, have contributed to three more, and have presented my work at national and international conferences and workshops. In 2019, I was able to visit the Max Planck Institute for astronomy in Heidelberg for three months. For three semesters, I have been the teaching assistant for the course Bachelor Research Project. I was also involved in the bachelor's theses of Kasper Roewen, Lotte Jansen and Nikki Geesink and the master's project of Drishyaman Kashyap.

After more than a decade of astronomy at Leiden University, I will say goodbye to academia and astronomy. I am grateful for the years I have spent learning about the cosmos and I am excited to learn what the future will bring.

Acknowledgments

During my years at Leiden University – from the start of my bachelor to the end of my PhD – I have met a large number of amazing people. I hereby want to express my gratitude to those who have helped me, directly or indirectly, along the way. I have tried to be as comprehensive as possible while acknowledging that such an attempt will inevitably contain unintended oversights, for which I apologize.

First of all, I would like to acknowledge the scientific guidance from both Jackie and Huub throughout the last years as well as from Tiago, Francesco, Huib and Benne in the years prior. Thank you for the opportunity to work with you and your guidance along the way. I would like to thank all members of Jackie's Group, Alex, Cristy, Gaby, Ivana, Lucie, Marta, Matus, Piyush and Thomas, for the weekly discussions. I also enjoyed the meetings and discussions with Dazhi, Leindert, Paul, Sander and Rychard and the other Dust Mites attending the dusty galaxy meetings. I had the pleasure of supervising several excellent bachelor and master students. Drishya, Kasper, Lotte and Nikki: I learned a lot from supervising you; I wish you all a great future career. Not much science would get done at the Sterrewacht without the work of the secretaries and computer group. Thank you for making the day to day life at the Sterrewacht run smoothly. Then a word of gratitude to the people I have met along the way at the observatory. Dario, Dilovan, Omar, Patrick, Sarah and Turgay, you made the journey easier and I want to thank you for accompanying me. Kirsty and Hiddo, thank you for going with me on our post-conference journeys, I have some great memories of those trips.

Tenslotte wil ik een aantal mensen noemen waarvan de bijdrage aan dit proefschrift misschien minder direct, maar daarom niet minder belangrijk is. Allereerst mijn vrienden die ik al ken vanaf het begin van mijn studie: Bas, Irene, Isabel, Koen, Marlize, Marten, Matthijs en Peter. Dank voor alle lol tijdens game nights, etentjes en vakanties. Mijn ouders, broer en zusje wil ik bedanken voor hun liefde, steun en het feit dat jullie mij altijd aan het lachen weten te maken. Tot slot wil ik Anne noemen. Ik kan niet onder woorden brengen hoeveel je voor mij betekent. Zonder jou had ik dit niet kunnen bereiken. Ik hou van je.

